UNIVERSITY OF CALABRIA
DEPARTMENT OF MECHANICAL ENERGY AND MANAGEMENT ENGINEERING

PhD COURSE IN INDUSTRIAL AND CIVIL ENGINEERING

***XXX* CYLE**

STUDY OF AN UNFIRED CLOSED JOULE-BRAYTON CYCLE IN A CONCENTRATING SOLAR TOWER PLANT WITH A MASS FLOW RATE CONTROL SYSTEM

Scientific Disciplinary Sector ING-IND/09

Coordinator: Prof. Franco Furgiuele

Supervisor: Prof. Mario Amelio

Supervisor: Prof. Manuel Silva Pèrez

PhD STUDENT: Francesco Rovense

UNIVERSITÀ DELLA CALABRIA

UNIVERSITA' DELLA CALABRIA

DIPARTIMENTO DI INGEGNERIA MECCANICA ENERGETICA E GESTIONALE

Dottorato di Ricerca in Ingegneria Civile ed Industriale

XXX CICLO

STUDY OF AN UNFIRED CLOSED JOULE-BRAYTON CYCLE IN A CONCENTRATING SOLAR TOWER PLANT WITH A MASS FLOW RATE CONTROL SYSTEM

Settore Scientifico Disciplinare ING-IND/09

Coordinatore: Ch.mo Prof. Franco Furgiuele

Firma _____

Supervisore: Ch.mo Prof. Mario Amelio

Firma _____

Supervisore: Ch.mo Prof. Manuel Silva Pèrez

Firma _____

Dottorando: Dott. Francesco Rovense

Firma _____

"Tu ricordatelo, che sbagliare è facile, fare bene è molto difficile…"

Nonno Aldo

Contents

List of figure

List of table

Sommario

Oggigiorno, la domanda di energia primaria è aumentata, raggiungendo un incremento del 62.5% rispetto a 20 anni fa. La necessità di risorse rinnovabili ha spinto le politiche governative di tutto il mondo a incoraggiare lo sviluppo di nuovi sistemi di produzione di energia. Fra questi vi sono i sistemi a concentrazione solare (CSPs), una tecnologia che concentra la radiazione solare rendendola disponibile, attraverso un fluido termovettore (HTF) come fonte di calore in un ciclo termodinamico di potenza. Il ciclo di potenza più efficiente, come noto, è quello Joule-Brayton, che in configurazione chiusa consente l'utilizzo di HTF diversi; inoltre, è possibile lavorare in condizioni di pressione elevate, con alta temperatura operativa ed efficienza di conversione. L'uso dell'aria come fluido di lavoro rende di facile gestione il sistema senza rischi. Inoltre unendo il ciclo chiuso con un sistema CSP, il sistema è totalmente privo di combustione e non essendo necessario l'uso di combustibile, non sono emessi inquinanti. Fra i sistemi CSP, la tecnologia a torre è in grado di poter raggiungere più alte temperature, disponibile quindi nel ciclo Brayton, e per questo motivo è stato considerato il suo uso nelle analisi. La risorsa imprevedibile, rappresentata dalla radiazione solare, richiede un metodo di regolazione per il controllo della potenza generata dall'impianto. In questo lavoro, quindi, è stata analizzata la fattibilità di un ciclo Joule-Brayton chiuso senza combustione, in un impianto solare a concentrazione a torre che utilizza un sistema di controllo della portata massica. Nel ciclo è operato un controllo della temperatura di ingresso della turbina della turbina a gas, quando varia la radiazione normale diretta (DNI) attraverso la regolazione della densità del fluido di lavoro; questa regolazione è attuata attraverso una variazione di pressione di base del ciclo. In questo sistema la turbina gas non cambia la portata volumetrica come anche i triangoli di velocità o i rapporti di pressione, quindi variando la densità del fluido di lavoro, attraverso una variazione di pressione, è possibile regolare la portata massica al fine di controllare la TIT. Controllando la TIT, quindi, è possibile controllare la potenza elettrica prodotta dalla turbina a gas sotto diversi carichi termici del DNI. In questo lavoro, diverse configurazioni, in termini di potenza delle macchine, come anche l'utilizzo di accumulo termico (TES) sono stati analizzate, ponendo particolare attenzione alla progettazione

del campo eliostati. I risultati mostrano che l'efficienza globale del ciclo, rimane costante sotto differenti carichi termici dovuti alla radiazione solare, indipendentemente dalla potenza della turbina a gas; l'utilizzo di accumulo permette di aumentare le ore di utilizzo dell'impianto come anche il fattore di utilizzazione (UF). L'analisi economica, effettuata attraverso il metodo del Levelised Cost of Electricity (LCoE) ha reso possibile ottenere un valore del multiplo solare (SM) differente rispetto ai valori tipici usati. In fine è stata considerata l'applicazione in micro scala di questo tipo di impianto, al fine di confrontarlo con un sistema commerciale esistente.

Abstract

Nowadays, the primary energy demand has increased, rising up to 62.5% compared to 20 years ago. The necessity of the renewable sources has prompted the government policies, around the world, to encourage the development of new energy production systems. One of this is the Concentrating Solar Power system (CSPs), a technology that concentrates the solar radiation making it available, through a heat transfer fluid (HTF), as a heat source in a power thermodynamic cycle. The most efficient power cycle, as we know is the Joule-Brayton one, that in a closed configuration allows to use different HTF; in addition, it is possible to work under pressurized conditions, with high operating temperatures and overall cycle efficiencies. The use of the air, as HTF, makes it easy to manage the system under pressure without risk. Moreover coupling the closed cycle, with CSPs, the system is safely unfired, and no fuel is needed as heat source, therefore no pollutants are produced. In CSPs, the solar tower system is able to gain high temperature, available for the Brayton cycle, so this technology has been taken into account in these analysis. The unplanned source represented by the solar radiation, requires an adjustment method able to control the power production by the plant. In this work it has been analysed a feasibility of an unfired closed Joule-Brayton cycle, in a concentrating solar tower plant, employing a mass flow control system. In the cycle, in order to control the turbine inlet temperature (TIT) of the gas turbine, under Direct Normal Radiation (DNI) variation, a working fluid density adjustment is adopted; this regulation is performed by a base pressure adjustment. In this system, the gas turbine engine, does not change neither the volumetric flow rate nor the speed triangles and the pressure ratios, therefore varying the density of the working fluid, through a pressure variation, the mass flow rate it is adjusted in order to control the TIT. By controlling the TIT, by a mass flow variation, it is possible to control the electrical power produced by the gas turbine under different thermal loads of DNI. In this work, several configurations have been analysed, in term of engines power rate as well as the thermal energy storage (TES) employing, paying particular attention on the heliostats field design. The results show that, the overall cycle efficiency remains constant under different solar radiation loads, independently of the gas turbine power rate; the

as well as the utilization factor (UF). The economic analysis, performed by the Levelized Cost of Electricity (LCoE) method, allowed to obtain, a particular value of solar multiple (SM), for the analysed system, respect to the one used up to now . Finally was considered, a case of study of a micro scale application for this kind of plant, in order to compare with a commercial system.

Acknowledgements

I would like to thank my research supervisor Prof. Mario Amelio, of the University of Calabria, because he was not only a simply advisor, but a real guide during these past years.

I am also grateful to Prof. Manuel Silva Perez, from the University of Seville, for his valuable comments and suggestions and for giving me the opportunity to meet prominent members of the research world field.

I also want to thank Prof. Vittorio Ferraro and Prof. Michele Scornaienchi for their precious guidance and support.

I would like to thank all my University colleagues as well as the Group of Thermodynamics and Renewable Energy of Seville, for all their help and support.

Least but not last a very special thank you goes to my family, my girlfriend, my friends and all the people that constantly sustained me throughout all these years of hard work.

Introduction

Nowadays, the world population raise up with a speed of 1.18% per year; there is a totally annual increasing of about 83 million. The United Nation (UN), during 2015 (Figure 1), estimated the world population growth and established that, keeping constant the growth rate, there will be about 9 billion people by 2030 and 9.7 billion by 2050 [71].

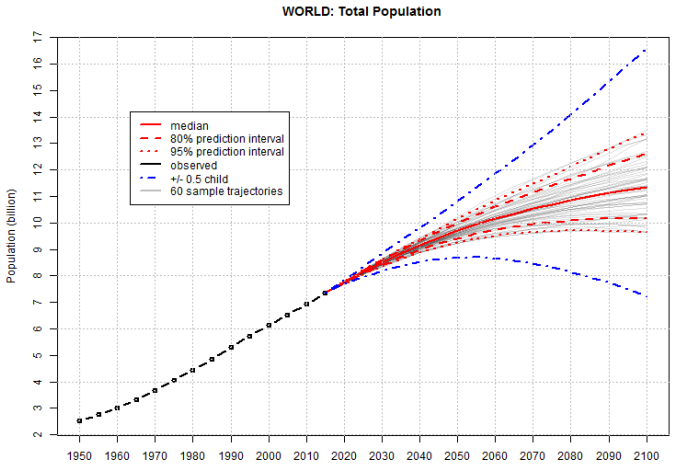

Figure 1: Demographic growth projection [71]

Energy consumptions are directly linked to this increase of population, therefore the requirement of primary energy resources is a perceived problem.

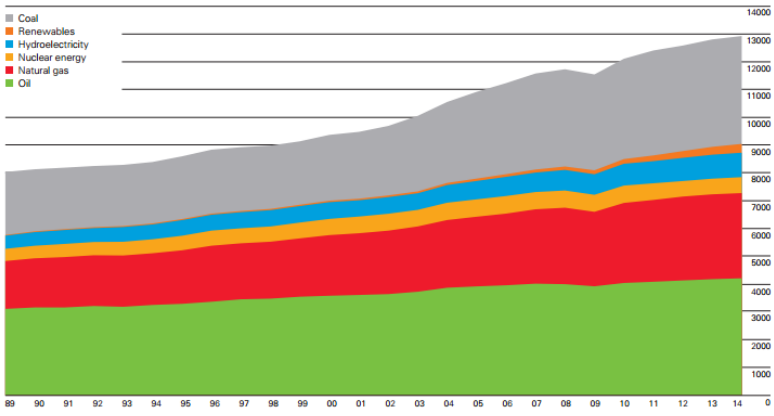

Figure 2: World Energy Consumption of Primary Energy in TEP [72]

A major security requirement of energy supply will be need, particularly in the presence of even much stronger restriction environmental impact laws.

Primary energy consumption refers to the direct use at the source, or supply to users without transformation, of crude energy, that is a type of energy not subjected to any conversion or transformation process. Some example are the exhaustible energy sources (coal, oil, etc.), renewable energy sources (solar, wind, biomass, hydro, geothermal…) and heat energy deriving from the ground of the Earth which allows to produce geothermic energy [72].

The measurement unit commonly used is TEP, (tons of petroleum equivalent, or TOE, tons of oil equivalent). 1 MTEP (10^6 TEP) is the energy content in one millions tons of oil that is equivalent to a 41.86 × 1015 Joule.

In last 25 years, from the 1990s up to the 2015, the primary energy demand has increased up to 8000 MTEP to 13000 MTEP, rising up to almost 62.5%.

Also, it is possible to observe from Figure 2, that 85 % of the total energy demand is satisfied by fossil fuels, while only a small part (orange trend) is supplied by renewable sources.

International energy policies, of the last years, promoted and incentivized the reduction of the environmental impact of thermoelectric power plants as well as greenhouse gases, using the development and diffusion of energy product by renewable energy source systems. An energy source is considered renewable, if it can regenerate itself in a short time, compatible with the human life cycle.

From the Kyoto protocol to the lasts European directives "2001/77/CE" / "2009/28/CE", a common framework for the promotion of energy from renewable sources have been established and mandatory national targets have been set. Regarding the European Union members states these objectives were set on June 30th 2010, the so called "20-20-20", which, among other goals, made mandatory the renewables contribution (20%) of the total energy consumption in a period of 10 years [73]. These policies have produced, naturally, big changes on electric systems and power grid: the plants performance of renewable system is totally dynamic, mainly because this kind of source is unplanned and random

so it is difficult a clear estimation of daily production. For this reason, actually renewable energy does not contribute to the frequency adjustment of the electricity grid. Employing the renewable sources connected to the grid trough the inverter generators, the rotating masses (generally employed in thermoelectric plants) are not used [75].

Renewable energy is an alternative to the traditional fossil fuel and some of it is not introduced pollutant substance, which are usually present in the atmosphere damaging the climate.

The following sources are considered renewable:

- Solar energy
- Wind energy
- Biomass
- Sea energy
- Hydroelectric source

Solar energy is the most widespread on the Earth because is renewable, available, completely free and largely in excess of the energy demand of the world population. It is necessary to pay attention that, every year, the sun irradiates on the Earth face about 19 billion of MTEP of energy, while the demand, as described before is about 13000 MTEP. The potential energy obtainable from the sun could be a large part of the electric demand.

Nowadays, it is used only a very small part of the huge quantity of energy coming from the sun. In perspective, solar energy will play a significant role, to allow the reversal of the current trend, which is essential for the ecology safe of the planet. The thermal energy arising from solar irradiation can be "intercepted" in many ways and used for various energy needs: for example, thermal energy could be useful for the production of hot water for primary necessities, instead of employing the solar thermal systems for the production of electricity [76].

There are three kinds of technology that allow to use the solar sources:

- Photovoltaic systems (PVs)

- Solar thermal systems (STs)
- Solar thermodynamics systems (CSPs)

Solar thermal technology is employed to produce heat (for primary necessity), while photovoltaic systems, as known, are suitable to generate electric energy.

Photovoltaics systems, convert directly global normal irradiance, incident on the panel surface, in electricity by employing semiconductor cells (Siliceous) trading on the photovoltaic effect.

Solar thermodynamics, called Concentrating Solar Power (CSP) systems, operates intercepting the direct normal radiation (DNI) by a concentrator, in a receiver, increasing the enthalpy of a heat transfer fluid. This energy is suitable for a power unit to produce electric energy or heat source.

CSP technology, started to be commercialized during the 1980's, after the first oil crisis, but the decreasing of oil cost and the development of photovoltaics plants declare a temporary downfall of this technology. One of the CSPs disadvantages is the "specific location" compared to the photovoltaics one; practically concentrating systems could gain good plant efficiency only through sites with high solar insolation [78]. These areas, particular adequate for this technology, are usually called "sun belt", shown in figure 3.

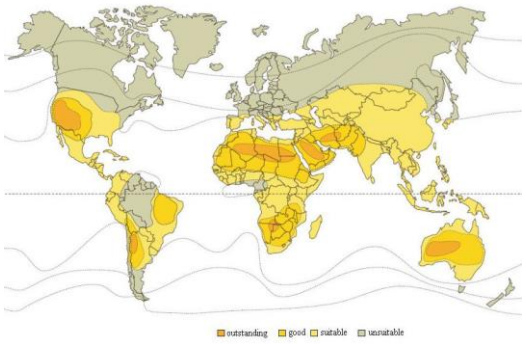

Figure 3: "Sun belt" in the World [77]

However, CSP technology has some advantages compared to the photovoltaic (PV) one [79]:

- It is possible to obtain a net conversion efficiency higher than the PVs;
- Possibility of storage, by the Thermal Energy Storage (TES) employing molten salt (or other heat transfer fluid) cheaper than the electrochemical storage systems used in the PVs;

Looking at this topic and considering the energy problems examined, the objective of this thesis is to demonstrate the feasibility of a closed Joule-Brayton cycle, in a Concentrating Solar Tower system (CSTs) as a heat source. It has been demonstrated that it is possible the use of air, as heat transfer fluid, without the use of fuel (so unfired). In the cycle is performed a mass flow adjustment, in order to control the Turbine Inlet Temperature (TIT). As will be explained, in this way the electrical power production will be controlled as well.

Firstly it has been used the Joule-Brayton cycle due to the fact that it has the highest the gas turbine yield of the cycle. Secondly, the Brayton cycle is useful in concentrating solar system, and in addition, the closed configuration allows to employing air as heat transfer fluid, working with high temperature obtaining excellent overall cycle efficiency.

The solar tower system, is the only CSP technology that makes it possible to gain high temperature, respect to other technologies, for this reason this kind of plant, has been taken into account in the analysis.

The exploration of the air as HTF, has been conducted because it is a totally free fluid, not polluting, and mainly, working under pressure condition, is not dangerous.

The unplanned source represented by the solar radiation, requires an adjustment method able to control the electrical power produced by the plant.

The core of this work is the mass flow control systems, employed in the cycle, to control the Turbine Inlet Temperature of the gas turbine under different solar radiations load.

In this kind of cycle, the volumetric flow rate, as well as the pressure ratio and the speed triangle of the gas turbine, do not vary; changing the base

pressure of the cycle, along with the average density of the working fluid, it is to obtain a mass flow variation.

Keeping fixed the main temperatures and pressures of the cycle, controlling the TIT it is possible to control the electrical power produced.

Different power rates, have been analysed, in different configuration (regarding the use of storage or solar multiple) to optimize the cycle and all component used in the system.

Particularly attention, will be focused on the design of solar field, because it represents the only heat source in the cycle and the major cost voice of the plant.

In chapter 1 it will be described the history of concentrating solar systems, the state of the art of the operational and R&D solar tower with gas turbine plants.

Chapter 2 will be dedicated to the model description of the mass flow control system studied in this work, and its parameters as well as the cycle optimization.

In chapter 3 there will be performed an analysis for different power rate sizes, at MW scale, of the gas turbine and of the heliostat field, along with the comparison with an open simple cycle.

In chapter 4 it will be considered the design of the heliostats field for the plant that has employed the control systems.

In chapter 5 a case of study using storage will be analysed; particular attention will be focused on the use of an innovative molten salt, cheaper and more suitable for the high temperature storage.

Chapter 6 will treats the simulation of the control systems and its advantages, in a modified micro gas turbine of a peak power of 500 kW.

Finally it will be presented, the conclusions of these analysis and the outlook for this kind of technology.

Chapter 1
Concentrating solar power (CSPs) system

1.1. Solar concentrating fundamentals

Solar radiation is an energy source at high temperature, with an available irradiance, near the sun, about of 65 MW/m^2. However only a very small part of this flux, about 1 kW/m^2, irradiates the Earth and is available, owing to the huge distance (149.600.000 km) between the Sun and our planet. It is possible to use this "low density" energy, employing optic concentrating systems.

Adding an optic device between the radiation source and the absorbent surface (receiver), it is possible to concentrate this radiation on a smaller surface, increasing the density and achieving both higher thermal flux and lower thermal loss. This mechanism allows to achieve high temperature on the receiver surface (absorber), and then increasing the conversion efficiency from heat to mechanical work.

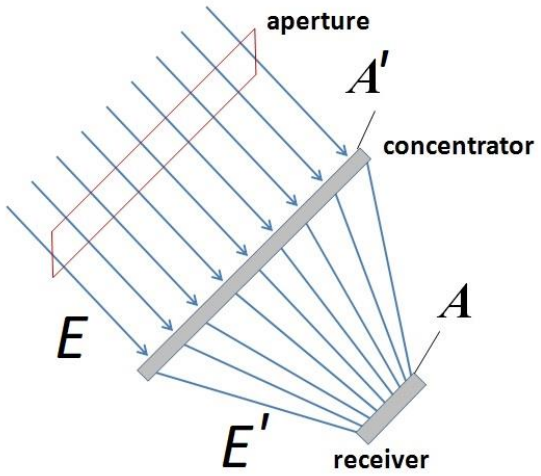

Figure 1.1 : Schematic solar concentrating fundamentals

In figure 1.1 it is possible to observe the operating fundamentals of concentrating technology; flux E across the A section and exit from A' < A.

Assuming that there are no losses inside the concentrating system, we can write the following conservation law:

$$E \cdot A = E' \cdot A' \qquad (1.1)$$

The geometric concentrating ratio, so, has been defined as:

$$C = \frac{A}{A'} \qquad (1.2)$$

This ratio has an upper limit depending of the kind of concentrating system, which could have two configurations:

- Three-dimensional (point-focus);
- Bi-dimensional (line-focus).

The upper limit for three- dimensional system, could be described following the Rabl methodology [1]

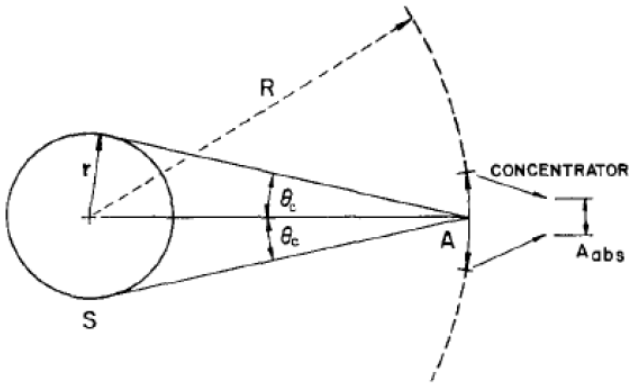

Figure 1.2: Schematic solar concentrating fundamentals

The Sun (S) and the absorbent surface (A_{abs}) were considered as black bodies. The Sun could be assumed as isotropic sphere having radius r and a distance from the Earth R. The temperatures assumed for the Sun and absorbent surface are respectively T_s and T_{sa}. The black body is defined as an ideal body or surface that completely absorbs all radiant energy incident upon it, with no reflection and that radiates at all frequencies with a spectral energy distribution dependent on its absolute temperature. Then, it is possible to write:

$$\alpha = \varepsilon = 1 \qquad (1.3)$$

$$\tau = \rho = 0 \qquad (1.4)$$

Referring to figure 1.2 and considering an ideal concentrating system, the incident irradiance on absorbent surface is proportional to the radiation intercepted by the aperture A. This effect is expressed by the equation:

$$Q_{rad} = 4\pi r^2 \sigma T_s^4 \qquad (1.5)$$

Where σ is the Stefan-Boltzmann constant. The view factor is defined below F_{S-A}:

$$F_{S-A} = \frac{A}{4\pi R^2} \qquad (1.6)$$

Replacing the equation (1.6) in (1.5) we obtain:

$$Q_{rad,S-A} = F_{S-A} \cdot Q_{rad} = A\,\frac{r^2}{R^2}\sigma T_s^4 \qquad (1.7)$$

Following the same methodology for the receiver (absorbed) surface:

$$Q_{rad,as} = A_{as}\sigma T_{as}^4 \qquad (1.8)$$

Also defining for this case, the view factor$F_{A_{as}-S} < 1$, and replacing in (1.8) we obtain:

$$Q_{rad,A_{as}-S} = F_{A_{as}-S} \cdot Q_{rad_{as}} = A_{as}F_{A_{as}-S}\sigma T_{as}^4 \qquad (1.9)$$

Under steady state conditions, both bodies havet the same temperature T; it is possible to write the following equality between flows:

$$Q_{rad,S-A} = Q_{rad,A_{as}-S} \qquad (1.10)$$

Replacing (1.7) and (1.9) in (1.10) equation, we obtain:

$$A\frac{r^2}{R^2}\sigma T^4 = A_{as}F_{A_{as}-S}\sigma T_{as}^4 \qquad (1.11)$$

From this last equation, the concentration ratio is obtained:

$$C = \frac{A}{A_{as}} = \frac{R^2}{r^2} \cdot F_{A_{as}-S} = F_{A_{as}-S} \cdot \frac{1}{sen^2\theta} \qquad (1.12)$$

Analysing the (1.12) it is obvious that the following inequality will always be valid:

$$C \leq \frac{1}{sen^2\theta} \qquad (1.13)$$

If the absorbent surface is added in a transparent medium, of refractive index *n*, the incident radiation is enclosed in the range ± θ with $\theta \leq \theta_n$.

According to the Snell law, when the medium changes, the following equation keeps constant:

$$\frac{sen\ \theta_c}{sen\ \theta_n} = \frac{n}{n_c} \qquad (1.14)$$

Where:

- θ_c is the incidence angle;
- θ_n is the refraction angle;

Assuming, hypothetically, n_c=1 we have:

$$sen\theta_n = \frac{1}{n} sen\theta_c \qquad (1.15)$$

The half-opening θ_c angle for the Sun-Earth system is 4.653 mrad. Consequently, for a three-dimensional concentration system, the ratio of maximum concentration is:

$$C_{3D} \leq \left(\frac{1}{sen^2\theta_c}\right) \approx 46225 \quad (1.16)$$

This limit can be reached with an ideal three-dimensional concentrator. For a two-dimensional concentration system, we have:

$$C_{2D} \leq \left(\frac{1}{sen^2\theta_c}\right) \approx 215 \qquad (1.17)$$

The obtained value (C_{2D}) is significantly lower than the three-dimensional one (C_{3D}), so a higher temperature of heat transfer fluid (in general) could be reached in solar tower, compared to the parabolic trough collector. This topic will be in depth explained in the following sessions.

The available power, upstream of the concentration system, can be obtained with the equation (1.18), however only a part of this power will be transferred to the receiver.

The relation between these two powers determines the optical efficiency of the concentration system:

$$\dot{Q}_{disp} = \int_S I_{b,n} dS \qquad (1.18)$$

$$\eta_{opt} = \frac{\dot{Q}_{rec}}{\dot{Q}_{disp}} \qquad (1.19)$$

The receiver has been designed to absorb the maximum power from the solar radiation concentrated on it; an ideal receiver, in fact, it has a thermal behaviour like a black body and the only loss is for radiative emission.

In real applications, the same situation does not occur because there are other losses: an example are the convention losses. When the solar rays are concentrated on the receiver surface, its temperature begins to increase together with the loss mechanisms.

This process is time-variant until the stationarity conditions are not achieved: at this point, the input power, coming from the concentration system, matches the sum of the power transferred to the heat transfer fluid while it takes from the thermal and optical losses. A part of the input thermal power is absorbed by the surface; the other part is reflected and transmitted according to the optical properties of the absorber surface.

The power transferred to the heat transfer fluid is:

$$\dot{Q}_{abs} = \dot{m}_{HTF}(h_{out} - h_{in}) \qquad (1.20)$$

Where:

- $\dot{m}_{HTF}$ is heat transfer fluid mass flow rate (kg/sec)
- $(h_{out} - h_{in})$ is the enthalpy variation from inlet and outlet of the receiver (J/kg)

Total inlet thermal power includes the absorbed power and the losses:

$$\dot{Q}_{in} = \dot{Q}_{abs} + \dot{Q}_{loss} \qquad (1.21)$$

Explicate the $\dot{Q}_{loss}$ we obtain:

$$\dot{Q}_{loss} = \dot{Q}_{rad} + \dot{Q}_{conv} + \dot{Q}_{cond} + \dot{Q}_{rifl} \qquad (1.22)$$

From all these losses explained in (1.22), the most significant is the radiation loss: the surface of the receiver emits thermal power proportional to the fourth

power of the temperature; it is clear that this is a phenomenon which dispels a lot of energy. In order to simplify the discussion, constant receiver surface temperature is assumed; the power lost by radiation is equal to:

$$\dot{Q}_{rad} = \varepsilon\sigma A_{rec} F_{r-ex}(T_{rec}^4 - T_{ex}^4) \qquad (1.23)$$

Where:

- A_{rec} is the scatter receiver surface [m²];
- T_{rec} is the scatter homogenous surface receiver temperature [K];
- T_{ex} is the ambient temperature [K];
- $F_{r\text{-}ex}$ is the view geometric factor receiver-external ambient.

The air motion around the receiver causes convection losses; in almost all of them CSP plants are the sum of two contributions: forced convection caused by wind and natural convection are caused by local temperature gradients. It is difficult to evaluate these losses, because very often there are influenced by the radiation and vice versa.

There are numerical methods that, albeit with great approximation, allow to separate the two contributions [2]. A general expression for this kind of loss is:

$$Q = hA_{rec}(T_{rec} - T_{ex}) \qquad (1.24)$$

Where:

- h is average heat transfer convective coefficient (W/m²K)

There is reflection loss because the receiver is not a (perfect) black body and, therefore, it cannot absorb all of the incident radiations. One part is absorbed and the other is reflected:

$$\dot{Q}_{refl} = (1 - \alpha)A_{rec} C I_{b,n} \qquad (1.25)$$

Finally, the conduction losses (one-dimensional) can be expressed by (1.26):

$$Q_{cond} = K\frac{S}{L}(T_{s1} - T_{s2}) \qquad (1.26)$$

Where:

- K is the thermal conductivity of the material [W/m K];
- L is the thickness [m];

- S is the dispersing surface[m²];
- $(T_{s1} - T_{s2})$ is the temperature difference between the two sections [K].

The receiver efficiency can be expressed as:

$$\eta_{rec} = \frac{\dot{Q}_{in} - \dot{Q}_{loss}}{\dot{Q}_{disp}} \qquad (1.27)$$

To evaluate the dependence of this efficiency on the surface temperature and the concentration ratio, conduction and reflection losses can be neglected in a first approximation. Combining the relations (1.23), (1.24) and (1.25) we get:

$$\eta_{rec} = \alpha - \frac{\varepsilon\sigma(T_{rec}^4 - T_{ex}^4)}{\mathrm{CI}_{b,n}} - \frac{h(T_{rec} - T_{ex})}{\mathrm{CI}_{b,n}} \qquad (1.28)$$

Assuming, hypothetically that:

- $\varepsilon = \alpha = 0.97$
- $T_{ex} = 298\ K$
- $\mathrm{I}_{b,n} = 850\ W/m^2$
- $h = 20\ W/m^2K$

In figure 1.3 it has been shown the trend efficiency as function of the source temperature for different concentration ratio (C).

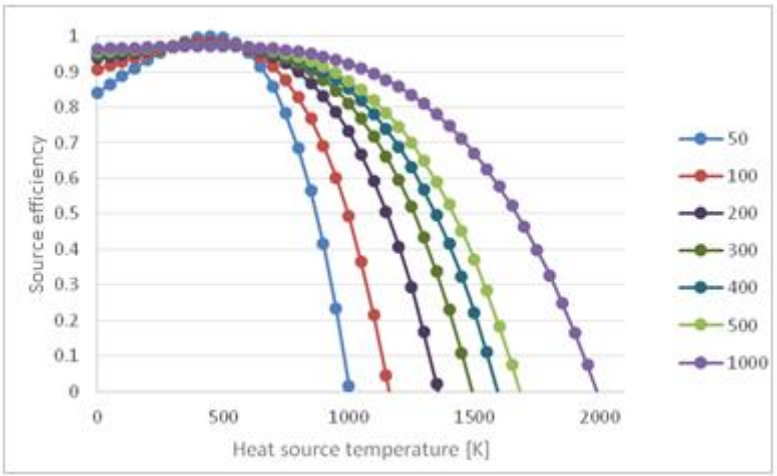

Figure 1.3: Solar collector efficiency vs source temperature for different concentration ratio.

Increasing the temperature, automatically the radiation and convection losses rise as well. When losses match the energy produced, the net useful energy is nil and the receiver achieves its maximum temperature [3]. In practice, the coefficients α and ε cannot be considered constant along the entire solar spectrum. It is preferred to achieve a receiver with higher absorption coefficient and lower possible emissivity. Typically, selective coatings compose the absorbing surface, which plays a fundamental role in stabilizing the losses [4].

According to Kirchhoff's law, in thermal equilibrium (constant temperature), for a particular surface, we have that:

$$\varepsilon(\lambda) = \alpha(\lambda) \qquad (1.29)$$

If the solar spectrum and the radiation spectrum, emitted by the receiver, are sufficiently different from each other, it is possible to use a material whose α is characterized by a strong dependence on the wavelength, to obtain high values of α and low emissivity values ε [5]. This is a proven fact because the solar spectrum is comparable to the one of a black body at a temperature of 5777 K, while a solar receiver can reach temperatures in the range of 1000 ° C during its operation.

The best solution, therefore, is to obtain high values of α in the range of visible light (390 - 700 nm) and, at the same time, to limit the emissivity ε to the range 700nm – 1mm, below the infrared.

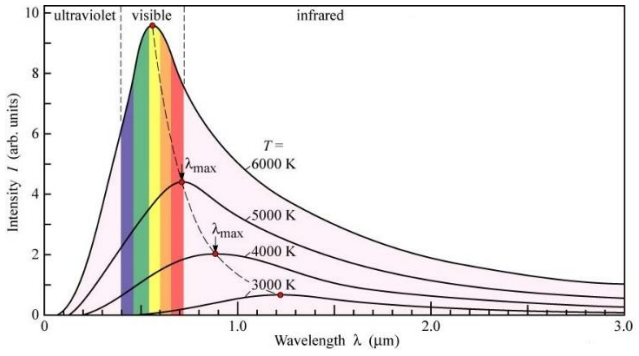

Figure 1.4: Black body emission spectrum, for different temperatures

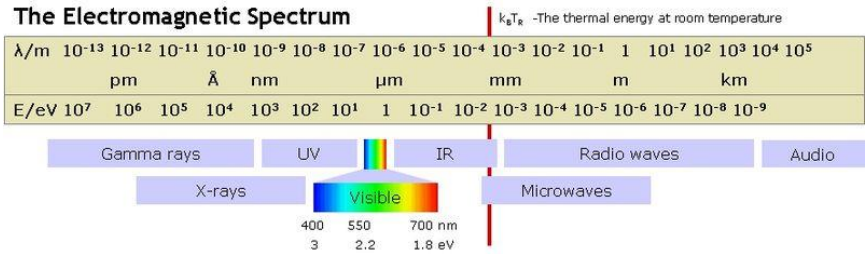

Figure 1.5: Electromagnetic spectrum and visible radiation range

The reason for which it is necessary to have the highest receiver temperature possible is related to the conversion efficiency: a higher temperature allows to gain a higher conversion efficiency.

Usually the heat produced by concentrating systems, it is converted into mechanical work, by means of conventional generation systems (thermodynamic cycles) and, subsequently, in electricity. It is possible to evaluate the global efficiency of the system, linking the receiver efficiency with the one of an ideal Carnot cycle, operating between the receiver temperatures and the ambient.

Considering the following equation:

$$\eta_{Carnot} = 1 - \frac{Q_{out}}{Q_{in}} = 1 - \frac{T_{ex}}{T_{rec}} \qquad (1.29)$$

From the product between the Carnot efficiency, defined by (1.29), and the receiver efficiency, obtained with the (1.28), overall efficiency has been evaluated:

$$\eta_{Overall} = \eta_{Carnot} \cdot \eta_{rec} \qquad (1.30)$$

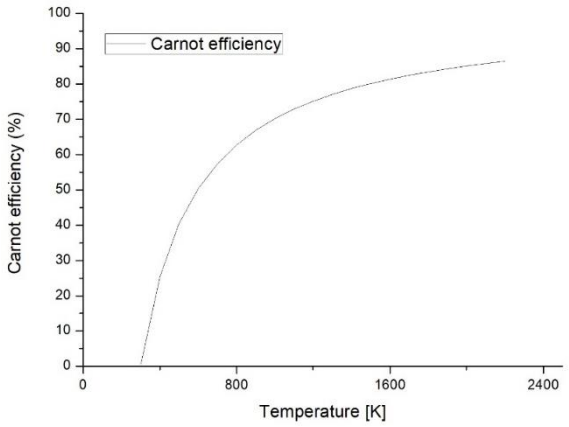

Figure 1.6: Carnot efficiency vs temperature

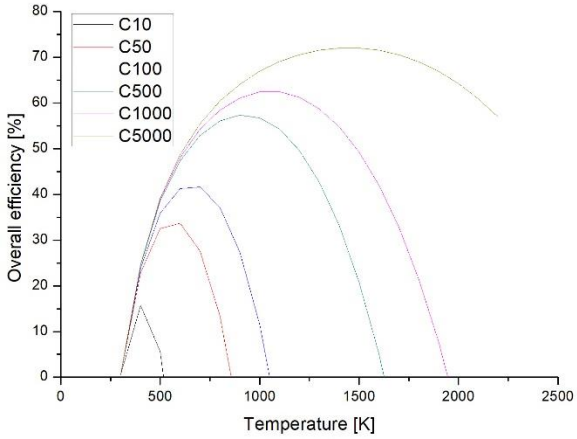

Figure 1.7: Global efficiency vs temperature for different concentration ratio C

Observing the trend in figure 1.7 appears that there is an optimum operative temperature for every concentration ratio; this optimum temperature can be calculated by calculating the derivate of the overall efficiency with respect to temperature equal to zero:

$$\frac{\partial \eta_{Overall}}{\partial T} = 0 \qquad (1.31)$$

This temperature will be the optimal temperature for the operation of the solar receiver and it is an important parameter for a CSP plant.

1.2. Brief history of the concentrating solar technology

The technology of concentrating solar plants is often traced to the legend of the "burning mirrors" of Archimedes. The development for the purpose of energy production of solar concentration technology was at the began at the last century with prototypes already very similar to the current ones, in shape and concept.

In this regard, it can lead as an example the plant built by Frank Schumann (1862-1918) in Egypt, which was completed in 1912. The system was used for the production of steam, to pump water from the Nile with storage in hot water (Figure 1.8).

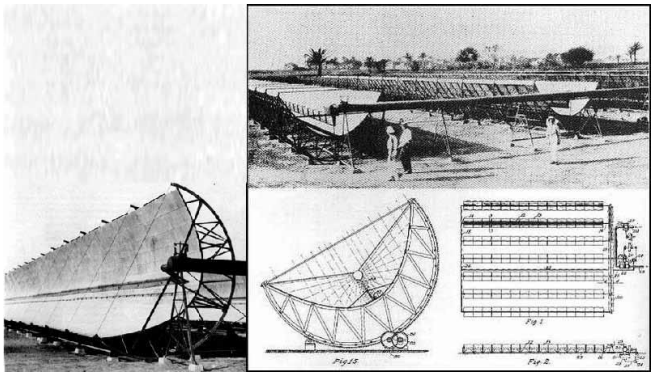

Figure 1.8 : Linear Parabolic Solar System (44-51 kW) built by Frank Schumann at Meadi in Egypt in 1912

The real development started, however, in the 60s and 70s in the United States, in France and in Russia, through experiments related to the strength of materials subjected to high radiant flux and high temperatures caused by the solar concentration.

Professor G. Francia in 1964 created a system of mirrors with fixed directional linear collector, which is prior to the current technology of Fresnel mirrors. The absorber were protected by honeycomb cells to decrease the losses due to convection and radiation.

The plant that applied these concepts, built in Marseilles, was able to produce steam that was collected from the top of the collector and was intended to give power to a turbine in order to produce power generation (Figure 1.9).

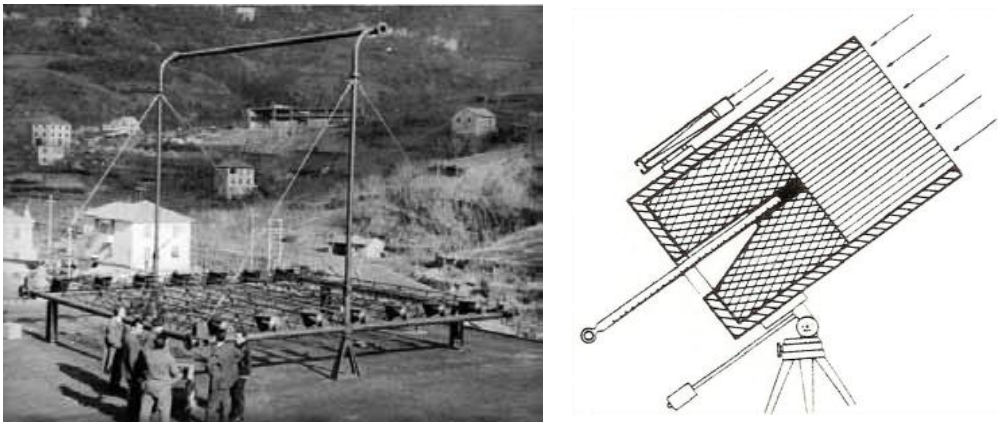

Figure 1.9: Concentrating solar system with linear mirrors and honeycomb absorber for steam production (left), absorber diagram (right).

After these pioneering achievements in the late '70s, the Plataforma Solar de Almeria was created, thanks to an European collaboration, dedicated to research on solar concentration and other environmental applications of solar energy. Following, the first real installations were built in Adrano (Sicily) in 1981; the Eurelios project was the first solar tower system built in the world. the International Energy Agency's Small Solar Systems

The tower (IEA-SSPS) was built the nor of the national Spanish project Central Electro solar de Almeria-1 (CESA-1). The IEA-SSPS project was the first demonstration project that delivered electricity to the grid in Europe. The combination of the IEA-SSPS and CESA-1 infrastructures in around 1987 was the origin of the Plataforma Solar de Almeria, which has played a pivotal role in the second take-off of CSP technologies worldwide.

Another important project was VastSolar sodium receiver modular technology demonstration plant, in Australia, or of Graphite Solar Power graphite storage tower technology demonstration plant also in Australia.

In the middle of the 80's also began the construction of parabolic trough plants (United States) and also started the first tests on the Dish-Stirling technology (parabolic dish) [39].

1.3. Concentrating solar technology

A generic CSP (Concentrated Solar Power) plant is characterized by its own main components:

- Concentration and reflection system;
- Receiver;
- Heat transfer fluid;
- Storage system;
- Conversion system or power unit.

With regard to this last component, the conversion unit choice has been usually made on the economic evaluation and on the use heat-produced: air conditioning, generation of heat for industrial processes and for the production of energy.

Concentration solar plants can be divided into two main groups: line focus and point focus, and are respectively two-dimensional concentration and three-dimensional systems.

As mentioned previously, the first kind has the concentration ratios C = 25-26 and maximum temperatures not more than 550 ° C, the second one however, could have a concentration ratios C> 500 and maximum temperatures of about 1000 ° C.

Nowadays, the market leaders are the parabolic trough system , due to their relative ease construction. Central Receiver Systems (CRSs) are experiencing a very rapid growth period as all efforts to lower their LCOE (Levelized Cost of Energy) are yielding their benefits.

1.3.1. Linear Parabolic Collectors (PTCs)

The concentration system consists of parabolic mirrors which rotate on a single axis. These mirrors reflect and concentrate the direct normal radiation on a receiver tube placed in the optical axis of the cylinder.

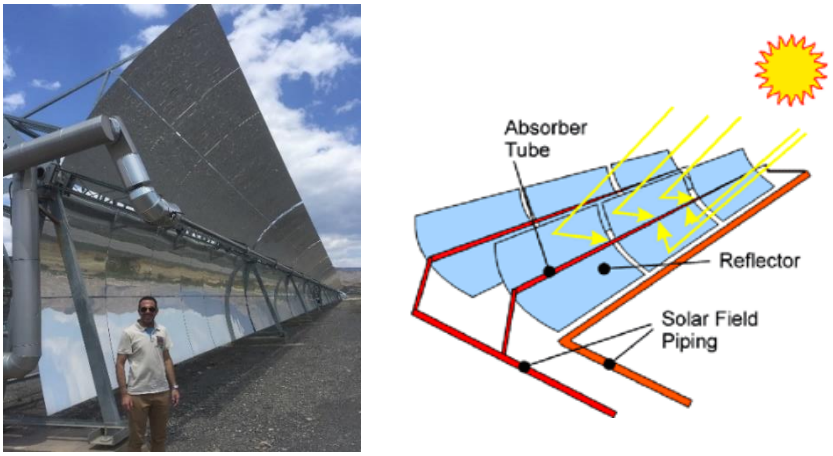

Figure 1.10: Parabolic linear collectors

They have an average concentration ratio of about 60-100; the heat transfer fluid flows inside the receiver tube, absorbing heat and reaching the desired temperature. A series of heat exchangers (evaporators, super heaters, condensers) located downstream of the solar field, allow the generation of steam, which is then expanded into a turbine.

The structure is made of galvanized steel. The reflector, with the receiver, moves, rotating around an axis, called tracking axis, which follows the Sun in its apparent motion in the sky.

In figure 1.11, it is possible to observe a typical parabolic troughs technology, of 50 MWe size (such as Andasol-1 for example), which uses synthetic oils such as heat transfer fluid and mixtures of molten salts for energy storage.

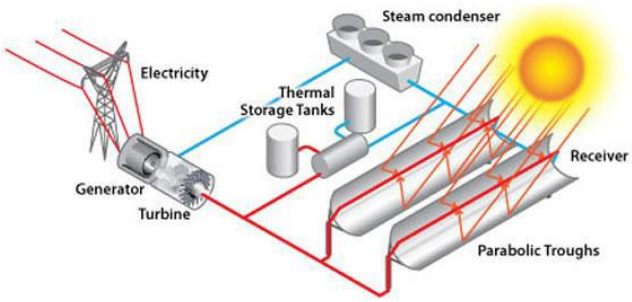

Figure 1.11: Parabolic troughs collector system

The performance of this type of plant is strongly influenced by the heat fluid transfer. It works with synthetic oils with temperatures above 200 ° C: VP-1, an

eutectic mixture consisting of 73.5% of diphenyl oxide and 26.5% of biphenyl is the most used synthetic oil with a maximum temperature of about 395 ° C. The most important factor to consider is the stability of the heat transfer fluid: solidification at about 14 ° C requires the use of auxiliary heating systems; the maximum temperature limit also places a limit on the thermodynamic efficiency of the power cycle. Several research programs have concentrated their work on the study of alternative fluids: molten salts, atmospheric air, water / steam [3].

The DISS project in started 1999 (Direct Solar Steam) at the Almeria Solar Platform in Spain, to facilitate the production of steam and to avoid losses of irreversibility of heat exchange in the exchangers; steam at 100 bar and 400 ° C has been generated directly within the linear receiver. Although this solution seemed very advantageous, there has been a small increase in the efficiency of the plant but great difficulties in dealing with a more complex two-phase fluid and storage systems [6].

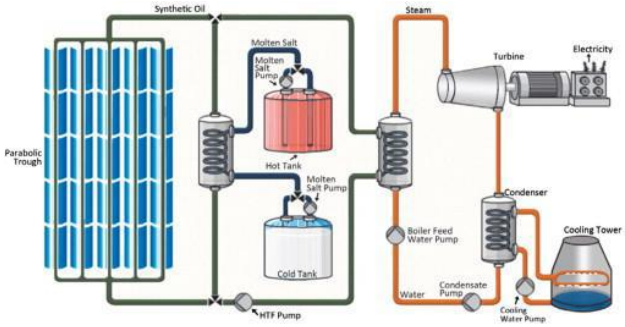

Figure 1.12: Direct Solar Steam System Plant

When the energy storage becomes a priority, the best performing fluid so far is a mixture of molten salts: that consists in a mixture composed of 40% of potassium nitrate (KNO3) and 60% sodium nitrate (NaNO3). High availability, low cost, non-flammability, high thermal capacity and temperatures in the range between 260-600 °C make this fluid directly usable both as a heat transfer fluid in the field of linear parabolic collectors as well as a storage medium.

The first company to investigate the operation of PTC plants with molten salts was the "Archimede Solar Energy Company", that produced a molten salt plant and also used selective coatings, able to withstand the higher temperatures for the molten salts, for the linear receiver. [7]

Unfortunately, despite all the benefits that molten salts can offer, their solidification occurs at very high temperatures (238° C) which represents a problem rather important, during cold start-up [8].

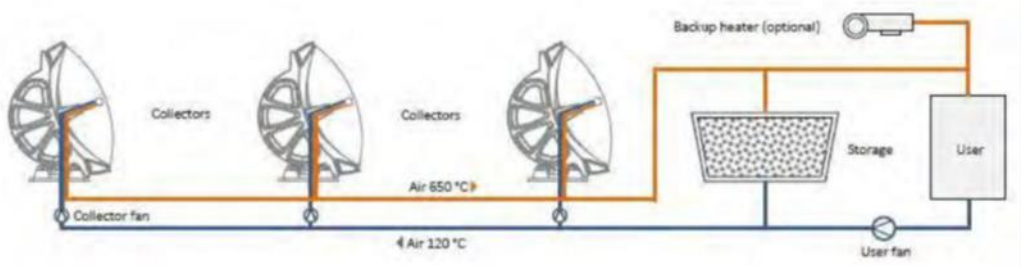

Figure 1.13: Pressure Air System Design

Finally, even the used as the heat transfer fluid from the Airlight Energy has realized that linear parabolic collectors pressurized air at 650 ° C. The system schematization is shown in figure 1.13, as possible to observe the reflective surface of which is made with thin polyester film and the accumulation is based on siliceous sand masses.

The receiver of a linear parabolic collector, typically, is a tube made in steel surrounded by another glass tube. Vacuum is applied between the two tubes reducing convection losses [83]. On the steel tube, instead, there are selective coatings to obtain low emissivity (<30% in infrared) and high absorption coefficient (> 90%).

These coatings are used to reduce radiation losses and to increase the performance of the solar field [3]. The parabolic troughs are already the most developed form of technology, covering 80% of the total installed power CSP, with global efficiencies of 14-16% [9], offering modularity, cogeneration and hybridization possibility.

1.3.2. Linear Fresnel Reflectors (LFR)

Fresnel reflectors, shown in figure 1.15, are in essence a series of reflective elements, which are distributed linearly along a surface and constitute a larger reflector. Many files of these reflectors focus on the solar radiation on a linear receiver positioned parallel to the axis of rotation of the reflector. Also on the same receiver, a parabolic collector is installed, in order to optimize the interception of solar radiation.

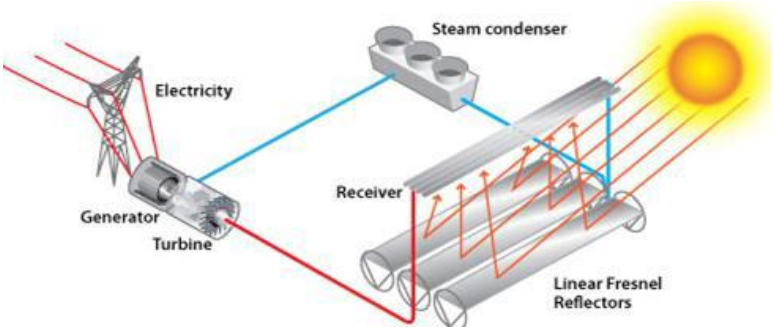

Figure 1.14 : Linear Fresnel reflector system

Figure 1.15 : Linear Fresnel reflector system in "Plataforma Solar de Almeria"

In the receiver tube, flows the heat transfer fluid, which usually consists of water. The water mainly used because there is no need of an additionally heat exchanger. Since Fresnel reflectors are the less efficient among the four CSP technologies analysed, adding heat exchanger would worsen even more the overall efficiency. The advantage of this technology is represented by the low cost of realization: each reflective element, in fact, has the same size and can be oriented. This allows the use of mirrors almost flat or slightly curved. Taking advantage of low costs and using in a smart way the land available, one can conceive a simple and inexpensive facility, though not very efficient, with the overall efficiencies not exceeding 12% [9]. Last researches in particular are pushing LFR to a different level which (called Advanced LFR), with higher performance second stage concentrators and new primaries (eaten due matched) to operate at higher temperatures than PTs even, at higher efficiency

and lower cost. With these kind of technology is expected to achieve annual plant efficiencies (solar to electricity) of up to 15%, operating directly with molten salts as heat transfer fluid [121].

1.3.3. Parabolic Dish Collectors (PDCs)

The parabolic dish collectors are three-dimensional concentrators; in fact, the solar radiation is focused on a point, using the two axis solar tracking systems. The receiver is located on focal point of the parabolic dish and, usually, the power unit is a Stirling engine, or in some experimental applications, a micro gas turbine.

Figure 1.16: Parabolic dish

The ideal shape of the reflective surface (paraboloid) allows to reach very high concentration ratios (> 1000). The parabolic dish systems reach high temperatures (> 750 ° C) and thermal flows on equally large receivers, and have a conversion efficiency that could reaches about 25-28% [9].

The size of the dish depends on the desired power level and conversion efficiency: a 5-kWe Stirling engine requires a disk of about 5 meters in diameter, while for a 25 kW_e plant a 10-meter diameter is sufficient.

The advantages of these systems include modularity, the ability to build standalone systems and the absence of cooling systems. On the other hand, the main disadvantage is the inability to accumulate thermal energy.

Parabolic dish systems although are already technologically developed, they have very high maintenance cost due to mechanical failure and thermal fluid leakage [82] (helium and hydrogen in Stirling engines).

From an economic point of view, these systems are not comparable with photovoltaic PV systems, as they also do not allow energy storage (cheap) and have a specific cost of about $ 2000 / kW against the $ 10,000 / kW of PDC systems [10].

1.3.4. Concentrating panel photolytic system(CPV)

CPV systems concentrate the solar beams on the PV (photovoltaic) cells . High performance PV cells are expensive and CPV collectors overcome this drawback. In CPV collectors, concentrated solar beams are reflected on the PV cells which are more cost-effective than stand-alone PV cells.

Therefore, the efficiency of this system would be higher than a common PV cell and this enhancement occurs with lower costs. On the other hand, the number of PV cells would be decreased by using CPV collectors. Also, PVT collector needs to be taken into account to generate both thermal and electrical energy simultaneously.

The back temperature of PV cells would be a waste heat recovery for increasing the performance of these cells by cooling and absorbing the thermal energy for other applications such as space heating or water heating.

CPVT system is a hybrid application of PVT(Photovoltaic Thermal) and CPV collectors for achieving more performance. There are two disadvantages of PVT systems. First, generating desired amount of electrical energy from PV cells needs high investments. Second, the thermal energy of these systems are used for only low-temperature applications.

In a CPVT system, both of these demerits are covered by maintaining the PV cells in a moderated temperature and utilizing the spectrum concentration. In Figure 1.17 it is shown a CPVT system.

Figure 1.17: Concentratin Photovoltaic panel

1.3.5. Solar tower systems with central receiver (CRS)

In these systems, a solar field composed by some mirrors, also known as heliostats, collect and concentrate the energy coming from the Sun on the receiver, placed at the top of a tower. The thermal power available to the receiver is then converted into mechanical energy by the power unit.

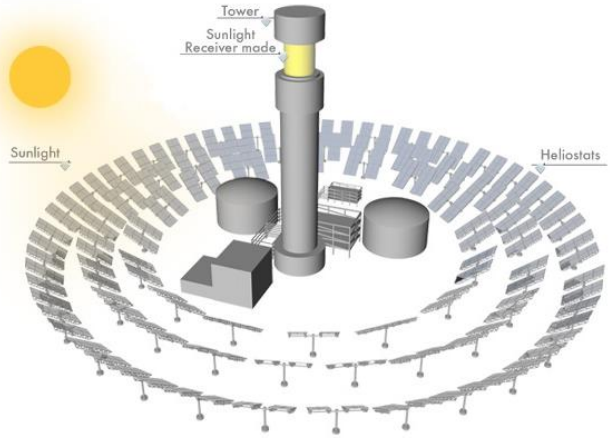

Figure 1.18: Solar tower system with central receiver

1.4. Solar tower system technology

This thesis focuses on the point-focusing systems and in particular, on the concentrating solar plants with a central receiver. For this reason in a deeper way, these systems are going to be described and analysed in the following sessions. The choice of using this technology is due to the following reasons:

- the possibility to obtaining a higher output temperature from the receiver due to the high concentration ratio, greater than the other technologies (line-focusing);
- the possibility to use air as a heat transfer fluid (fluid work);
- last but not least, high prospects in order to improve from a technical and costly points of view.

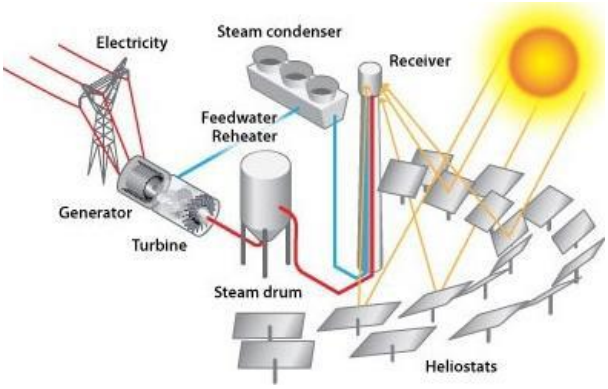

Figure 1.19: CRS plant design with direct steam production

In figure 1.19 it possible to observe a tower system; the heat transfer fluid in this case is a two-phase water-steam mixture. The feed water trough, found in the receiver, is heated by the solar radiation from the heliostat field; the steam is thus generated and evolves in the turbine and then is condensed. This type of system is not the only existing solution, but it is useful to identify the basic parts of which each plant CRS is composed. With reference to what has just been said, and observing the simplified block diagram in figure 1.20, any CRS system is divided into four basic parts:

- heliostats field;
- receiver (located at the top of the tower);
- power conversion system (power block);
- storage system (if it is provided for storage);

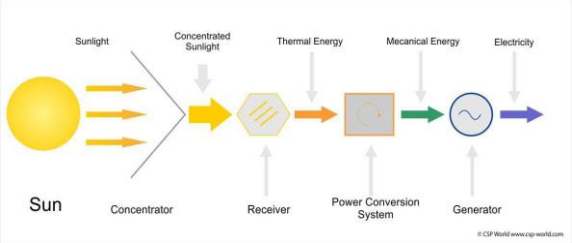

Figure 1.20: CRS plant operation fundamentals diagram

1.4.1. Heliostats field

The collection system of a central receiver tower system has the function of interception, reflection and concentration of direct normal radiation on the receiver. The system consists of heliostats, a tracking system, an optical forecasting system, solar tower, receiver and second concentrator.

The control system has the task of controlling the servomotors placed on the base of heliostat rotation system in order to defocus it when the thermal incident power on the receiver exceeds the maximum admissible value to avoid breakage.

1.4.2. Heliostats

The heliostats constitute the element through which is intercepted and reflected the solar radiation. The reflective element is composed by a series of polished panel mirrors with low iron content to prevent rust phenomena, since the heliostats are exposed to atmospheric agents [11]. The panels are installed on a structure to form a single module, or a single heliostat, with the possibility to realize a slightly concave shape.

The reflective surface is then installed on a support or on a pedestal, which allows the movement around the axis of the azimuth and of the solar height through which can track the sun's position. Two motors, are installed on the support supply to allow the movement of each axis. [12]

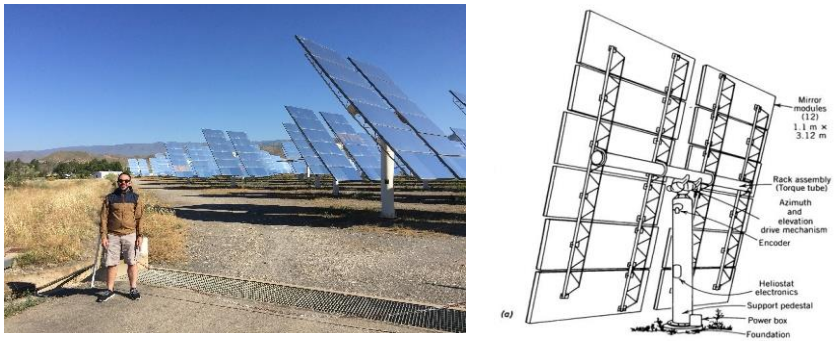

Figure 1.21: Left: CESA-1 heliostat, Right :Heliostat elements

The solar tracking systems can be classified as follows [11]:

- Passive system (mechanical): they are based on the thermal expansion of a substance (usually Freon) or of memory form alloy;
- Active systems (electronic) are composed on the use of a system computer based. The central computer runs the software, from data sent by the sensors, and processes the position of the sun and the commands to be send to the engines for the regulation of individual heliostats.

The solar field, consisting of hundreds or thousands of heliostats, is usually the most expensive part of a central receiver system, reaching even 50% of the total cost of the plant.

In this regard, several authors have performed studies on cost reduction LCOE (Levelized cost of electricity method) to search for more favourable economic conditions for the development of this type of plant [90] [91] . The solution depends on various factors and it is difficult to identify the direction in which the market tends. From the results of these studies, it emerges that there is still no ideal dimension for the reflecting surface of the heliostat. There are heliostats operating with different sizes: from 1.14 m^2 (eSolar) [92] up to 120 m^2 (Abengoa Solar) [93], with a variety of heliostats that fall within that range, for example manufactured by BrightSource 15.2 m^2 [94], 62.5 m^2 [95]of Pratt & Whitney, 116 m^2 (Sener)[96] . Some Industries have recently increased the area of their heliostats: from 120 to 140 m^2 Abengoa, BrightSource from 15.2 to 19 m^2 and eSolar from 1.14 to 2.2 m^2 [98] , possibly allowing them to reduce the costs of solar tracking system (electric motors). Some makers, such as Abengoa Solar for example, have constructed at the same time heliostats of big and of small size, that offers simultaneously a 140 m^2 heliostat, while is developing one of 18

m² [97]. In the 80s, the most important point (at least in the USA) was that heliostats that had to be very large with efficient cost. The analysis of SANDIA National Labs in 2000, for instance, supported this point of view (figure 1.22), indicating that the heliostats should be at least 50 m² surface area and, preferably of 150 m² [13].

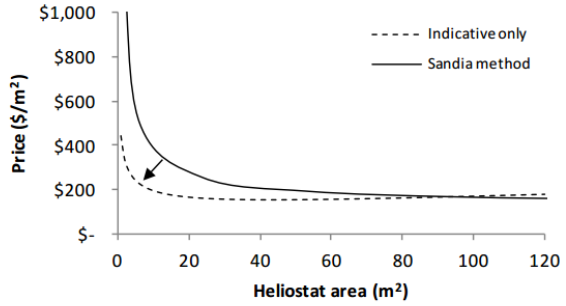

Figure 1.22: Reflective cost-area trend

It's clear that the specific cost dependents on the dimensions, particularly it grows vertiginously at the decrease in the heliostat area, especially for heliostats below 30 m² as declared for example from SANDIA Laboratory.

1.4.3. Heliostat field geometric layout

A heliostats field may assume two main geometric configurations:

- Surround Field
- Polar Field

In the first case, the heliostats are distributed on the field following a circular shape around the solar tower (figure 1.23). This configuration is best suited for large power plants (> 50 MW) and low latitudes, where the seasonally Sun has a high position in the sky for most of the day. The tower is usually slightly south of the centre, allowing the field to be optimized [14].

In particular, for thermal power less than 50 MW, depending on the latitude, it is preferable to use a polar (North or South) Field type configuration. For plants requiring higher thermal powers and therefore a higher number of heliostats, a Surround Field configuration is preferable. This is to avoid placing heliostats too far away from the tower, that would result in a loss of heliostats efficiency due to atmospheric attenuation. These considerations lead to force the

arrangement of the heliostats to the East and West sides of the tower where most of loss are caused by the cosine effect and by the atmospheric attenuation [14].

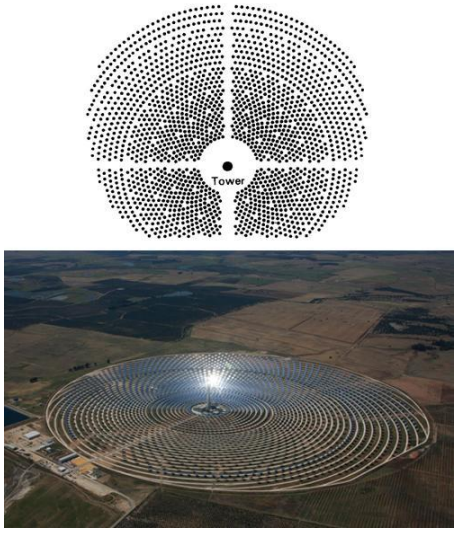

Figure 1.23: Top: A Typical Surround Field configuration; bottom: Gemasolar plant at Fuentes de Andalucía, Spain

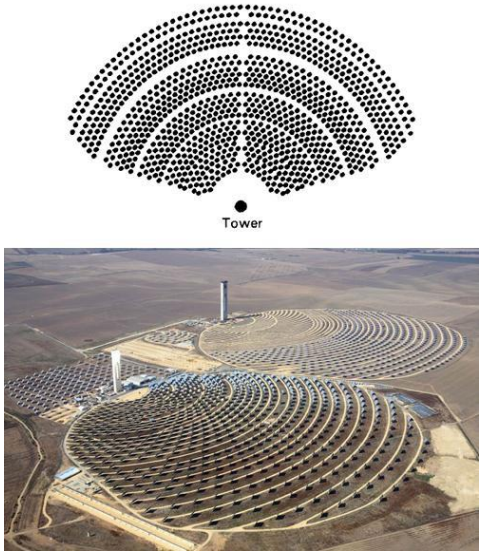

Figure 1.24: Top: A North Field configuration; down: PS10 and PS20 plants, 10 and 20 MW, respectively, in Seville, Spain

1.4.4. Optical efficiency

The efficiency of the heliostats field, is the ratio between the power available to the receiver and the total power incident on the reflective surface, and is expressed by the following relation:

$$\eta = \frac{\dot{Q}_{rec}}{\dot{Q}_{Tot,inc}} = \frac{\dot{Q}_{rec}}{DNI \cdot n \cdot A_{hel}} \qquad (1.32)$$

Where:

- DNI is the direct normal radiation on the horizontal plane [W/m^2];
- n is the number of heliostats
- A_{hel} is the area of the single heliostat [m^2].

The optical efficiency, as described in equation (1.32) is the product of a series of effects or attenuations:

- cosine effect
- shadowing
- blocking
- reflectivity
- Atmospheric attenuation
- Spillage

This efficiency is not to be confused with the total efficiency of the plant that instead includes the receiver's efficiency and the efficiency of the power cycle.

Cosine effect

The radiation reflected by the heliostats is proportional to the amount of radiation intercepted. The cosine effect depends on the Sun's position, and the heliostats with respect to the tower [12].

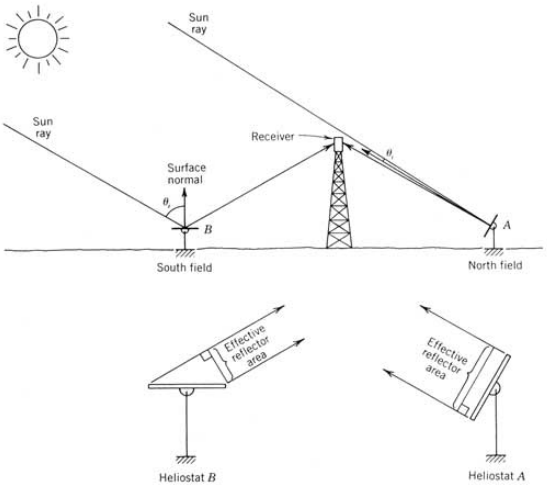

Figure 1.25: Cosine Effect

The reflected power is proportional to the cosine of the incidence angle θ (figure 1.25), formed to the normal of the reflecting surface $\hat{\mathrm{n}}$ and the direction of the solar rays.

The relationship between the effective reflective surface area, intercepted by the rays, and the total reflective surface, determines the magnitude of this effect:

$$\eta_{cos} = \cos\theta = \vec{s} \cdot \hat{n} = \vec{r} \cdot \hat{n} \qquad (1.33)$$

Where:

- $\vec{s}$ is the vector that identifies the direction of the solar rays;
- $\vec{r}$ is the vector that identifies the direction of the reflected rays;
- $\hat{n}$ is normal to the reflecting surface;
- θ is the angle between $\vec{r}$ and $\hat{n}$ (or between $\vec{s}$ and $\hat{n}$).

To calculate the incidence angle it has been taken in to account the following equation [12]:

$$\cos 2\theta_i = \frac{(z_0 - z_1)\sin\alpha - e_1\cos\alpha\sin A - n_1\cos\alpha\sin A}{\left[(z_0 - z_1)^2 + e_1^2 + n_1^2\right]^{1/2}} \qquad (1.34)$$

Where:

- α is the solar height which determines the position of the sun;
- A is the solar azimuth, which determines the position of the sun;
- z_0 is the tower height [m];
- z_1, e_1, n_1 are the heliostat coordinates.

Through this equation, it can be noted that the heliostats arranged to the West in the early hours of the morning have a high efficiency, as opposition to those exposed to the East that have reduced efficiency. The situation is reversed in the afternoon hours.

During winter, when the Sun is located South of the tower and down in the sky, the heliostats which are located at the North of the tower, will be oriented perpendicular to the direction of the Sun's rays and, therefore, will have the highest cosine efficiency values, close to the unit. However, the heliostats that are located South of the tower, will suffer more of the cosine effect.

Given that the greater portion of solar radiation is related to the period of the year, when the Sun is South of the filed, overall, the efficiency of the annual average cosine will be higher in the northern part of the field.

Shadowing e Blocking

The shadowing effect, occurs, when part of the reflective surface of a heliostat is obscured by the shadow produced by heliostats near or by the tower itself. The shadowing efficiency for general heliostat is defined as followed:

$$\eta_{shad} = 1 - \frac{A_{shad}}{A_{hel}} \tag{1.35}$$

Where:

- A_{shad} is the obscured surface potion [m²];
- A_{hel} is the heliostat surface [m²].

The heliostat orientation varies during the day and substantially changes its projected shadow. Constant evaluation of this effect thought-out the whole field is computationally difficult owing to the huge heliostat field. The shadowing effect is more pronounced when the Sun is in low position and is more concentrated in the central part of the solar field, where the density of heliostats is greater [14].

Efficiency can be expressed as:

$$\eta_{block} = 1 - \frac{A_{block}}{A_{hel,net}} \tag{1.36}$$

Where:

- A_{block} is the "blocked" surface portion [m^2];
- $A_{hel,\ net}$ is the net reflective surface, without shadowing [m^2].

In the design phase, it is possible to define the blocking losses, choosing appropriate radial spacing values and azimuth [15]. As in the case shadowing losses, the most affect areas, by blocking losses, are the field areas with higher density array of the heliostat.

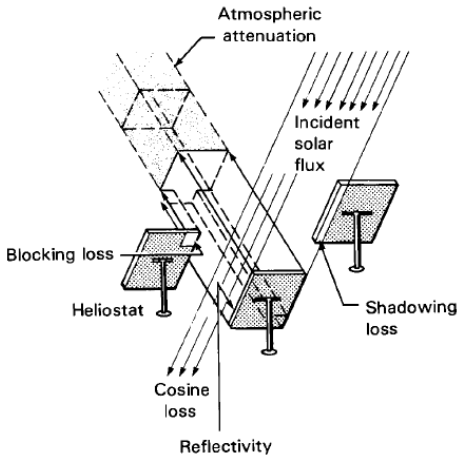

Figure 1.26: Optical leakage

Atmospheric attenuation

Not all of the reflected radiation reaches the receiver; a portion is dispersed and absorbed by the atmosphere. The dispersion, interesting the whole spectrum, and consists in the elastic deflection of the photons from their initial trajectory. Small particles, smaller than the wavelength of the light, are responsible of this phenomenon.

The absorption, however, is caused by the presence of water vapour particles and/or aerosols in the air [14]. Because such losses occur between the heliostats and the receiver, the atmospheric attenuation models, usually, are expressed as a function of distance from the receiver and visibility, as follows:

$$P\ (\%) = c_1 + c_2 S + c_3 S^2 + c_4 S^3 \qquad (1.37)$$

Where:

- c_1, c_2, c_3, c_4 are constant depending of the location;
- S is the distance from the receiver [m] [16].

Below are the atmospheric attenuation estimates made with main computational codes:

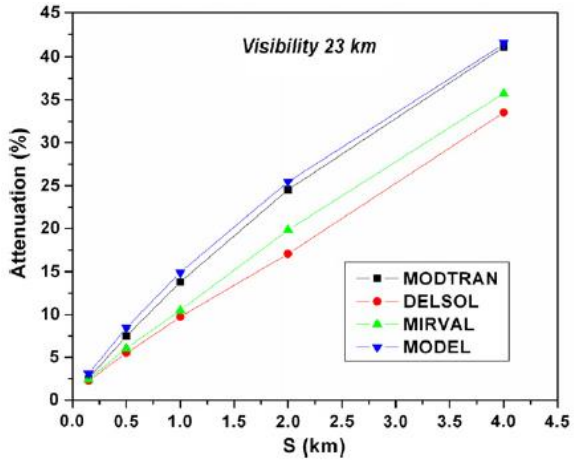

Figure 1.27: Atmospheric attenuation, visibility 23 km[16]

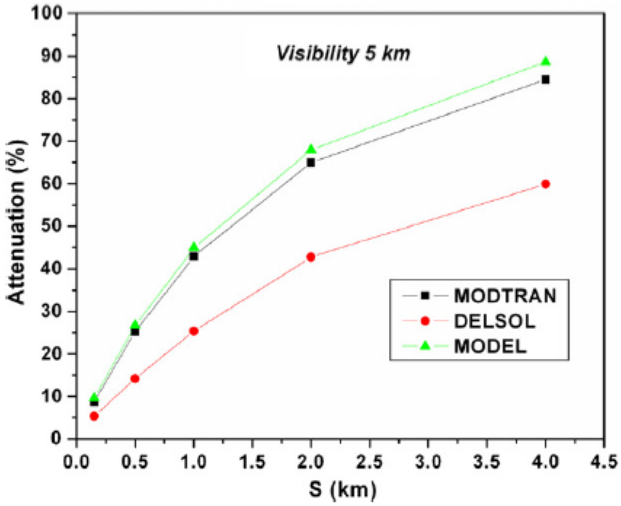

Figure 1.28: Atmospheric attenuation, visibility 5 km[16]

The trends obtained, in both cases, are similar to a clear day (visibility 23 km) while the difference is higher in case of the results obtained with different codes for the hazy conditions (visibility 5 km).

Reflectivity effect

The heliostat does not reflect all the incident solar radiation, there is a part that is absorbed and another remaining part that is transmitted. The reflectivity ϱ, of a heliostat, is defined as the ratio between the reflected radiation and the total incident, and it represents the property of the material. In literature typical values of this parameter are within the range 0.92 - 0.96 [17].

It is important to specify that the reflectivity of a heliostat, continuously exposed to the weather, decreases on average about 2% per month, but may also fall by 20%, mainly due to accumulated dirt [18].

Therefore, it is a must to clear systems designed for this purpose. In Table 1.1, are reported the main data of some heliostats built in the past years [13]:

Modell	Year	Maker	A_{hel}	Material	Reflectivity
Colon 70	1997	Inabensa, Abengoa, S.A	69,3 m²	Glass mirror fixed to steel frame	0,92 - 0,93
PSI 120	1996	Inabensa, Abengoa, S.A	122,1 m²		0,92 - 0,93
Sanlucar 90	1999	Inabensa, Abengoa, S.A	91 m²		0,92
HELLAS 01	1999	GHER S. A	19,2 m²	Glass mirror	0,94
ATS H100	1983	Advanced Thermal Systems, Inc.	95 m²	Silvered glass	0,94
AMS H150	1995	Babcock Borsig Power Environment	150 m²	Metal stretched membrane	0,94

Table 1.1.1: Specification of some heliostats ,built in the past

The projected image size on the receiver depends on the surface of heliostat, how is focused and aligned and on the regularity of that surface. A heliostat perfectly aligned and focused cannot concentrate sunlight into a single point, but it will be definite area. The minimum diameter of this area is about 9.3 meters per kilometre of distance from the receiver [14]. It is deduced that if the receiver is not large enough, there will be a part of lost energy "spilled" by the edges. In this case, it is necessary to increase the receiver surface. However,

increasing the receiver size, automatically there is an increase in thermal losses and costs.

1.4.5. Heliostat arrangement field layout

Defined the geometric aspect of the mirror field (Surround or Polar Field), the heliostats should be placed on the field with a defined pattern: the local density of heliostats is the result of a compromise between cost and performance.

The plant costs include the heliostats, the installation, the wiring, the tower, the ground and all the control systems.

By increasing the density of heliostats, placing them very close, there is a reduction of the cost of the land and of the wiring, but at the same time, there is an increase of the shadowing and blocking losses because the heliostats interfere more with each other.

Among different ways of distributing heliostat field, two are the most used [19]:

- Cornfield arrangement;
- Stagger arrangement.

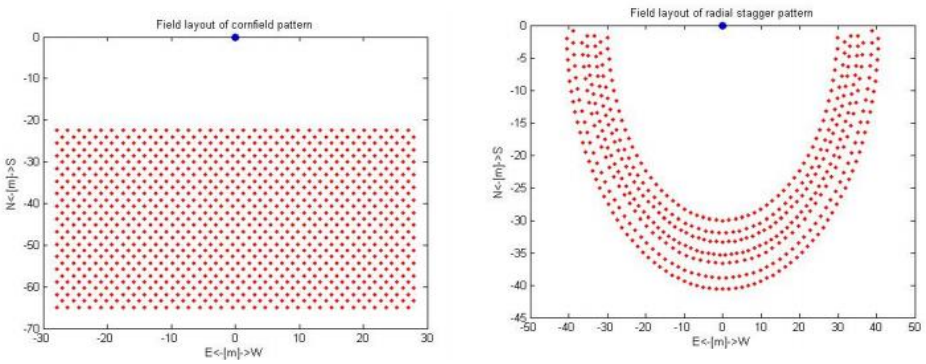

Figure 1.29: Left: cornfield layout; right: radial layout stagger [19]

The radial distribution, developed at the University of Houston, is the most efficient, as it reduces the losses due to atmospheric attenuation; is characterized by the efficient use of the land, and for this reason it is used by almost all installed solar plant.

This configuration consists in arranging heliostats of concentric circles (Surround Field) or in parallel equally spaced arcs (Polar Field) [19].

The term stagger indicates the heliostats disposition: the two different rows are offset or shifted between them.

Practically, the empty spaces in the i^{th} row are filled by heliostats in the next row, as shown in figure 1.30:

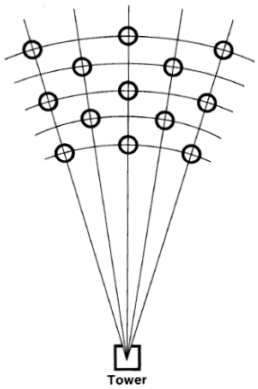

Figure 1.30: Stagger radial layout

Since there are many variables in play, the optimization of the solar field layout has been elaborated by numeric codes.

1.4.6. Heat transfer fluid

Another important parameter relating to the receiver is the Heat Transfer Fluid (HTF) used. It is possible to divide the HTF in:

- Mixtures of molten salts
- Steam
- Air
- Supercritical CO_2
- Solid particles

In practice, according to the heat transfer fluid, the heat exchange mechanism changes. The heat transfer fluid and the constructive materials dictates the working maximum temperature, the operating pressure and the solar flux limit. The use of molten salts and liquid sodium it is favoured by the possibility to work with higher temperatures and thermal flux.

Mixtures of molten salts can reach temperatures of about 540-565 ° C and admit heat flux of 0.8 MW/m^2, while the liquid sodium allows to achieve a flux of about 1 MW/m^2; both fluids facilitate the increasing of hours storage, for their high thermal capacity. An important limit for mixtures of molten salts is represented by the decomposition temperature; it occurs at 600-630 ° C, while the point of solidification is at 220 ° C.

Other problems such as corrosion and reactivity in the presence of oxygen are not to be neglected [23].

1.4.7. Solar Tower

In solar tower systems, incident radiation on heliostats is reflected on a receiver placed on the top of a tower. Before describing the receiver, a tower-height discussion is introduced, because it is an important parameter that affects the performance of the concentration system. In this regard, it is important to mention the Battleson's work (1981) [20] that correlates the rated power of the system with the height of the tower. In particular, figure 1.29 shows how the height of the tower varies depending on the thermal power required, for the North and Surround field configurations. This parameter is also important with respect of the increasing cost to create larger towers.

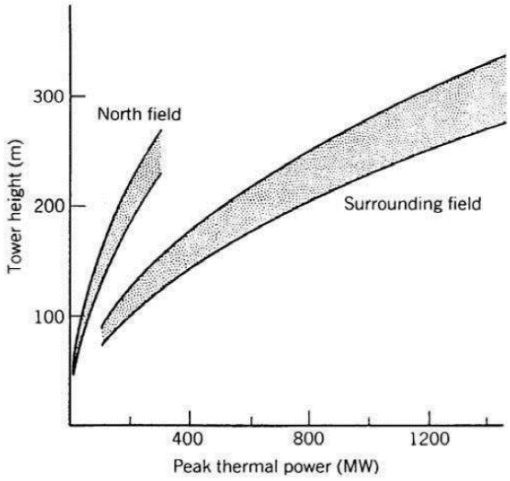

Figure 1.31: Tower height according to the power of the plant

1.4.8. Receiver

The receiver has the function of absorbing the solar radiation and to transfer it to the heat transfer fluid, which can then be used for industrial, chemical processes or to be converted into electrical energy. The energy that can be supplied depends on the size of the heliostats field and on the receiver which makes it is possible to achieve a power up to hundreds of megawatts. The method proposed by Vant-Hull and Izygon in 2003 [21] is useful in evaluating the thermal power on the receiver.

The authors suggest the use of the following correlation:

$$P_{rec} = \frac{SM \cdot \left(P_n + P_{parass}\right)}{\eta_{cycle}} \tag{1.38}$$

Where:

- SM is the solar multiple;
- P_n is the nominal design power [MW_{th}];
- P_{parass} are parasitic losses [MW_{th}];
- η_{cycle} is the efficiency of the power cycle.

Considering a solar multiple of 1.3, that is the optimal value for the system without storage [22], a power rate of 50 MW, a parasitic losses of 5 MW and assuming an efficiency value of 40% it obtains a value of the thermal power to the receiver equal to 180MW_{Th}.

There are direct exchange receivers (where the fluid is directly exposed to solar radiation) or indirect exchanges (when a component converts solar radiation into heat and then transfers it to the fluid through a convective exchange).

Among the components that make up a CRS, the receiver is the most critical part. It may happen that excessive heating on the absorbent surface causes damage on it, so it is necessary to study systems that automatically can defocus the heliostat field in the case that the thermal flux on the receiver exceeds the maximum admissible value dictated by the properties of the materials.

Since the 1980s, many kinds of prototypes have been analysed, but none of them have prevailed over others. The receivers can be characterized based on

the heat transfer fluid, maximum heat flux, geometry materials construction and many other parameters.

1.4.8.1. Receiver Geometric classification

A first classification of solar receivers could be (figure 1.32):

- External receivers;
- Cavity Receivers;
- Volumetric receiver;
- Solid particles receiver.

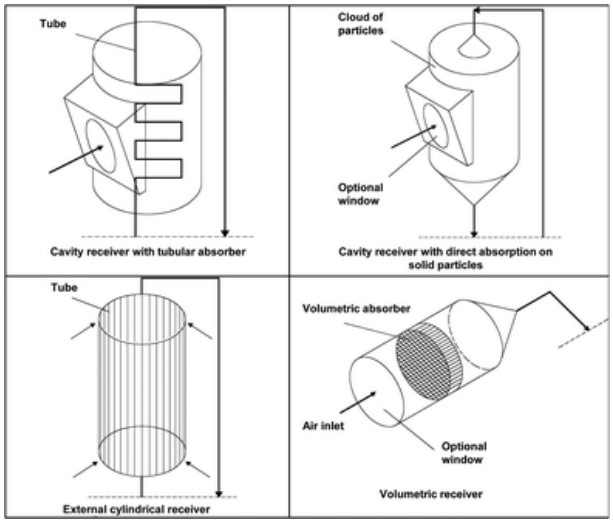

Figure 1.32: Receiver Type

A typical external receiver consists of multiple absorbing panels that form a polyhedron approximating a cylindrical surface. The absorbing surface is similar to that of a boiler. It is composed, in fact, of tubular beam panels welded to each other.

The heat transfer fluid, passing through the tube bundles, removes the heat. The operating conditions of the receiver are very variable. The heat flux depends on the available solar radiation, which depends on the weather conditions, the position of the Sun and from the solar field configuration. Externally, the receiver is subject to the action of the wind, atmospheric pressure and variable outside temperature. For an external receiver, the height/diameter ratio generally ranges from 1: 1 to 2: 1 [14].

In cavity receivers, radiation passes through an aperture obtained in the receiver's external structure, affecting the absorbent surface.

The outer structure contains the cavity inside. There are multiple cavity receivers and single cavity receivers; the latest is used for North Field layouts.

Figure 1.33: Cavity aperture on CESA-1 Tower on "Plataforma Solar de Almeria"

The absorbent surface is similar to that used in external receivers, also composed of tube bundles. The geometry of the cavity is concave, in order to improve the collection of solar radiation coming from the field.

Unlike external receivers, where the absorbent surface is practically the entire outer surface, in the cavity receivers, some internal parts, such as the walls and the cover, for example, are made with different types of materials.

These parts must be adequately insulated, to minimize heat losses, and protected from direct sunlight to prevent permanent damage. Although these surfaces are subjected to low incident radiation, they are heated by the heat from the absorbent panels placed inside the cavity and are not cooled in any way, they can even exceed the limit temperature.

The area of the inner surface together with that of the absorbent panels is about 2/3 times the area of the opening. The opening is typically square or rectangular [14].

Several factors distinguish the two types of receivers. Irradiation losses are generally higher for external receivers, as their absorbent surface is mostly exposed to the outside environment.

The absorbent panels in the cavity receivers are more protected, as they are connected with the outside panels through the only rectangular opening. Even reflection losses for an external receiver are slightly higher, while cavity receivers are more affected by the spillage effect, since solar radiation has to be concentrated and passes through a relatively small aperture [14].

On the other hand, they have some thermal inertia during the start-up of the plant or during the variable conditions of the weather can provide some continuity of service.

Tubular bundles in cavity receivers are more protected and, compared to external receivers, the thermal coating degrades less.

1.4.8.2. External tubular receiver

External tubular receiver are still the most common ones: the heat transfer fluid makes multiple passages in the tube bundles thus increasing its enthalpy, before being sent to the power block or, if there is provision to storage. The system has been tested and operated with mixes of molten salts, steam and temperatures not exceeding 600 ° C. There are few data on the use of such receivers with atmospheric air or heat transfer fluids such as supercritical CO_2 [24].

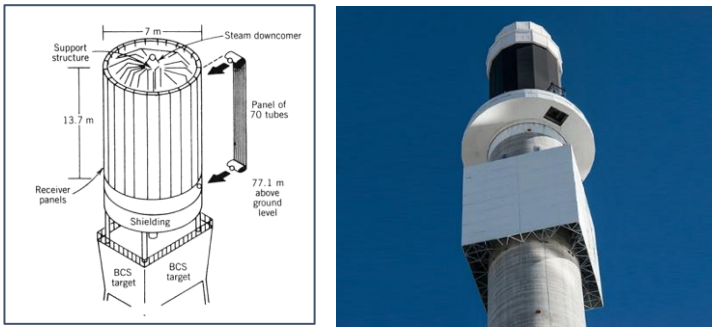

Figure 1.34: External Receiver Solar Two

The Solar Two plant in Nevada uses an external tubular receiver (figure 1.34), a primary circuit with salts and a secondary circuit designed to generate saturated steam at 40 bar and 250 ° C, and then evolves into a turbine. However it has some limitations: the maximum allowable flux of 0.6 MW/m^2, there are

also difficulties in raising the pressure of the steam to the conventional value of 13 MPa and a rather poor storage [25].

1.4.8.3. Cavity receiver

Below is an overview of existing or developing projects and experiments. Nowadays, only German Aerospace Centre (DLR) and Israel's WIS (Weizmann Institute of Science) have continued their work in this area: both research facilities have developed volumetric cavity receivers that can also reach temperatures above 1000 ° C. One of the main possible applications, with air as a heat transfer fluid, is to use a gas turbine whose performance is strongly dependent on the TIT (Turbine Inlet Temperature) [26].

Currently, commercial heavy-duty gas turbine reach up to 1350 ° C [35]. The temperature gap is usually compensated by the input of heat from the fuel, thus adding a combustor. Table 1.2 shows the data of the developed cavity receivers:

Project	Receiver	T_{max} (°C)	Start project
DIAPR	Cavity volumetric	1200	1992
REFOS	Cavity volumetric	800	1996
SOLHYCO	Cavity tubular	800	2006
SOLUGAS	Cavity tubular	800	2008
SOLGATE/HST	Cavity volumetric, Cavity tubular	1030	2001
SOLTREC	Cavity volumetric, Cavity tubular	1000	2010

Table 1.2: Air receivers currently developed [100], [101], [33],[102], [36], [103]

Cavity tubular receivers are composed by a series of multiple tubular panels, which form the absorbent surface, and are generally coated with black varnish in order to increase its absorption coefficient.

These modules are connected in series or in parallel to each other, through the collector tubes, collect and distribute the heat transfer fluid. The HTF, flowing in the tubes, absorbs the thermal power from inner walls of the tubes, which receive the incident radiation on the outer surface. Actually, there are two

commercial cavity tubular receiver; the first one, built in 2006 is the SOLHYCO system and the second one is SOLUGAS built in 2010.

SOLHYCO receiver is composed by 40 tube of alloy INCONEL 600, connected by two toroidal collectors in a conical trunk structure. During the test phase performed in 2010 at the CESA - 1 Tower in Almeria, the receiver was able to give power to a micro gas turbine of 100 kWe at a pressure of 4.5 bars and an temperature inlet turbine of 800 ° C [116].

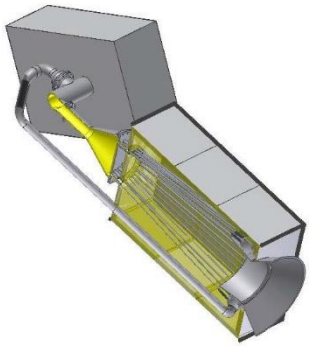

Figure 1.35: SOLHYCO receiver

SOLUGAS was design instead for the MW scale, in fact was able to powered a gas turbine of 3MW. Ten panel, arranged circularly, composes the receiver; in figure 1.35 it is possible to observe the component. The receiver consists of a hollow with 170 tubes in parallel with a length of 60 meters, arranged in a circular shape of 5 meters diameter [36].

The Solugas project uses a modified Mercury 50 gas turbine to pass the air inside the solar receiver. The main characteristic of this system is the use of an innovative tubular receiver which allows to heat the pressurized air from 330 ° C up to 800 ° C.

During the test, which lasted 1000 hours the receiver worked at 10 bars of pressure and 800 °C of operative temperature [36].

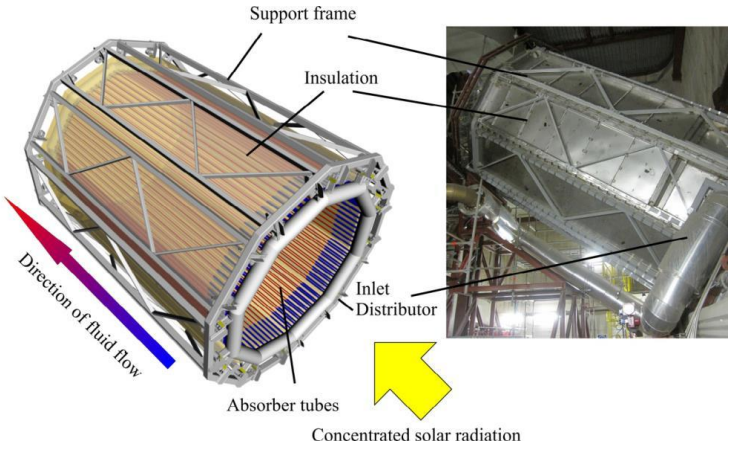

Figure 1.36: SOLUGAS receiver

1.4.8.4. Volumetric receiver

Employing air, as heat transfer fluid, it is possible to allow temperatures of 1000-1200 ° C ; these high temperatures allow to approach metal pipes, in respect to the limits imposed by the physical properties of metals at these temperatures [28]. In a volumetric receiver (figure 1.36), a porous absorbent material, which heats the HTF, for example the air that passes through, captures the solar radiation. In this case, the maximum temperature of the receiver is close to that of the air, in this way the solar radiation can be concentrated more than in the case of tubular receiver, allowing to reach higher maximum temperatures.

Another consideration for the benefit of the volumetric receiver consists of the external surface temperature, which must be as low as possible to reduce the radiative losses. In the volumetric receiver, the outside is cooled down by the lower incoming airflow decreasing the leakage [28]. The results bring advantages of the volumetric receivers: the atmospheric air is fully available; has no impact on the costs and most importantly it is not-polluting, is not-toxic and there is no change phase. Furthermore, the physical properties of air, does not undergo to decomposition at high temperatures. Higher temperatures allow to achieve high conversion so for this reason the receiver is used in the Brayton cycle more so than the classic Rankine cycle.

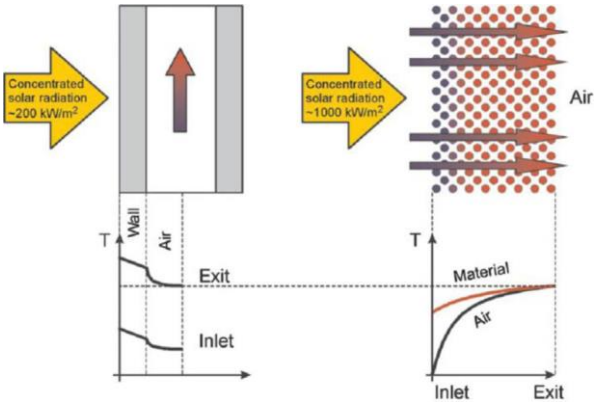

Figure 1.37: Left, absorbing and transferring heat for tubular receiver, right absorbing and transferring heat for volumetric receiver

Desert areas are therefore suitable for the construction of new CTS plants. Problems related to the durability of the absorbent materials, the instability of the flow, and the cost of construction are still to be solved [29].

Among the first receivers built there is REFOS created in 1996 by DLR. The technical data of this receiver is [101]:

- Thermal power absorbed for a single module: 350 kW_{th};
- Air outlet temperature: 800-1030 ° C;
- Operating pressure: 15 bars;
- Receiver efficiency: 80%.

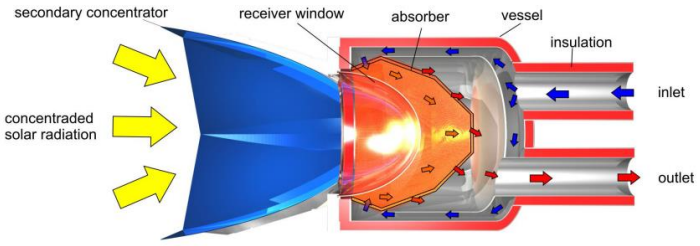

Figure 1.38: Module of a REFOS volumetric receiver

The pressurized air passing through the receiver is maintained in pressure inside the REFOS through a quartz window that has a semi-elliptical profile with 620 mm diameter at the end and a depth of 420 mm. The thickness is 8 mm and allows withstanding a maximum pressure of 19.5 bars [29].The absorber is finally mounted on a secondary hexagonal shape concentrator to better allow

reflection of the solar rays towards the absorber itself and to facilitate the coupling of multiple modules to meet the required thermal power.

In parallel with DLR, the WIS research centre (Weizmann Institute of Science) has developed a volumetric pressurized cavity receiver called the DIAPR (Directly Irradiated Annular Pressurized Receiver) [100]. The design of the DIAPR receive comes from "porcupine" absorber: solar radiation is concentrated on a series of high-temperature resistant aluminium-silicon needles. A pressurized air stream lays the needles warming during this process.

The cross section of a receiver is shown in figure 1.39.

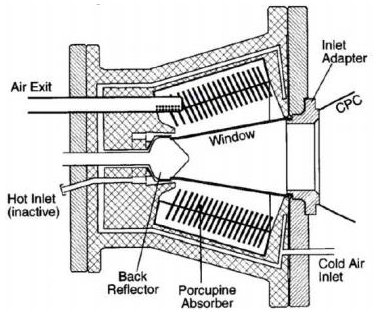

Figure 1.39: Cross Section receiver DIAPR

The DIAPR was the first receiver to pass the 1200 ° C temperature; during the test phase it has been proven to achieve extraordinarily high thermal fluxes up to 10 MW/m^2 with efficiencies between 90% -70% at temperatures of 850 ° C and 1200 ° C. To reach high thermal flux it is extremely important and necessary high concentration ratios. Thus, there is a need for huge solar fields with high density of heliostat, which increase the losses due to shadowing, blocking and spillage [26].

Figure 1.40: Volumetric receiver and second concentrator on "Plataforma solar de Almeria"

1.4.8.5. Combined receivers

Other kinds of receivers are the combined one, the ones that use volumetric and tubular receivers. There are two existing combined receivers: Solgate and Soltrec.

The Solgate project started in 2001, it is a project aimed to demonstrate the feasibility of a solar hybrid Brayton cycle [33]. The plant consists of a gas turbine, of aeronautical derivation, modified to allow air heating through three receivers.

In this case, both tubular and volumetric technologies were combined to build the receiver by dividing it into:

- Low temperature receiver: composed by a tubular receiver;
- Medium temperature receiver: REFOS [34] volumetric receiver;
- High temperature receiver: modified REFOS volumetric receiver, where the metal absorber, has been replaced with a ceramic absorber to allow the desired temperature of 1000 ° C.

In series with the solar receiver, a combustor was added with the aim of raising the working fluid temperature to a minimum of 1150 ° C to rise up the design power.

The tests demonstrated the feasibility of the technology by measuring a temperature of 959 ° C [33]. The receiver is shown in figure 1.41.

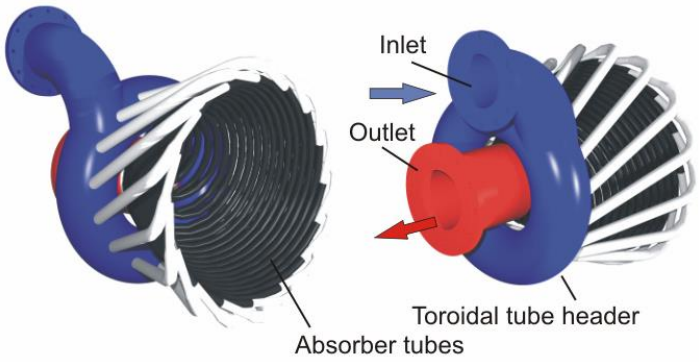

Figure 1.41: SOLGATE Receiver

Soltrec project is a demonstration project of a pressurized volumetric receiver started in 2010 under the framework of Eureka Programme and

developed by Abengoa Solar New Technologies. The prototype receiver module is integrated into the pre-commercial Solugas demonstration plant in series with the tubular one, increasing the temperature from 750°C to 1000°C. The Soltrec receiver has a window of 816mm and insulation thickness of 100 mm. The 816 mm quartz window has been designed based on the knowledge acquired in previous projects (Solgate, Refos) [103].

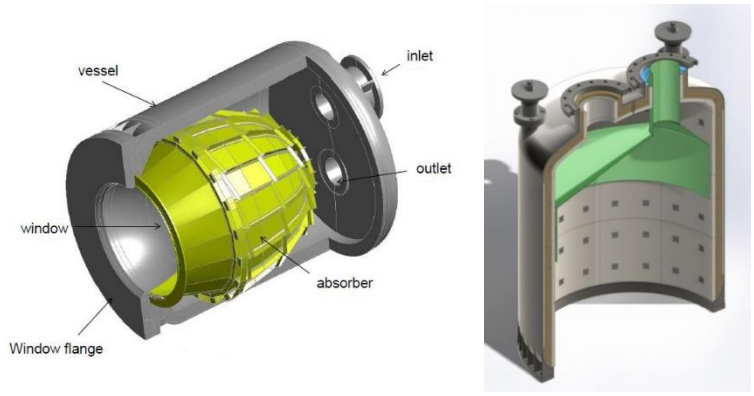

Figure 1.42: SOLTREC Receiver and its integration

1.4.8.6. Solid particle receiver

The solid particle receivers (SPR) uses small particles as a heat transfer fluid within a cavity receiver structure. The components required to operate a SPR includes the receiver (to heat the particles), bottom hopper (to catch the falling particles), particle lift elevator (to lift particles back to the top of the receiver), top hopper (to store particles before being dropped through the receiver), and ducting. [117]

The particles may be stored in an insulated tank and/or used to heat a secondary working fluid (e.g., steam, CO2, air) for the power cycle.

In figure 1.43 it is represented a system employing the solid particle receiver.

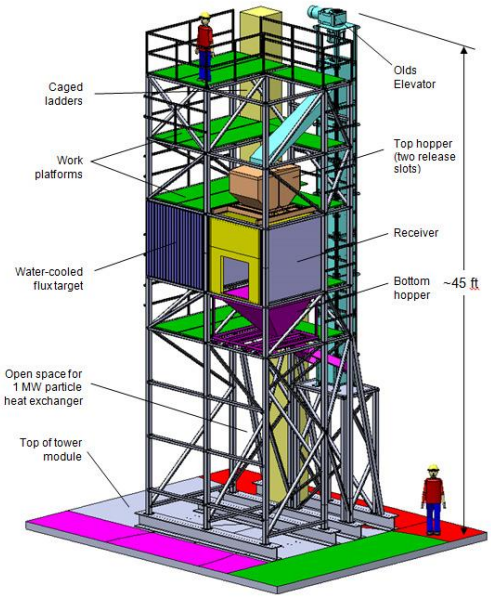

Figure 1.43: Solar particle receiver system

1.4.9. Power block

In the concentrating solar systems, it is not possible to use all the cycles; for example, it is not possible to use an internal combustion engine where the heat is produced internally. Only those cycles where the heat is added from the outside can be integrated into the solar part, transferring the heat to the HTF through heat exchangers, or through the receivers, as described in last paragraphs. The usable cycles are three: Rankine, Stirling and Brayton [12].

Currently, the most commonly used cycle for electric power generation is the Rankine cycle, in which is used a working fluid (usually water) which changes phase during the heat transfer process.

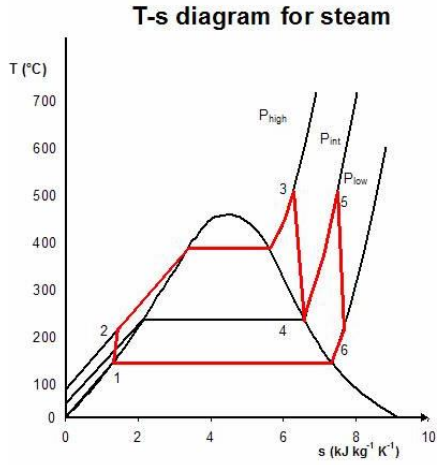

Figure 1.44: T-S diagram of the Rankine cycle with reheat

It is to use the heat from the absorbent surface of the receiver to vaporise the water and overheat the steam produced; it is then sent to a turbine for the production of mechanical work and therefore, through an alternator, of electricity. Finally, the low temperature steam is sent to a condenser to reset the cycle start condition. In some cases, vaporisation occurs directly in the receiver.

This involves sizing this component for high process pressures. The most commonly used solution is to use the receiving surface to heat a vector fluid, usually synthetic oils or molten salts, used as HTF. Afterword, it is performed a second heat exchange between the carrier fluid and the working fluid for the generation and to heat the steam. As already mentioned before, however, there are technological constraints in the use of these fluids which limit the maximum temperature to about 500-600 ° C [30].

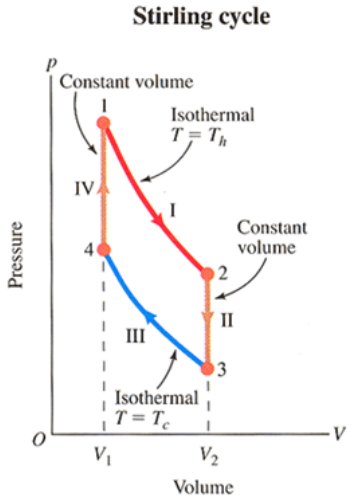

Figure 1.45: Stirling Cycle P-V Diagram

The Stirling cycle (figure 1.44) has been proposed instead for small applications (10 to 100 kW) to exploit its characteristics of high efficiency. They are usually used in "solar dish" systems.

Finally, the Joule-Brayton cycle or, Brayton cycle is used for both small and large power plants. The advantage of this technology is the simplicity of construction and adaptation, but it requires high operating temperatures for a reasonable system efficiency [12], [27]. The ideal cycle consists of adiabatic compression of incoming air, isobaric heating, adiabatic expansion and isobaric heat release.

In solar thermodynamics systems, the heating in the cycle occurs by the concentration system [30]. To sum up, one can say that the solar-Brayton technology, compared to a steam-powered Solar System, offers the following advantages:

- Fluid that evolves in the cycle, which circulates through the receiver and the working fluid coincide, however, in the Rankine plants, a different heat transfer fluid (usually thermal oil or molten salts) is required. So a limit on the maximum operative temperature, of about 500-600 ° C, of the receiver has been imposed. Differently the Brayton cycle, uses operative temperatures that can achieve 1000-1200 ° C.
- High water consumption required by the steam cycle for cycling and cooling purposes. In the Brayton cycle, there is a significantly lower water consumption; so it could be successfully installed in arid and desert places

characterized by a high direct radiation, and large areas of land available for the installation of heliostats.

- Using air as a heat transfer fluid in the Brayton cycle, there is not a changing phase .

Of course, there are also disadvantages to the technology of solar-Brayton:

- The heat transfer fluid, air in this case, has low thermal conductivity and low density (though pressurized) and this involves the adoption of heat exchangers with more extended exchange surfaces;
- The high temperatures reached in the receiver do not allow the use of tubular exchangers, but the use of volumetric receivers are more expensive and at present less reliable technology.

1.5. State of the art of solar Brayton Cycle

In this session will be presented some systems and projects that operate with a gas turbine as power block.

1.5.1. CSIRO Solar Air Turbine Project

CSIRO (Commonwealth Scientific and Industrial Organization) together with Mitsubishi Heavy Industries (MHI) have developed and tested components needed for the construction of the thermodynamic solar plant [31].

Figure 1.46: CSIRO Solar Air Turbine Project

The plant, built in Newcastle, Australia, completed in 2014, uses a gas turbine that does not need cooling water, one of the critical aspects of CSP plants. The solar field consists of 450 heliostats that concentrate solar radiation on the

receiver surface placed on top of a 25-meter tower. The gas turbine is also located at the top of the tower (figure 1.45). The turbine has a nominal power of 200 kW of aeronautical derivation.

1.5.2. SANDIA sCO2 Brayton Cycle

This project has tested an innovative solution, by using a gas turbine, receiver and storage systems, operating with supercritical carbon dioxide. Pressurized CO_2 is heated by solar energy, captured by the heliostats, and concentrated on the receiver, with a concentration ratio of C = 1000. The supercritical CO_2 is then evolved into a turbine to generate electricity. The output carbon dioxide is then compressed and re-heated. This is therefore a closed loop, CO_2 represents the thermal fluid and never goes out of the loop itself.

The use of supercritical CO_2 opens up various thermal energy storage solutions, which can hardly be achieved by operating at very high temperatures at around 1000 ° C. This plant, which began in 2012, will be completed in SANDIA National laboratories to examine the performance of the S-CO_2gas turbine in a solar tower.

1.5.3. AORA solar

Installed in the desert near Kibbutz Samar (Israel) and at the Almeria solar platform (Spain), the Aora solar system is the first and only hybrid micro gas turbine built for micro generation. Based on 100 kW micro gas turbine of Ansaldo Turbec T100 engine the construction was completed in 2009.

The plant is composed by a tower high 30 meter, by 30 heliostats (or 50 in Almeria) and DIAPR receiver of six meters high. It is possible to reach the temperature of 1000 ° C, to allow the compressed air to be introduced directly into the turbine without the use of the combustor.

The combustor is still present and used as an adjustment, and at start- up of the gas turbine; it comes into operation when the temperature drops below 950 ° C to ensure constant power generation. To reduce costs, the tower was built using recyclable materials [35].

Figure 1.47: Aora Solar Plant on "Plataforma Solar de Almeria"

1.5.4. 247Solar system

The last hybrid micro gas turbine is produced by 247Solar, that employing an engine of 300 kWe. An innovative air receiver, that works at very low, near-zero pressure, heats the working fluid to 970°C. The system is also provided of a thermal storage, employing firebrick or small pieces of ceramic and has a capacity of 10-15 hours. In addition waste heat can be used for a variety of purposes, e.g., to drive a bottoming cycle (e.g., an ORC); for process steam; for water purification or desalination; for crop drying; for driving absorption chillers; etc. [118]

Figure 1.48: 247Solar plant[118]

1.5.5. THEMIS tower

The THEMIS solar tower, built at the end of 70s to test at a 10 MW_{th} scale the production of electricity from concentrated solar energy, is being refurbished and upgraded under PROMES-CNRS research centre direction to study next generation high performance solar tower components and thermodynamic or thermochemical cycles at industrial prototype scale [37].

New high performance high precision heliostats tracking system is being qualified to allow receiver temperatures beyond 900°C, still with low power consumption and low maintenance to accurately demonstrate real-world industrial-grade operating cost. The THEMIS solar tower offers two experimental areas:

- PEGASE project, the original large scale area is being prepared;
- "Mini Pegase" a smaller experimental area.

Figure 1.49: THEMIS Solar System

1.5.6. SOLUGAS plant

Plant located in Sanlúcar la Mayor, Spain, began operation in 2013. Designed for use in research and development, it is capable of producing 4.6 MW, employing a Mercury Turbomach T50 gas turbine.

Figure 1.50: SOLUGAS plant

1.6. Conclusions

In this chapter, the fundamentals of solar topic have been introduced and the concentrating solar technology has been displayed.

After a briefly description of the history of CSP systems, in the second part it is found the description of the solar tower technology, and all components employing described.

Finally, a state of art of solar Joule-Brayton cycle were shown in order to introduce the following chapters dealing with this topic.

Chapter 2
Unfired closed Joule Brayton Cycle with mass flow control system description

2.1. Introduction

This chapter deals with the method of regulating the power of a gas turbine engine using air as a working fluid in a closed cycle powered by solar energy collected in a solar tower system. Technical and economic feasibility is not considered here and will be dealt with in the following chapter.

The problem with these kind of power plants, compared to the conventional ones, powered by fossil fuel, are the strong variation in thermal power that occurs during the hours of the day and the days of the year [84].

With the use of a gas turbine, which uses the solar source, there is the solution of combining solar energy with a conventional fuel, so that a reduction in solar power is counterbalanced by fuel input [85].

2.2. Control system of a gas turbine engine with solar energy source

It is known that the mechanical power provided by a thermodynamic conversion plant can be expressed by the following equation:

$$N(W) = G \cdot L_s \qquad (2.1)$$

Where:

- G is the working fluid mass flow rate circulating in the thermodynamic cycle [kg/sec]
- L_s is the specific work delivered by the thermodynamic cycle [kJ/kg]

This specific work depends on two main parameters: compression ratio and turbine inlet temperature, which define the cycle. They are optimized to get the best performance.

Traditional power adjustment methods, through acting on the mass flow rate, alter the cycle, pushing it out of the conditions to get optimum energy conversion.

The mass flow variation obtained by conventional methods drastically changes the speed triangles in the machine, with obvious effects on the conversion efficiency [86].The adjustment method that is going to be illustrated, allows the gas turbine power to follow the solar power variation, with constant conversion efficiency, for any value of the input power within the allowable limits and without the usage of the auxiliary source of energy (fuel)

The proposed method requires the gas turbine plant to operate according to a closed Brayton cycle. The working fluid, therefore, recirculates; the air expelled from the turbine is cooled and reintroduced into the compressor. Since the performance of the thermodynamic cycle depends on the compression ratio and the temperatures, maintaining these parameters constant, it is always guaranteed to work under almost nominal conditions.

Closed loop is useful to achieve this result, because it allows varying the mass flow rate, and thus the power output, to change the fluid density and not the velocities, which would instead make the machine's behaviour different from the designed one.

In figure 2.1 it is possible to see the entire plant.

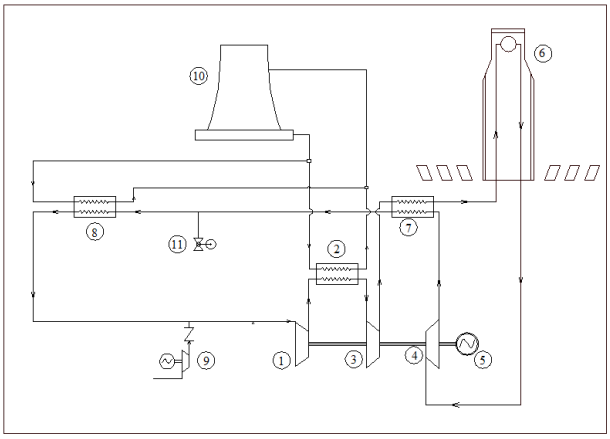

Figure 2.1: Plant scheme: air cooler (8), regenerator (7), concentrated solar tower (6), auxiliary air compressor (9), bleed valve (11), first compressor of gas turbine (1),

intercooler (2), second compressor of gas turbine (3), turbine of gas turbine (4), electric generator

The working fluid mass circulating in the plant is contained in the plant's volumes (gas turbine, receiver, heat exchangers, circuit pipes, etc.).

The mass content of the working fluid in the ith component is calculated by multiplying the internal volume of the component to the density of the fluid. This is considered constant and equal to the arithmetic mean of the values at the input and output of the component itself.

The working fluid density in this component depends on the pressure and the temperature in the component (medium). For a generic component could be possible to write:

$$M_c^j = \rho_c^j V_c^j = \frac{p_c^j}{RT_c^j} V_c^j \qquad (2.2)$$

Where:

- ρ_c^j is the average density of the working fluid in a generic component j [kg/m^3]
- M_c^j is the mass of working fluid contained in generic component j [kg]
- V_c^j is the volume content the air mass generic component j [m^3]
- p_c^j is the pressure (maximum) in a generic component j [Pa]
- T_c^j is the temperature in a generic component j [K]
- R is the ideal gas constant of air

Considering the average pressure and temperature values in the component (at first approximation between the input and output of the component) it is possible to write:

$$M_c^j = \rho_c^j V_c^j = \frac{p_{c,in}^j + p_{c,out}^j}{R(T_{c,in}^j + T_{c,out}^j)} V_c^j \qquad (2.3)$$

Where:

- $p_{c,in}^j$ is the inlet pressure of a generic component j [bar];

- $p_{c,out}^{j}$ is the outlet pressure of a generic component j [bar];
- $T_{c,in}^{j}$ is the inlet temperature of a generic component j [K];
- $T_{c,out}^{j}$ is the outlet temperature of a generic component j [K];

By considering all the components of the plant that contain working fluid, it is possible to obtain the total mass of the working fluid simply summing up all the masses contained in the various components.

$$M_{tot} = \sum_{1}^{n} M_c^j = \sum_{1}^{n} \rho_c^j V_c^j = \rho_m V_{tot} \qquad (2.4)$$

Where:

$$V_{tot} = \sum_{1}^{n} V_c^j \qquad (2.5)$$

is the total volume and ρ_m is an average density, defined by eq. 2.4 itself .

The working fluid evolves in the various system components and takes pressures and temperatures that define the thermodynamic cycle. It should be emphasized that the thermodynamic efficiency of the cycle depends only on the temperature and pressure ratios:

$$\frac{T_{\max cycle}}{T_{\min cycle}} = \frac{T_3}{T_1} = \tau \; ; \qquad \frac{p_{\max - cycle}}{p_{\min cycle}} = \frac{p_2}{p_1} = \beta \qquad (2.6)$$

To maintain constant thermodynamic efficiency for a wide range of loads, the principle of regulation must be able to modify power output without modifying τ and β values.

The values T_1 and T_3 are often fixed (the first, at the lowest possible - the second as high as possible - compatible with the resistance of the materials).

Regarding the cycle pressure ratio β, it is possible to keep it constant regardless of the values p_1 and p_2.

2.3. Adjustment method

As illustrated previously, the mass contained in the system depends on the value of an average density (multiplied by the total volume occupied by the working fluid). It is clear that the volumes occupied by the working fluid remain fixed irrespective of the operating conditions of the plant.

To control the system, allowing a power change without decreasing efficiency, the temperature and pressure ratios must remain constant. This leaves the thermodynamic cycle unchanged. Fluid density, on the other hand, can be changed by playing a role of control variable.

The fluid density depends on the mass within the volume plant (equation (2.4)).

It should be emphasized that, under operating conditions, the relative density variation is the same at any point in the plant and in all N components, that is:

$$\frac{\Delta\rho_c^j}{\rho_c^j} = \frac{\Delta\rho_c^k}{\rho_c^k} \quad \forall \text{ j, k; } 1 \le j \le N; \; 1 \le k \le N \qquad (2.7)$$

If the cycle temperatures remain unchanged, the density variation can be obtained by changing the pressure in the circuit, thus imposing the law (2.7).

Practically, increasing the density in the cycle, the power increases, and being constant the total volume of the plant, the density increases only by adding working fluid into the cycle. An auxiliary compressor provides addition of mass to the plant.

As more mass is loaded, the density increases and therefore increases the power. The rate of power change is directly related to the rate of addition of mass and therefore to the mass flow rate of the auxiliary compressor.

2.4. Selection of parameters defining the thermodynamic cycle

The thermodynamic parameters that define the thermodynamic cycle (Brayton) are the minimum temperature, that has been assumed equal to 308 K (35 ° C), the maximum temperature, assumed equal to 1073 K (800 ° C) and the compression ratio will be defined below as it is part of an optimization process.

The minimum inlet pressure of the compressor should also be specified (in our case is constant and equals to 1 bar). The latter magnitude is not strictly necessary to define the thermodynamic cycle, but it is interesting for the definition of plant size as such value affects the density of the fluid and therefore the size of the engine, by means of the volumetric flow rate.

As the cycle is closed loop, the compressor inlet pressure value of the cycle could also be unknown; therefore, the pressure value is freely adjustable. Thus, in each instant, the pressure set the density ρ value, so it is possible to determine the mass flow (corresponding to this pressure):

$$G = \cdot\rho \cdot C \cdot A \quad (2.8)$$

Where :

- ρ is the average density of the air in the cycle;
- c is the velocity of the working fluid;
- A is the area of the passage section.

In which the magnitudes are relative to any reference point of the circuit.

The mass flow rate G, in turn, with an unaltered specific work, generates the desired power $N(W)$ (according to eq. (2.1)).

This is achieved by adding/removing working fluid through the use of an auxiliary compressor/ bleed valve. For example, if the maximum pressure of the receiver is set to 5 times the maximum pressure of the Brayton base cycle, it means that at any point in the system, at peak load, there will be pressures and densities 5 times the minimum values tested in the same points. Moreover, these minimum values correspond to low power operation.

In particular, the intake pressure of the compressor in the cycle, ad maximum load, is 5 bars and is always the minimum pressure in the plant, if compared to any other contemporary value observed in the cycle.

It is clear that, having to introduce working fluid into the plant circuit, it is convenient to do it at the point where the pressure is the lowest i.e. at the main compressor inlet. Therefore, an auxiliary compressor must be connected there. If the working fluid is air, the auxiliary compressor can take it directly from the atmosphere. In the above condition, the auxiliary compressor should provide a

maximum pressure ratio of 5. (Where 5 is the ratio between the maximum pressure at the main compressor inlet, 5 bar, and the ambient pressure).

2.5. Estimation of the auxiliary compressor power

The auxiliary compressor must provide a compression ratio to bring the pressure at the GT compressor inlet to that corresponding to the maximum power of the plant.

Under these conditions, the specific work of the auxiliary compressor is expressed by:

$$L_{c-aux} = \frac{kR}{k-1} T_{asp} (\beta_{aux}^{\frac{k-1}{k}} - 1) / \eta_{c-aux} \qquad (2.9)$$

- $L_{c\text{-}aux}$ is the work of auxiliary compressor;
- T_{asp} is the temperature of the air in inlet section of compressor;
- $\eta_{c\text{-}aux}$ is the efficiency of the auxiliary compressor;
- k is C_p/C_v;
- β_{aux} is the compression ratio of the auxiliary compressor;

β_{aux} should be chosen to satisfy the maximum power of the system.

The power absorbed by this auxiliary compressor is:

$$P_{c-aux} = \dot{m}_{caux} \cdot L_{c-aux} \qquad (2.10)$$

- $\dot{m}_{caux}$ is the mass flow rate; it should be evaluated on the basis of the faster changes of incoming thermal power.

The power rate of the plant is given by (2.10)

For the mass flow rate of the plant, it is always expressed by the equation (2.8) $G = \rho$ c A. Starting from a working condition of the plant in which power N_1 is produced, and assuming that the solar power increases from value 1 to value 2 in a time $\Delta t = t_2 - t_1$, the power output from N_2 rises up and the density varies from ρ_1 to ρ_2 so that:

$$\Delta N = N_2 - N_1 = (\rho_2 - \rho_1) cAL_s \qquad (2.11)$$

The mass must be added in the circuit to bring the density from ρ_1 to ρ_2; as seen above, which is given by the equation (2.4):

$$M_{tot} = \sum_1^n M_c^j = \sum_1^n \rho_c^j V_c^j = \rho_m V_{tot} \qquad (2.4)$$

And the density can be expressed as:

$$\rho_m = \frac{M_{tot}}{V_{tot}} \qquad (2.12)$$

Referring to two generic points, inside the loop, initial point 1 and final point 2, equation 2.12 is expressed as:

$$\rho_{m1} = \frac{M_{tot1}}{V_{tot}} \text{ and } \rho_{m2} = \frac{M_{tot2}}{V_{tot}}; \rho_{m2} - \rho_{m1} = \frac{M_{tot2} - M_{tot1}}{V_{tot}} = \frac{\Delta M_{tot}}{V_{tot}} \qquad (2.13)$$

$$\Delta\rho = \rho_2 - \rho_1 = (\rho_{m2} - \rho_{m1}) \frac{\rho_1}{\rho_{m1}} = \frac{\Delta M_{tot}}{V_{tot}} \frac{\rho_1}{\rho_{m1}} = \frac{\Delta M_{tot}}{V_{tot}} \frac{p_1}{p_{m1}} \frac{T_{m1}}{T_1} \qquad (2.14)$$

From (2.10) and (2.12):

$$\Delta N = \frac{\Delta M_{tot}}{V_{tot}} \frac{p_1}{p_{m1}} \frac{T_{m1}}{T_1} cAL \qquad (2.15)$$

$$\frac{\Delta N}{N_1} = \frac{\Delta M_{tot}}{M_{tot}} \qquad (2.16)$$

$$\Delta M_{tot} = M_{tot} \frac{\Delta N}{N} = \dot{m}_{c_{aux}} \cdot (t_2 - t_1) \qquad (2.17)$$

$$\dot{m}_{c-aux} = \frac{\Delta N}{N} \frac{M_{tot}}{(t_2 - t_1)} \qquad (2.18)$$

$$P_{c-ausi} = \frac{\Delta N}{N} \frac{M_{totale}}{(t_2 - t_1)} \cdot \frac{kR}{k-1} T_{asp} (\beta_{ausiliario}^{\frac{k-1}{k}} - 1) / \eta_{c-aus} \qquad (2.19)$$

Equation (2.19) is expresses to define the field excursion of the adjustment and the total mass present in relation to the power, the power of the auxiliary compressor depends on the ratio:

$$P_{c-aux} = Cost \cdot \frac{\Delta N}{\Delta t} \qquad (2.20)$$

Where:

$$Cost = \frac{M_{tot}}{N} \cdot \frac{kR}{k-1} T_{asp} (\beta_{aux}^{\frac{k-1}{k}} - 1) / \eta_{c-aux} \quad (2.21)$$

When there is a decrease of the thermal power input to the cycle, for example, due to a decrease of DNI, the power adjustment always takes place on the circulating mass, bleeding the mass which results in excess through a dedicated valve.

2.6. Estimation of the plant optimal compression ratio

The closed-loop system leads to constructive complications mainly due to the need of heat exchangers that must return the working fluid from the exhaust temperature to the inlet temperature of the compressor.

By doing so, the exhaust gas heat energy is removed, as in the open loop.

In order to recuperate this thermal energy, regeneration is needed, so the compressed air from the compressor outlet is heated by the hot air in outlet from the turbine.

On the other hand, it is known that heat regeneration is only possible when there is a positive temperature difference between the turbine's outlet gases and the compressed air exiting the compressor. The existence and magnitude of this temperature difference depends on the compression ratio and on the ratio between the maximum and minimum temperatures, of the thermodynamic cycle.

Since the maximum and minimum temperature values of the thermodynamic cycle are set (equation 6), regeneration depends only on the compression ratio of the thermodynamic cycle.

The optimization process, with simplified hypotheses on specific compression and expansion heat values, will be illustrated with the aid of Figure 2.2.

Therefore, it is not possible to exploit all the temperature drops for the restrictions of the heat exchanger. Regarding this, regeneration degree is defined as follows:

$$R_{rig} = \frac{T_B - T_2}{T_4 - T_2} \qquad (2.22)$$

The temperatures are referred to the T-s diagram in figure 2.2.

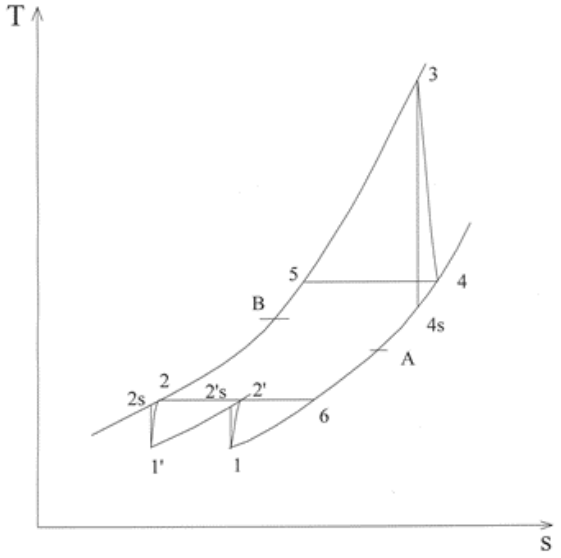

Figure 2.2: T-s diagram of regenerated Joule-Brayton cycle

In the process of optimizing the cycle compression ratio, the compression is divided into two stages of equal magnitude ($\beta_{1stage} = \beta_{2stage} = \sqrt{\beta_c}$), with an intercooling process between them, in order to bring the start temperature of the second compression step equal (35 ° C) to the temperature at the first compressor inlet (Figure 2.2).

Referring to figure 2.2 it is possible to define the thermodynamic efficiency of the plant as:

$$\eta_{term} = \frac{L_t - L_c}{c_p(T_3 - T_B)} \qquad (2.23)$$

Where:

- L_t expansion work ;
- L_c compression work;

$$L_t = c_{p3-4}(T_3 - T_4) = \eta_t c_{p3-4}(T_3 - T_{4s}) = \eta_t \frac{kRT_3}{k-1}(1 - \frac{1}{\beta_e^{\varepsilon_e}}) \qquad (2.24)$$

The intercooled compression work is defined as:

$$L_c = L_{c1} + L_{c2} = c_{p2'-1}(T_{2'} - T_1) + c_{p2-1'}(T_2 - T_{1'}) = 2\frac{k}{k-1} RT_1 \frac{(\beta_c^{\frac{\varepsilon_c}{2}} - 1)}{\eta_c} \quad (2.25)$$

Where:

- $T_{1'} = T_1$;
- $T_{2'} = T_2$;
- η_t adiabatic expansion efficiency;
- η_c adiabatic compression efficiency;
- $\varepsilon_c = \frac{k-1}{k}$ compression exponent;

$$\eta_t = \frac{T_3 - T_4}{T_3 - T_{4s}} \qquad (2.26)$$

$$T_4 = T_3 - \eta_t(T_3 - T_{4s}) = T_3[1 - \eta_t(1 - \frac{1}{\beta^{\varepsilon_e}})] \qquad (2.27)$$

$$\eta_c = \frac{T_{2s} - T_1}{T_2 - T_1} \qquad (2.28)$$

$$T_2 = T_1 + \frac{T_{2s} - T_1}{\eta_c} = T_1(1 + \frac{\beta_c^{\frac{\varepsilon_c}{2}} - 1}{\eta_c}) \qquad (2.29)$$

From eq. (2.21), the temperature T_B is obtained:

$$T_B = T_2 + R_{rig}(T_4 - T_2) \tag{2.30}$$

$$\eta_{term} = \frac{\eta_t \frac{\tau}{\varepsilon_e}\left(1 - \frac{1}{\beta_e^{\varepsilon_e}}\right) - \frac{2}{\varepsilon_c}\frac{\left(\beta_c^{\frac{\varepsilon_c}{2}} - 1\right)}{\eta_c}}{\frac{\tau}{\varepsilon_e}\left(1 - \frac{T_B}{T_3}\right)} \tag{2.31}$$

$$\frac{T_B}{T_3} = (1 - R_{rig})\left(1 - \eta_t\left(1 - \frac{1}{\beta^{\varepsilon_e}}\right) + \frac{R_{rig}}{\tau}\left(1 + \frac{\beta^{\frac{\varepsilon_c}{2}} - 1}{\eta_c}\right)\right) \tag{2.32}$$

Where:

- $\tau = \frac{T_3}{T_1}$

Figure 2.4 shows the trend of the temperature difference $T_4 - T_B$. It is possible to notice how the difference of temperature is close to the null value at $\beta = 10$. By these calculations, as shown in figures 2.2 and 2.3, it is noticeable that the compression ratio β of the thermodynamic cycle should be between 5 to 6. In this case a value of 6 has been chosen.

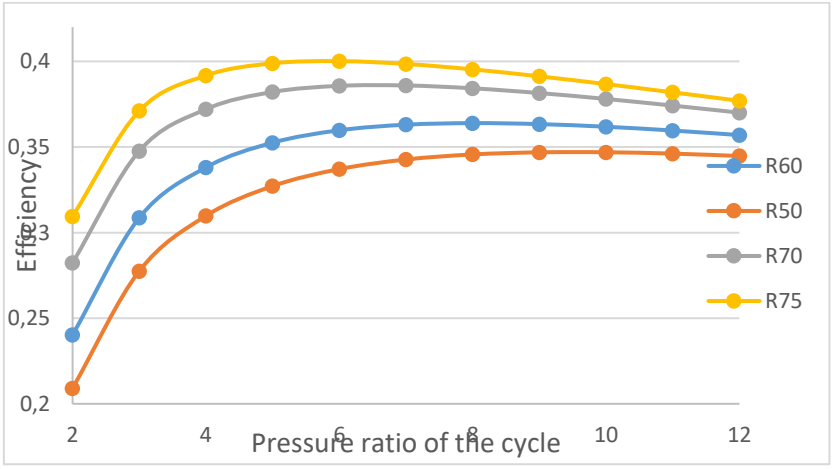

Figure 2.3: Efficiency vs compression ratio

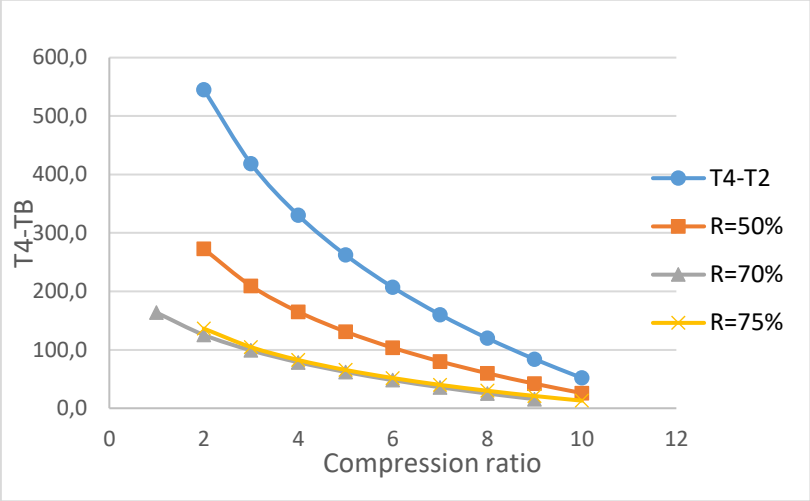

Figure 2.4: Trend of the temperature difference between the outel gas and compressed air, at different degrees of regeneration

2.7. Effect of mass flow control system

The main vantages of mass flow control system is the capability to keep constant the system efficiency under different thermal load.The already mentioned invariability of the temperature and the compression ratio of the thermodynamic cycle has the visible effects in the T-s diagram (Fig. 2.5). The thermodynamic Brayton cycle will shift, depending on the load fixed by the solar source, on different entropy values, on different isobaric curves, without altering the temperatures of each thermodynamic point.

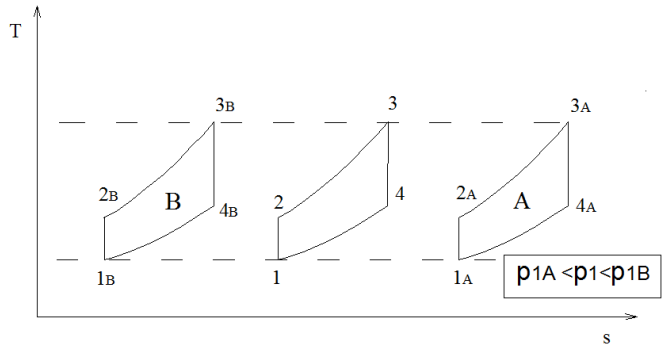

Figure 2.5: T-s diagram effect of mass flow adjustment

Particularly, as can be seen in figure 2.5, during an increase in incident radiation power, the expected effect is a translation of the thermodynamic cycle

towards higher isobaric values, due to increased air mass in the cycle following the pressure rises provided by the auxiliary compressor.

Vice versa, the decrease in the thermal power input moves the thermodynamic cycle towards the lower isobaric values. An air mass reduction is therefore indispensable and it is performed by the opening of the bleed valve.

2.8. Choosing of polytrophic efficiency

To model the system behaviour and to predict its performance an important parameter has to been set: the polytrophic efficiency of compression and expansion processes, since it has a heavy consequence on overall efficiency of the plant (solar plant and gas turbine).

It is known that the performance of the machines depends on their size because different design variables do not change strictly according to the geometric similarity, and there are some important fluid-dynamic losses among them.

Therefore, we base the polytrophic efficiency value on studies that statistically correlate it with parameters that summarize the effect of the dimensions. In particular, a size parameter will be used defined as [27]:

$$SP = \frac{V^{0.5}}{\Delta h_{is}^{0.25}} \quad (2.33)$$

Where:

- V: is the volumetric flow, flowing in every stage of compressor/turbine;
- Δh_{is}: is the enthalpy variation between the inlet and outlet for the compressor/turbine.

The volumetric flow is calculated as:

$$V = \frac{\dot{m}}{\rho} \quad (2.34)$$

The mass flow flowing in the cycle depends on the power rate of the gas-turbine:

$$\dot{m}_{comp/turb} = \frac{P_{comp/turb}}{\bar{C}_p \cdot \Delta T} \quad (2.35)$$

Where:

- $P_{comp/turb}$: is the power of the compressor or the turbine [kW];
- $\bar{C}_p$is the average specific heat of the air in compression/expansion [kJ/kgK];
- ΔT is the temperature difference between inlet and outlet of compressor or turbine [K].

The equation (2.34) is referred independently to the compressor or turbine for the evaluation of the mass flow.

The compressor work is evaluated as in [38]:

$$W_C = \frac{C_p \cdot T_1 \cdot [\beta^{\frac{\gamma-1}{\gamma}} - 1]}{\eta_m \eta_c} \qquad (2.36)$$

Where:

- C_p is the specific heat [J/kgK];
- T_1 is the base temperature of the cycle [K];
- β is the compressor ratio;
- η_m is the mechanical efficiency;
- γ is $=\frac{C_p}{C_v} = 1.4$;
- η_c is the compressor efficiency;
- W_c is the specific compression work [J/kg].

While the turbine work has been expressed as in [38]:

$$W_t = C_p \cdot TIT \cdot \eta_t \cdot \left[1 - \frac{1}{\beta^{\frac{\gamma-1}{\gamma}}}\right] * \eta_m \qquad (2.37)$$

Where:

- C_p is the specific heat [J/kgK];
- TIT is the inlet turbine temperature of the cycle [K];
- β is the compressor ratio;
- η_m is the mechanical efficiency;
- γ is $=\frac{C_p}{C_v} = 1.4$;
- η_t turbine efficiency;
- W_t is the specific expansion work [J/kg].

The network of the gas turbine (W_{net}) is calculated from the equation:

$$W_{net} = W_t - W_c \qquad (2.38)$$

The output power from the gas turbine (P) is expressed as:

$$P_{net} = W_{net} \cdot \dot{m} \qquad (2.39)$$

In addition, at the same time the compressor power is:

$$P_c = \dot{m} \cdot W_c \qquad (2.40)$$

Moreover, the turbine power is:

$$P_t = \dot{m} \cdot W_t \qquad (2.41)$$

Where:

- $\dot{m}$ is the mass flow flowing in the cycle [kg/s].

The outlet temperature of the compressor stage is evaluated as [38]:

$$T_2 = T_1 \cdot [1 + \frac{\beta^{\frac{\gamma-1}{\gamma}} - 1}{\eta_c}] \qquad (2.42)$$

Where:

- T_1 is the base temperature of the cycle (35 °C);
- γ is $=\frac{C_p}{C_v} = 1.4$;
- β is the compressor ratio;
- η_c is the isentropic efficiency of the compressor.

The density of the air crossing the turbine was evaluated as:

$$\rho_{Turb} = \frac{P_{max}}{T_3 * \bar{R}} \qquad (2.43)$$

Where:

- T_3 is the inlet turbine temperature i.e. TIT (800°C);

The density for the compressors (two intercooled compressor stage) has been evaluated as:

$$\rho_{comp} = \frac{P_{max}}{T_{in,comp} * \bar{R}} \qquad (2.44)$$

The maximum pressure of the cycle is:

$$P_{max} = \frac{\mathrm{P_{max,rec}}}{\beta} \qquad (2.45)$$

Where:

- P_{max} is the maximum inlet pressure of the cycle;
- $T_{in,comp}$ is the inlet air temperature of the compressors (35°C). The same base temperature will be considered in both cases, because an intercooled compression has been considered;
- $\bar{R}$ is the ideal gas constant of air .

P_{max} of the cycle depends of the cycle pressure ratio (evaluated in the past session as 6) and the maximum operative pressure of the receiver ($P_{max,rec}$).

This pressure was evaluated from the bibliography as 30 bars [29].

It is clear that, increasing the base pressure, and consequently the mass of working fluid, it follows an increase of the power (peak power) of the cycle. Particularly, in this case, the power (for this kind of engine) increases five times respect to the design condition.

Following to the SP calculation, the evaluation of the polytrophic efficiency for the compressor and the turbine will be illustrated [27].

Compressor:

if SP<1 $\eta_p = 0.915 \cdot [1 - 0.07108 \cdot \log_{10}{}^2 SP\ ];$ (2.46)

if SP≥1 $\eta_p = 0.915;$ (2.47)

Turbine:

if SP<1 $\eta_p = 0.94 \cdot [1 - 0.02688 \cdot \log_{10}{}^2 SP\ ];$ (2.48)

if SP≥1 $\eta_p = 0.94;$ (2.49)

As easily perceived, the parameter SP, for the turbine and the compressors, depends on the power rate of the gas turbine.

In figure 2.6 it is possible to observe the SP trend versus the power rate for both compressors considered, from 0.01MW to 50 MW. Particularly the blue line represents the size parameter for the first stage compressor while the red one for the second stage.

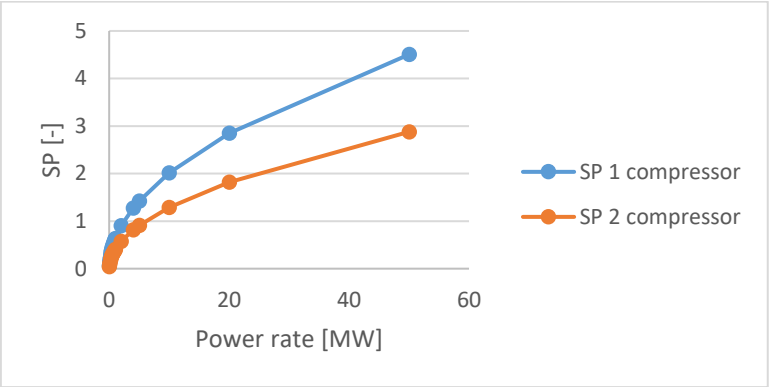

Figure 2.6: Size parameter vs power rate for first and second compressor stage

Figure 2.7 and figure 2.8 show the polytrophic efficiency trend vs SP for the first stage and the second stage, respectively.

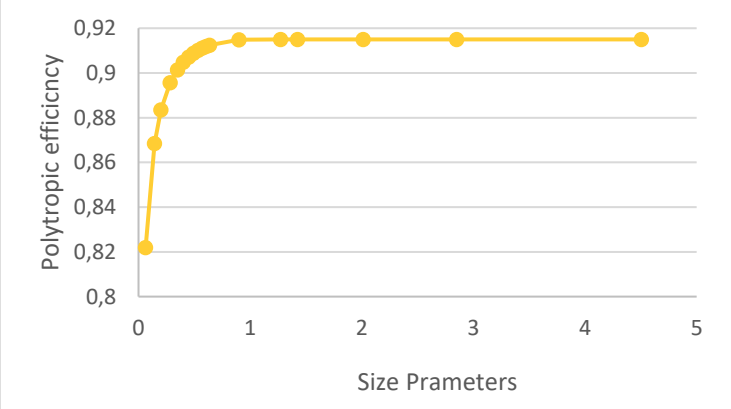

Figure 2.7: SP vs polytropic efficiency for first compressor stage

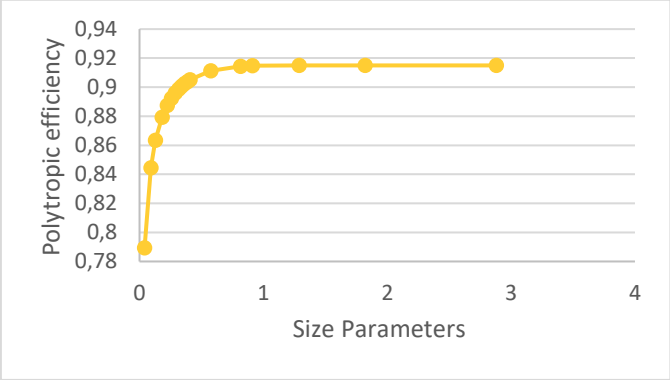

Figure 2.8: SP vs polytropic efficiency for second compressor stage

In the following figure 2.9 it is possible to observe the SP trend for the turbine vs the power rate.

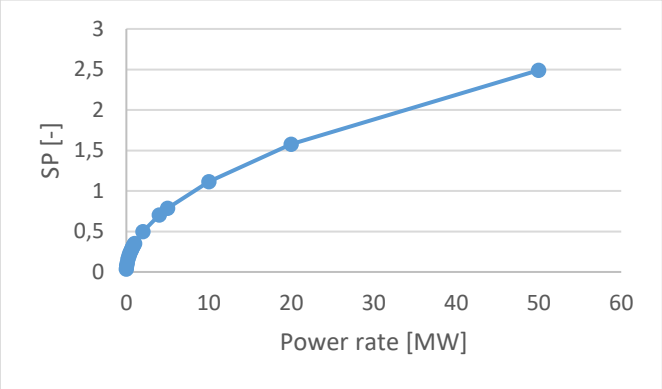

Figure 2.9: Size parameter vs power rate for the turbine

Figure 2.10 shows the polytrophic efficiency trend vs the SP of the turbine.

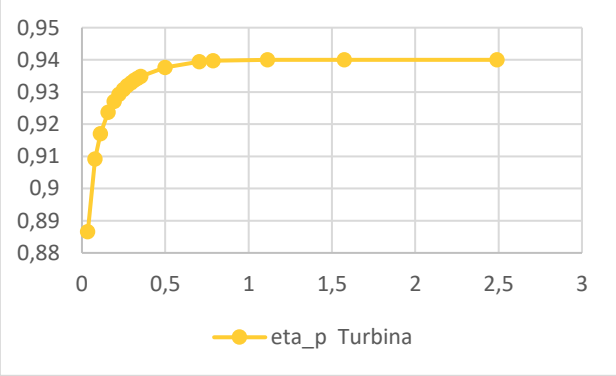

Figure 2.10: Polytropic efficiency vs power rate of the turbine

The evaluation of the SP , and consequently the polytrophic efficiency, is needed for the selection of the power plant configuration; in fact, the mass flow flowing in the cycle depends on the polytrophic efficiency, so the net power (the difference between turbine power and compressor power) rely on the SP . Selected the power rate of the gas turbine, and calculated the power rate of compressors and turbine, the polytrophic efficiency has been calculated by means of SP.

2.9. Coupling with solar collector

Choosing the main parameters for the gas turbine, in this session the coupling with the solar collector (solar tower) will be illustrated.

As described in Chapter 1, the use of the solar tower is needed to allow high temperatures.

The collector efficiency could be expressed as [70]:

$$\eta_{coll} = \eta_{opt} - \frac{U_l \cdot (T_r - T_a)}{CR_g \cdot I_{b,a}} - \frac{\varepsilon \cdot \sigma_B (T_r^4 - T_a^4)}{CR_g \cdot I_{b,a}} \qquad (2.50)$$

Where:

- η_{opt} is the optimum collector efficiency (0.9);
- U_l is the receiver overall heat-loss coefficient (70 W/m^2 K);
- T_r is the receiver operating temperature (K);
- T_a is ambient temperature (298 K);
- CR_g is the geometric concentration ratio;
- $I_{b,a}$ is the beam (direct) aperture irradiance (850 W/m^2);
- ε is the emittance (effective) of receiver (0.9);
- σ_B is the Stefan-Boltzmann constant (5.6696 × 10^{-8} W/m^2 K^4);

The efficiency of a regenerative Joule-Brayton cycle depends, in addition to the pressure ratio, on the ratio between the maximum and minimum temperature:

$$\eta_{GT} = 1 - \left(\frac{T_1}{T_3}\right) \cdot (\beta)^{\frac{k-1}{k}} \qquad (2.51)$$

Where:

- T_1 is the base cycle temperature (35°C);

- T_3 is the turbine inlet temperature;
- β is the compressor ratio (6);
- k is $\frac{c_p}{c_v} = 1.4$;

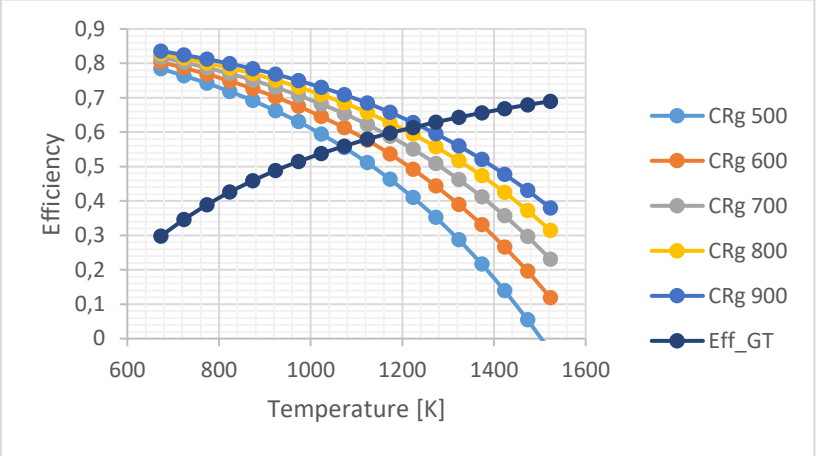

Figure 2.11: Collectors/ Gas turbine efficiency vs Temperature

Figure 2.11 describes the efficiency trend versus the temperature for different value of solar collector concentration ratio and for the gas turbine. From this graphic is possible to choose the operating temperature of solar collector and gas turbine.

It is also possible to observe, that for concentration ratios in the range between 500 and 900, the operating temperature is around 800°C (1073 K); so it is reasonable to choose this value for our system, as maximum cycle temperature.

The other reasons come from the operating temperature restrictions of solar receivers [34] for technical issues due to material resistance.

From the product between the gas turbine efficiency and the collector one, it is possible to obtain the overall cycle efficiency; the following figure 2.12 represents for different concentration ratio, the trend of the efficiency versus the maximum operative temperature.

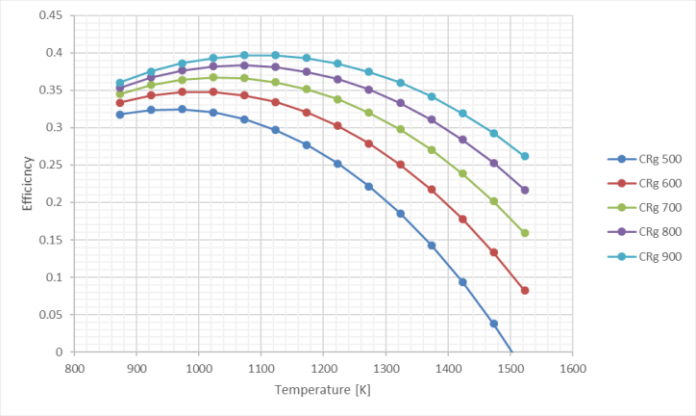

Figure 2.12: Overall cycle efficiency vs maximum operative temperature

2.10. Conclusions

In this chapter, the power plant with mass flow control system has been presented; all equations that describe the thermodynamic model of the cycle have been displayed.

In addition, the main parameters have been chosen in order to optimize the simple cycle efficiency, and then the solar collector has been added; so, the characteristic temperature and base pressure of the cycle have been selected for the entire plant.

In conclusion, as described, the cycle efficiency, employing this control strategy, keeps constant under all operation conditions, without use of fuel, and this characteristic plays a fundamental role in solar power systems.

Chapter 3
Parametric analysis, simulation and comparison of the closed loop Brayton with mass flow control

3.1. Introduction

A parametric analysis a solar closed loop Brayton plant as a function of the power rate to obtain the performance in terms of energy production, average efficiency and performance of control system is presented in this chapter.

The simulation has been performed by using a commercial software and the results will be compared with an unfired open Brayton cycle, working in atmospheric condition.

3.2. Sited and parameters design selection

The first step is to choose the location for the installation. A procedure which implies several steps could be the following [40]:

1) Cartographic analysis (GIS) and solar mapping maps on a regional scale to locate the site;
2) Use of data related to direct radiation (DNI), as well as main parameters, from satellite sources to reach a mean average annual average direct radiation;

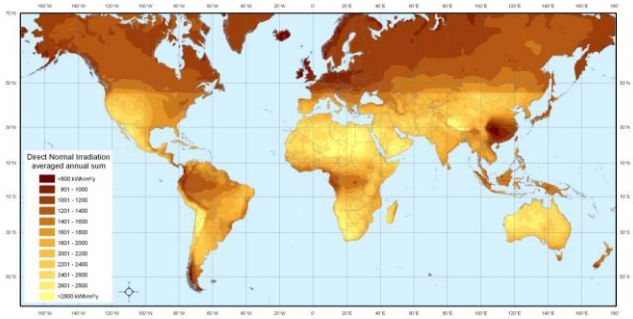

Figure 3.1: DNI map on "Sun belt".

The minimum solar energy per unit of surface must be 1800-2000 kWh / m^2 / year and the best conditions are for latitudes between 10 ° and 40 ° North or

South, for semi-arid areas characterized by days clear, high altitudes, where the absorption and dispersion of sunlight are much lower;

3) Confirmed the interest for the site, it is good practice to install a measuring station for measuring ground on direct solar radiation, taking advantage of the time required for planning and authorization phases;
4) It is good practice to have measured data for a time span of at least one year;

The location of eligible sites must take into account a number of aspects related to the technology to be used:

- The need for a large amount of space (in particular for solar tower systems);
- Possibility of proximity to transport and power evacuation routes;
- Need for high levels of radiation;
- Specific gradient requirements depending on the technologies to be used;
- Environmental constraints.

The regions of the world that fully meet these requirements are located in the called "sun belt" (Figure 3.1). It can be deduced that the optimal choice falls over areas close to the equator and for low rainfall. Desert areas are, in this respect, very favourable, but have the opposite of the fact that the wind also brings sand that can deteriorate heliostats and receivers [87].

One of the most important data is latitude: at latitude changes the geometry of the field and also changes the high of the tower. Moving to higher latitudes, the size of the field increases, and the layout evolves from a circular form to the equator, towards an elongated shape north to the highest latitudes, approaching a North Field configuration.

At lower latitudes the field is much more compact as the heliostats will work mainly in a horizontal position and therefore are less affected by shadowing and blocking phenomena, but they will have a higher tower height.

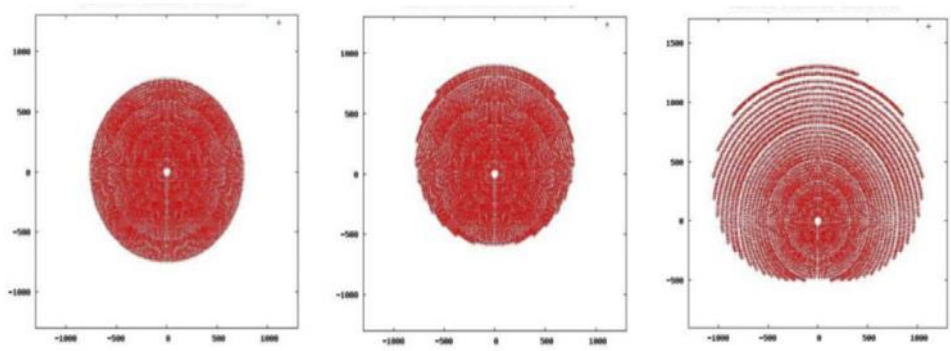

Figure 3.2: Variation in field layout for latitude 0 °, 20 ° and 60 °

In this work we will be choosing as plant site Seville Town sited in south of Spain in Andalusia region (Latitude 37.41 N, Longitude 5.90 W, Altitude 31 m). In this place, the average annual direct normal irradiation (DNI) is of 2,068 kWh /m². The typical meteorological year of Seville (TMY) [41] have been used , in particular the weather data of ambient temperature, relative humidity and Direct Normal Radiation have been employed in the simulation.

The climate is Mediterranean with oceanic influences, characterized by mild winters and hot summers. The average annual temperature is around 18.5 °C. Precipitation is concentrated in the months between October and April, with tips in December for a total of about 55 days of rainfall.

One of important parameters for the heliostat field design is the DNI and sun position design point. In this work, solar noon on the 21st June , summer solstice, has been chosen. The position of the sun is: Azimuth 180° and elevation 76°.

To choose the DNI design point, we use the percentile 95 of the cumulative distribution function from data of TMY3 of Seville [41], resulting in a design point 850 W/m² . In figure 3.3 is possible to note the graph of the cumulative distribution function.

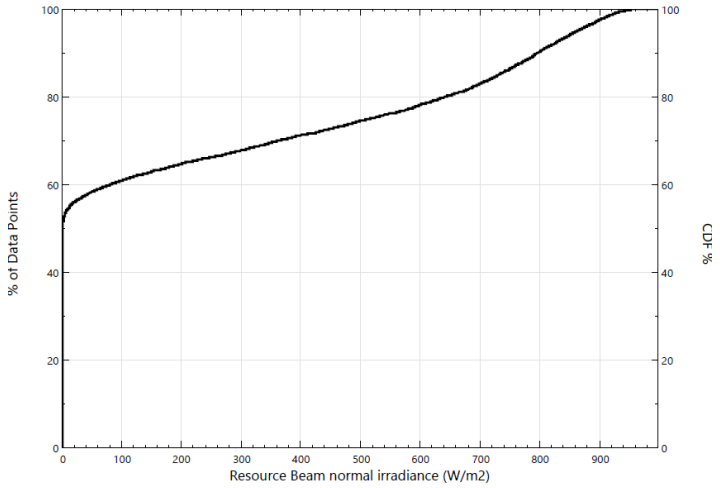

Figure 3.3: CDF of DNI (TMY 3) for Seville elaborated by thermodynamic group of University of Seville (source SAM)

Another important parameter is the solar multiple. It is a way of expressing the opening of the solar field according to the power of the cycle being subjected. The solar multiple is defined as the ratio between the nominal power of the capturing surface (concentrator surface) and the nominal electrical power of the plant [40].

The optimal value of the solar multiple, ie the one that minimizes costs, is typically between 1.2 and 1.4 for systems without accumulation system, while it can reach 2 or higher values in plants where there is a thermal energy storage system [22].

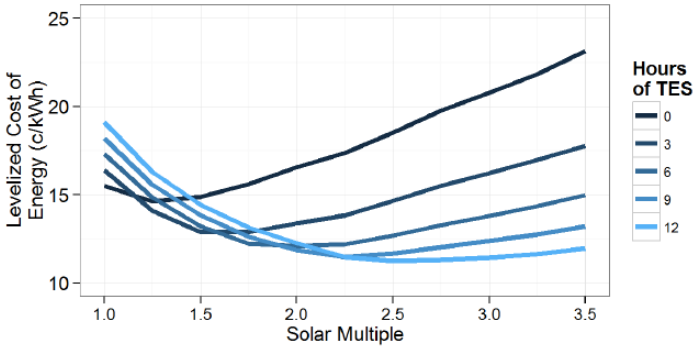

Figure 3.4: Solar multiple trend vs LCoE

3.3. Software used

In this session the simulation of the system, performed by two commercial softwares, WinDelsol [43] regarding the solar field and Thermoflex [44], for the entire plant will be illustrated.

3.3.1. Thermoflex software

The design of the entire plant was performed using Thermoflex commercial software, produced by the American company Thermoflow. Software widely used in the analysis of industrial plants of various kinds. Thermoflex is a simulation program for the realization and modelling of energy balances with graphical interface that allows building the plant component by component.

The Plant Engineering and Construction Estimator extension provides the engineering details of each component as well as an estimate of costs. Thermoflex is organized according to the structure shown in figure 5.

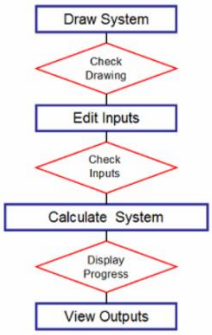

Figure 3.5: Thermoflex operative flowchart

The first step is to build the system to be simulated by selecting the different components of the plant. The software performs a check drawing by checking the pairs between the various components.

The next step is to enter the user data. Once this input phase has been completed, the software checks the entered values by searching for any conflicting situations. In the event of errors, the software signals the presence of a problem by highlighting the flow and the component involved.

The third stage involves a real simulation during which the software performs a series of calculation cycles, determining the configuration that meets the constituent equations and the mass, energy, and thermal exchange (thermodynamic design simulation) equations. Finally, the results are shown.

To get a pre-design of components, including an estimation of their cost, it is necessary to run the simulation in engineering design mode. The results of the design in engineering simulations are presented according to the same procedures as in thermodynamic design with the addition only for the Preliminary plant engineering and cost estimation module (PEACE) components, a tabulated form of all the output values, including the construction schemes of the component and an estimate of costs of the same. Then the system is designed to operate and any modifications to the installation level is necessary to return to the previous steps

To simulate the behaviour of the plant dimensioned off-design, Thermoflex allows the off-design work environment within which it is possible to assess the impact of the change of external conditions on the computing performance.

3.3.2. WinDelsol software

In this part, the heliostat field optimization will be addressed. There are several codes that allow the optimum design and sizing of the mirror field [88]:

- ASAP
- DELSOL
- MIRVAL
- SAM

However, in this analysis Delsol and its Windows interface (WinDelsol) have been used, because it is destined for large-scale plants for the production of electricity[88], which makes it suitable for the purposes of this thesis.

WinDelsol is a software developed by Aicia -Solucar-Ciemat in 2002. It is a graphical interface written in Visual Basic 6 for the DELSOL code. It is a post-processing tool that facilitates the input of input variables, especially useful for those who do not know the FORTRAN language, signalling syntax errors that could lead to inconsistent and completely wrong results [43]. In addition, WinDelSol interprets the results generated by the DELSOL algorithm and

presents them graphically, in the form of charts and tables, allowing a quick interpretation of such data.

DELSOL is a FORTRAN77 code, developed at the University of Houston and initially dedicated to Solar One Solar System. This code, based on user-defined input variables through text files, allows you to perform performance, optical and economic analysis of a CRS (Central Receiver System) system. Using a Hermite-based analytical method, DELSOL can predict flow images on the receiver, dimension a solar tower system, optimize the mirror field, receiver size, and tower height. The code examines a number of input parameters and optimizes the system taking into account costs, solar variability, cosine effect, shadowing and blocking effects, spillage, atmospheric attenuation, and reflectivity of heliostats, receiver absorbency as well as radiation, convection and piping losses.

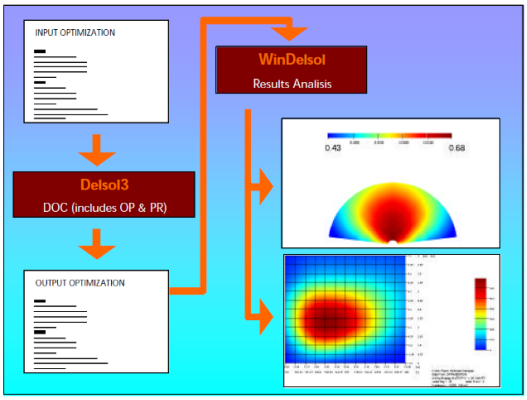

Figure 3.6: WinDelsol flowchart

3.4. Solar field parametric analysis

In this part the methodology and the results obtained for the heliostats field sensibility analysis; these results, then, will be used in Thermoflex to characterised the solar filed part will be illustrated.

Keep in mind that, the solar field will be designed for four power rate plant of 5, 10, 20 50 MW of peak power.

The first part illustrates the data input employed in WinDelsol for the optimization, while in the second one will be shows the result in term of heliostats field layout, field efficiency, optical matrix efficiency (function of

Azimuth and Zenith), receiver dimensions, and incident flux on the receiver surface. In last part will be compared the results with other plant with the same power rates but, with the Variable Inlet Guide Vane (VIGV) to control the Turbine Inlet Temperature due to the mass flow variation. First of all, as described in chapter 1, the solar field configuration is the North filed, because the peak power is lower than 50 MW. As said before a SM equal to 1.3 is assumed (reasonable for a CSP system without storage). The receiver type assumed is the volumetric pressurized, described in the chapter 1, because, as said, the cycle operates under pressurized condition (30 bar); the operative temperature of the receiver is 800°C and it is the same of the maximum cycle temperature.

The solar radiation, on the receiver, is absorbed inside the structure "volume" (volumetric effect). The air is forced through the absorber (a porous structure) and is heated by convective heat transfer [45]. In the pressurized volumetric receiver, generally, the absorber is inside an internally insulated pressure vessel closed by a transparent quartz window and usually connected to a secondary concentrator. Because of the restricted size of quartz windows, a number of volumetric receivers (cluster) is required to achieve the desired power levels [46]. An average flux incident on the receiver of 400 kW/m^2 and an air temperature at the receiver outlet of 800 ºC are assumed as described in chapter 2[29]. Last parameters are the heliostat dimension and reflectivity, that were assumed of 120 m^2 and 92%, respectively [19].

Table 3.1 shows the data used in WinDelsol to design the solar fields.

Solar multiple	1.3
Flux incident [kW/m^2]	400
Efficiency cycle	0.4
Referring day	172
DNI design [W/m^2]	850
Receiver absorptance	0.97

Table 3.1: Main data input on WinDelsol

WinDelsol also requires to add the radiative losses, so to determine it (for first step simulation) we using following equation:

$$Q_{rad} = \alpha \cdot A \cdot \sigma \cdot T_s^4 \qquad (3.1)$$

Where :

- T_s is the operative temperature of the receiver,
- α is the absortance of the receiver surface at his mean temperature,
- A is the square receiver surface calculated by equation ()

$$A = \frac{P_{Th,\max}}{Flux_{incident}} \qquad (3.2)$$

Where:

- $Flux_{incident}$ is the average flux incident
- $P_{Th,max}$ is the maximum power incident into the receiver surface

The maximum thermal power was evaluated as:

$$P_{Th,\max} = P_{Th} * SM \qquad (3.3)$$

Where :

- SM is the solar multiple
- P_{th} is the nominal thermal power

The nominal thermal power was evaluated as:

$$P_{Th} = \frac{P_{el}}{\eta_c} \qquad (3.4)$$

Where :

- P_{el} is the net electric power i.e. the power rate chosen for the analysis
- η_c is the cycle efficiency.

Considering an employing of a volumetric receiver, have been supposed the surface temperature of the receiver the same of outlet air temperature from the receiver. In this section the solar receiver will be considered as a "black box" in order to evaluate the solar field dimensions and the heat transfer to the working fluid.

In follow table 3.2 are resumed these data, employing in the code

P_{el} [MW]	P_{Th} [MW]	$P_{Th,max}$ [MW]	A [m^2]	Q_{rad} [kW]
5	12,5	16,25	40,62	2963,4
10	25	32,5	81,25	5926,8
20	50	65	162,5	11853,6
50	125	162,5	406,25	29634,0

Table 3.2: Receiver first step size and radiative losses.

No calculation about the convective losses was performed, because considered of a low magnitude order respect the radiative one [11].Table 3.1, shows the values of the sensibility analysis results performed on maximum ratio of outer and inner radius and span angle of the solar field. The outer radius is the maximum radial distance in terms of equivalent tower heights that heliostats may be placed in the field. The inner radius is the minimum radial distance in terms of equivalent tower heights that heliostats may be placed in the field. [43].The span angle is the aperture of heliostat field in degrees. For the 5 MW receiver a tilt angle of 105° have been used [47]. A value of 90° have been used for others solar fields.

	5 MW	10 MW	20 MW	50 MW
Minimum ratio outer/inner radius	0.9	0.9	0.9	0.9
Maximum ratio outer/inner radius	10	10	10	12
Span angle [°]	100	100	90	120

Table 3.3: Input data in WinDelsol for field dimensions. Radii are expressed in terms of tower heights.

3.5. Solar field parametric analysis results

In this this session the results performed by WinDelsol for each configuration will be illustrated.

Follow figure 3.7 shows the solar field layout for the 5 MW power plant with the efficiency scale. As possible to note from, the plant is composed by 337 heliostats; the

peak power incident on the heliostats field is 23.578 MW. The heliostats field annual optical efficiency is 65.25 %.

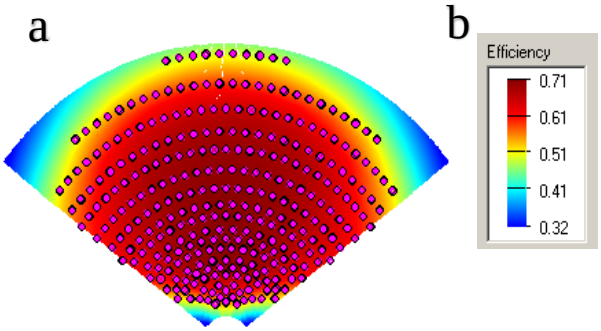

Figure 3.7: 5MW power plant, a) solar field layout with efficiency scale, b) scale values

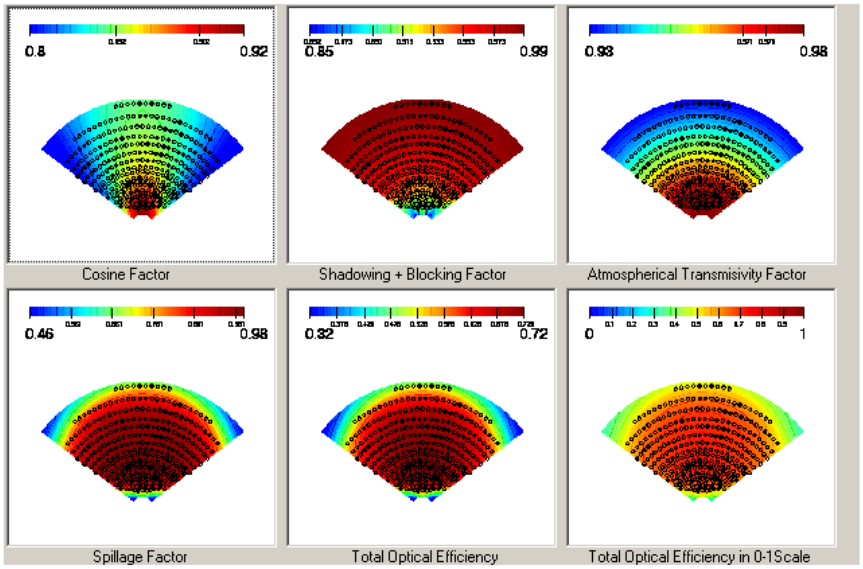

Figure 3.8: Factors losses solar fields' layout of 5 MW power plant

In figure 3.8 it is possible to note the 5 MW fields layouts including the loss for cosine factor, shadowing + blocking, atmospherical, and spillage.

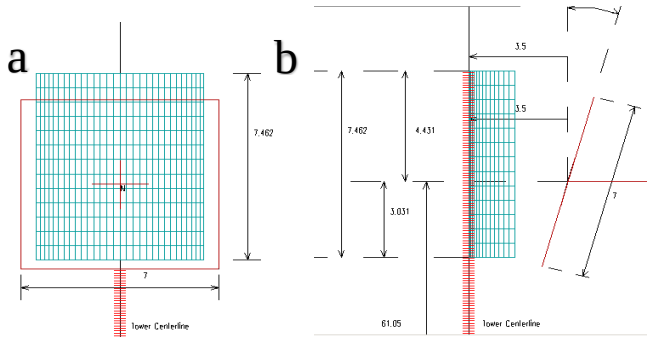

Figure 3.9: a) front view of receiver b) lateral view of receiver for 5 MW solar field

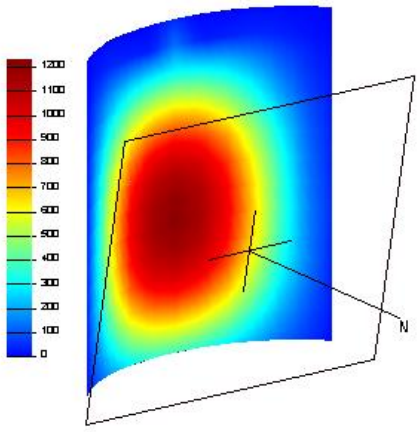

Figure 3.10:Flux incident receiver on receiver surface in 3D for 5 MW power plant

Figure 3.9 a) and b) show the receiver for the 5 MW solar field; in particular fig 9a show the front view of the receiver, while 9b the lateral one. Could be possible to observe, in figure 9 b as the receiver has a tilt angle of 15 degrees. The receiver efficiency is about of 79.60 % .

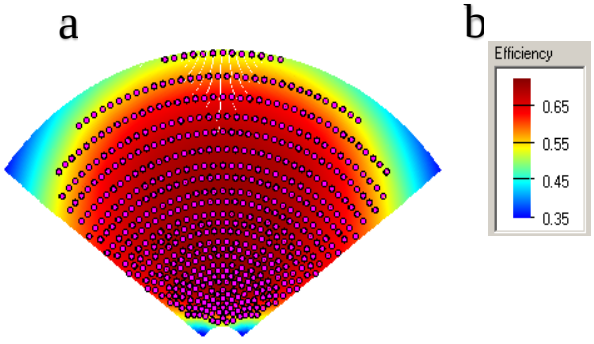

Figure 3.11: 10 MW power plant, a) solar field layout with efficiency scale, b) scale values

From figure 3.11 it is possible to observe that the 10 MW solar field has 650 heliostats; the nominal power incident on heliostats surface is 45.843 MW, the annual optical efficiency was estimated as 66.40% and the annual incident energy is 104.28 GWh. Figure 3.12 shows the 10 MW solar field layout with inclusive the factors losses, explained in chapter 1.

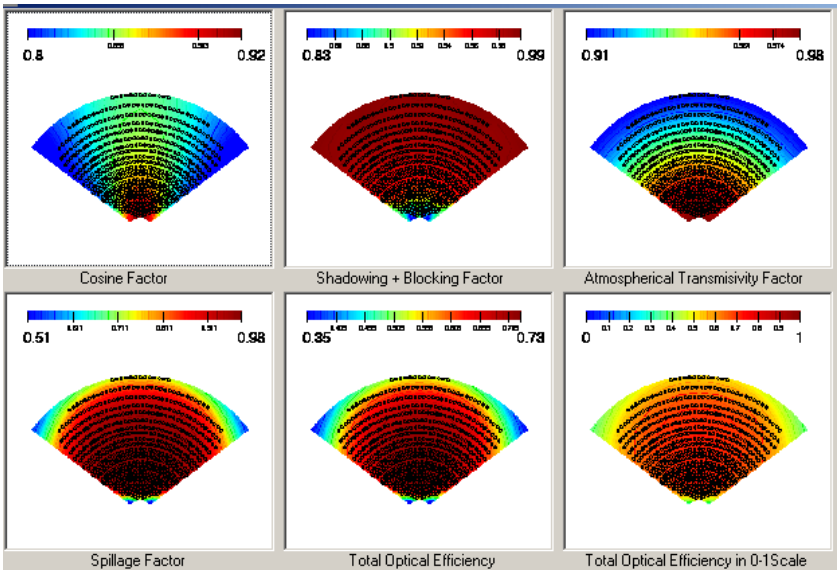

Figure 3.12: Factors losses solar fields layout of 10 MW power plant

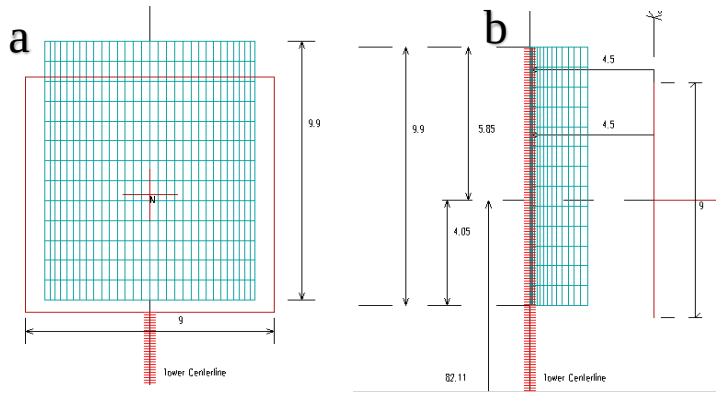

Figure 3.13: a) front view of receiver b) lateral view of receiver for 10 MW solar field

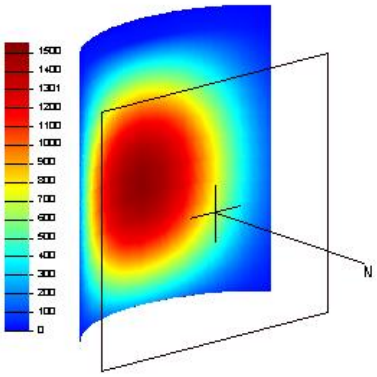

Figure 3.14: Flux incident receiver on receiver surface in 3D for 10 MW power plant

Figure 3.14 illustrates the 3D receiver of the 10 MW power plant, including the flux incident on its surface that has a maximum value of 1550 W/m^2. The receiver efficiency is of 82.12 %.

In figure 3.15 the 20 MW solar power plant is shown; this field is composed by 1289 heliostats and the annual optical efficiency amount to 68.30 %. The design power on the reflective surface is 91.45 MW while the annual energy is equal to 210 GWh.

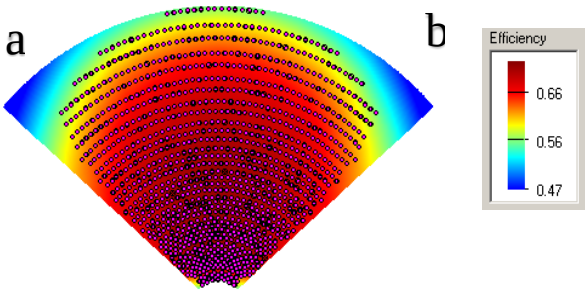

Figure 3.15: 20 MW power plant, a) solar field layout with efficiency scale, b) scale values

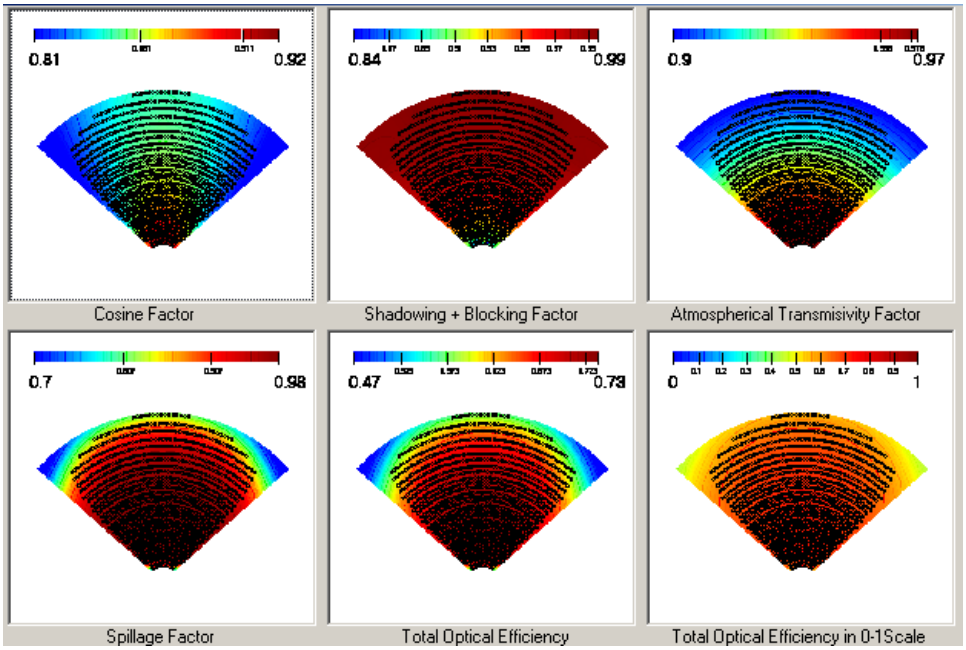

Figure 3.16: Factors losses solar fields layout of 20 MW power plant

In figure 3.16 it is possible to note the 20 MW fields layouts including the loss for cosine factor, shadowing + blocking, atmospherical, and spillage.

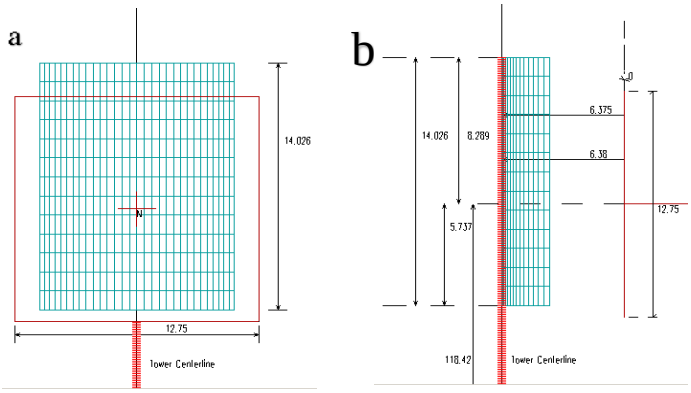

Figure 3.17: a) front view of receiver b) lateral view of receiver for 20 MW solar field

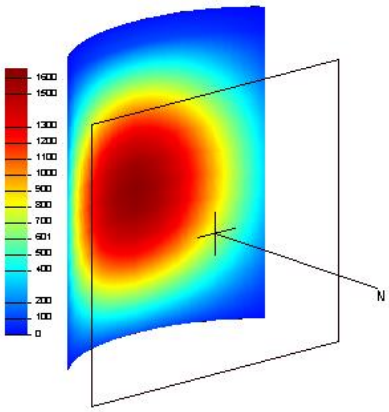

Figure 3.18: Flux incident receiver on receiver surface in 3D for 20 MW power plant

Finally in figure 3.18 and figure 3.17 a) and b) could be possible to observe the receiver dimension, and the flux incident in 3 dimensions of 20 MW power plant. The maximum solar flux allowed is 1660 W/m^2 while the receiver efficiency is 82.09 %.

Follow 3.19 picture shows the heliostats field of 50 MW power plant, that is composed by 3326 heliostats and has an annual optical efficiency of 66.24 %. In this configuration at design point, the power incident on heliostats surface is 227.51 MW, while the energy ones is about 524 GWh.

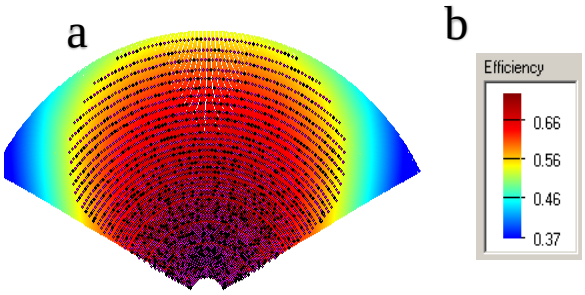

Figure 3.19: 50 MW power plant, a) solar field layout with efficiency scale, b) scale values

Lasts figures represent, respectively, figure 3.20 the factor layout field losses for 50 MW power plant, figures 3.21 a) and b) the front and lateral view of the receiver.

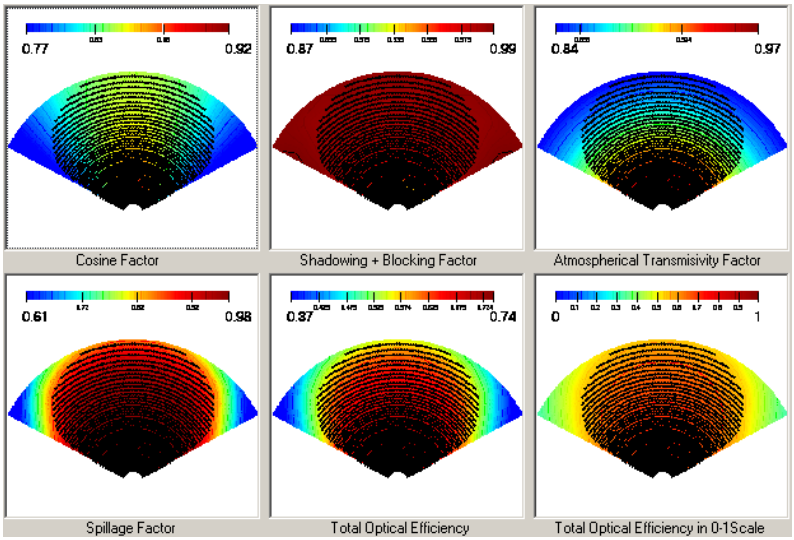

Figure 3.20: Factors losses solar fields layout of 50 MW power plant

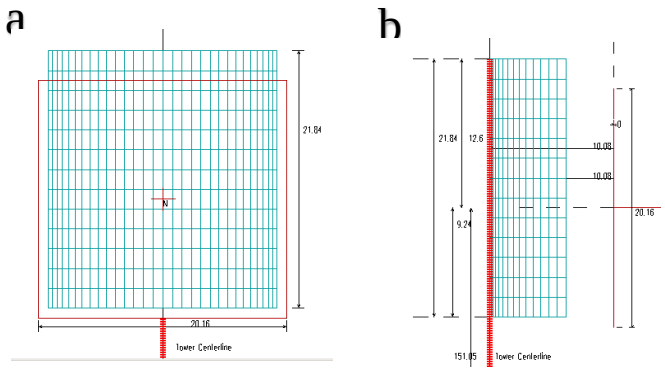

Figure 3.21: a) front view of receiver b) lateral view of receiver for 50 MW solar field

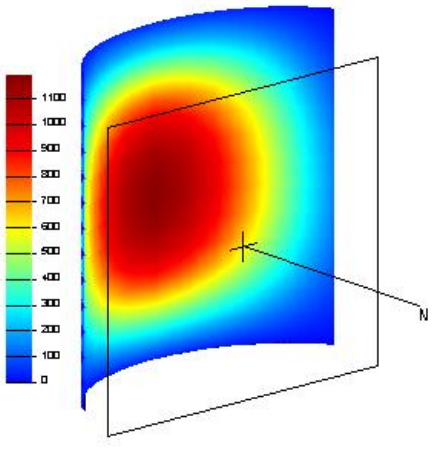

Figure 3.22: Flux incident receiver on receiver surface in 3D for 50 MW power plant

Another important parameter is the solar matrix optical efficiency that describes the efficiency trend of the solar collectors during the year and the days. In this discussion, a matrix performed by WinDelsol has been taken into account that includes all optical and thermal losses but not the absorbance one [43]; the data used to calculate these matrixes was explained in session 2.9.5

Follows tables 3.4, 3.5, 3.6 and 3.7 are a 2-D representation of the field efficiency as a function of solar zenith (Y) and azimuth (X) angles of the 5 MW, 10 MW, 20 MW and 50 MW power plants.

	0	30	60	90	120	150	180	210	240	270	300	330
0.5	0.60	0.60	0.60	0.60	0.60	0.60	0.60	0.60	0.60	0.60	0.60	0.60
7	0.62	0.62	0.60	0.59	0.58	0.57	0.57	0.57	0.58	0.59	0.60	0.62
15	0.64	0.63	0.60	0.56	0.54	0.52	0.51	0.52	0.54	0.56	0.60	0.63
30	0.66	0.65	0.59	0.53	0.48	0.43	0.41	0.43	0.48	0.53	0.59	0.65
45	0.67	0.65	0.58	0.49	0.41	0.35	0.33	0.35	0.41	0.49	0.58	0.65
60	0.64	0.62	0.54	0.44	0.34	0.28	0.27	0.28	0.35	0.44	0.54	0.63
75	0.53	0.51	0.45	0.39	0.28	0.22	0.20	0.22	0.29	0.39	0.46	0.52
85	0.39	0.38	0.37	0.33	0.23	0.17	0.14	0.17	0.24	0.34	0.38	0.40

Table 3.4: Matrix of efficiencies of the 5 MW solar field

	0	30	60	90	120	150	180	210	240	270	300	330
0.5	0.59	0.59	0.59	0.59	0.59	0.59	0.59	0.59	0.59	0.59	0.59	0.59
7	0.61	0.61	0.60	0.59	0.58	0.57	0.56	0.57	0.58	0.59	0.60	0.61
15	0.64	0.63	0.61	0.58	0.55	0.53	0.52	0.53	0.55	0.58	0.61	0.63
30	0.66	0.65	0.61	0.56	0.51	0.46	0.45	0.46	0.51	0.56	0.61	0.65
45	0.66	0.64	0.60	0.53	0.46	0.40	0.37	0.40	0.46	0.54	0.60	0.65
60	0.63	0.61	0.57	0.49	0.40	0.32	0.29	0.32	0.40	0.49	0.57	0.62
75	0.48	0.47	0.43	0.38	0.29	0.22	0.19	0.22	0.30	0.38	0.44	0.48
85	0.25	0.26	0.25	0.23	0.19	0.15	0.12	0.15	0.19	0.24	0.26	0.27

Table 3.5: Matrix of efficiencies of the 10 MW solar field

	0	30	60	90	120	150	180	210	240	270	300	330
0.5	0.59	0.59	0.59	0.59	0.59	0.59	0.59	0.59	0.59	0.59	0.59	0.59
7	0.61	0.61	0.60	0.59	0.58	0.57	0.57	0.57	0.58	0.59	0.60	0.61
15	0.63	0.63	0.61	0.58	0.55	0.54	0.53	0.54	0.55	0.58	0.61	0.63
30	0.67	0.65	0.62	0.57	0.52	0.48	0.46	0.48	0.52	0.57	0.62	0.65
45	0.68	0.67	0.62	0.55	0.48	0.42	0.40	0.42	0.48	0.56	0.62	0.67
60	0.66	0.65	0.60	0.52	0.43	0.36	0.33	0.36	0.43	0.52	0.60	0.65
75	0.53	0.52	0.47	0.41	0.33	0.26	0.23	0.26	0.33	0.42	0.48	0.52
85	0.31	0.31	0.29	0.27	0.22	0.18	0.16	0.18	0.23	0.28	0.31	0.32

Table 3.6: Matrix of efficiencies of the 20 MW solar field

	0	30	60	90	120	150	180	210	240	270	300	330
0.5	0.59	0.59	0.59	0.59	0.59	0.59	0.59	0.59	0.59	0.59	0.59	0.59
7	0.61	0.61	0.60	0.59	0.57	0.57	0.56	0.57	0.57	0.59	0.60	0.61
15	0.63	0.62	0.60	0.58	0.55	0.54	0.53	0.54	0.55	0.58	0.60	0.62
30	0.66	0.65	0.61	0.57	0.52	0.48	0.47	0.48	0.52	0.57	0.61	0.65
45	0.68	0.66	0.62	0.56	0.48	0.43	0.41	0.43	0.49	0.56	0.62	0.67
60	0.66	0.65	0.60	0.52	0.44	0.37	0.34	0.37	0.44	0.53	0.60	0.65
75	0.53	0.52	0.47	0.42	0.34	0.27	0.25	0.27	0.34	0.42	0.48	0.53
85	0.32	0.32	0.30	0.28	0.23	0.19	0.17	0.19	0.24	0.28	0.31	0.33

Table 3.7: Matrix of efficiencies of the 50 MW solar field

The matrixes have been employed to characterize the solar field part on Thermoflex; in fact, the software evaluated the power absorbed by the working fluid (so transfer to the bottom cycle) as:

$$Q_{SF} = DNI \cdot A_{Tot} \cdot \eta_{SF} \qquad (3.5)$$

Where :

- DNI is the direct normal irradiance [W/m^2];
- A_{tot} is the heliostats total area [m^2];
- η_{SF} is the solar field efficiency.

Particularly the solar field efficiency is the product between optical efficiency of heliostats field and the receiver efficiency (that includes thermal losses):

$$\eta_{SF} = \eta_{HF} \cdot \eta_{Rec} \qquad (3.6)$$

Where:

- η_{HF} is the heliostats field optical efficiency expressed in chapter 1;
- η_{Rec} is the receiver efficiency;

So, because the solar field efficiency is function of Azimuth and Zenith, the solar optical matrix efficiency allow to the Thermoflex software to estimate, in steady state condition the thermal power transfer to the fluid.

In this way, employing the TMY 3 data, with a time step of 1 hour, of DNI, ambient temperature, relative humidity, and the solar position (by Azimuth and Zenith) the plants performances have been evaluated.

3.6. Gas turbine parametric analysis

In this session will be describe the gas turbine parametric analysis; in particular, with referring to chapter 2 will be shows the peak power rate for each gas turbine and his main parameters (required from Thermoflex).

Than will be introduced the data of heat exchanger (but this part will regard in detail another part of this work) used in the simulations

3.6.1. Turbine and compressors

As described in chapter 2 too, the mass flow control system, produced by an increment of pressure base of the cycle (so of the gas turbine), cause an increasing specific work and peak power.

As mentioned in same section, there are an increase of pressure, depending on the receiver operative pressure, and pressure ratio equal to five time.

In this way, if in past session a peak power rate of 5 MW, 10 MW, 20 MW and 50 MW have been analyzed; in this one, the power rate of the gas turbines became:

$$P''_{GT} = \frac{1}{P_{Max}} \cdot P'_{GT} = \frac{\beta}{P_{Max,rec}} \cdot P'_{GT} \quad (3.7)$$

Where:

- P''_{GT} is the new pressurized gas turbine power rate;
- P'_{GT} is the nominal gas turbine power rate;

So, the nominal power rate of the 1 MW, 2 MW, 4 MW and 10 MW will be examined. First of all, will be characterized, following the treatise of session 2.8, singularly the compressors (keep in mind that is two compressors stage) and the turbine. Will be calculate, for compressors and turbine, the volumetric flow rate, the enthalpy variation, so the size parameters and finally the polytrophic efficiency.

Table 3.8 shows the main result of the compressors stage; as possible to note, the polytrophic efficiency of both compressors, increasing the power rate of the gas turbine became more or less the same.

	1 MW	2 MW	4MW	10 MW
Volumetric flow rate first stage [m^3/s]	6.29	12.59	25.17	62.93
Δh first stage [kJ/kg]	240.25	240.25	240.25	240.25
SP first stage	0.64	0.90	1.27	2.01
η_{pol} first stage	91.25%	91.49%	91.50%	91.50%
Volumetric flow rate second stage [m^3/s]	2.57	5.14	10.28	25.69
Δh second stage [kJ/kg]	240.25	240.25	240.25	240.25
SP second stage	0.41	0.58	0.81	1.29
η_{pol} second stage	90.51%	91.13%	91.45%	91.50%
η_{mec}	98	98	98	98

Table 3.8: Main data evaluated for first and second stage

	1 MW	2 MW	4 MW	10 MW
Volumetric flow rate stage [m^3/s]	2.78	5.55	11.11	27.77
Δh stage [kJ/kg]	500.83	500.83	500.83	500.83
SP stage	0.35	0.50	0.70	1.11
η_{pol} stage	93.48%	93.77%	93.94%	94.00%
η_{mec}	98	98	98	98

Table 3.9: Main data evaluated for turbine

3.7. Heat exchangers

In this part, will be introduced, the main data using for the heat exchanger (intercooler, regenerator and low temperature heat exchanger) [89]. Table 3.10 shows the main data employed, for the regenerators [99] while table 3.11 illustrates the main data used for the intercoolers.

Thermal efficiency [%]	90
Normalized heat loss [%]	1
Minimum Pinch [°C]	2
Hot side pressure drop [%]	3
Cold side pressure drop [%]	3
Design point UA [kW/°C]	257.7

Table 3.10: Main Gas turbines regenerators data

Thermal efficiency [%]	90
Normalized heat loss [%]	1
Minimum Pinch [°C]	2
Hot side pressure drop [%]	3
Water side pressure drop [%]	5
Design point UA [kW/°C]	266.4
Temperature air outlet state after first stage [°C]	35

Table 3.11: Main Gas turbines intercoolers data

Last table 3.12 shows the data of low temperature heat exchanges.

Thermal efficiency [%]	90
Normalized heat loss [%]	1
Minimum Pinch [°C]	2
Hot side pressure drop [%]	3
Water side pressure drop [%]	5
Design point UA [kW/°C]	197.7
Temperature air outlet state [°C]	35

Table 3.12: Main low temperature heat exchangers data

3.8. Simulations results and comparison

In this session, the simulation results regarding the entire plants performed by Thermoflex will be illustrated, in terms of energy production and average efficiency.

Then, this result will be compared with other four solar power plant, using an open cycle, having, in this case, the gas turbine of a peak power of 5 MW, 10 MW, 20 MW and 50 MW and employing the same solar fields and receiver just analyzed.

3.8.1. Comparison plants

Figure 3.2 shows the open solar Bryton cycle, analyzed by Thermoflex too, used for comparison, with the closed pressurized one.

In this second case however, the mass flow control, so the TIT control, is not performed by the auxiliary compressor and bleed valve; the cycle is open, works on ambient pressure and there is not low temperature heat exchanger. The mass adjustment, in this case, is acted employing the variable inlet guide vane (VIGV) that changing their opening or closing depend on the thermal power absorbed by the fluid, so by the solar field collector [86].

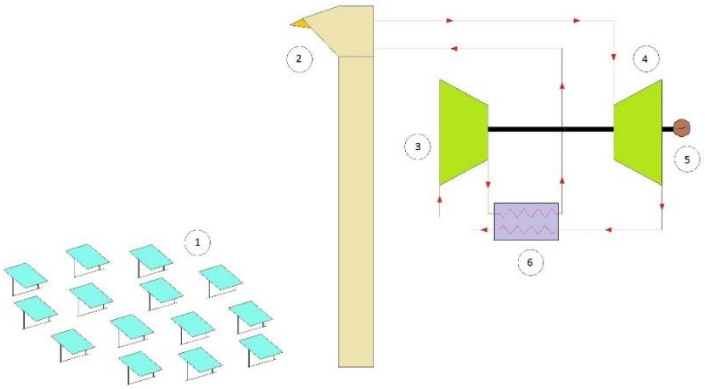

Figure 3.23: Open cycle Brayton

The goal is to keep the temperature inlet turbine constant to 800°C, as in the closed cycle. Keep the same the pressure ratio, the heats exchangers employed (regenerator and intercoolers) but changing the volumetric flow, the size parameters than the polytrophic efficiency.

In the following tables 13 and 14 will resume these mains data employed for the Thermoflex simulation, as performed for the closed plant. Table 13 shows the data for the two compressors stages, while table 14 shows the one of the turbine.

	5 MW	10 MW	20 MW	50 MW
Volumetric flow first stage [m3/s]	31.46	62.93	125.85	314.63
Δ h first stage [kJ/kg]	240.25	240.25	240.25	240.25
SP first stage	1.42	2.01	2.85	4.51
η_{pol} first stage	91.50%	91.50%	91.50%	91.50%

Volumetric flow second stage [m3/s]	12.84	25.69	51.38	128.45
Δ h second stage [kJ/kg]	240.25	240.25	240.25	240.25
SP second stage	0.91	1.29	1.82	2.88
η_{pol} second stage	91.49%	91.50%	91.50%	91.50%

Table 3.13: Main data of open cycle compressors

	5 MW	10 MW	20 MW	50 MW
Volumetric flow stage [m^3/s]	13.89	27.77	55.54	138.86
Δ h stage [kJ/kg]	500.83	500.83	500.83	500.83
SP stage	0.79	1.11	1.58	2.49
ηpol stage	93.97%	94.00%	94.00%	94.00%

Table 3.3.14: Main data of open cycle turbine

3.8.2. Results

In this part will illustrate the result performed by Thermoflex. The results simulations show how the plant with density control system (pressurized one) can achieve, in all size analyzed, an average annual efficiency around 40 %. In table 3.15 the yearly energy production and the average annual efficiency of the four size plant analyzed of the closed loop cycle are summarized.

Power rate [MW]	5	10	20	50
Yearly energy [GWh]	11.9	23.8	47.3	121.9
Annual average efficiency [%]	38.6	38.9	39.2	40.0

Table 3.15: Closed cycle size parametric analysis results

It is possible to note in figure 3.24 that the efficiency keeps constant during all operational hours. Particularly in the figure is shown the system performance, in term of hourly power product and efficiency vs hour of a generic day for 5 MW plant.

Could be possible to observe, in red line, that the efficiency values during the time examined are around 40 % (except during hours of sunset and sunrise for low DNI values), so near the design condition.

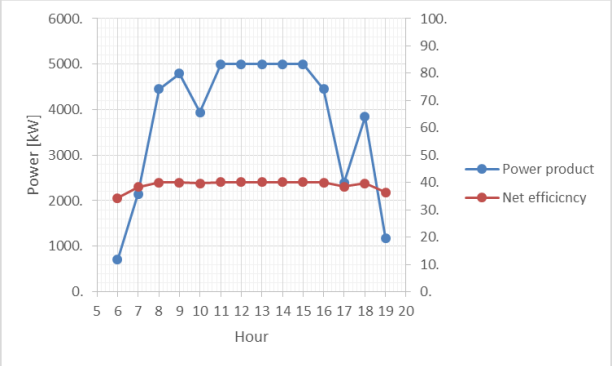

Figure 3.24: Power and efficiency vs hour of the day considered

Figure 3.25 shows the DNI vs hour of the considered day.

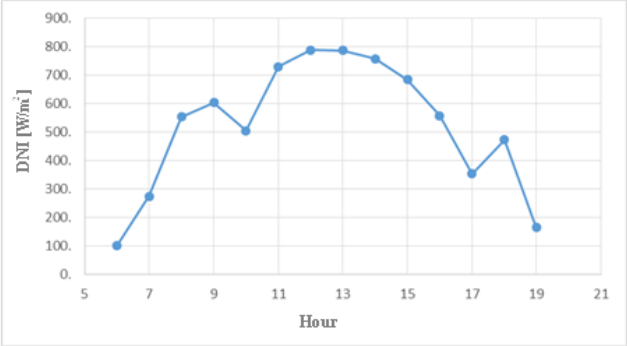

Figure 3.25: DNI trend vs hour of the day considered

Power rate [MW]	5	10	20	50
Yearly energy [GWh]	10.8	21.6	43.0	111.5
Annual average efficiency [%]	32.9	33.4	33.8	34.3

Table 3.16: Open cycle size parametric analysis results.

On the other hand, in table 3.16 it is shown the results simulation performed by Thermoflex for the open cycle; could be possible to observe that the yearly energy

production as well as the annual average efficiency are lower than the closed loop cases.

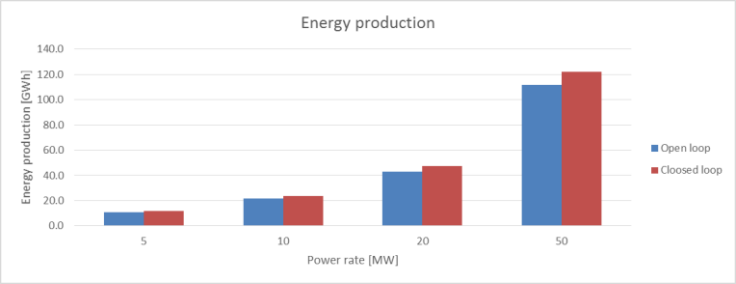

Figure 3.26: Comparison of energy production between open and closed cycle for each size power plant.

From the figure 3.26, it is evident that the energy production of the pressurized cycle is higher than the open one; in particular, the energy variation between two configurations is around the 9 % for each power rate examined.

In table 3.17 are resumed the energy consumed by the auxiliary compressor for the mass flow regulation. Not having any information different plant volume have been supposed for the 50 MW power plant.

Plant volume [m^3]	Yearly efficiency [%]	Energy compressor [GWh]
50	40,24	0,0068
100	40,23	0,0135
150	40,23	0,0203
200	40,23	0,0270
250	40,23	0,0338
500	40,21	0,0676
1000	40,19	0,1352

Table 3.17: Energy comsuption by the auxiliary compressos for closed 50 MW power plant

As possible to observe from table 3.17, the energy employed from the auxiliary compressor is very low, for all volumes analysed ,compared to the energy produced from the power plant. This is a fundamental aspect in order to understand the mayor advantage of this kind of control system: a huge energy production obtained with a low energy regulation consumption.

3.9. Conclusions

In this chapter, a general methodology about the simulations used in this thesis have been introduced. After, a comparison for four power plant, employing the mas flow control system, with an open simple solar Brayton cycle, have been performed.

From this analysis it is possible, sustain that the mass flow control system (i.e. closed loop cycle) can reach an higher theoretical energy production, employing engine gas turbines of a nominal power lower than the open cycle one, keeping constant the efficiency systems.

As observed, this effect is almost independent of the power rate chosen, so, for this reason, in the following sessions, different power rates, will be analyzed in order to study other power plants configurations.

Chapter 4
Solar field design for the unfired closed Joule cycle with mass flow control

4.1.Introduction

In this chapter, it will be analysed as the mass flow regulation, core of this work, also influences the solar field dimensions. In the following analysis, a solar multiple optimization for a power plant of 10 MW will be performed in order to optimized the Levelized Cost of Energy (LCoE). As described in chapter 1, the major cost of a concentrating solar power system is imputable to the heliostats and tower.

The proposed adjustment, works along with the heliostat field control system; so in this part will be analysed the interaction of these two kinds of control systems. In chapter 3, a parametric analysis for different power plant configuration has been performed, particular the performance of a 10 MW solar power plant with a solar multiple of 1.3 has been evaluated.

At this point, regarding the analysis on solar multiple of 1.0, 1.1, 1.2, 1.3, the same plant of 10 MW has been taken into account. The plant has all the same characteristics, in term of gas turbine efficiency, main temperature as well as the pressure ratio or operative pressure; the only variant is the solar multiple value.

As described, the optical analysis of the solar field, as well as the receiver dimensions and the optical losses by WinDelsol have been analysed, while for simulation of the entire plant Thermoflex has been used.

4.2.Heliostats fields design

In this part the results simulations performed by WinDelsol will illustrate respectively for solar multiple equal 1.2, 1.1 and 1.0. The field having the SM of 1.3 in chapter 3 has been analysed and the same methodology has been used.

In table 4.1 are shown the solar fields dimensions, in term of minimum and maximum ratio of outer and inner radius as well as the span angle.

	SM 1.3	SM 1.2	SM 1.1	SM 1.0
Minimum ratio outer/inner radius	0.9	1	0.9	0.9
Maximum ratio outer/inner radius	10	10	10	10
Span angle [°]	100	100	100	100

Table 4.1: Solar field ratio dimensions and span angle

The first plant analysed has the solar multiple equal to 1.2, and has the tower high 81.05 m and figure 4.1 shows, that the field is composed by 548 heliostats. The estimate incident energy on the heliostat field is about 86.64 GWh while the thermal peak power is 41.91 MW and the annual optical efficiency is 65.48 %.

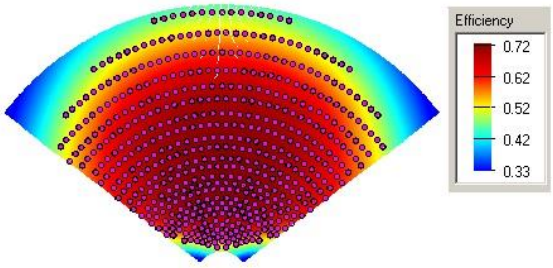

Figure 4.1: Heliostat field layout of SM=1.2 plant.

Figure 4.2 shows the field with solar multiple of 1.2 inclusive of all losses, while in table 4.2 are resumed the average, maximum and minimum values of each efficiency.

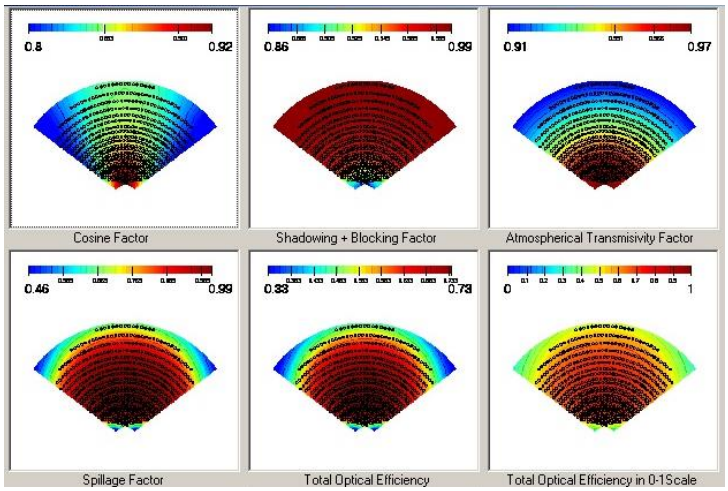

Figure 4.2: Factors losses solar fields' layout of SM 1.2

Efficiency	Average [%]	Maximum [%]	Minimum [%]
Cosine	85.02	92.6	80.2
Shadowing + Blocking	97.1	99.7	86.5
Transmissivity	94.64	98	91.1
Spillage	92.08	99.8	46.4
Total	66.2	73.98	33.22

Table 4.2: Average, maximum and minimum value of each field efficiency of SM 1.2

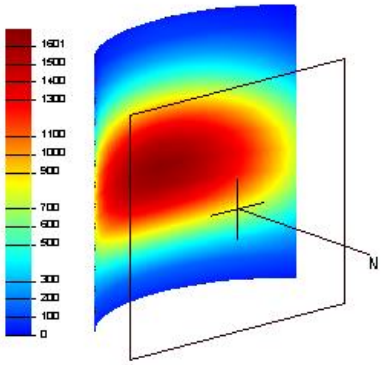

Figure 4.3: Receiver flux map of SM=1.2 configuration

Figure 4.3 shows the 3D flux incident on the receiver of the SM=1.2 configuration that has a yearly efficiency of 82.40 %

In figures 4.4a 4.4b, 4.4c are shown the receiver dimensions of the solar field with SM 1.2; figure 4.3a illustrates the front view while 4.3b and 4.c the lateral and the plant ones.

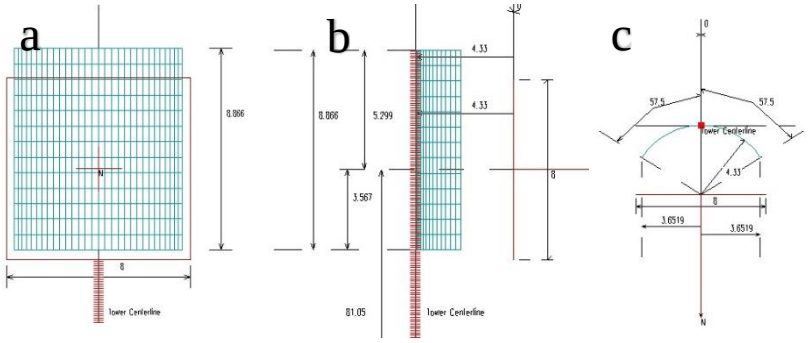

Figure 4.4: Receiver view and dimensions; a) front, b) lateral, c) plant of SM = 1.2 configuration.

In figure 4.5 could be possible to observe the solar plant having SM equal 1.1; the heliostat field is composed of 493 active heliostats and has an annual

optical efficiency of 65 %. The power incident of surface area is 36.21MW and the annual incident energy is 83.2 GWh.

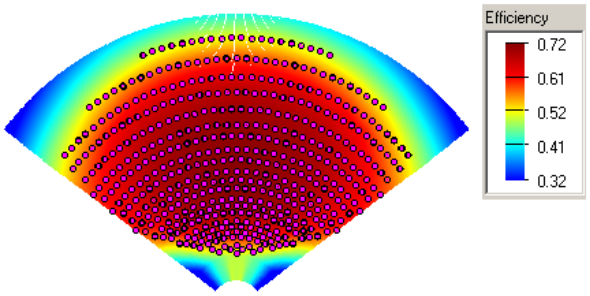

Figure 4.5: Heliostat field layout of plant with SM=1.1

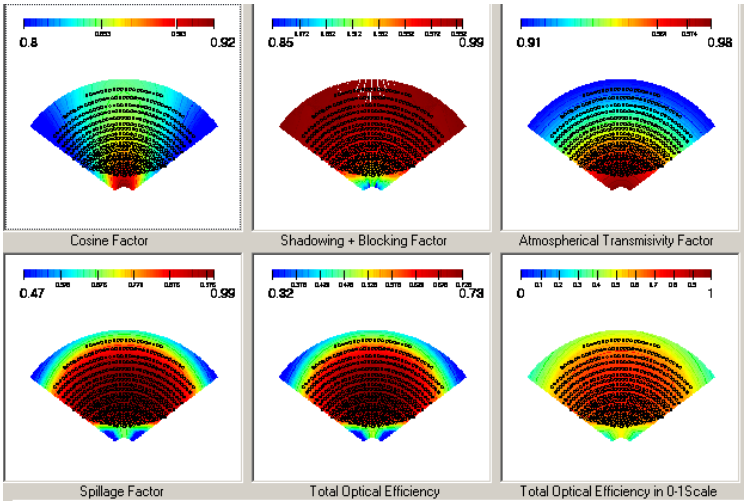

Figure 4.6: Factors losses solar fields' layout of SM 1.1

In figure 4.6 are represented the factor losses of the solar multiple 1.1 solar field and in table 4.2 are resumed the values of average, maximum and minimum efficiencies.

Efficiency	Average [%]	Maximum [%]	Minimum [%]
Cosine	84.75	92.8	80.2
Shadowing + Blocking	97.3	99.7	85.2
Transmissivity	94.94	98.2	91.9
Spillage	92.12	99.8	47.5
Total	65.64	73.01	32.75

Table 4.3: Average, maximum and minimum value of each field efficiency of SM 1.1

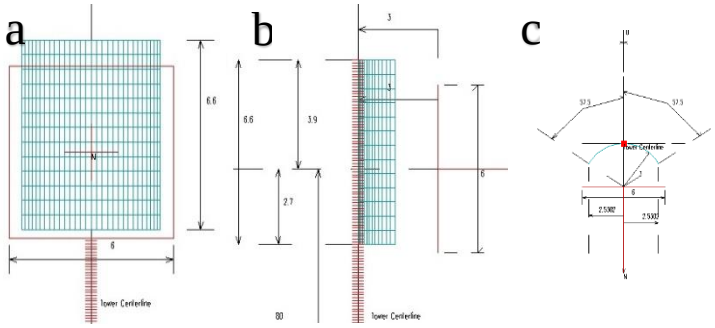

Figure 4.7: Receiver view and dimensions; a) front, b) lateral, c) plant of SM = 1.1 configuration.

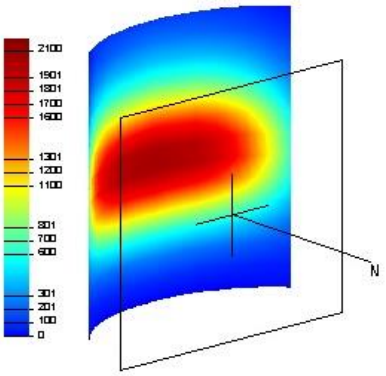

Figure 4.8: Receiver flux map of SM=1.1 configuration

In figure 4.8 it is represented the solar flux on the receivers configuration SM=1.1; the yearly efficiency is of 87.40%.

The last solar field analysed is the one with solar multiple equal 1 represented in figure 4.9;it has an annual optical efficiency of 66.47 %. The power incident on heliostat surface is 33.16 MW while the yearly energy incident is 76.1 GWh.

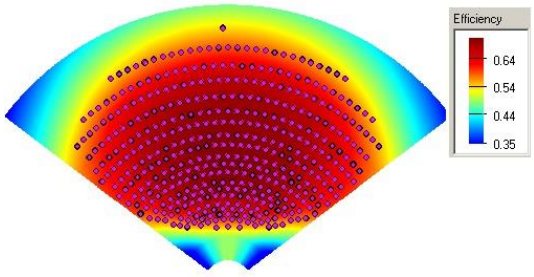

Figure 4.9: Heliostat field layout of plant with SM=1.0

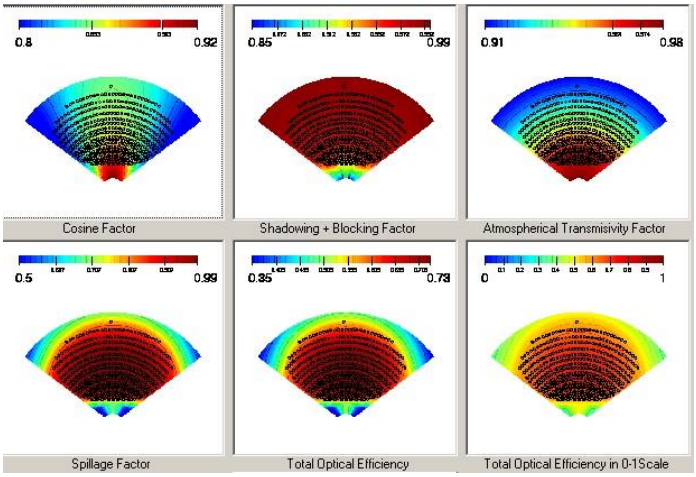

Figure 4.10: Factors losses solar fields' layout of SM 1.0

Efficiency	Average [%]	Maximum [%]	Minimum [%]
Cosine	84.85%	92.8	80.2
Shadowing + Blocking	97.22	99.7	85.2
Transmissivity	95.06	98.2	91.9
Spillage	93.69	99.8	50.6
Total	66.86	73.01	35.47

Table 4.4:Average, maximum and minimum value of each field efficiency of SM1.0

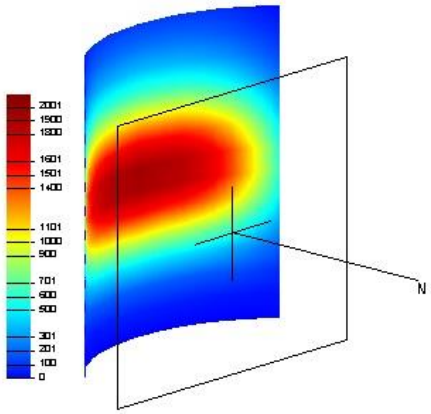

Figure 4.11: Receiver flux map of SM=1.0 configuration

Figure 4.11 shows the receiver, inclusive of solar flux incident of configuration solar multiple 1.0; in this case, the yearly device efficiency is of 86.68 %.

In the following tables 4.5, 4.6, 4.7 are shown the matrix's efficiency of the three solar multiple configurations function of Azimuth and Zenith; these efficiencies "maps" were used in Thermoflex to allow to calculate the net thermal power absorbed by the fluid in the solar field (of Thermoflex). As described in chapter 3, the annual data of DNI, Azimuth and Zenith, have been imposed in the software, as data input. For each iteration, Thermoflex calculates the entire plant performance.

	0	30	60	90	120	150	180	210	240	270	300	330
0.5	0.595	0.595	0.594	0.594	0.593	0.592	0.592	0.592	0.593	0.594	0.595	0.595
7	0.617	0.613	0.604	0.592	0.579	0.571	0.568	0.571	0.581	0.593	0.606	0.614
15	0.641	0.633	0.614	0.587	0.56	0.54	0.534	0.543	0.563	0.59	0.616	0.635
30	0.676	0.662	0.626	0.574	0.518	0.475	0.46	0.478	0.523	0.58	0.63	0.664
45	0.7	0.681	0.631	0.557	0.475	0.407	0.38	0.41	0.481	0.564	0.636	0.684
60	0.706	0.685	0.624	0.533	0.427	0.337	0.301	0.34	0.433	0.54	0.631	0.688
75	0.64	0.624	0.54	0.452	0.338	0.258	0.222	0.262	0.342	0.462	0.552	0.628
85	0.407	0.427	0.349	0.297	0.226	0.188	0.158	0.198	0.227	0.315	0.383	0.436
89.99	0.274	0.323	0.256	0.234	0.192	0.156	0.125	0.168	0.195	0.248	0.302	0.335

Table 4.5: Matrix of efficiencies SM=1.2 solar field

	0	30	60	90	120	150	180	210	240	270	300	330
0.5	0.556	0.556	0.555	0.554	0.553	0.552	0.552	0.552	0.553	0.554	0.555	0.556
7	0.581	0.577	0.567	0.553	0.538	0.528	0.524	0.528	0.539	0.554	0.568	0.578
15	0.609	0.601	0.581	0.551	0.519	0.495	0.486	0.496	0.521	0.553	0.582	0.602
30	0.648	0.635	0.599	0.544	0.48	0.427	0.407	0.43	0.483	0.547	0.602	0.637
45	0.67	0.653	0.604	0.528	0.437	0.356	0.321	0.358	0.441	0.532	0.608	0.654
60	0.678	0.657	0.596	0.5	0.384	0.28	0.235	0.283	0.387	0.504	0.599	0.659
75	0.613	0.601	0.515	0.422	0.295	0.207	0.16	0.209	0.297	0.426	0.518	0.604
85	0.389	0.408	0.33	0.272	0.198	0.151	0.11	0.155	0.198	0.28	0.36	0.425
89.99	0.271	0.308	0.247	0.209	0.169	0.124	0.091	0.128	0.169	0.217	0.285	0.334

Table 4.6: Matrix of efficiencies SM=1.1 solar field

	0	30	60	90	120	150	180	210	240	270	300	330
0.5	0.566	0.566	0.565	0.564	0.563	0.562	0.562	0.562	0.563	0.564	0.565	0.566
7	0.592	0.589	0.578	0.564	0.549	0.537	0.533	0.538	0.549	0.564	0.579	0.589
15	0.621	0.613	0.592	0.561	0.528	0.504	0.495	0.504	0.53	0.562	0.593	0.614
30	0.661	0.648	0.612	0.555	0.489	0.434	0.413	0.436	0.491	0.557	0.613	0.649
45	0.684	0.667	0.618	0.539	0.446	0.36	0.324	0.362	0.448	0.542	0.62	0.668
60	0.693	0.672	0.61	0.511	0.391	0.283	0.235	0.285	0.394	0.514	0.612	0.673
75	0.632	0.617	0.526	0.432	0.299	0.209	0.158	0.211	0.301	0.435	0.533	0.623
85	0.408	0.43	0.336	0.281	0.201	0.151	0.108	0.158	0.2	0.291	0.384	0.453
89.99	0.299	0.337	0.253	0.219	0.171	0.125	0.09	0.131	0.171	0.231	0.32	0.369

Table 4.7: Matrix of efficiencies SM=1.0 solar field

4.3.Operating performance of both control systems

In this part will be analysed the behaviour of both control systems (heliostats and mass flow control) in order to show their performance together. The analysis will bring the attention on the three configuration systems, in term of solar multiple, and in particular, will display the performance of both the mass flow control system as well as the defocusing one.

The Solar Multiple is defined as [40]:

$$SM = \frac{P_{Th,SF}}{P_{Th,cyle}} = \frac{A_{Tot,Hel} \cdot DNI \cdot \eta_{ov,SF}}{P_{Th,cyle}} \quad (4.1)$$

Where:

- $P_{Th,cyle}$ is the thermal power required by the thermodynamic cycle;
- $P_{Th,SF}$ is the thermal power offered by the solar field system;
- $A_{Tot,Hel}$ is the total heliostat area;
- DNI is the DNI design point;
- $\eta_{ov,SF}$ is the overall solar field efficiency(receiver and heliostats), expressed in chapter 1.

The design point of the solar field is DNI 850 W/m^2, the Azimuth 180 ° and elevation 75°. When the incident thermal power receiver allows to the maximum value, the heliostats field control system performs; so there is a defocusing of a percentage of reflective area. During this operations, the mass flow control system does not perform, operating at maximum base pressure.

Vice versa, when thermal power, offered by the solar field, is too low, the mass flow adjustment starts to work.

To explain the performance and the interaction of both control systems, the yearly Thermoflex simulation results have been used; in the following session, the results of the 21st of June has been taken into account, in order to explain the mass flow regulation.

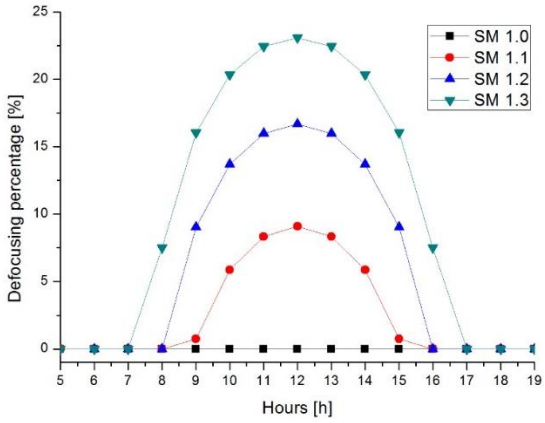

Figure 4.12: Heliostats field area percentage defocusing vs. hours of considered day

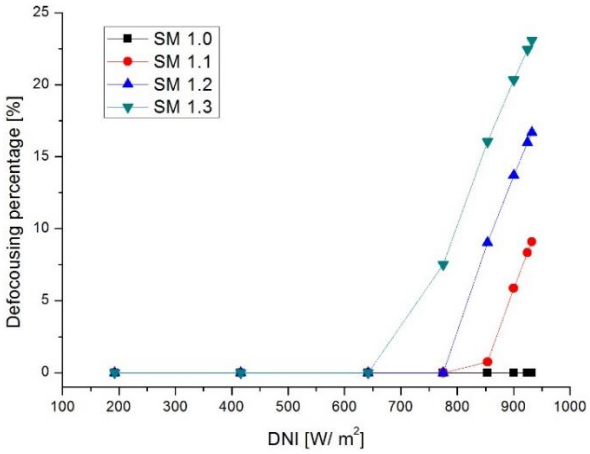

Figure 4.13: Heliostats field area percentage defocusing vs. DNI

Figure 4.12 shows the defocusing heliostats area percentage during the hours of 21st of June; it is possible to observe how the control system of the heliostat field performs, i.e. through the defocusing of a determined number of heliostats when the thermal power is too high compared to the design point. In particular in figures 4.12 and 4.13 it is possible to observe that for SM=1 no defocusing of the heliostats is performed for the day taken in consideration.

By increasing, the SM and, thus, the number of available heliostats, it is necessary to defocus more heliostats in the central hours of the day with high DNI values. Figure 3 shows the trend of heliostat defocusing during this day (June 21st) with a DNI peak of 932 W/m^2 . In Figure 4.13,it is shown the

performance of the heliostats control system vs direct normal radiation for the same day.

In both cases, it is possible to note as the adjustment of the heliostats is activated, when the DNI design point is achieved, especially in the middle hours of the day. The adjustment of the heliostats is not necessary for low DNI values. In this period of time, there is the maximum solar flux on the receiver, in order to provide the maximum value of thermal energy and no adjustment is needed.

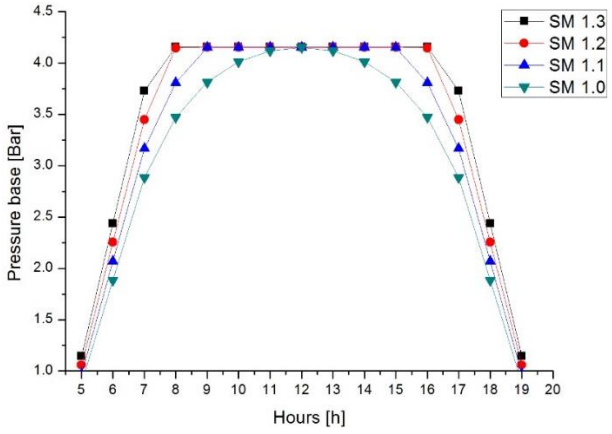

Figure 4.14: Base pressure of the cycle vs hours of the considered day

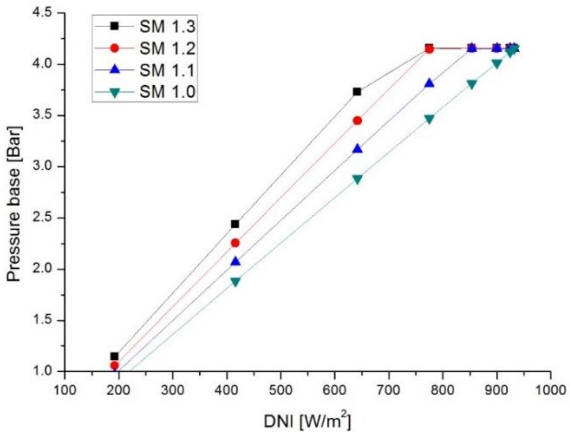

Figure 4.15: Base pressure of the cycle vs DNI

From figures 4.14 and 4.15 it is possible to observe how the solar multiple values equal to 1 and 1.1 is not able to exploit the hours of the day with the direct radiation low values, in these cases the inlet pressure of the gas turbine is near the ambient pressure.

If, however, the solar multiple increases and therefore the size of the field, it is also possible to use the plant for the remaining hours of the day when the DNI is lower than the design one.

It is possible to observe from figure 4.14 and 4.15, that, even when the solar multiple and the normal direct radiation get higher, the base pressure does not vary; therefore, no mass flow adjustment is carried out.

For the solar multiple equal one, however, the mass flow control is active during almost all hours.

The two adjustments, the pressure and the heliostats, intervene in a separate way. Specifically, when the value of the solar multiple is greater than one, the mass flow control system intervenes for low direct radiation values, and when high radiation values are triggered, the heliostat field regulation is activated.

Figure 4.16 shows the energy production. As obvious, the production of energy increases with the solar multiple and for a unitary solar multiple is possible to reach the peak rated power only in the design conditions, while during the day is produced a lower values of nominal power.

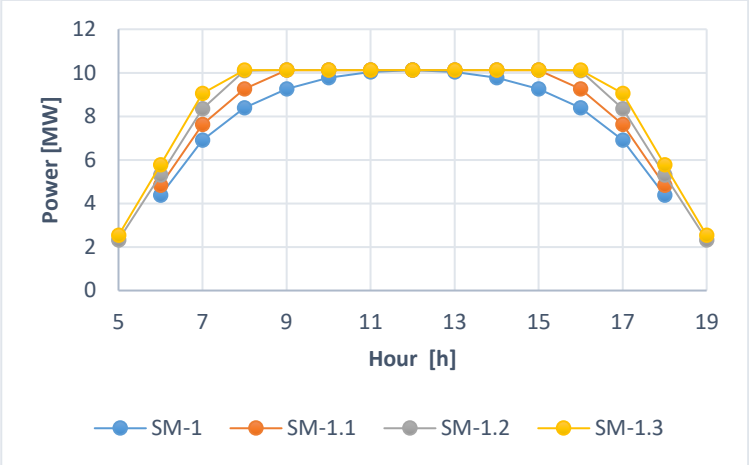

Figure 4.16: Energy production vs hours of 21st june

Increasing the size of the heliostats field, it is possible to operate the system under nominal design conditions for an increasing period and it is possible to exploit the hours of the day with lower direct radiation. It can be noticed from figure 4.16, as in the hours when the direct radiation is low, the nominal power values can not be guaranteed, but the mass flow control system being used is

able to adjust the gas turbine power up at values close to 20% of the nominal power.

4.4.Seasonal control systems behaviours

In this part, there is a comparison of the behaviour of the plant control systems during different periods of the year, with different direct normal radiation from the design state.

Figure 4.17 shows the performance in three days of the year, June 21, March 21, and December 22, without considering particular weather conditions in terms of cloudiness, where the values of the direct radiation are limited.

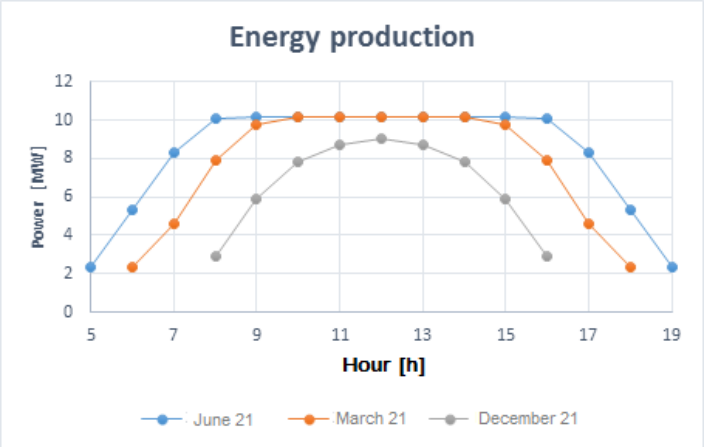

Figure 4.17: Energy production during June 21, March 21, December 22, SM 1.2

From Figure 4.17 one can notice that the energy production is higher in June for the more direct available radiation. It is also possible to notice that thanks to the oversizing of the solar field (due to the increased solar multiple of 1) in June and March, the plant works for more hours per day under nominal conditions. This does not occur in the month of December, where the size of the heliostats field are not sufficient to ensure the rated operating conditions.

In figure 4.18, it is possible to notice the performance of the mass flow control system; in particular, it is shown the inlet pressure of the gas turbine versus the hours of the three days considered. During the period when the solar radiation reaches high values, i.e. in the central hours of the summer months, the mass flow control system does not work and the pressure of the starting of the cycle does not vary. This explains the ability to produce electricity at nominal design

conditions for more hours. During the winter months, or in presence of low DNI values or heliostat field efficiency, it is possible to notice how the pressure regulation is activated even in the central hours by modifying the mass flow that evolves in the cycle.

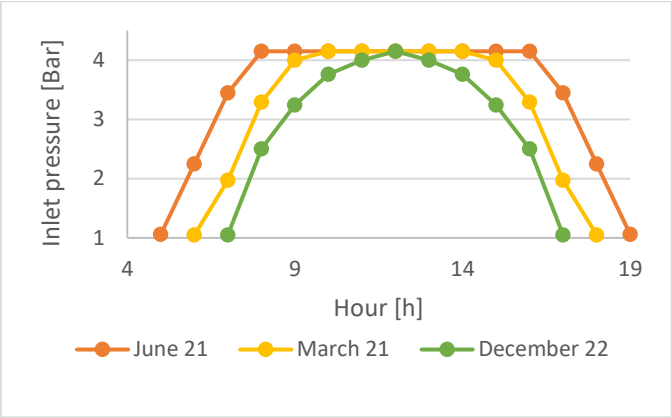

Figure 4.18: Energy production during June 21, March 21, December 22

Consequently the mass flow control system works many hours during the day, when the solar field efficiency or DNI are very low, in order to produce energy without plant stop.

In the following table 4.8 are resumed the hours that performs the mass flow adjustment for the three days considered in this analysis.

Day	June 21	March 21	December 22
Mass flow working hour [h]	6	8	12

Table 4.8:Mass flow-working hours for June 21, March 21 and December 22

As expected, the operational hours of the regulation system increases in presence of less solar radiation; to allow the plant to work, the control system has to adjust its pressure for a longer time.

It is interesting, analyzing when the defoucusing is acted by the heliostat field control system, in order to compare the mass flow one. In the following figure 4.19 it is shown the percentage of defoucusing area for the three considered day of the heliostsat field.

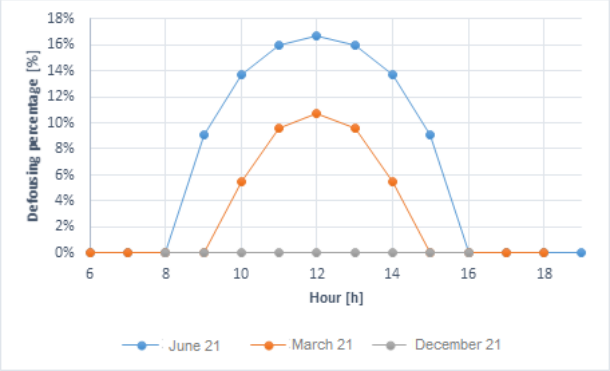

Figure 4.19: Defocusing percentage of the heliostats field

It is possible to observe how the system does not make any adjustments in presence of low DNI values, in this case in December, since the entire heliostat field is necessary to provide the required thermal power. When the radiation is higher, in the months of June or March, for example, the defocusing of part of the reflecting surface is performed.

It is therefore possible to say that the two systems are involved in a separate way, they are one of the complement of the other and both are needed to maximize the production of the energy plant.

In fact, over-sizing the reflective area and its regulations, by defocusing part of the heliostats, focuses on the central hours of the day when there are sufficiently high direct radiation conditions. With this adjustment, it is possible to guarantee the operation of the system under nominal conditions for a greater number of hours during the year. On the contrary, the mass flow control system intervenes during days when the direct radiation settles down to low values and therefore in the early hours of the day and in the last hours of the afternoon.

The advantage of using this system is to maintain unchanged the thermodynamic conditions of the cycle, increasing the hours of operation of the plant during the year even if the energy produced settles at values lower than the design conditions, around 10% of the nominal power.

As shown in the SM analysis, increasing the available heliostat area, there is an increase of the energy production, but at the same time, it causes an increase in the defocused heliostat area and fewer operating hours of the mass flow control system.

Choosing the best configuration is certainly the most economically advantageous one; for this reason, the Levelized Cost of Energy (LCoE) has been used as a merit parameter. The next session will be dedicated to the cost analysis.

4.5.Economic analysis

Renewable energy technologies can help countries achieve their political goals, to ensure energy-generating part of the environment. However, without reliable information on the costs and benefits of renewable energy technologies, it is difficult, if not impossible, for governments to accurately assess what technology is best suited to their needs [48].

The issue of costs is of paramount importance in the development of solar thermal power market and is the most critical aspect to be overcome in order to break down the barriers that prevent their spread. It is no coincidence, then, that the research activities are oriented right on the drastic reduction of the costs, in order to make this technology competitive against the other, and not renewable.

Detailed economic analysis is essential to understand the current status and future prospects of the market development. However, the difficult access to this information and the growth of installed capacity in recent years, with consequent reductions in costs, may lead to a not always precise and reliable assessment, with risk of overestimating or underestimating the cost of electricity.

All this constitutes a barrier not only to the development of the solar thermal market, but also to the whole renewable energy market [49].

4.5.1. Methodology

The economic analysis can be performed with different methodologies, in fact there is not a standard procedure and the results obtained depend on the initial conditions which are inserted and to which reference is made.

The analysis can be developed in a detailed manner, however, it is appropriate to find some summary measures that can be a simple reference, straightforward and intuitive, but equally reliable and meaningful.

First, the cost of a solar thermal power plant can be divided into two macro-categories:

- Investment costs: they include the capital expenditure to build the plant and can be further divided into:
  I. Direct costs: are the cost items related to the major components of the system and directly attributable to the electrical output achieved;
  II. Indirect costs: concern the costs involved in engineering, site preparation and other cost items. They are expressed as a percentage of direct costs.
- Operation and maintenance costs (O & M): it is necessary to ensure the correct operation of the plant once completed.

From the estimate of the costs mentioned above it is possible to carry out an assessment which allows to determine which is the economic convenience of the system to vary the size and the solar multiple.

A very useful procedure for a quick comparison between different technologies from renewable sources is through the economic-financial indicator Levelized Cost of Electricity (LCOE) expressed in USD / kWhel.

The LCoE turns out to be the most used indicator simple because, complete and synthetic. In fact, it takes into account all the life cycle of the plant and reports the plant's productivity with all the costs incurred, also considering the maintenance costs.

The LCoE value may vary depending on the technology of the country, the specific project, the renewable sources, operating costs and investment, efficiency and performance of the technology.

Thanks to the potential of the measure LCoE, depending on several factors, it is appropriate to make some simplifying assumptions so that the analysis is transparent and easy to interpret [49].

The LCoE relation used in this work is the following [50]:

$$LCoE = \frac{\alpha \cdot C_{inv} + C_{fuel} + C_{O\&M}}{E_{net}} \qquad (4.2)$$

Where:

- α is the economic return factor;
- C_{inv} is the initial investment cost;
- C_{fuel} is the annual fuel cost;
- $C_{O\&M}$ is the operation and maintenance costs;
- E_{net} is the annual energy production.

The economic return facto is expressed as:

$$\alpha = \frac{i \cdot (1+i)^n}{(1+i)^n - 1} + k_{ins} \quad (4.3)$$

Where:

- i is the real discount rate;
- n is the useful life of the plant;
- k_{ins} is the annual insurance rate.

This simplified equation has limitations and is not a definitive parameter to discuss the related costs. In particular, the economic value of electricity produced at different times, the complications due to the transmission and distribution of energy and the costs that may occur during the life of the project are not taken into account.

In particular, this simplest version of the LCoE assumes that all generated electricity is of equal value. However, due to peak loads, exchange rates and system constraints this is not true and the generation value will vary day by day.

4.5.2. Main cost items

The costs of a solar thermal power plant with central receiver may vary greatly as a function of the technical characteristics and the plant performance.

The investment costs as mentioned in the previous session can be divided into direct and indirect costs. Direct costs in turn can be divided as follows [51]:

- Solar field: in this case the components of the higher cost of the field are: mirrors, pedestal, support, engines for tracking the sun, connections and wiring and installation;
- Tower : it is formed by the cost of tower structure, piping and insulation;

- Receiver: it consists of the cost of the receiver, the pipes, the insulation, the pumps;
- Power block: this cost item refers to generating power from a traditional source for a Brayton cycle, namely a gas turbine.

Indirect costs are used to account for those costs that can not be assessed by means of commercial software and take into account expenses for the land to be occupied, legal fees, geotechnical and environmental surveys, taxes, interest during construction.

Some of these categories are listed explicitly, while others are enclosed in a single cost called EPC & Owner Cost as will be subsequently shown in Table 4.9.

Operation & Maintenance (O & M) costs for solar tower technology are difficult to identify in the absence of estimates. The best data available are those for the DOE program and those relating to Solar One, which operated in a mode of daily production of about four years after the test phase [52].

The following tables report the cost estimates that were used for the economic analysis. The direct solar field costs were determined as a Thermoflex output. Thermoflex through its PEACE module makes it possible to estimate costs according to the size of the components.

Thermoflex, in particular, processes these costs by dividing them into two categories:

- Reference cost;
- Labor cost.

For the other cost items, reference is made to the data available in the literature [14] and [15], in particular, will be considered:

Direct Cost Category	
Solar field	Thermoflex
Power Block [USD/kW]	1000
Indirect Cost Category	
EPC & Owner Cost [% of DC]	25

Sales Tax Rate [applied to 80% of DC]	7.75% (CA)
Combined Indirects [% of DC]	31.2
O&M Cost Category	
Fixed Cost by Capacity [MUSD/kW-yr]	70

Table 4.9: Direct and indirect cost items

Table 4.10 shows the results obtained from the cost analysis for the four values of solar multiple 1, 1.1, 1.2, 1.3.

It may be evaluated as the incidence of the total cost increases with the multiple solar because of the greater economic resources necessary for the realization of the part of the solar plant, while the costs related to the Power Block and Operation & Maintence remain constant.

The last line of the table 4.10 shows the total values of the costs necessary for the realization and the maintenance of the plant and the percentage of cost increases with increasing solar multiple.

SM	**1**	**1.1**	**1.2**	**1.3**
Receiver reference cost [MUSD]	9590	10518	11440	12358
Receiver reference labor cost [MUSD]	3848	4221	4591	4959
Total Receiver cost [MUSD]	13439	14739	16032	17318
Heliostat reference cost [MUSD]	10279	11274	12263	13248
Heliostat reference labor cost [MUSD]	1716	1882	2047	2212
Total Heliostat cost [MUSD]	11996	13157	14311	15460
Tower reference cost [MUSD]	212	233	253	274
Tower reference labor cost [USD]	299	329	358	388
Total Tower cost [MUSD]	512	562	612	663
Installed cost [MUSD]	2470	2709	2947	3184

Power Block cost [MUSD]	10000	10000	10000	10000
Direct cost [MUSD]	38418	41168	43904	46627
Indirect cost [MUSD]	11986	12844	13698	14547
Investiment cost [MUSD]	50404	54013	57602	61175
CO&M [MUSD/yr]	70	70	70	70
Total cost[MUSD]	51104	54713	58302	61875
Percentage increase in costs	0,0%	7,1%	14,1%	21,1%

Table 4.10: Cost analysis Thermoflex results

From the table 4.10 it could be possible to notice how the costs of investment grow from about 50 million dollars for multiple solar 1 until you get to about $ 61 million for solar multiple of 1.3.

To have an immediate reference of the cost increase, it is reported in the last row of the table the percentage increase of the costs. It was taken as a reference the total cost which is obtained by multiple solar unit and it is possible to note how to switch to a value of the solar multiple equal to 1.3 serves an increase of 21.1% of the costs.

Table 4.11 highlights the cost structure and demonstrates a quantification in Chapter 1, namely that the costs pertaining to the solar field (receiver, mirror field, tower and installation costs) affect about 50% of the total costs.

In fact, it can be estimated from both Table 4.11 and Figure 4.20, as the sum of the costs due to the solar field, is equal to 55.6% of the total costs per solar multiple equal to one.

The remaining part of the costs is distributed for 24.8% on indirect costs and O & M costs and 19.6% for the costs attributed to the Power Block. We also notice how by increasing the solar multiple the cost incidence varies up to 2 percentage points.

Increasing the characteristics of the solar part, the cost items to which they refer have a greater impact on the cost item of the Power Block, the gas turbine used, in fact, remains the same for different solar field configurations.

SM	1	1.1	1.2	1.3
Total Receiver cost	26,3%	26,9%	27,5%	28,0%
Total Heliostat cost	23,5%	24,0%	24,5%	25,0%
Total Tower cost	1,0%	6,0%	6,1%	6,2%
Installed cost	4,8%	5,0%	5,1%	5,1%
Power Block cost	19,6%	18,3%	17,2%	16,2%
Indirect cost+CO&M	24,8%	24,8%	24,7%	24,6%

Table 4.11: Cost structure vs solar multiple

Figure 4.20 shows the cost structures for a solar multiple of 1.2. It can be noticed from the graphic how the incidence of the components concerning the solar field are predominant and therefore must carry out an economic evaluation to assess the best configuration, to make the initial investment profitable.

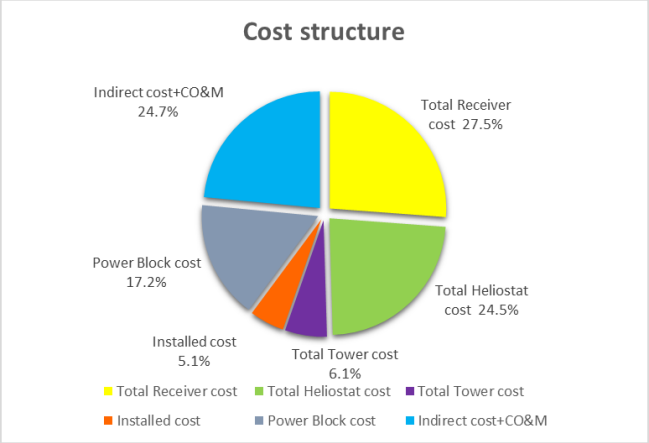

Figure 4.20: Cost structure for SM=1.2 configuration

Before closing the discussion on the costs it is interesting to go to make an analysis of the power of the test technology costs per kilowatt installed to be able to show a first and quick comparison with other renewable energy technologies.

In Table 4.12 it is possible to estimate how the specific cost expressed in USD / kW increases as a function of the solar multiple from a value of 5110 USD / kW at a value of 6188 USD / kW.

SM	1	1.1	1.2	1.3
Specific cost [USD/kW]	5110	5471	5830	6188

Table 4.12: Plant specific cost

Referring to an analysis of the specific costs for different sources and for diferent states performed by IRENA in 2015 (the International Renewable Energy Agency) [53], it is possible to estimate that the total costs in China and India are typically lower than in countries of OECD (Organization for Economic Co-Operation and Development), for which the specific cost per kilowatt installed is higher for each technology used.

In China and India, the average cost of energy from biomass, hydroelectric and wind power varies from 1240 to 1390 USD / kW. As far as photovoltaic modules have gone from 2646 USD / kW in 2009 to 1670 USD / kW in 2014.In OECD countries, the relative average cost of wind is around 2000 USD/kW, while for photovoltaic modules the cost is 2330 USD / kW.

The most efficient and environmentally friendly biomass has a significantly higher cost in OECD countries and is 4300 USD / kW.Even for offshore wind installations specific cost varies up to 4,500 USD / kW.

With regard to the solar concentration, the CSP technologies have an even higher cost which amounts to 6740 USD / kW.

4.5.3. Energy production

Energy analysis as anticipated was conducted using Thermoflex; It was simulated the behavior of the system hour by hour for an entire year, referring to the real direct radiation data referring to TMY3 Seville.

The simulations were conducted for increasing solar multiple, and has been made to vary the defocusing of the heliostats and the mass flow, as we saw in Chapter 3, so as to ensure the TIT, turbine inlet temperature, constant and equal to 800 ° C . Table 4.13 summarizes the net energy values calculated for each month to vary the solar multiple, while in table 4.14 are shown the capacity factor (CF), the equivalent hours and capacity factor reported to the solar part (SF-CF). Table 4.15 shows the operating working hours.

SM	1	1.1	1.2	1.3
January	1.15	1.27	1.37	1.43
February	1.15	1.26	1.36	1.42
March	1.35	1.48	1.59	1.66
April	1.56	1.70	1.83	1.91
May	2.03	2.22	2.39	2.51
June	2.18	2.40	2.60	2.72
July	2.59	2.83	3.02	3.12
August	2.28	2.50	2.68	2.80
September	1.64	1.81	1.98	2.08
October	1.28	1.42	1.54	1.63
November	1.07	1.18	1.28	1.34
December	1.01	1.10	1.18	1.23
TOT	19.28	21.18	22.82	23.86

Table 4.13:Monthly energy production (GWh)

SM	1	1.1	1.2	1.3
CF	22.01%	24.17%	26.05%	27.23%
SF-CF	25.33%	25.45%	26.34%	22.88%
Equivalent hours	1928	2118	2282	2386

Table 4.14:CF, SF-CF and equivalent hours

SM	**1**	**1.1**	**1.2**	**1.3**
January	189	192	193	195
February	180	182	187	191
March	223	227	231	233
April	248	252	256	259
May	328	331	337	344
June	344	351	357	362
July	379	385	391	392
August	346	350	352	361
September	274	282	286	286
October	212	215	218	224
November	170	172	177	180
December	161	166	167	170

Table 4.15:Monthly working hours

Since there is no thermal storage, the maximum working outlook would be 4380 hours a year, representing the exact half of the hours in a solar year.

In the present case, it has reached a value from 3054 hours for SM 1 to a maximum of 3197 hours for SM 1.3. It is possible to notice that there is not a high increase in operating hours and the system is able to effectively convert Solar thermal energy in electricity for about 35% in a year time. The energy analysis term ends, highlighting in Table 4.16 the hours in which the mass flow control system intervenes.

SM	**1**	**1.1**	**1.2**	**1.3**
January	186	168	140	118
February	162	143	117	105
March	218	178	158	136
April	242	203	169	142
May	315	266	235	207
June	338	306	245	204
July	366	280	222	177
August	338	277	219	175
September	271	264	222	182
October	212	186	164	139
November	170	153	115	105
December	159	127	108	94
Tot	2977	2551	2114	1784
Operational hours [%]	97.5%	82.2%	67.1%	55.8%

Table 4.16: Montly mass flow control system working hours

It is possible to notice how increasing the solar multiple and therefore increasing the size of the solar field, the heliostats control system works much more. While for lower solar multiple, the operatational hours of the mass flow control system increases. The last line shows the percentage value of the operating hours of the control system, expressed as the total operating hours of

the system, divided by the operating hours of the mass flow control system. The complement of these values is the operating hours in which the heliostats field control system is activated. It is possible to highlight how multiple solar equal to one, works almost exclusively the flow control system, while if we move to a multiple of 1.3 solar, the two control systems work both for about 50% of the hours of operation.

4.5.4. Levelized Cost of Energy (LCoE) estimation.

In the previous sessions we have analyzed and reported all the elements necessary to LCOE evaluation as proposed in the report in session 4.3.1. In order to carry out the analysis there is no financial data for determining the economic return factor, α. Reference has been made to the data supplied from the report [54], which sets for CSP technologies the following values reported in table 4.17:

n	i	k_{ins}	α
30	0.08	0.01	0.0988

Table 4.17: Financial data of economic return factor

Considering zero the fuel cost, because the system doesn't use any fuel, the data given in Table 4.18 is obtained.

SM	*1*	*1.1*	*1.2*	*1.3*
Cinv [MUSD]	*50.40*	*54.01*	*57.60*	*61.17*

Table 4.18: Investment cost used il LCoE analysis

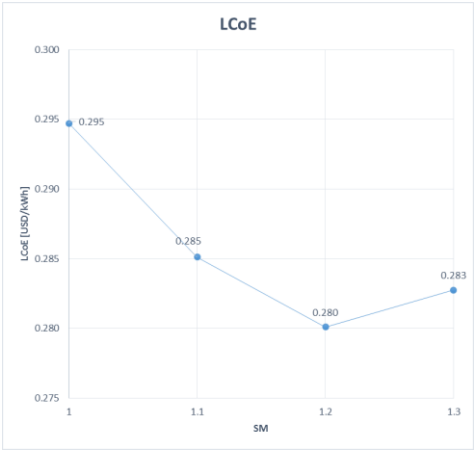

Figure 4.21: LCoE Trend vs solar multiple

Figure 4.21 shows the trend of the LCOE value as a function of SM; it is possible to notice that the minimum energy cost value for a SM equals 1.2; the minimum cost is of 28 c$/kW. Considering a SM value of 1.3, savings on investment costs of 3.57 M$ were achieved.

It is interesting to give some brief general consideration to the results obtained in relation to other sources of energy, renewable and non-renewable energy technologies, thus delineating current positioning in the electricity market. On the other hand, the cost of energy evaluated in this session, underline the novelty of the concept that for this reson has a higher LCoE values respect the actual renewable energy source.

The cost-competitiveness of electricity generation from renewable technologies has reached very competitive levels in recent years. Generating energy from sources such as biomass, hydroelectric power and onshore winds are now competitive compared to the traditional source of fossil origin. Photovoltaic solar energy is also reaching a very competitive economic value; in fact, it is sufficient to think about reducing about half of the LCOE between 2010 and 2014 [53].

The LCOE values are included in a range, of which we will evaluate the mean value. This variability depends on several factors, mainly depending on the choice of the installation site and the type of plant. The average value of photovoltaic solar photovoltaic (LCOE) varies from 0.11 to 0.12 USD / kWh in South and North America, up to 0.31 USD / kWh for projects in Central America.

New projects in countries with good solar resources, such as the United Arab Emirates, count on the creation of competitive plants with an LCOE of 0.08 USD / kWh of 0.07 per cent without financial support. Competitive values are also gained in China, Asia in general, and Africa with an average value between 0.07 and 0.09 USD / kWh.

In North America, there are also very competitive projects for onshore wind with average values of 0.02 USD / kWh. For hydroelectric sources, the weighted average for Asia and South America is 0.04 with a maximum value in Oceania equal to 0.12 USD / kWh. The economic cost rises for offshore wind power plants and CSP plants.

The weighted average of the LCOE for CSP plants ranges from 0.20 USD / kWh for Asia up to a maximum of 0.25USD/kWh in Europe [53].

4.6.Conclusions

In this chapter, a heliostats field optimization were made in order to minimazing the Levelized cost of electricity of the power plant.

The mass flow control system works at the same time of the heliostat adjustment; so a trade off between the lost energy due to defocusing and working time of auxiliary control system have been performed.

The value of the solar multiple generally is equal to 1.3 1.4; in this chapter the economic analysis brings to ligh that the mass flow regulation system adopted could reduces the solar field size, therefore the SM. In particular the minimum value of the LCoE is for SM equal 1.2.

So, this brings to a saving on plant costs and to a reduction of Levelized cost of energy and unit power installed.

Chapter 5
Analysis of molten salt thermal energy storage employing and optimal plant configuration

5.1.Introduction

Due to the high variability of the primary energy source, the CSP systems must cope with a time lag, between the supply of solar energy and the demand for electricity. The possibility of introducing a thermal storage system thus represents a considerable advantage compared to other sources of renewable energy, such as wind or PV.

In fact, little more than half of the existing systems provides the possibility to store the thermal energy , while 80% of those under construction will be integrated with this technology, with peaks of 88% in the central tower and linear parabolic systems [80].

Obviously, the daily and annual variations of solar radiation, combined with the demand for electricity, influence the operational strategies of the storage system, which can offer the following functions [81]:

- Compensation of small variations caused by meteorological transients;
- Shifting the phase of power generation by the peak hours of solar radiation to the power demand peak hours;
- Extend the production time of the absence of solar energy;
- Preheat the system components before starting the system.

Storage systems are classified according to the operating principle used to store energy, enabling them to be classified in sensitive heat, latent or thermo-chemical heat systems.

In the first type, thermal heat storage, is achieved by the temperature variation of a medium (usually solid or liquid) which, within the operating temperature range, is not subject to phase changes.

Sensible heat storage depends heavily on the properties of the medium, in particular by the thermal capacity, which in fact defines the accumulated energy

per unit of volume. Another parameter is the thermal diffusion, the rate of velocity with which the heat can be released.

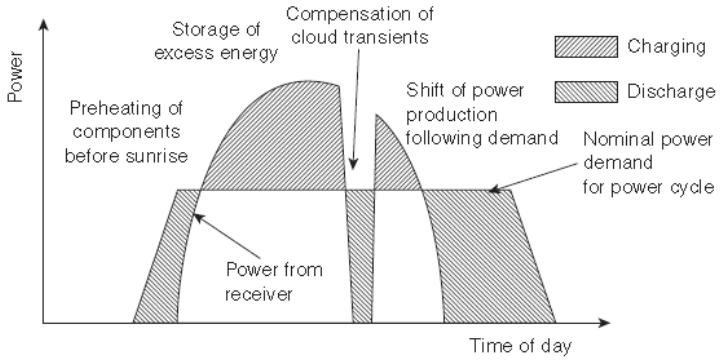

Figure 5.1: Operation strategy of storage systems

The accumulated energy Q is given by the following equation:

$$Q = m \cdot C_p \cdot \Delta T \qquad (5.1)$$

Where:

- Q is the energy stored [J];
- m is the medium mass storage [kg];
- C_p is the specific heat [kJ/kgK]
- ΔT is the difference temperature of the heat transfer process.

The latent heat storage uses, instead, materials that change phase to a temperature that is between the lower and upper limits of those of the solar collector considered.

It is then used the latent heat, or the enthalpy associated with the phase change, which can be of three types: from solid to solid, from liquid to vapour or from solid to liquid. Usually, are preferred phenomena based on the last type, since it is characterized by a low volumetric expansion, when compared to the transition from liquid to vapour, due to the high latent heat, or to the solid - solid passage.

A mass m subjected to a phase change from solid to liquid is able to accumulate the following amount of energy:

$$Q = m \cdot [c_{p,s} \cdot (T_m - T_s) + \lambda + c_{p,l} \cdot (T_l - T_m)] \qquad (5.2)$$

Where:

- $c_{p,s}$ is the specific heat of salt in solid phase;
- $c_{p,l}$ is the specific heat of salt in liquid phase;
- T_m is the melting temperature of the salt;
- T_s is the solid temperature;
- T_l is the liquid temperature;
- λ is the latent liquefaction heat.

Significant advantages of latent systems are the isothermal process, that allows to store a greater amount of mass than the systems based on sensitive heat operating at the same temperature ranges.

Finally, the thermochemical accumulation represents the one with the greatest potentiality due to the reaction heat. Such systems are based on reversible chemical reactions that are triggered by the heat coming from the solar field. For this reason, the storage material must be able to dissociate in the range of temperatures between which the installation operates. The process could be a direct reaction that is exothermic, which generates heat, or the inverse reaction is endothermic, and thus absorbing thermal energy. The amount of energy accumulated by the reaction depends on the reaction heat and the degree of progress of the transformation:

$$Q = a \cdot m \cdot \Delta H \qquad (5.3)$$

Where:

- a is the fraction of reaction mass;
- ΔH is the reaction heat for mass unit.

The thermochemical storage is advantageous, compared to the sensitive one, since the elements that react, potentially can be stored indefinitely at ambient temperature, reducing thermal losses.

Unfortunately, these systems are limited by their commonly impediments of other system components, such as limitations in the transmission of heat, cyclic stability, reversibility and costs.

A further distinction of storage systems is on active and passive systems. When the storage material is a fluid that can flow from one tank to the other, the system is defined as active. If this fluid also acts as a heat transfer fluid, and thus receives the energy absorbed in the receiver, it is called direct active systems.

If, however, there is a distinction between the storage fluid and the thermal fluid, the system takes the name of an indirect active, as it needs an additional heat exchanger.

If the storage medium is solid, the system is de-passive where the heat transfer fluid flows into the storage material only during charge and discharge phases.

Among the active storage modes are two-tank systems, each of which is dedicated to the storage of hot fluid or cold fluid, thermocline systems.

The passive systems on the contrary are typically made up of packed bed bodies, where there is a storage material of different shapes and sizes. In fact, it exchanges heat with the heat transfer fluid, thanks to the contact between the parts of the systems with integrated heat exchanger.

In this chapter, a solar power plant employing the mentioned closed Joule-Brayton cycle, of 5 MW power rate, with molten salts thermal storage, is presented.

In this chapter will be considered the use of storage, in addition to the mass flow control system; before the economic analysis ,a screening of available molten salts will be made in order to choose the best mixture which is suitable for this kind of plant.

The analysed plant that uses mass flow control system and that is coupled with storage, needs a different cost analysis, respect to a plant that employs fuel. As mentioned, in chapter 4, there are two different strategy of control, of the direct solar radiation capturing, that working together and are complementary to each other.

The adding of storage makes more complex this analysis for the ulterior trade-off between the lost energy (for defocusing) and the possible energy storage. An economic analysis trough the Levelized Cost of Electricity, in order to choose the best solar multiple, and storage hours of salt tank to elect the best configuration.

5.2.Preliminary comparison of Heat Transfer Fluid

Thermal solar plants that employ indirect cycle, already existing, use molten salts or synthetic oil as heat transfer fluids.

The fundamental phenomenon, in these plants, is the one of heat transfer; in most cases, it is possible to observe as the exchange is with a fluid under forced convection conditions inside the tubes.

Very important parameter to describe the performance of a heat transfer fluid, is the ratio between the mechanical power required to maintain the motion of the fluid and the thermal power exchanged by it (W / Q) : lower is this value, more indicated is the heat transfer fluid.

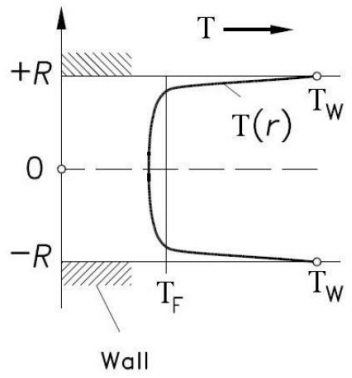

Figure 5.2: Temperature profile of a HTF inside the tube.

For the calculation of the thermal power exchanged inside a tube, as shown in Figure 5.1, is used the equation 5.1:

$$Q = h \cdot A \cdot (T_w - T_f) \qquad (5.4)$$

Where:

- T_f is the adiabatic mixing temperature of the fluid;
- T_w is the wall temperature;
- A is the contact surface between fluid and wall;
- h is the heat transfer coefficient.

The contact surface could be expressed as:

$$A = \pi \cdot \mathrm{D} \cdot \mathrm{L} \qquad (5.5)$$

Where:

- D is the diameter;
- L is the length.

The heat exchange coefficient h present in the Newton equation can be calculated by using an equation of the type $Nu = f(Re, Pr)$, where:

$$Nu = \frac{hD}{L} \qquad (5.6)$$

$$Re = \frac{\rho v D}{\mu} \qquad (5.7)$$

$$Pr = \frac{\mu C_P}{k} \qquad (5.8)$$

Where:

- k is the thermal conductivity of the fluid;
- μ is the dynamic viscosity of the fluid:
- ρ is the density of the fluid;
- C_P the specific heat at constant pressure of the fluid.

For the heat transfer in internal forced convection in turbulent motion, it is possible to use the equation of Dittus-Boelter:

$$Nu = 0{,}023 Re^{0.8} Pr^{0.4} \qquad (5.9)$$

Combining equations from 5.1, to 5.6 it is possible finally to obtain:

$$Q \propto Re^{0.8}\, Pr^{0.4} k L (T_w - T_f) \qquad (5.10)$$

Mechanical power could be expresses as:

$$W = \dot{m} \cdot \frac{\Delta P}{\rho} = A_c \cdot v \cdot \Delta P \qquad (5.11)$$

Where:

- $A_c = \pi \frac{D^2}{4}$ is the section of the pipe in which flows HTF;
- v is the velocity of the HTH;
- ΔP is the pressure loss of the fluid;

The pressure loss could be evaluate as:

$$\Delta P = f \cdot \rho \cdot \frac{L}{D} \frac{v^2}{2} \qquad (5.12)$$

The friction factor f, calculated by Colburn equation is:

$$f \propto Re^{-0.2}\, Pr^{-0.6} \qquad (5.13)$$

Combining equation 5.9 and 5.10 could be obtain:

$$Q \propto \rho \cdot L \cdot D \cdot v^3 Re^{-0.2}\, Pr^{-0.6} \qquad (5.14)$$

Dividing 5.8 between 5.11, the ratio W/Q has been obtained:

$$Q \propto \frac{v^2}{(T_w - T_f)} \cdot \frac{1}{C_P} \qquad (5.15)$$

Keep constant the temperature difference $(T_w - T_f)$ is possible to obtain a direct comparison with the synthetic oil, for the molten salt and gases, as shown in table 5.1

HTF	$\frac{(W\ /\ Q)}{(W\ /\ Q)_{oil}}$
Synthetic oil	1
Molten salt	0.8
Gases	10-30

Table 5.1: W/Q ratio for different HTF (T=250°C, P=100 bar) [64]

It is possible to observe, from the table 5.1, that the gases require high pumping power, for the same heat transfers, compared to the molten salt, that have a lowest value of W/Q. This is one of the main reasons why molten salts are currently the most used in solar power plant and core of research topics.

5.3.Alternatives to the molten salt currently used in CSP plants

In this session, the main alternatives to the classical salts with KNO_3-$NaNO_3$ mixtures will be analysed, making a review of the main chemical-physical properties.

Many extensive analyses have been made, in the nuclear research for the Next Generation Nuclear Plant and the Nuclear Hydrogen Initiative [55].

These new types of reactors will operate at much higher temperatures and pressures than the previous ones, so the properties of the coolant salts will have to be quite different.

Stable at temperatures above 700 ° C, new compositions have been considered, mainly based on the literature available. Salts containing oxygen (nitrates, sulphates and carbonates) will not be taken into account for their thermochemical instability to these temperatures.

These are also incompatible with carbon containing materials, because decomposing at high temperatures, the same release oxygen that reacts with the carbon present, causing oxidation phenomena and decreases the useful life of the materials.

On the following fundamental properties:

- Chemical stability at T > 700 ° C;
- Solidification temperature less than 500 ° C and vapour pressure not too high;
- Compatibility with high temperature steels, graphite and ceramic materials;
- Plant life of 20-30 years.

The major classes of analysed salts are: fluorides, chlorides and fluoroborate. In addition to the properties of these components it has been included those of water, liquid metals for a quick comparison.

5.3.1 Solidification temperature and vapour pressure

The solidification temperature is one of the most important physical properties of salts: this influences considerably the design of the power plant and the thermal storage system. If salt possesses a high specific heat could bring to a less drop in temperature than other HTF; operating with a closed gas cycle with high TIT, a lower solidification temperature of 500 ° C is required for an effective design [69]. An extensive database of phase diagrams simplifies the evaluation process, minimizing the use of approximation techniques.

None single component solidifies at sufficiently low temperatures, a binary or ternary mixture is required as usage as a heat transfer fluid. In general, adding

a first salt to a pure component, causes a lowering of the solidification temperature (even of 500 ° C).

An addition of another element involves a further decrease in the phase transition but of modest entity, about 50 ° C. Adding other components is essential for some salts for the thermochemical stability.

Table 5.2 illustrates the molten salts taken into consideration in order of increasing solidification temperature. Many of the available salts have been excluded for two reasons:

- Vapour pressure too high, for example for $AlCl_3$, $ZrCl_4$, and $BeCl_2$;
- Too much corrosion in the temperature ranges analysed.

Fluorides		ZrF_4		Fluorocarbon		Chlorides	
		$NaF-ZrF_4$	500 °C				
LiF-NaK-KF	454 °C	$LiF-NaF-ZrF_4$	460 °C	$KF-KBF_4$	460 °C	$NaCl-MgCl_2$	475 °C
		$LiF-NaF-ZrF_4$	436 °C	$RbF-RbF_4$	442 °C	$KCl-MgCl_2$	426 °C
		$NaF-RbF-ZrF_4$	420 °C				
						$LiCl-KCl-MgCl_2$	402 °C
		$KF-ZrF_4$	390 °C	$NaF-NaBF_4$	384 °C	$NaCl-KCl-MgCl_2$	396 °C
						LiCl-KCl	355 °C
						$LiCl-KCl-MgCl_2$	323 °C
						LiCl-RbCl	313 °C

Table 5.2: Solidification temperature for analysed molten salts [64]

This analysis also excluded heavy salts containing bromine and iodine due to their high cost and poor thermal exchange properties.

The main characteristics of the pure components and the salts contained in Table 5.2, such as boiling temperature and vapour pressure at 900 ° C, are also illustrated. It can be noticed a huge decrease of the vapour pressure, in the various elements analysed, with respect to the main components contained therein: this is mainly the case for the formation of coordinated complexes. Table

5.3 shows boiling temperature, solidification temperature, and vapour pressure at 900 ° C for analysed salts.

Molten salt	Solidification Temperature [°C]	Boiling Temperature [°C]	Vapor Pressure @ 900 °C [mmHg]
LiF	845	1681	0,1
NaF	995	1704	0,07
KF	856	1502	1,2
RbF	775	1408	0,75
ZrF_4	912	905	722
BF_3	-126	-100	NA
$NaF\text{-}NaBF_4$	385	694	9500
$KF\text{-}KBF_4$	460	1070	100
$RbF\text{-}RbF_4$	442	>1070	<100
LiCl	610	1382	7
NaCl	808	1465	2,5
Kcl	772	1407	2
RbCl	717	1381	3,8
$MgCl_2$	714	1418	7
LiCl-KCl	355	1400	5,8
$NaCl\text{-}MgCl_2$	445	>1465	<2,5
$KCl\text{-}MgCl_2$	426	>1418	<2
LiF-NaF-KF	454	1570	0,5
$NaF\text{-}ZrF_4$	500	1350	6
$KF\text{-}ZrF_4$	390	1450	1,2

Table 5.3: Boiling and solidification temperature, vapour pressure at 900 ° C for analysed salts [64]

The vapour pressure trend versus temperature is shown in figure 5.3.

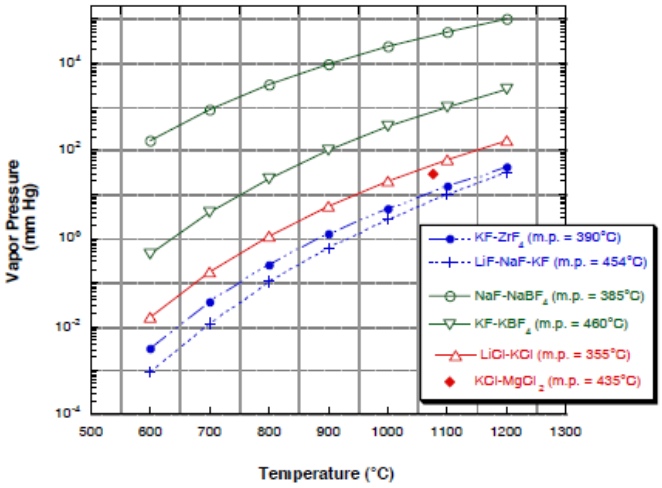

Figure 5.3: Vapour pressure vs operative temperature for analysed salt [64]

Table 5.3 shows that the $NaBF_4$ vapour pressure is too high and will be excluded from further analysis.

5.3.2 Density

The density of many salts was measured by the Oak Ridge National Laboratory, and are reported in Table 5.4[56]. Density equations have been experimentally determined. It is possible to note that in general these elements have high densities values, greater than that of water, for example.

This is an advantage especially for the compactness of heat exchangers and the reduced size of thermal storage tank. However, the work of the circulation pump is proportional to the tank dimensions, so a high value causes higher energy consumption and therefore a lower net energy production of the plant.

Molten Salt	Molar composition [%]	Density Equation	Density @ 500 °C [kg/l]
LiF-NaF-KF	46.5-11.5-42	2.53-0.00073×T	1.9657
NaF-ZrF_4	59.5-40.5	3.584-0.000889×T	2.8968
KF-ZrF_4	58-42	3.416-0.000887×T	2.7303
LiF-NaF-ZrF_4	26-37-37	3.533-0.000517×T	3.1334
LiCl-KCl	59-41	1.8772-0.00087×T	1.2047
LiCl-RbCl	58-42	2.7416-0.000689×T	2.2090
NaCl-$MgCl_2$	58-42	2.2971-0.000507×T	1.9052
KCl-$MgCl_2$	67-33	2.05458-0.000474×T	1.6882
NaF-$NaBF_4$	8-92	2.2521-0.000711×T	1.7025
KF-KBF_4	25-75	2.258-0.0008026×T	1.6376
RbF-RbF_4	31-69	2.9246-0.001047×T	1.4853

Table 5.4: Density equation for selected molten salt[57]

5.3.3 Thermal capacity

The thermal capacity, of the analysed salts, have been obtained experimentally by ORNL [56]. For specific cases, they were estimated based on the thermal capacity data of pure components, mediating then as a function of the percentage by weight of the various elements.

Whenever possible these data were determined at temperature of 700 ° C. Table 5.5 shows the molar composition and the specific heat of the analysed molten salt.

Molten Salt	Molar composition [%]	Specific heat [kJ $kg^{-1}K^{-1}$]
LiF-NaF-KF	46,5-11,5-42	2,0096
NaF-ZrF_4	59,5-40,5	1,1723
KF-ZrF_4	58-42	1,0509
LiF-NaF-ZrF_4	26-37-37	1,1262
LiCl-KCl	59-41	1,2016
LiCl-RbCl	58-42	0,8918
NaCl-$MgCl_2$	58-42	1,0802
KCl-$MgCl_2$	67-33	1,1555
NaF-$NaBF_4$	8-92	1,5072
KF-KBF_4	25-75	1,3063
RbF-RbF_4	31-69	0,9127

Table 5.5: Molar composition and specific heat for the main salts taken into consideration [57]

5.3.4 Viscosity

Chlorides and fluorocarbons usually have very low viscosities. They do not exhibit major variations in temperature and have a lower viscosity than most fluorinated blends. The trend of temperature versus viscosity can be seen in figure 5.5.

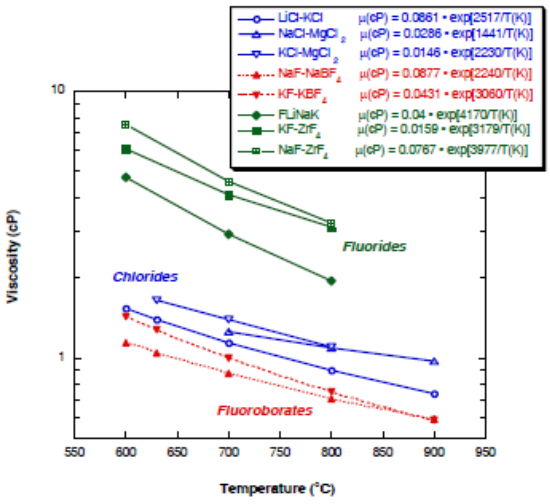

Figure 5.4: Viscosity trend versus temperature of the main salts taken into consideration [64]

It is not possible to find experimental values of the mixtures, therefore it has been calculated , based on the viscosity of the pure components, and according to the following equation 5.12:

$$\mu_{ideal,mix} = \left(\sum(x_i\mu_i)^{1/3}\right)^3 \qquad (5.15)$$

Where:

- μ_i is the dynamic viscosity of the component;
- x_i is the molar fraction of the component.

The viscosity is an important parameter to be taken into account, because it influences the characteristic curves of the pumps as well as their operating point. Because the auxiliaries have to move a large mass flow of salts, it is preferable to choose a fluid with a low viscosity value to lighten the power absorbed by the pump.

5.3.5 Thermal conductivity

Previous studies and extensive publications underline the difficulty in measuring the thermal conductivity at high temperature [68]. Recent measurements indicate a much-reduced dependence as a function of temperature. The general trend is that light salts (with low atomic number) have high thermal conductivity. As can be seen in figure 5.5, it is also clear that different types of salts, belonging to the same families, fall on a single correlation curve, estimated as a function of the ratio of average atomic weight and the number of ionic species.

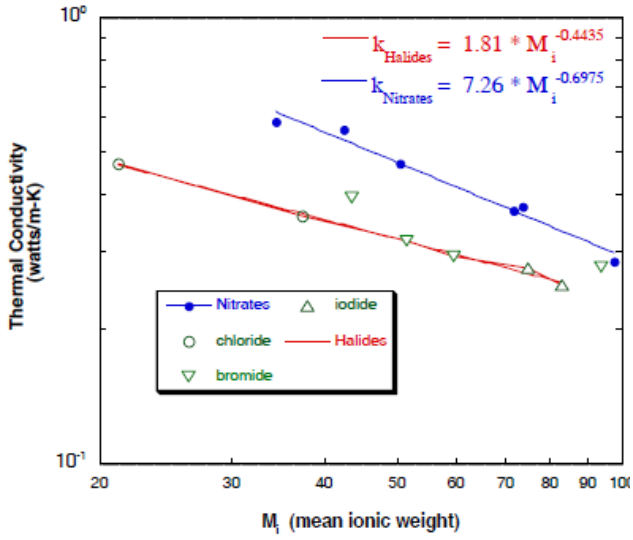

Figure 5.5: Correlation of thermal conductivity according to the average ion weight for different salt families [64]

The main thermal conductivity values are shown in table 5.7

Molten Salt	Mm [g mol^{-1}]	Temperature [°C]	K [W−m^{-1}K^{-1}]
LiF-NaF-KF	41,3	500	0,60
NaF-ZrF_4	92,7	700	0,36
KF-ZrF_4	103,9	700	0,32
LiF-NaF-ZrF_4	84,2	700	0,36
LiCl-KCl	55,5	700	0,38
LiCl-RbCl	75,4	700	0,39
NaCl-$MgCl_2$	76,1	700	0,43
KCl-$MgCl_2$	81,4	800	0,39
NaF-$NaBF_4$	104,4	621	0,4
KF-KBF_4	109	621	0,4
RbF-RbF_4	151,3	621	0,4

Table 5.6:: Thermal conductivity at the corresponding temperature of the various salts taken into account [64]

5.3.6 Heat exchanger analysis

A fundamental part in the choice in the design plant, consists in evaluating the heat exchange performance of the various salts and compare it , for example, to water and other liquid metals.

Bonilla et all, suggested a synthetic parameter, Figures of Merit (FOM), based on the pumping work due to temperature increase during forced internal convection thermal exchange [65]:

$$FOM_{pf} = \frac{\mu^{0.2}}{\rho^2 C_p^{2.8}} \qquad (5.16)$$

Where:

- μ is the dynamic viscosity;
- ϱ is the density;
- C_p is the specific heat.

Sanders et all also proposed a further figure of merit parameter proportional to the area required by the heat exchanger [66]:

$$FOM_{af} = \frac{\mu^{0.2}}{\rho^{0.3} C_p^{0.6} k^{0.6}} \qquad (5.17)$$

Where:

- k thermal conductivity.

Generally, as already mentioned, the molecules with lower molecular mass have better thermal exchange characteristics.

FOM_{pf}		FOM_{sf}	
Water@300 °C	0.2	Na	1.6
2Li-BeF_2	0.7	Pb	5.4
NaF-BeF_2	0.91	Water@300 °C	13
LiF-NaF-BeF_2	1.02	2Li-BeF_2	21.5
LiF-NaF-KF	1.13	LiF-NaF-KF	21.6
LiF-NaF-ZrF_4	1.42	LiF-NaF-BeF_2	22.6
LiF-ZrF_4	1.82	NaF-BeF_2	25.2
NaF-ZrF_4	1.98	NaF-$NaBF_4$	28
NaF-$NaBF_4$	2.2	LiF-NaF-RbF	31.8
KF-ZrF_4	3.39	NaCl-$MgCl_2$	35.1
KF-KBF_4	3.53	KF-KBF_4	35.4
LiF-NaF-RbF	3.79	LiF-NaF-ZrF_4	35.9
RbF-ZrF_4	4.82	NaF-ZrF_4	37.4
KCl-$MgCl_2$	5.66	LiCl-KCl	37.5
RbF-RbF_4	5.67	LiF-ZrF_4	37.5
LiCl-KCl	5.88	KCl-$MgCl_2$	39.7
NaCl-$MgCl_2$	6.4	KF-ZrF_4	42.5
LiCl-RbCl	8.99	LiCl-RbCl	44.5
Na	13.15	RbF-RbF_4	45.4
Pb	33.63	RbF-ZrF_4	48.7

Table 5.7: Figure of merits of the main castings taken into account [57]

5.3.7 Cost of molten salts

The parameter of primary importance for the choice of the molten salt, more suitable for the application in this work, is certainly the cost. Unfortunately, it is not really clear the exact costs of all salts, since some are not in commercial phase, and it is therefore not possible to obtain data relating to an economy of scale [56].

According to the elements present in two major salt categories, it is possible to categorize as followed:

- Commercial and economic components (NaF, NaCl, KCl, $MgCl_2$)
- Moderately expensive components, already large-scale products (Zr, LiF, LiCl).

Table 5.8 shows the prices of the main salts. It is clear that salts containing chlorides are the cheapest ones, followed by fluoroborate and finally fluorides. The cost of RbF and KF is the most uncertain due to the low commercialization.

In a concentrating solar plant high quantities of salt are needed, with consequent high costs, then a specific savings on the cost of the salt, allows a big saving on large scale. Low-cost components of the first category in the table 5.8 are definitely the most promising ones.

Molten Salt	Molar composition [%]	Mass composition [%]	Cost (€/kg)	Cost ($€/dm^3$)
Low cost salts with $MgCl_2$				
$KCl\text{-}MgCl_2$	68-32	62-38	0.26	0.43
$NaCl\text{-}MgCl_2$	58-42	46-54	0.31	0.52
$NaCl\text{-}Kcl\text{-}MgCl_2$	20-20-60	14-18-68	0.34	0.62
$LiCl\text{-}KCl\text{-}MgCl_2$	9-63-28	5-61-34	0.91	1.39
Medium cost salts with fluoroborate and chlorides				
$KF\text{-}KBF_4$	25-75	13-87	4.53	7.70
$LiCl\text{-}KCl\text{-}MgCl_2$	55-40-5	40.5-51.5-8	5.56	8.62
LiCl-KCl	59.5-40.5	45.5-54.5	6.24	9.48
$NaF\text{-}NaBF_4$	8-92	3-97	6.00	10.52
High cost salts				
$NaF\text{-}ZrF_4$	59.5-40.5	27-73	4.94	15.54
$KF\text{-}ZrF_4$	58-42	32.5-67.5	5.97	16.70
LiF-NaF-KF	46.5-11.5-42	29-12-59	9.62	19.42

Table 5.8: Specific cost of the salts taken into account

5.3.8 Corrosion

Corrosion plays a key role in choosing a particular component. It is well known that molten salts, operating at high temperatures, have very critical characteristics from this point of view. Some of these are the depth of attack or the removal of material during the crossing of the salt, for example in the tubes [67]. Often in fact, even the tests to characterize salts and materials have been not carried out in optimum conditions.

Use a different container material and the specimen for the test, has caused an increase of thermo-chemical potential difference, with consequent corrosion values inaccurate and overstated.

Unfortunately, exact and confirmed values are not available in the bibliography at this time: this limits the choice of materials to be used and the estimation of the damage caused by the phenomenon.

Research confirms that some super alloys nickel-based or Fe-Cr-Ni steel, such as Hastelloy Haynes 230, Incoloy800HT have good resistant corrosion with

salts containing chlorides [58]. These materials, in future, could be the application solution. However, in this part it was not treated this technical issue.

5.4.Choice of the molten salt

The main advantages and disadvantages of the most commonly used heat transfer fluids have been analysed. For the choice, the thermal exchange properties and the main physical-chemical properties of new possible alternatives to the use of common solar salt as HTF for the case study have been evaluated [60].

The variables taken into account were : solidification temperature, density, thermal capacity, viscosity and thermal conductivity. Table 5.9 summarizes these properties valued at 700 ° C.

Molten salt	T_{sol} [°C]	Mm [g/mol]	ρ [kg/m^3]	Cp [kJ/(kgK)]	C [kJ/(m^3K)]	μ [cP]	K [W/(mK)]
LiCl-KCl	355	55.47	1.515	1.201	1.821	1.15	0.42
LiCl-RbCl	313	75.37	1.883	0.892	1.679	1.3	0.36
NaCl-$MgCl_2$	450	76.09	1.677	1.097	1.838	1.36	0.5
KCl-$MgCl_2$	426	81.44	1.664	1.155	1.921	1.4	0.4
NaF-$NaBF_4$	384	104.38	1.754	1.507	2.646	0.9	0.4
KF-KBF_4	460	108.96	1.696	1.306	2.214	0.9	0.38
RbF-RbF_4	442	151.26	2.213	0.913	2.018	0.9	0.28

Table 5.9: Summary of physical and chemical properties for the molten salt analyzed.

After considering the previous information, the figure of merit of heat exchange and the cost of the salts, the choice fell on the KCl-$MgCl_2$ salt. The main benefit is the low cost, due to the fact that it easily findable materials. The low cost is also an additional advantage in order to obtain a specific low cost of energy.

5.5.Plant description

As described in the introduction, will analysed the case of a gas turbine of 5 MW of peak power. Some study about the storage have been analysed the advantageous for HGST systems with TES [59]; in this case also, no fuel has been used. The Thermal Energy Storage is composed by two storage tanks ("hot" and "cold") operating at temperatures between around 800°C and 450°C and a circulation molten salt pump. A heat exchanger air-salt is connect to the storage system with the power plant.

In figure 5.5 it is possible to observe the plant scheme, where there are : the auxiliary compressor (1), the compressor of GT (2), the solar tower (3), the turbine of GT (4), the cold salt storage tank (5), the hot salt storage tank (6), the air-salt heat exchanger (7), the recirculation pump (8) . The medium thermal storage, as described in 5.2.9 is a mixture of molten salts KCl-$MgCl_2$.

The performance of the control system has been described in chapter 2; in this chapter, there is more information regarding the storage system. In particular, during high solar resource presence, the air mass flow, coming out from the solar receiver, crosses the heat exchanger (7) to transfer the thermal power onto the storage system. The pump system provides the circulation the salt from the cold tank to the hot tank.

Vice versa, in lack of solar source, the storage system, diverting its direction to transfer the thermal power to the mass flow coming out from the solar system.

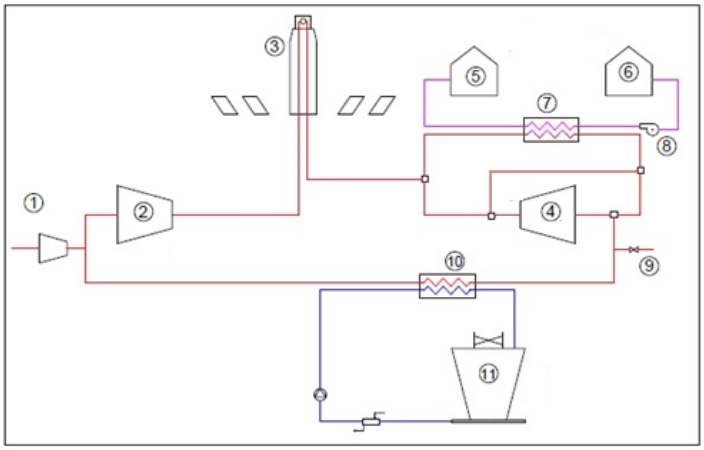

Figure 5.6: Plant scheme; 1. Auxiliary compressor, 2. Compressor of GT, 3. Solar tower, 4. Turbine of GT, 5. Cold salt storage tank, 6 Hot salt storage tank, 7 Air-salt heat exchanger, 8 recirculation pump.

5.6.Simulations

In Thermoflex was performed the simulation of the entire plant, while WinDelsol was used for the design of the solar field. In particular, in Thermoflex, in addition to the solar field, considering that the molten salt selected is not actually in commercial stage, it was necessary to implement its behaviour because not present in the library's software.

In fact, Thermoflex needs the density, viscosities, specific heat and transfer heat coefficient equations function of the temperature to add a user defined HTF. Data from bibliography has been take into to account [55] and following equations have been used:

$$\rho_{KCl-MgCl_2} = 2.05458 - 0.000474 \cdot T \qquad (5.18)$$

$$\mu_{KCl-MgCl_2} = 0.0146 \cdot \exp(\frac{2230}{T}) \qquad (5.19)$$

$$Cp_{KCl-MgCl_2} = 1.1555 + 0.0002 \cdot T \qquad (5.20)$$

$$k_{KCl-MgCl_2} = 1.408 \cdot 10^{-4} \cdot \frac{\exp(2261.3)}{T} \qquad (5.21)$$

$$\nu_{KCl-MgCl_2} = 0.0001408 \cdot \frac{\exp(2261.3)}{T} \qquad (5.22)$$

Where:

- $\rho_{KCl-MgCl_2}$ is the density of the molten salt;
- $\mu_{KCl-MgCl_2}$ is the dynamic viscosity of the molten salt;
- $Cp_{KCl-MgCl_2}$ is the specific heat of the molten salt;
- $k_{KCl-MgCl_2}$ is the transfer heat coefficient of the molten salt;
- $\nu_{KCl-MgCl_2}$ is the cinematic viscosity of the molten salt;
- T is the temperature.

In equations 5.15, 5.17 and 5.18 the temperature is expressed in °C while in 5.16, and 5.19 in K.

In WinDelsol, was optimized the solar field for solar multiple from 1 to 2.4, and then the results, have been used in Thermoflex.

The mass of molten salt was calculated as function of the hours storage desired; it has been considered that, to perform for one hour, using only the storage, the cycle needs 20000 kWh of thermal power. So the volume was calculated as follows:

$$V_{Tank} = \frac{N_h E_{Cycle}}{\Delta T_{KCl-MgCl_2} \cdot Cp_{KCl-MgCl_2} \cdot \rho_{KCl-MgCl_2}} \qquad (5.23)$$

Where:

- V_{Tank} is the volume of one storage tank [m^3];

- E_{Cycle} is the energy required by the cycle to perform [kWh];
- $\Delta T_{KCl-MgCl_2}$ is the operative delta temperature of the salt [kg/m^3];
- N_h is the number of hours of storage.

In table 5.10 are shown the storage system results, in term of tank volume and salt mass for each hour of storage.

Hours of storage [h]	1	2	3	4	5	6	7	8
Energy [MWh]	20	40	60	80	100	120	140	160
Tank volume [m^3]	97.3	194.7	292.0	389.4	486.7	584.1	681.4	778.7
Salt mass [q]	155.7	311.5	467.2	623.0	778.7	934.5	1090.2	1246.0

Table 5.10: Storage system results

In table 5.11 are resumed the results obtained by WinDelsol, for different heliostats field in term of heliostat total area and heliostats number; in this part the attention will be focused, only on the thermal power coming from the solar collector.

SM	1	1.2	1.4	1.6	1.8	2	2.2	2.4
Heliostat total area [m^2]	31372	37647	43921	50196	56470	62745	69019	75294
Heliostats number	261	314	366	418	471	523	575	627

Table 5.11: Optimization solar field results

In follow table 5.12 are shown the results performed in Thermoflex, regarding the energy production for each power plant configuration.

	Solar Multiple							
Hours of storage	1	1.2	1.4	1.6	1.8	2	2.2	2.4
2	9.15	10.98	13.33	14.70	15.99	16.73	17.28	17.71
3	9.15	10.98	13.33	14.70	16.43	17.60	18.34	18.87
4	9.15	10.98	13.33	14.70	16.43	18.14	19.18	19.88
5	9.15	10.98	13.33	14.70	16.43	18.15	19.78	20.71
6	9.15	10.98	13.33	14.70	16.43	18.15	19.86	21.34
7	9.15	10.98	13.33	14.70	16.43	18.15	19.86	21.56
8	9.15	10.98	13.33	14.70	16.43	18.15	19.86	21.56

Table 5.12: Yearly energy production [GWh] function of solar multiple configuration and hours of storage

As noticeable, the energy production for SM equal 1.0 and 1.2 is the same as the products by the power plant with the mass flow control system, because no

energy is stored. While for SM from 1.4 to 2.4 there is an energy increasing with the storage hours.

Figure 5.7 shows the energy production, coming only from TES function of the hours of storage, i.e. tanks volumes, and solar multiple.

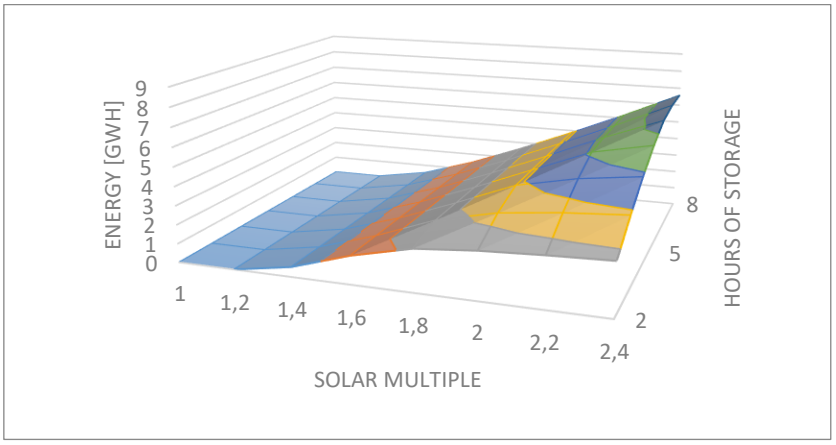

Figure 5.7: Energy produced by thermal energy storage [GWh]

On the other hand, increasing the SM, there is an increase of loss of energy, that could not be possible to use, nor in part stored, due to limited salt volume. In figure 5.8 it is possible to observe this trend for all solar multiple values and different hours of storage

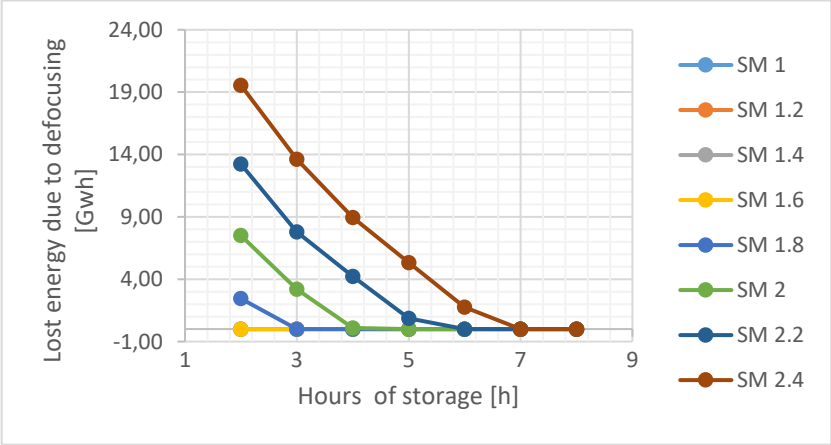

Figure 5.8: Energy lost vs hours of storage

For this reason, an economic analysis it is necessary, in order to select the best configuration.

5.7.Economic analysis

In this part will be shown the costs analysis; first it will be introduced the cost voice taken into account for the evaluation of the total cost, then it will also be presented the direct and indirect cost, with the investment cost, and finally, the Levelized Cost of Electricity.

For the cost analysis of the tower and receiver, heliostat as well as the engine gas turbine, have been referred to [61][52][62][60][63]. As described in chapter 4, the simple LCoE method has been used in order to choose the best SM and tank volume configuration [50].

In table 5.13 it could be possible to observe the unit cost voice employing in the economic analysis, while in table 5.14 the molten salt total cost.

GT cost [USD/kW]	1000
Heliostat field [USD/m2]	200
Tower and receiver [USD/kWth]	200
O&M [MUSD/Yr]	70
Storage cost [USD/kWth]	8.0

Table 5.13: Units costs of plants

Storage hours [h]	Salt total cost [kUSD]
1	40.49
2	80.99
3	121.48
4	161.98
5	202.47
6	242.97
7	283.46
8	323.96

Table 5.14: Molten salt total costs.

As calculated in solar multiple optimization in chapter 4, cost in two main categories have been divided: direct and indirect costs. In table 5.15 and 5.16 will be illustrated these two kinds of cost voices, one direct and one indirect, function of the solar multiple and hours of storage.

Direct cost depends directly on solar field, engine and storage cost, while indirect cost, as described in chapter 4, depends on k, fcr, α, and main direct cost [50].

	Solar Multiple							
Hours of storage	1	1.2	1.4	1.6	1.8	2	2.2	2.4
2	16.62	17.87	19.13	20.38	21.64	22.89	24.15	25.40
3	16.87	18.13	19.38	20.64	21.89	23.15	24.40	25.66
4	17.13	18.38	19.64	20.89	22.15	23.40	24.66	25.91
5	17.39	18.64	19.90	21.15	22.41	23.66	24.91	26.17
6	17.64	18.90	20.15	21.41	22.66	23.92	25.17	26.43
7	17.90	19.15	20.41	21.66	22.92	24.17	25.43	26.68
8	18.15	19.41	20.66	21.92	23.17	24.43	25.68	26.94

Table 5.15: Direct costs [MUSD] of cost analysis

	Solar Multiple							
Hours of storage	1	1.2	1.4	1.6	1.8	2	2.2	2.4
2	5.18	5.58	5.97	6.36	6.75	7.14	7.53	7.93
3	5.26	5.66	6.05	6.44	6.83	7.22	7.61	8.01
4	5.34	5.74	6.13	6.52	6.91	7.30	7.69	8.09
5	5.42	5.82	6.21	6.60	6.99	7.38	7.77	8.17
6	5.50	5.90	6.29	6.68	7.07	7.46	7.85	8.24
7	5.58	5.98	6.37	6.76	7.15	7.54	7.93	8.32
8	5.66	6.06	6.45	6.84	7.23	7.62	8.01	8.40

Table 5.16: Indirect costs [MUSD] of cost analysis

The investment costs are the sum of direct and indirect cost; with this cost it is possible finally to evaluate the LCoE for each configuration. In table 5.17, are shown the investment costs results.

	Solar Multiple							
Hours of storage	1	1.2	1.4	1.6	1.8	2	2.2	2.4
2	21.80	23.45	25.10	26.74	28.39	30.03	31.68	33.33
3	22.14	23.78	25.43	27.08	28.72	30.37	32.02	33.66
4	22.47	24.12	25.77	27.41	29.06	30.71	32.35	34.00
5	22.81	24.46	26.10	27.75	29.40	31.04	32.69	34.33
6	23.15	24.79	26.44	28.08	29.73	31.38	33.02	34.67
7	23.48	25.13	26.77	28.42	30.07	31.71	33.36	35.01
8	23.82	25.46	27.11	28.76	30.40	32.05	33.70	35.34

Table 5.17: Investment costs [MUSD] of cost analysis

As described in the past session, the minimum value of this cost is suitable to choose the best configuration, in term of hours of storage and solar field setup. Equation 4.2, used in chapter 4:

$$LCoE = \frac{\alpha \cdot C_{inv} + C_{fuel} + C_{O\&M}}{E_{net}} \qquad (4.2)$$

In table 5.18 are presented the LCoE results performed for all configurations, in term of storage hours and solar multiple while in table 5.18 the unit costs.

	Solar Multiple							
Hours of storage	1	1.2	1.4	1.6	1.8	2	2.2	2.4
2	0.388	0.338	0.291	0.275	0.263	0.261	0.262	0.265
3	0.392	0.341	0.294	0.277	0.258	0.250	0.249	0.251
4	0.396	0.344	0.296	0.280	0.260	0.244	0.240	0.239
5	0.399	0.347	0.299	0.282	0.262	0.246	0.234	0.231
6	0.403	0.350	0.301	0.284	0.264	0.248	0.235	0.226
7	0.406	0.354	0.304	0.286	0.266	0.250	0.236	0.225
8	0.410	0.357	0.306	0.289	0.268	0.252	0.238	0.227

Table 5.18: Levelized Cost of Energy [USD/kWh]

	Solar Multiple							
Hours of storage	1	1.2	1.4	1.6	1.8	2	2.2	2.4
2	3.32	3.57	3.83	4.08	4.33	4.58	4.83	5.08
3	3.37	3.63	3.88	4.13	4.38	4.63	4.88	5.13
4	3.43	3.68	3.93	4.18	4.43	4.68	4.93	5.18
5	3.48	3.73	3.98	4.23	4.48	4.73	4.98	5.23
6	3.53	3.78	4.03	4.28	4.53	4.78	5.03	5.29
7	3.58	3.83	4.08	4.33	4.58	4.83	5.09	5.34
8	3.63	3.88	4.13	4.38	4.63	4.89	5.14	5.39

Table 5.19: Unit Cost of the plants configurations [kUSD/kW]

As it can be possible to observe from table 5.17, the lowest cost of the LCoE is for solar multiple equal to 2.4 and for 7 hours of storage. This could represent the best configuration for this kind of plant employing the mass flow control system and TES.

Vice versa, observing table 5.18, the unit cost increases with the solar field dimensions and tank volume, so the minimum value coincides with SM 1 and 2 storage hours, while for the best setup the price is 5.34 kUSD/kW.

5.8.Conclusions

In this chapter, the employing of thermal energy storage for a plant of 5 MW was analysed. From the molten salts screening, Manganese-chloride ($KClMgCl_2$) appears suitable as HTF for the analysed plants.

The economic analysis, performed by the LCoE method, shows how the best configuration is for SM 2.4 and 7 hours of storage.

Finally, the unit cost, of the best configuration, as well as the LCoE price, equal respectively to 5.34 kUSD/ kW and 22.5 ₡$/kWh, shows as this technology could be competitive with the actual Energy Power System, as described in chapter 4.

Chapter 6
Micro scale application of the mass flow control system in a micro gas turbine.

6.1.Introduction

In this chapter, a case of study of the mass flow control system application to a 100 kW micro gas turbine has been analysed.

In chapter 3, the analysis for different size of power plants have been performed, concluding that the cycle efficiency remains constant under different load condition, since all the temperatures of the cycle (compressor inlet temperature, TIT, TOT, etc.) don't change.

In this part the results of studies on the performance of a micro gas turbine engine, that operates with the mass flow variation will be exposed. A first aspect is the peak power increase; in chapter 3 it has been shown that increasing the inlet pressure of the gas turbine, changes the output power of the engine.

As mentioned, the maximum value of the base pressure was set to 5 bars, due to the operating pressure of the solar receiver. Therefore, the nominal power of the micro gas turbine at this pressure becomes 5 times the nominal one at atmospheric pressure, i.e. 5x100kW=500 kW.

In February 2017 (during the start of this part of the thesis) it was released, by NREL, Solar Pilot, an open source software useful for the heliostat field optimization. The curiosity and the necessity of a code suitable for small solar power plant, lead to take in consideration this new code.

In first part of this chapter, the performance of the solar field and its design will be analysed, employing Solar Pilot. Then, in the second part, a numerical model, implemented in Matlab/Simulink will be shown, in order to analyse the dynamic behaviour of the plant.

Finally, a comparison with a commercial plant, of a hybrid micro gas turbine in solar tower system will be made.

6.2.Micro gas turbine employed description

The technical-scientific interest for the micro gas turbine (MGT) dates back to the 1970s, when the gas turbine industry tried to use this engine instead of the internal combustion engines in the automotive field. This project was not successful and therefore the MGT continued to be used for the electrical generation [104].

Nowadays, MGT are used mainly for cogeneration, continued generation, off grid generation, support generation (UPS), generation by biofuel, and for small electrical application.

The main manufacturers of micro gas turbine are listed in table 6.1 together with the MTG products and their main technical data [105].

Mfr	Model	Rating*	NOx Emissions*		CO Emissions*	
			PPMV	LBM/MWh	PPMV	LBM/MWh
Capstone	C30	30 kW	< 9	< 0.49	< 40	Not Available
	C60	60 kW	< 9	< 0.49	< 40	Not Available
Elliott Energy Systems	TA-80	80 kW	< 25	Not Available	< 30	Not Available
	TA-100	100 kW	< 20	Not Available	< 40	Not Available
Ingersoll-Rand Power Works	70 SM 70 LM	70 kW	< 9	< 0.413	< 9	< 0.252
	250 SM	250 kW	<9	< 0.413	< 9	< 0.252
Turbec	T100CHP	105 kW	< 15	Not Available	< 15	Not Available

* ISO Day, Corrected to 15% Oxygen

Table 6.1: Main MGT manufactures and engine data

In this research, the Ansaldo Turbec T 100 has been analysed. The Turbec T100 PH Heat and Power is a module of the T100 Power, combined with a heat exchanger (recuperator) to recover thermal energy from the exhaust gases and produce hot water.

The micro gas turbine uses a centrifugal compressor, whose compression ratio is equal to 4.5, and it is spliced to the same shaft of the radial inflow single stage turbine and the electric generator. The presence of a recuperator allows the efficiency increase. The air, pre-heated in the recuperator, is sent to the combustor,where, with the addition of natural gas, combustion takes place, bringing the air temperature up to about 950 ° C. The TIT (turbine inlet temperature) is more or less 950 °C and the expansion ratio is approximately 4.5, while the TOT (turbine outlet temperature) is 650 ° C [106].

A permanent magnet generator, rotating at high speed (from 50000 to 70000 rpm), produces a rated power of 100 kW, with a net electrical efficiency of around 30%.

The Turbec T100 is controlled and supervised by an automatic control system, located inside the Power Module Controller (PMC). Operation is unattended, even in an emergency mode.

In Figure 6.1 and 6.2 are shown respectively the components and the construction scheme of MGT.

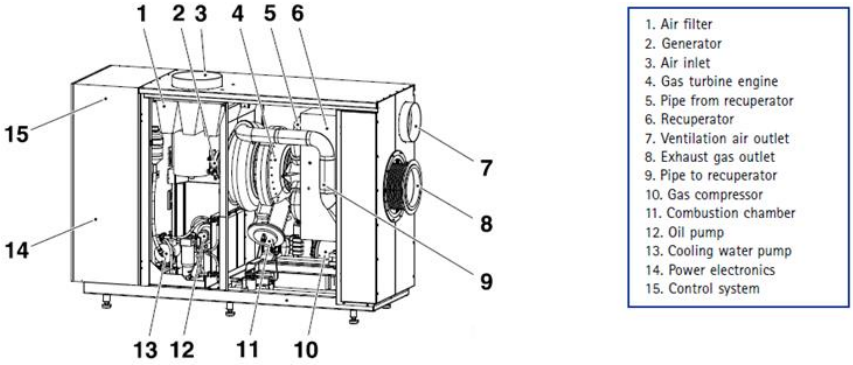

Figure 6.1: Micro turbine components Turbec T100 PH

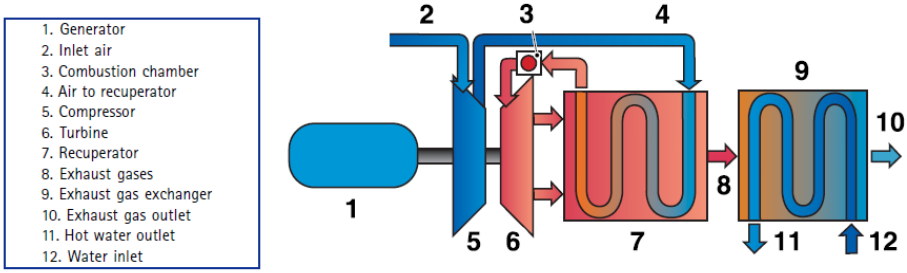

Figure 6.2: Construction scheme of Turbec T100

The same turbine, conveniently customized, is employed in Aora Solar system [107].This is the reason why the T100 micro gas turbine was taken into consideration.

In the following figures 6.3, 6.4, and 6.6 the main part of the MGT are shown.

Figure 6.3: Ansalo Turbec T 100 entire view*[1]

Figure 6.4: Radial inflow turbine of Turbec T 100*[1]

Figure 6.5: Centrifugal compressor of Turbec T 100*[1]

6.1. Heliostat field optimization

As mentioned in the introduction, for the heliostat field design SolarPilot (Solar Power Tower Integrated Layout and Optimization Tool) have been employed. SolarPILOT™ is a software able to generate and defines the

[1] Photo authorized by Ansaldo Energia, thanks to Enrico Bianchi, Ansaldo micro gas turbine division

characteristics of the central receiver systems and which was developed by NREL (National Renewable Energy Laboratory). [108]

The software consists of a graphical interface and a programming interface through which external programs can access to its functions. SolarPILOT™ resumes the DELSOL3 functions, but it is based on the Hermite code, which allows to calculate the performance of each heliostat, instead of considering a group, in the field, as the previous software. It is also able to create heliostats fields, considering land constraints through the use of Google Hearth, create systems with multiple geometries of heliostats and receivers, run parametric simulations, optimize the size of the field and the receiver, reduce the cost of energy and evaluate the entire system costs.

In this part, the optimization for different solar multiple (from 1 to 1.3) and heliostat size will be performed, in order to maximize the overall cycle efficiency. First, it is necessary to choose the model to approximate the emission of radiation by the Sun, and SolarPILOT allows the use of different methodologies [109]:

- *Pillbox Sun*: it is an almost ideal case that allows to model the Sun as a square wave. The solar radiation has a constant value within a predefined neighbourhood and zero value outside of the same neighbourhood;
- *Gaussian Sun*: solar radiation has a normal distribution centred on the centre of the solar disc;
- *Limb-Darkened Sun*: solar radiation φ is the function of the angular distance θ between the point considered and the centroid of the solar disk according to the following equation:

$$\phi(\theta) = 1 - 0{,}5138 \left(\frac{\theta}{0{,}00465}\right)^4 \qquad (6.1)$$

- *Point Sun*: the Sun is represented as a point;
- *CRS Suns*: Sun is modelled using a parameter called "Circumsolar Ratio";
- *User Sun*: in this case, the template is implemented directly by the user.

Limb-Darkened model has been used in the optimization while for the atmospherical attenuation has been employed *Delsol3 Clear Day*, which provides

a visibility of 23 km in a clear day, for the DNI density, and TMY data of Seville for the meteorological data. It was necessary to evaluate the cycle efficiency, imposed equal to 30%, and the auxiliary yield equal to 97%. The code calculates the gross and net power of the cycle as follows:

$$\dot{W}_{cycle} = \dot{Q}_{pb} \cdot \eta_{cycle} \qquad (6.2)$$

$$\dot{W}_{net} = \dot{W}_{cycle} \cdot \eta_{aux} \qquad (6.3)$$

Where:

- $\dot{W}_{cycle}$ is the gross power of the cycle;
- $\dot{Q}_{pb}$ is the power needed for the power block;
- η_{cycle} is the referring efficiency of the power block;
- $\dot{W}_{net}$ is the net power;
- η_{aux} is the auxiliary efficiency.

The code evaluate the net power of the heliostat field:

$$\dot{Q}_{field} = \dot{Q}_{inc}\,\alpha - \dot{Q}_{loss} - \dot{Q}_{pipe} \qquad (6.4)$$

Where:

- $\dot{Q}_{inc}$ is the power incident on the heliostats;
- α is the absorbance of the receiver;
- $\dot{Q}_{loss}$ are the radiative losses;
- $\dot{Q}_{pipe}$ are the pipe losses.

In table 6.2 are resumed the net power absorbed by the heliostat field for different solar multiple.

SM	Q_{field}
1	1.7
1.1	1.87
1.2	2.04
1.3	2.2

Table 6.2: Heliostat field power results

It is also necessary to define two angles; the first one is the angle at the top of heliostats position, calculated in an anticlockwise direction, while the second

represents the angle below of heliostats position, calculated in a clockwise direction. Both were imposed to 180 °.

By setting the radial limits of the field, it is possible to choose boundaries condition on the height of the tower (H_t) ;in this case it was chosen a minimum distance of 0.75 H_t and as a maximum 7.5 H_t.

Then the optical tower height (i.e. the distance between the centroid of the heliostat and the midpoint of the receiver) has been chosen, set at 57 m. The field configuration considered is the radial stagger layout, while as radial spacing method the "No Blocking-dense" has been selected , because minimizes the blocking effect between the rows.

It has also been imposed the azimuthal spacing limit, equal to 1.33 [109].

6.2.1. Heliostats characterization

It is necessary to define the geometry of the heliostats, defining the height H_h and width W_h, if the heliostat is composed by multiple panels, the number of panels in the horizontal and vertical directions and the space between the panels in every direction, as shown in Figure 6.6

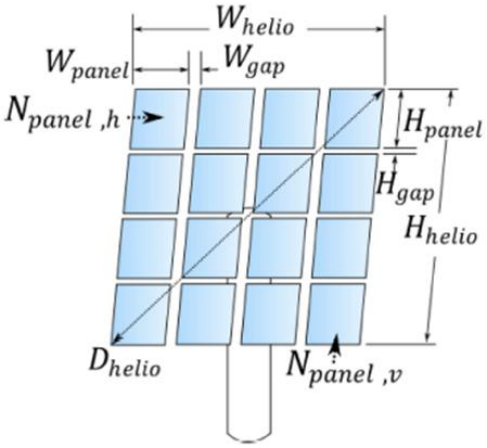

Figure 6.6: Geometric dimensions of heliostat

The software, via the height and width of the heliostats, calculates the diagonal dimension D_h as:

$$D_h = \sqrt{{W_h}^2 + {H_h}^2} \qquad (6.5)$$

Another important parameter to design the heliostat field is the canting method. The methodology for this process is not unique, but it is possible to classify into two main groups: "on-axis" "off-axis" [110]. In the first case, the panels are aligned to give a perfect reflection of the image when the centre of the heliostat, the receiver, and the Sun are all aligned; in the second case, the panels are arranged to optimize the convergence of all the reflected images on the solar receiver for a particular time of the year.

The methodology chosen for optimization is "On-Axis at Slant": where the panels are aligned when the heliostat reflects on the tower. The parameters chosen for the focusing of the heliostats is the kind "At Slant" in which the focusing distance of the heliostat is equal to the distance between the centroid of the heliostat and that of the receiver.

All the heliostats are characterized by optical errors, due to the uncertainty of the tracking system, along the σ_{el} and azimuthal σ_{az} zenithal directions. Other are caused by the distortion of the surface along directions x σ (s, x) and σ(s, y) and the reflection of solar radiation, along the directions x σ(r, x) and σ(r, y), which are influenced by the wind, the gravity and the temperature. SolarPILOT assumes a normal distribution of these magnitudes and the user can set them by inserting the standard deviation of each individual magnitude. The software then goes to calculate the actual standard deviation of the image reflected by the heliostat σ_{tot} considering all error sources:

$$\sigma_{tot} = \sqrt{4\left({\sigma_{el}}^2 + {\sigma_{az}}^2 + {\sigma_{s,x}}^2 + {\sigma_{s,y}}^2\right) + {\sigma_{r,x}}^2 + {\sigma_{r,y}}^2} \qquad (6.6)$$

The σ_{el} and σ_{az} values have been chosen equal to 0 while for $\sigma_{(r,\,x)}$ and $\sigma_{(r,\,y)}$ have been selected a value that could range between 1.3 to 2.6 mrad. The surface distortion instead varies for each type of heliostat.

Then the reflectivity ratio, i.e. the ratio between the effective reflective area of the mirror and the total area, the reflectivity of the heliostat and the fouling factor, relative to the reflection of the heliostat when it is not perfectly clean has been chosen, and is was selected from 95% to 92% [111].

As mentioned, three different types of heliostat (Type 1. large size, Type 2. intermediate sizes, Type 3. small size) have been analysed and then a

comparison has been made in order to evaluate which of them worked best for the plant . The heliostats data are shown in Table 6.3 [110].

	Type 1	Type 2	Type 3
Area [m²]	115.56	43.33	16.69
Height [m]	9	6.42	3.21
Length [m]	12.84	6.75	5.2
Number of panel X direction [-]	4	3	2
Number of panel Y direction [-]	4	2	1
Surface reflectivity ratio [-]	0.9583	0.97	0.92
Optical error [mrad]	2.6	1.8	1.3

Table 6.3: Characteristic data of heliostats

6.2.2. Receiver

In this part will be analysed the receiver design, for the micro gas turbine application. The methodology is the same used in chapter 3. First of all a flat plate receiver has been selected in SolarPilot, so height and length of this component has been chosen to evaluate the receiver area.

Then it has been imposed the average incident flux on the receiver, elected equal to 400 kW/m² [29], the maximum one of 600 kW/m² and a absorbance of 0.96, (because it was supposed that it was an absorbed of silicon carbide) [112]. After this evaluation, the power to working fluid was the following:

$$P_{wf} = \frac{P_{net}}{\eta_{cycle}\eta_{aux}} \qquad (6.7)$$

The incident power on the receiver, have been calculated as:

$$P_{Inc,rec} = \frac{SM \cdot P_{wf}}{\eta_{th,ric}} \qquad (6.8)$$

The ratio between the incident power on the receiver and the average flux is the absorber area:

$$A = \frac{P_{Inc,rec}}{Flux_{ave}} \qquad (6.9)$$

The shape of the absorber chosen is square, so height and width have the same value.

Then it was chosen the limit angle, which causes the radiation reflected by the heliostats, placed beyond this limit, which does not reach the receiver; so a square limit has been selected.

The azimuth orientation equal to 0° and a start value of 0° for the zenith orientation of the receiver (then optimized in the calculation software progress) has been set.

The horizontal and vertical acceptance angles, through which the receiver can accept the incident radiation, have been imposed equal to 180°. The thermal losses of the receiver have been calculated of 71.72 kW/m^2 while the pressure losses of the tower of 0.77 %.

For the ray tracing , the Hermite method has been used, and to not damage the receiver, and to keep the highest possible efficiency of the system, the "image size priority" has been employed as a point focusing strategy.

This choice is important, in fact, due to the not regular flux distribution, there are very high thermal gradient that causes a decrease of the lifetime and efficiency of the receiver [113].

A offset value of 2.5 for edge- x and edge-y was selected while the horizontal and vertical flux grid resolution equal to 25 has been chosen.

To evaluate the incident flux, efficiency matrix, receiver dimension and solar field, several number of simulation have been performed; in particular, the start values of 2.3 m of length and height and a zenith orientation of 0° have been set.

Then the receiver area value was keep constant, varying the height, length and the zenith orientation from -65° to -45° generating for each simulation, a new solar field layout.

6.2.3. Heliostat field results

In this session it will be shown the solar field result obtained by solar pilot, used in Simulink/Matlab for dynamic transient simulation of the system.

At first it will be illustrated the result obtained for the Type 3 heliostats for the three solar multiple analysed, in design point, or rather azimuth 180° and zenith 76°.

SM	1	1.1	1.2	1.3
Heliostats	206	223	241	257
Reflective area [m²]	3163.5	3424.5	3701	3354.7
Cg	586	634	685	731
Receiver height [m]	1.8	1.8	1.7	1.8
Receiver length [m]	3	3	3.18	3
Tilt angle [°]	-47	-47	-47	-47
Incident power on solar field [kW]	2688.9	2910.9	3145.8	3354.7
Absorbed power by the receiver [kW]	2081.1	2248	2419	2572.9
Absorbed power by HTF [kW]	1649.9	1816.8	1987.3	2141.7
Receiver efficiency [%]	79.3	80.8	82.2	83.2
Receiver absorbance [%]	96	96	96	96
Optical solar field efficiency [%]	80.6	80.4	80.1	79.9
Optical total efficiency [%]	77.4	77.2	76.9	76.7
Cosine effect [%]	93.7	93.6	93.5	93.3
Blocking effect [%]	100	100	100	100
Shading effect [%]	100	100	100	100
Atmospherical attenuation [%]	98.3	98.3	98.3	98.3
Reflection efficiency [%]	90.7	90.7	90.7	90.7
Interception efficiency[%]	96.4	96.3	96	95.9
Average flux on the receiver [kW/m²]	401.4	433.6	466.1	496.3
Max flux on the receiver [kW/m²]	561.9	610.2	641.5	693.9

Table 6.4: Type 3 heliostats field data

As is possible to observe from table 6.3, increasing the SM, there is also an increase of the heliostats number, while the optical efficiency decreases due to the distance. In fact, becoming numerous the heliostats, consequently, it rises

up the distance between the last heliostats row and the tower; this effect is a consequence of the interception effect.

In figure 6.7 it is shown the solar field for SM equal 1 with type 3 heliostats and in the others figures 6.8, 6.9 and 6.10 respectively for SM 1.1, SM 1.2 and SM 1.3.

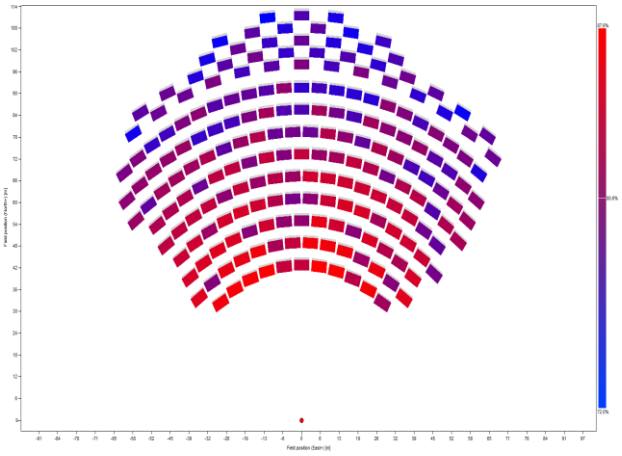

Figure 6.7: Solar field SM 1 Type 3 heliostats

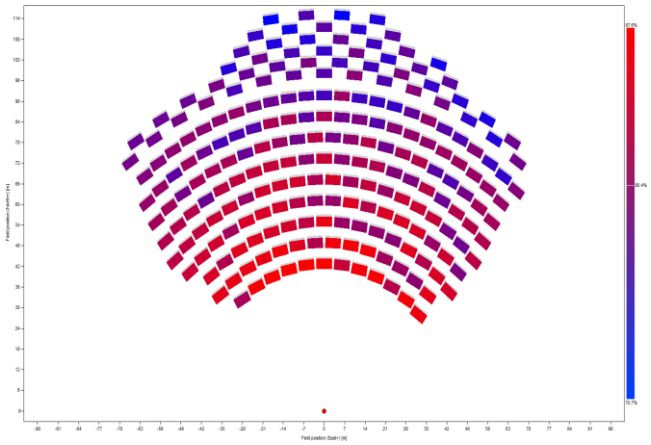

Figure 6.8: Solar field SM 1.1 Type 3 heliostats

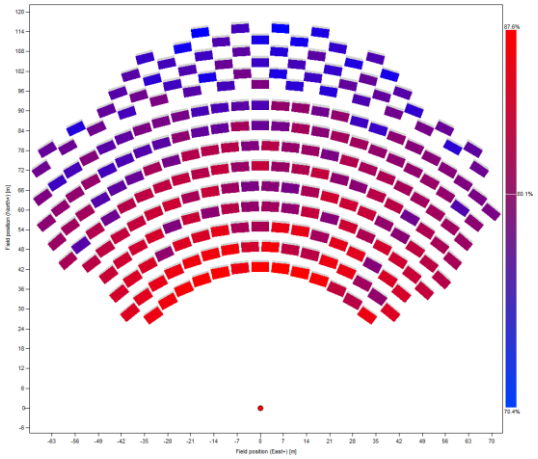

Figure 6.9: Solar field SM 1.2 Type 3 heliostats

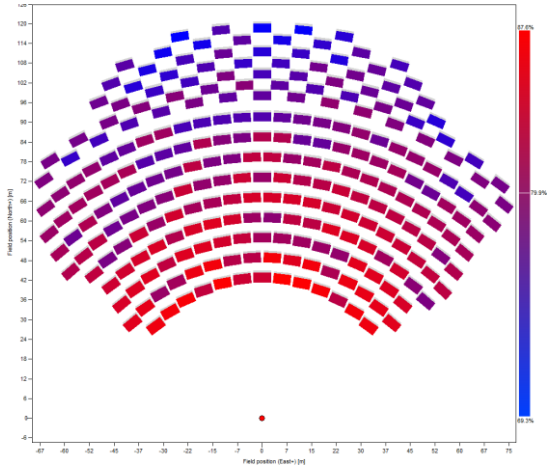

Figure 6.10: Solar field SM 1.3 Type 3 heliostats

As it can be seen, the maximum efficiency is related to the heliostats closest to the tower, i.e. for SM 1, and is 87.6%, while the minimum is relative to the heliostats farther from it and is 72%, for SM 1.3.

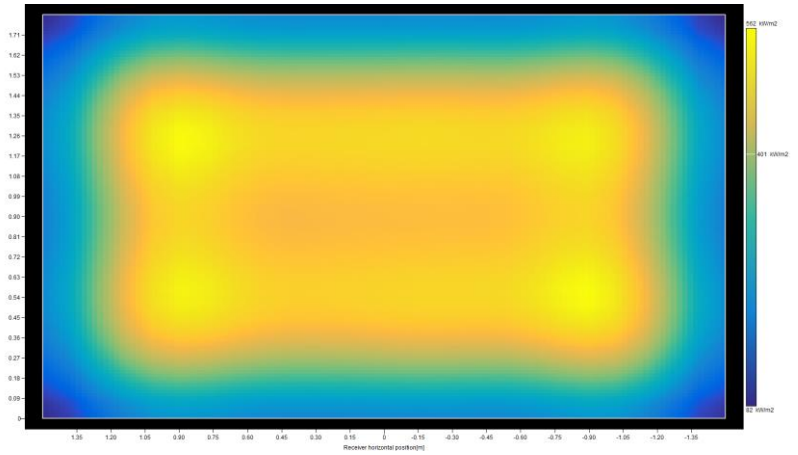

Figure 6.11: Incident flux on the receiver for SM 1 and heliostat type 3

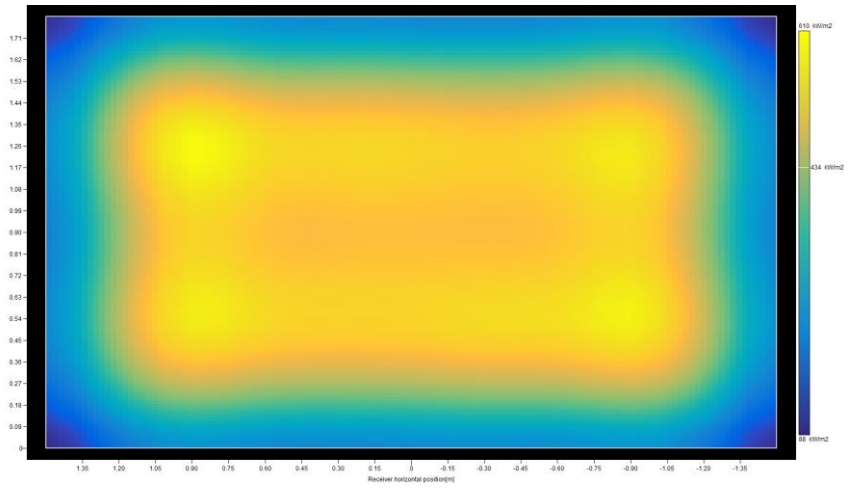

Figure 6.12: Incident flux on the receiver for SM 1.1 and heliostat type 3

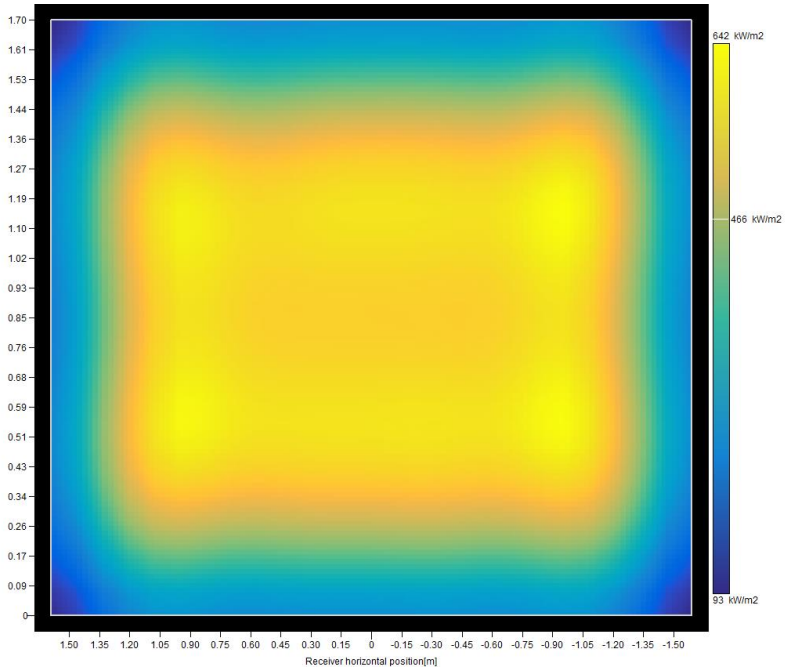

Figure 6.13: Incident flux on the receiver for SM 1.2 and heliostat type 3

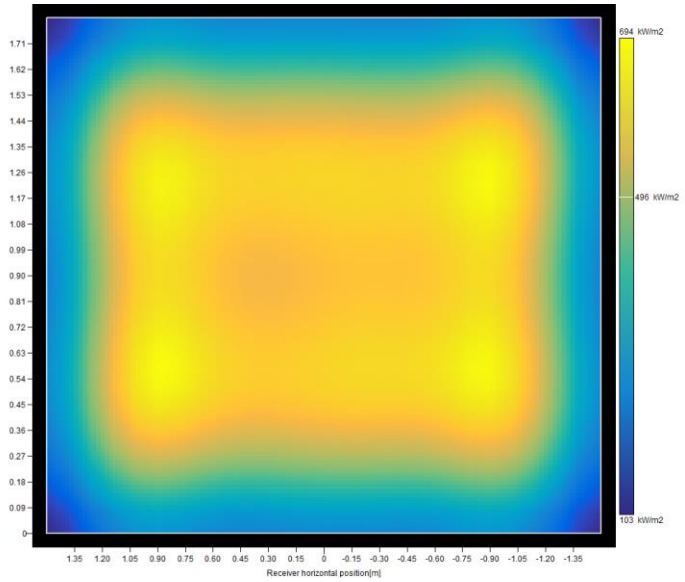

Figure 6.14: Incident flux on the receiver for SM 1.3 and heliostat type 3

In the figures from 6.11 to 6.14 it could be possible to observe the solar flux incident on the receiver surface for SM from 1 to 1.3 respectively, obtained with heliostats type 3. As could be observed increasing the solar multiple, there is an increase of both the average and the maximum flux, because was kept constant the aiming point on the receiver, showed in figure 6.15.

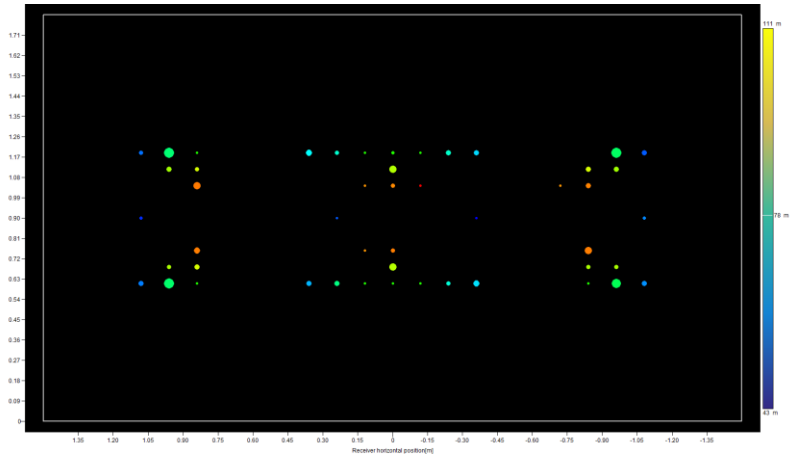

Figure 6.15: Aiming point of the heliostats for SM 1, SM 1.1, SM 1.2, SM 1.3 and heliostats type 3

For all configuration, the maximum value of the solar flux is reached in areas aiming more heliostats; vice versa in areas with less aiming of heliostats, the solar flux is lower.

In appendix B are the solar matrix of the simulations performed for heliostats type 3.

SM	1	1.1	1.2	1.3
Annual average heliostats field efficiency [%]	66.08	65.89	65.53	65.49

Table 6.5: Performance results of the solar fields for heliostats type 3

In table 6.5 are resumed the performance results obtained for heliostats type 3 in term of annual average efficiency.

In follow table 6.6 are showed the results obtained for heliostats type 2 or rather the intermediate size.

SM	1	1.1	1.2	1.3
Heliostats	76	82	88	94
Reflective area [m²]	3194.7	3446.9	3699.1	3951.3
Cg	592	638	685	732
Receiver height [m]	1.9	1.7	1.9	1.9
Receiver length [m]	2.84	3.18	2.84	2.84

Tilt angle [°]	-48	-49	-46	-47
Incident power on solar field [kW]	2715.5	2929.8	3144.2	3358.6
Absorbed power by the receiver [kW]	2100.5	2258.8	2416.2	2571.7
Absorbed power by HTF [kW]	1669.6	1827.2	1985.3	2140.8
Receiver efficiency [%]	79.5	80.9	82.2	83.2
Receiver absorbance [%]	96	96	96	96
Optical solar field efficiency [%]	80.6	80.3	80.0	79.8
Optical total efficiency [%]	77.4	77.1	76.8	76.6
Cosine effect [%]	93.7	93.8	93.5	93.5
Blocking effect [%]	99.8	99.8	99.7	99.7
Shading effect [%]	100	100	100	100
Atmospherical attenuation [%]	98.3	98.3	98.3	98.3
Reflection efficiency [%]	90.7	90.7	90.7	90.7
Interception efficiency[%]	96.5	96.1	96.3	95.9
Average flux on the receiver [kW/m^2]	405.5	435.2	466.4	496.4
Max flux on the receiver [kW/m^2]	564	620.7	649.2	700.1

Table 6.6: Type 2 heliostats field data

As described for heliostat type 3, is possible to observe from table 6.6 the results for heliostat field type 2; increasing the SM decreases the field efficiency due to the distance to the tower centre.

In figures from 6.16 to 6.19 are presented the solar field layout results performed for the heliostats type 2 for SM from 1 to 1.3.

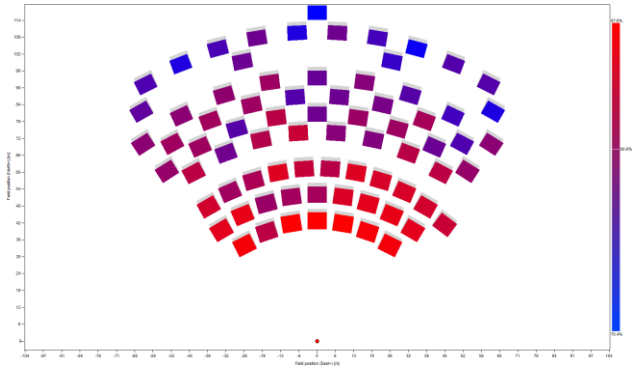

Figure 6.16: Solar field SM 1 Type 2 heliostats

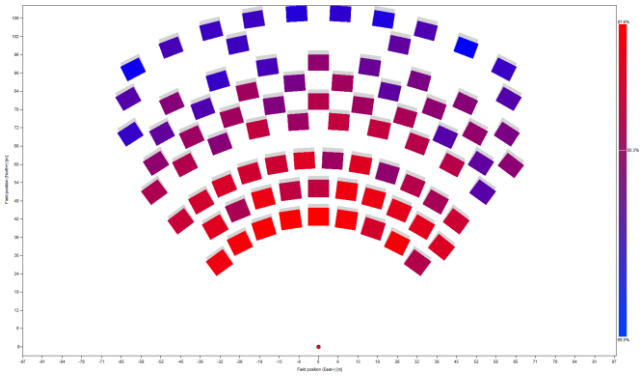

Figure 6.17: Solar field SM 1.1 Type 2 heliostats

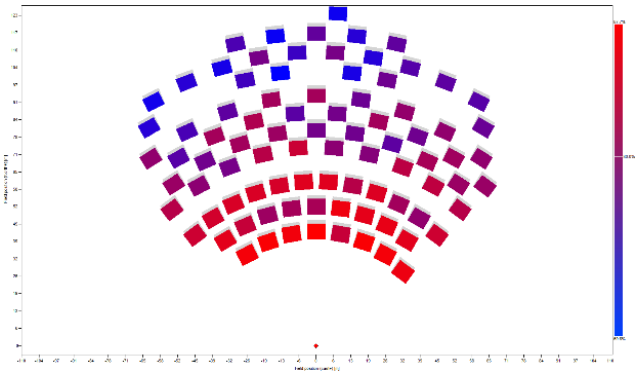

Figure 6.18: Solar field SM 1.2 Type 2 heliostats

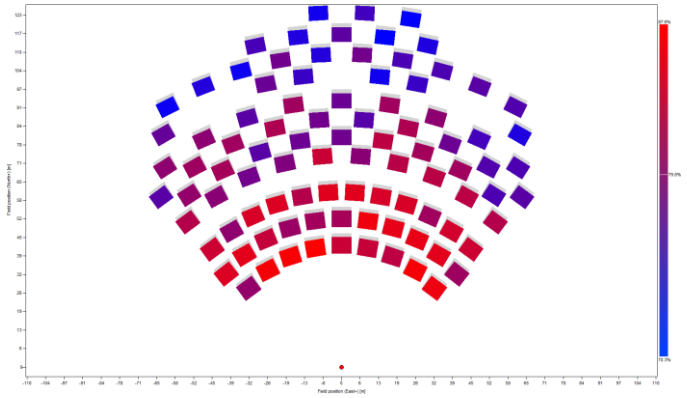

Figure 6.19: Solar field SM 1.3 Type 2 heliostats

In figures from 6.20 to 6.23 are shown the incident flux results for the heliostats type 2. As mentioned for heliostats type 2 the flux density dependents on the aiming point.

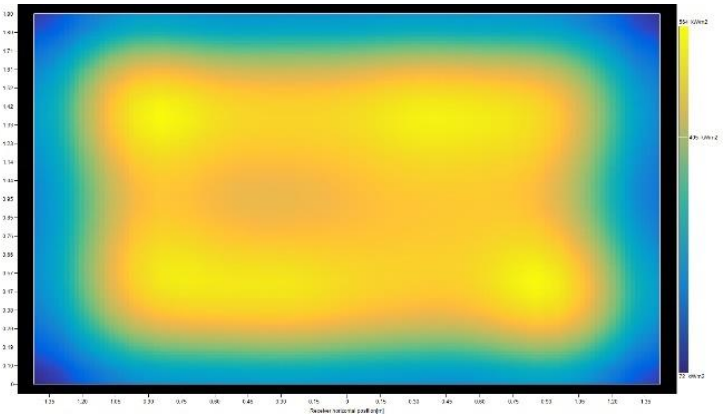

Figure 6.20: Incident flux on the receiver for SM 1and heliostat type 2.

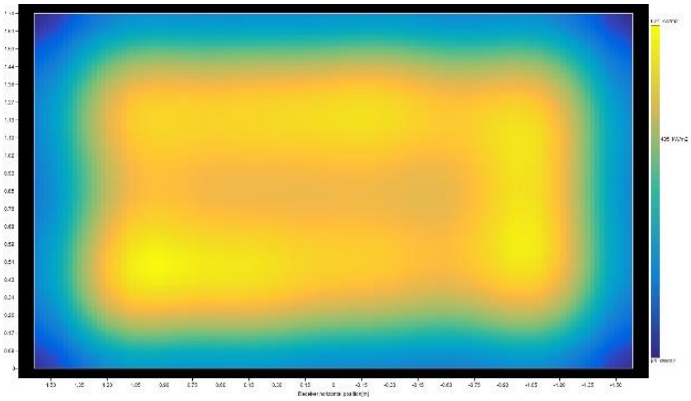

Figure 6.21: Incident flux on the receiver for SM 1.1 and heliostat type 2.

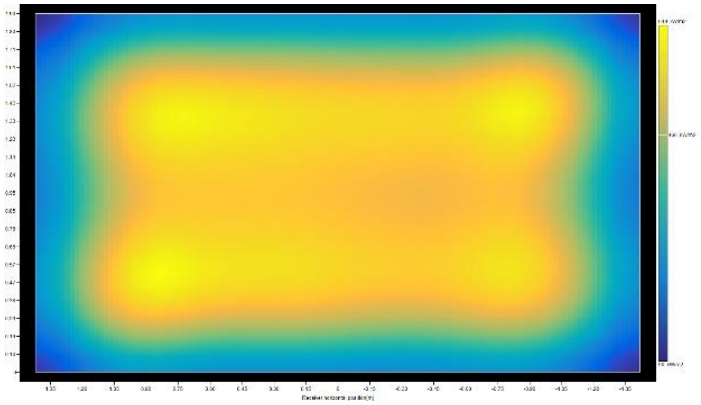

Figure 6.22: Incident flux on the receiver for SM 1.2 and heliostat type 2.

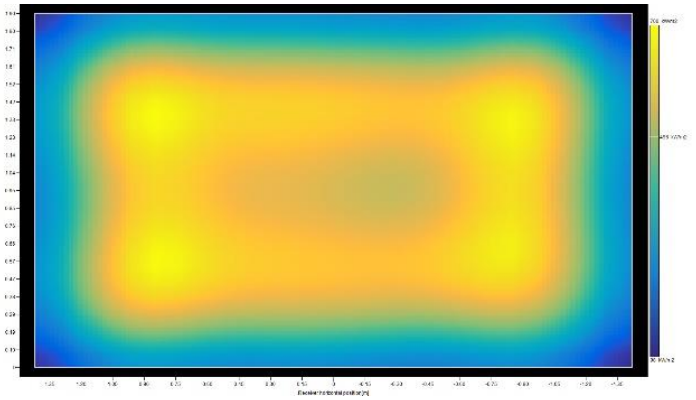

Figure 6.23: Incident flux on the receiver for SM 1.3 and heliostat type 2.

In appendix C are the solar matrixes, and the aiming point map of the simulations performed for heliostats type 2.

SM	1	1.1	1.2	1.3
Annual average heliostats field efficiency [%]	64.83	64.15	64.21	63.96

Table 6.7: Performance results of the solar fields for heliostats type 2

Last heliostats type analysed is the big one, or rather type 1; in the following tables are resumed the main results obtained for this kind of heliostats.

SM	1	1.1	1.2	1.3
Heliostats	31	33	36	39
Reflective area [m^2]	3443	3654.5	3986.7	4318.9
Cg	636	677	738	800

Receiver height [m]	2.6	2.5	2.4	2.4
Receiver length [m]	2.08	2.16	2.25	2.25
Tilt angle [°]	-46	-42	-41	-45
Incident power on solar field [kW]	2918	3106.3	3388.7	3671.1
Absorbed power by the receiver [kW]	2141.1	2252.5	2434.8	2621.3
Absorbed power by HTF [kW]	1709.4	1821.3	2003.7	2190.1
Receiver efficiency [%]	79.8	80.9	82.3	83.6
Receiver absorbance [%]	96	96	96	96
Optical solar field efficiency [%]	76.4	75.5	74.8	74.4
Optical total efficiency [%]	73.4	72.5	71.9	71.4
Cosine effect [%]	94.2	94.1	93.9	93.8
Blocking effect [%]	100	100	100	100
Shading effect [%]	100	100	100	100
Atmospherical attenuation [%]	98.4	98.4	98.3	98.3
Reflection efficiency [%]	90.7	90.7	90.7	90.7
Interception efficiency[%]	90.8	89.9	89.3	88.8
Average flux on the receiver [kW/m^2]	412.4	434.5	469.7	505.7
Max flux on the receiver [kW/m^2]	720.1	751.6	859.8	912.5

Table 6.8: Type 3 heliostats field data

As it is possible to observe, the heliostats numbers, for each SM configuration, is low due to the high dimension of the heliostats, while the total optical efficiency is decrease respect to the type 2 and type 3 cases. It is interesting to observe, how substantial is the reduction of the interception effect, increasing the SM (2%), respect to the other two kinds of heliostats. In the following figures 6.24, 6.25, 6.26 and 6.27 there are represented the heliostats field layout for all solar multiple analysed (1, 1.1, 1.2, 1.3) .

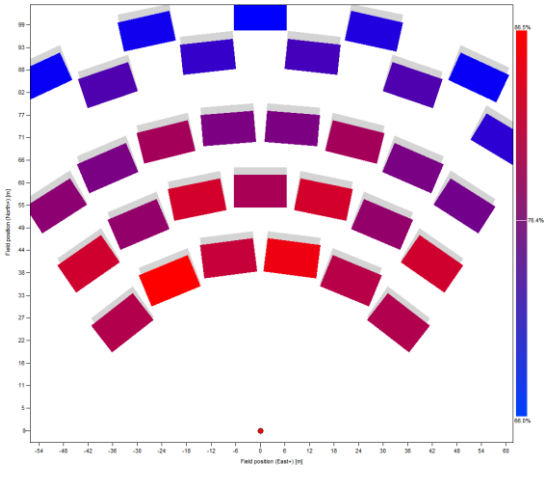

Figure 6.24: Solar field SM 1 Type 3 heliostats

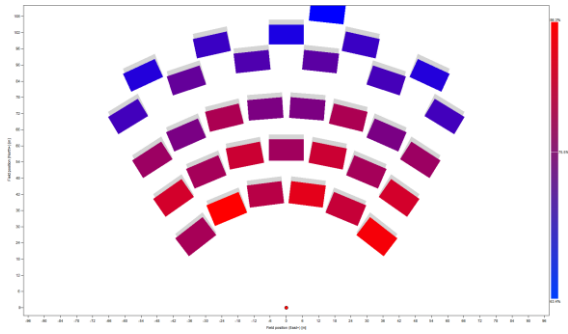

Figure 6.25: Solar field SM 1.1 Type 3 heliostats

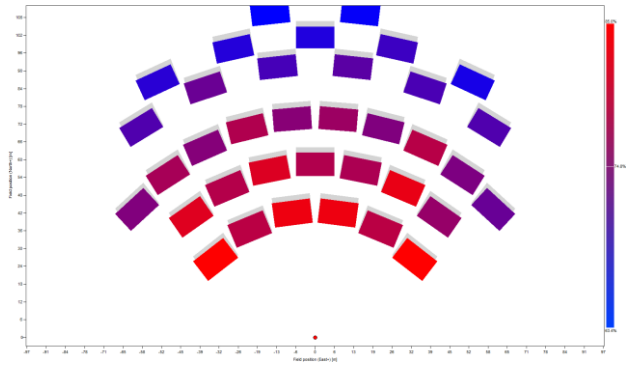

Figure 6.26: Solar field SM 1.2 Type 3 heliostats

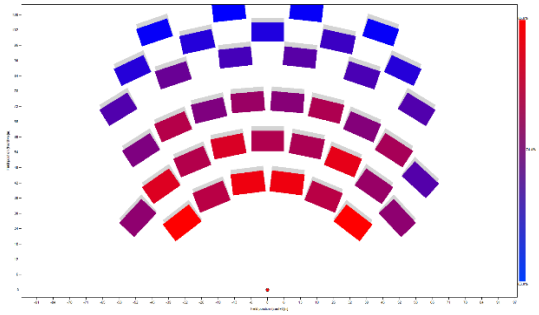

Figure 6.27: Solar field SM 1.3 Type 3 heliostats

In figure from 6.28 to 6.31 are represented the solar flux incident, for SM from 1 to 1.3.

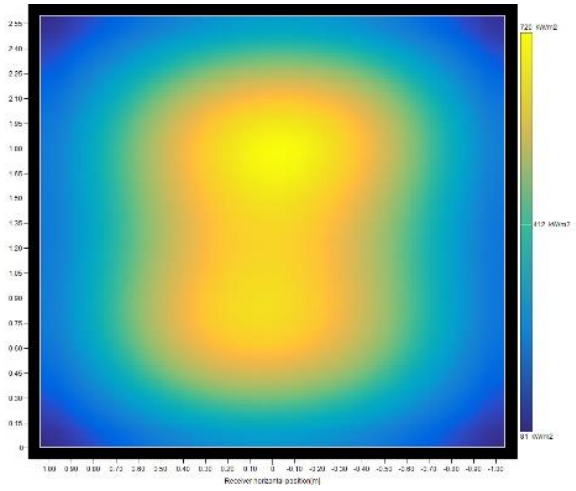

Figure 6.28: Incident flux on the receiver for SM 1 and heliostat type 3.

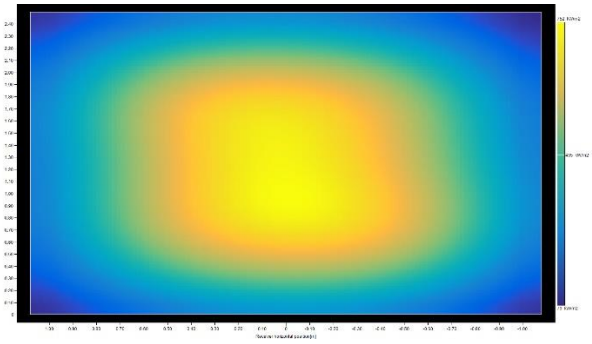

Figure 6.29: Incident flux on the receiver for SM 1.1 and heliostat type 3.

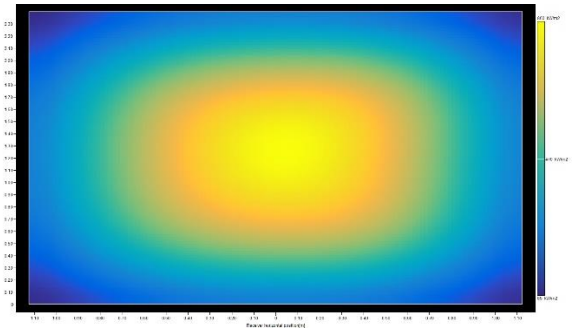

Figure 6.30: Incident flux on the receiver for SM 1.2 and heliostat type 3.

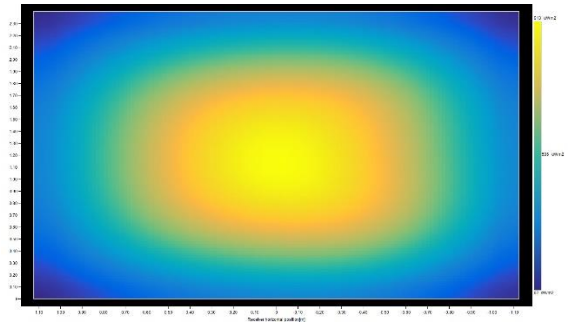

Figure 6.31: Incident flux on the receiver for SM 1.3 and heliostat type 3.

SM	1	1.1	1.2	1.3
Annual average heliostats field efficiency [%]	59.38	58.85	58.1	57.49

Table 6.9: Performance results of the solar fields for heliostats type 3

In appendix D, the solar matrixes are reported, together with the aiming point map of the simulations performed for heliostats type 3.

6.2.4. Comparison of the results

In this part, the results obtained for the three kinds of heliostats will be compared. The comparison will be based on parameters as concentration ratio, total optical heliostats field efficiency, interception efficiency, annual average optical efficiency and receiver fluxes (average and maximum).

Figure 6.32: Concentratio ratio for the three different kind of heliostats

It is apparent that the geometric concentration ratio increases as the solar multiple increases, for each heliostat size. In addition, while the values for the small heliostats (type 3) and intermediate (type 2) are almost equivalent, the results for the heliostats of greater size (type 1), assume higher values.

In Figure 6.33 are shown the heliostats field optical. It can be noted that the efficiency decreases as the SM grows, due to the number of heliostats that are more distant from the tower, and thus have a lower efficiency.

.

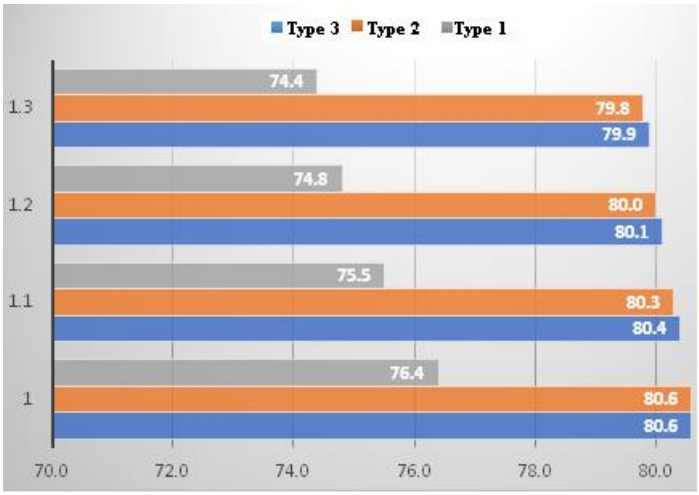

Figure 6.33: Heliostat field efficiency of the three size.

Even in this case, type 1 has worse performance than the others. The value of lower optical efficiency is mainly determined by the interception effect, as shown in Figure 6.34.

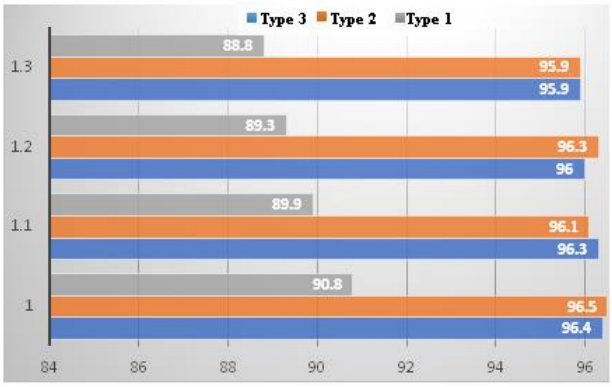

Figure 6.34: Interception effect of the heliostats type for the SM configuration analysed.

The interception effect is more evident for the heliostats type 1, because their size is greater than the one of the receiver (115.56 m^2 against 5.4 m^2)

The receiver is not big enough to intercept the entire image reflected by the heliostat, and part of the flux will be "spilled" by the edges.

Also for an annual efficiency, in the same way, there is the same effect as shown in Figure 6.35.

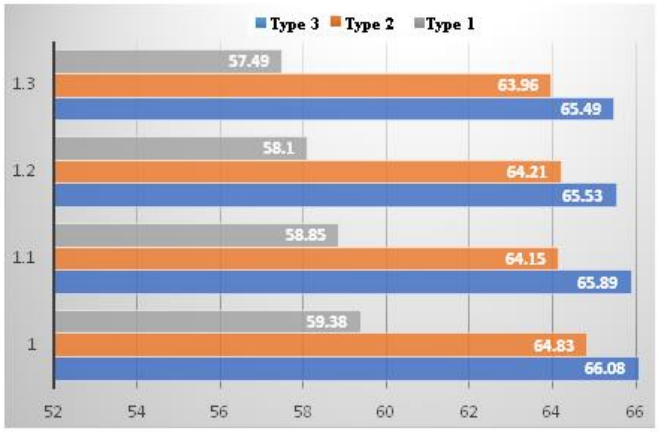

Figure 6.35: Annual efficiency for all configuration

6.3.Power plant numerical model

In this part, numerical modelling of the central tower concentrator solar system will be performed. For this purpose, Simulink® / MATLAB® was used to simulate and analyse the dynamic behaviour of the system in a block diagram programming environment (LEGO). Therefore, the control system will be modelled by varying the mass flow rate in order to compensate the DNI variations and to maintain a constant value of turbine inlet temperature (TIT).

Since gas turbines operate in optimal conditions only for a particular ratio between the rotation speed and the working fluid speed, this must be kept constant. The rotation speed does not change as well as the velocity triangles and the volumetric flow rate. With a variable density working fluid, the system can therefore operate at variable mass flow at fixed optimal operating condition. The mass flow variations in the cycle, for the adjustment of the TIT due to the variation of the thermal load (intercept by the CSP system), is caused by the air density variation. As mentioned, these effect is obtained through the air pressure variation at the inlet section of the compressor. The relation between these two variables, as mentioned could be expresses by the Ideal Gas Law:

$$\frac{p}{\rho} = R^{*}T \qquad (6.1)$$

Where:

- ρ is the density;
- p is the pressure;
- R^{*} is the gas constant;
- T is the temperature.

As mentioned in the previous chapters, to keep the main temperature constant, a variation in the base pressure, up to five times the atmospheric pressure is allowed; the auxiliary compressor and the bleed valve actuate it.

In the following sessions the numerical model of all components cycles will be described.

6.3.1. Receiver

As the system works under pressurized conditions, an employing of volumetric pressurized receiver have been supposed. An other important device is the quartz window, on the receiver aperture. The main reason for this choice is the requirement of reducing thermal radiative losses. The volumetric effect of this kind of receivers allows to obtain this reduction despite the high temperature inside the material. The absorber is made of silicon carbide (SiC), ceramic material with excellent radiative and thermal properties, able to withstand temperatures of 1400 ° C. [112]

The aperture of the receiver, which depends to the solar energy intercepting, and also the thermal losses values is expresser as:

$$A_{ar} = \frac{Q_{th}}{\Phi_{avg}} \qquad (6.2)$$

Where:

- Q_{th} is the required thermal power;
- Φ_{avg} is the average flux incident.

6.3.2. Heat balance equation

The equation on which is based the model, is the balance of the absorber inlet and outlet thermal power:

$$\frac{dU}{dt} = Q_{inc} - Q_{loss} - Q_{wf} \qquad (6.3)$$

Where:

- $\frac{dU}{dt}$ is the internal energy variation respect to the time;
- Q_{inc} is the incident thermal radiation;
- Q_{loss} is the thermal loss;
- Q_{wf} is the thermal power transfer to the HTF.

Introducing the thermal capacity, the internal energy variation (6.3) will be expressed as function of the temperature variation:

$$\frac{dU}{dt} = m\, c_p \frac{dT}{dt} \qquad (6.4)$$

Where:

- m is the absorber mass;
- c_p is the specific heat;
- $\frac{dT}{dt}$ is the average surface temperature variation of the absorber, respect to the time.

It was assumed to employ a flat plate-shaped absorber, with a porous honeycomb structure. This is characterized by a frontal area equal to the aperture of the receiver and a thickness of 9.5 cm.

Assuming a porosity of 49.51% [119], and considering that the density of silicon carbide is 3.21 g/cm^3, the mass of the absorber is:

$$m = \rho V(1 - p) \qquad (6.5)$$

Where:

- ρ is the density of the material;
- V is the volume;
- p is the porosity.

The heat capacity (C) is the product of c_p (1200 J/kgK [120]) for the mass (m):

$$C = c_p \rho V(1 - p) \qquad (6.6)$$

While the superficial average temperature of the absorber is:

$$\bar{T}_{abs} = \int \frac{1}{C} \frac{dU}{dt} \qquad (6.7)$$

This temperature was assumed to be equal to that of the air leaving the receiver. In this work, no thermal losses were considered in the transition between the receiver and the turbine, so the temperature expressed in equation (6.7), will also be considered as TIT.

6.3.3. Incident power

The power incident is mainly function of direct normal radiation (DNI), heliostats field efficiency and reflective heliostats total area. DNI and field efficiency depends on the azimuth and zenith which, in this model, are the input data with a one-minute step. The heliostats are instead constant, (table 6.2) so the incident power in this model is evaluated as follows:

$$Q_{inc,t} = \eta_{SF}\, DNI\, A_{SF} \qquad (6.8)$$

Where:

- η_{SF} is the heliostat field;
- A_{SF} is the eflective area.

By the optical matrix efficiency (in appendix C) function of azimuth and zenith, the value for the incident theoretical power could be to evaluated. Thanks to the thermodynamics department of University of Seville, the meteorological data, with one-minute time step (DNI, azimuth, zenith, ambient temperature etc.) have been used. The optical matrix, by a Matlab interpolating code, is available in Simulink.

6.3.4. Heliostat field

Using the power of the heliostats field, the code calculates the average flux that theoretically affects the absorber. In the case where this value is higher than the average flux set, the air coming out from the receiver exceeds the fixed value of 800 ° C. At this point, the maximum mass flow is flowing and therefore, it is not possible to remove excess heat from the receiver. To keep the constant air temperature, a part of the heliostats is then defocused, this is an operation that maintains the average incident flux on the receiver at the set values. The percentage of heliostats focused or focusing factor F_{ϕ}, is given by:

$$F_{\phi} = \frac{A_{eff}}{A_{SF}} = \frac{\phi_{avg}}{\phi} \qquad (6.9)$$

Where:

- A_{eff} is the heliostat effective area focused on the receiver;

- ϕ is the instant flux f (DNI, η_{SF}).

From 6.9 it can be noticed that the equation between the area of the heliostats that must be focused on the receiver and the nominal area of the field is also expressed as a ratio between the fluxes. The absorber incident flux is equal to the ratio between the instantaneous incident power and the aperture receiver area A_{ar}:

$$\phi = \frac{\eta_{SF}\, DNI\, A}{A_{ar}} \qquad (6.10)$$

Therefore, the flux ϕ is associated to the nominal area, while the average flux ϕ_{avg}, which is 400 kW/m^2, is associate to the instantaneous surface necessary to prevent to exceed this limit value. By the ratio between the fluxes, it is obtained the effective area of the heliostats field.

There is also a second defocusing type, based on the temperature derivative, which is carried out to prevent the overshoot of the TIT, due to rapid increases of solar radiation, in flux conditions lower than the design average value. This second focusing factor (F_T) is expressed as:

$$F_T = 2 - k\frac{\Delta T}{\Delta T_{lim}} \qquad (6.11)$$

Where:

- k is the adimensional gain, need to evaluate the heliostat defocused number (equal to 1);
- ΔT is the instantaneous temperature variation;
- ΔT_{lim} is the limit difference of temperature .

Additionally, as the heliostats are defocused due to the rapid increase in temperature, in the next step not all are focused on the receiver, but only a percentage. The reason why is to avoid temperature fluctuations that could arise a sudden refocus of a large amount of heliostats. Only 5 % of the heliostats defocused then will be active.

In each calculation loop, the code compares the two focusing factors, by choosing the lower value, in order to evaluate the heliostats area. The area value, evaluated from this comparison, requires a discretization, because is not a discrete number but only a percentage of defocusing area.

$$Q_{inc} = Q_{inc,t} \frac{A'_{eff}}{A_{SF}} \qquad (6.12)$$

Where:

- Q_{inc} is the incident power related to heliostats area A'_{eff};
- A'_{eff} is the heliostats area after the discretization .

6.3.5. Thermal losses

There are radiative and conductive losses in the receiver, but convective losses, due to the quartz window, installed in the receiver aperture, are neglected [11]. The thermal losses could be expressed as:

$$Q_{loss} = Q_{rad} + Q_{cond} = \varepsilon\sigma A_{ar}(\bar{T}_{abs}^4 - T_{amb}^4) + K \frac{A}{s}(\bar{T}_{abs} - T_{amb}) \quad (6.13)$$

Where:

- T_{amb} is the ambient temperature;
- ε=α is the emission coefficient (0.96 [120]);
- s is the thickness of the thermal insulator, 0.1 m (stone wool);
- K is the thermal conductibility of the insulator (stone wool) 0.1134 W/mK

In the case of conductive losses it is assumed that these occur through the case of the receiver cavity. It was supposed that the receiver had a performance of a grey body (ε=α).

6.3.6. Power to heat transfer fluid

The power absorbed by the air, during the passage of the porous matrix, is the function of the mass flow rate that flows in the cycle and of the enthalpy difference of the air incoming and outcoming from the receiver.

$$\mathrm{Q_{wf}} = \dot{\mathrm{m}}_{\mathrm{air}} \left(\mathrm{h_{out}} - \mathrm{h_{in}}\right) \quad (6.14)$$

Where:

- $\dot{\mathrm{m}}_{\mathrm{air}}$ air mass flow crossing the receiver;
- $\mathrm{h_{out}}$ is the air enthalpy outlet from the receiver;

- h_{in} is the air enthalpy inlet in the receiver.

6.3.7. Mass flow air

The air flow rate flowing in the cycle, has been modelled in order to vary both as a function of the incident flux on the receiver, to maintain a constant TIT, both in function of the temperature of the receiver, to simulate the transient start-up and shutdown of the plant.

The following significant mass flow rate values have been introduced, in order to explain the two adjustment mode:

- $\dot{m}_{min}$ is the standard mass flow rate, under ambient pressure;
- $\dot{m}_{max}$ is the maximum value of mass flow rate under pressurized condition.

The flow rate in the two conditions were evaluated as the product of the volumetric flow rate V, constant during all the different operating conditions, and the density of air.

$$\dot{m}_{air} = \rho_{air}(p,t)V \qquad (6.15)$$

Under ISO conditions the Turbec T100 air mass flow rate is 0.783 kg/s [122]; the air density is 1.22 kg/m^3, therefore the volumetric flow of the micro gas turbine is 0.642 m^3/s.

For the air density, the temperature and pressure, the inlet of the micro gas turbine are assumed as reference conditions. The pressure losses due to the regenerator of the micro gas turbine, have been estimated at 4.8% of the total pressure [25], and have been divided in the two sides of the regenerator in the same way. Load losses in the circuit, were supposed to equal 3% of the delivery pressure. The pressure at the inlet of the turbine is thus 5.4% lower than the one at the compressor outlet.

Considering that the micro gas turbine has a compression ratio of 4.5, under standard conditions, the pressure at main point of the cycle are:

- Compressor inlet pressure: 1.013 bar;
- Compressor outlet pressure 4.559 bar;
- Turbine inlet pressure 4.314 bar.

While under pressurized condition:

- Compressor inlet pressure: 5.065bar;
- Compressor outlet pressure 22.795bar;
- Turbine inlet pressure 21.570bar.

From equation 6.15 it is obtained therefore $\dot{m}_{min}$ and $\dot{m}_{\max}$, respectively equal to 0.9165 kg/s and 4.5564 kg/s. The first type of adjustment, which dependents on the receiver temperature, is calculated between 0 and $\dot{m}_{min}$; the aim is to simulate, in a simplified manner, the power-on and power-off phases. If the temperature of the receiver is powerful enough, it is possible to produce electrical power, which guarantees the base power of the micro gas turbine (MGT), the flow rate is incremented gradually to the value $\dot{m}_{min}$ in 5 minutes.

The minimum electrical power threshold was set at 20 kWe, corresponding to 20% of the nominal size of the (MGT). The temperature which allows to produce this threshold, and then start the ignition process, is slightly less than 600 ° C, while for lower values the plant is inactive. The receiver temperature (800 ° C must be reached), continues to increase if the solar flux also increases at the same time.

If, on the other hand, the operating temperature decreases below 600 ° C, a shutdown process begins, which leads from the minimum value to zero with an inverse procedure to the starting one.

Once the minimum flow rate has been reached, the flux adjustment is carried out. This allows to keep constant the TIT value, regulating the thermal power absorbed by the fluid, with a mass flow rate variation. Like the control strategy has been established that, the mass flow rate varies linearly with the incident flux on the absorber, according to the following equation:

$$\frac{\dot{m}-\dot{m}_{\min}}{\dot{m}_{\max}-\dot{m}_{\min}} = \frac{\phi-\phi_1}{\phi_2-\phi_1} \qquad (6.16)$$

Where:

- ϕ_2 is the average incident flux (400 kW/m²);
- $\phi_1$has a value of 144.5 kW/m²;
- $\dot{m}$ is the instantaneous mass flow rate;
- ϕ is the instantaneous incident flux;

6.3.8. Pressure and enthalpy variation

To calculate the pressure, the density values are interpolated (as shown in appendix E); the density is obtained as:

$$\rho = \frac{\dot{m}}{V} \qquad (6.17)$$

Consequently, enthalpy can be obtained from Table in appendix E, once the temperature and pressure have been set; while for the temperature the presence of the regenerator has been taken into consideration.

In fact, if the air has a sufficiently high temperature at the micro gas turbine outlet, the regeneration process starts; the exit temperature of the compressor is the variable that switches the regeneration.

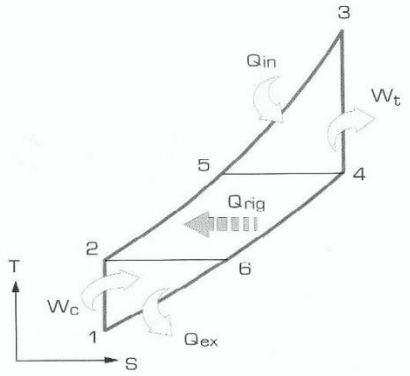

Figure 6.36: Referring TS regenerating Joule- Brayton cycle

In the real cycle, the temperature T_5 does not coincide with T_4 but is lower, so the efficiency of the regenerator ε is introduced. Assuming an efficiency of 0.9 [99], temperatures T_5 can be obtained from:

$$\varepsilon = \frac{T_5 - T_2}{T_4 - T_2} \qquad (6.18)$$

Now it is possible to evaluate the enthalpy variation of equation 6.14:

- Without regeneration h_{out} is evaluated under conditions (T_3, p_3) while h_{in} under conditions (T_2, p_2). The pressure at point 3 is lower than the one of point 2 because it takes in account the piping pressure drops;
- With regeneration h_{out} it is calculated in (T3, p3) while h_{in} under conditions (T5, p5). In point 5, the pressure takes into account the

pressure drops in the regenerator, while in point 3 also piping pressure losses are added.

6.3.9. Power production

The net electric power P_{net} generated by the power unit is calculated as the difference between the power produced by the turbine and the power absorbed by the compressor. Both powers are functions of the air enthalpy at inlet and outlet of the components:

$$P_{net} = \eta_{el}\, \dot{m}_{air} \left[\eta_{mec}\, (h_3 - h_4) - \frac{1}{\eta_{mec}} (h_2 - h_1)\right] \qquad (6.19)$$

Where:

- η_{el} is the electric efficiency (0.97);
- η_{mec} is the mechanical efficiency (0.94);
- $\dot{m}_{air}$ is the mas flow air.

The enthalpy values of the equation 6.19 are referred to figure 6.35, and have been evaluated from table in appendix E, function of temperature and pressure.

Finally, the cycle efficiency is evaluated as the ratio between the electrical power and the thermal power entering the cycle:

$$\eta_{cycle} = \frac{P_{net}}{Q_{wf}} \qquad (6.20)$$

6.4.Results

In the following part, the simulation results will be shown; first of all will be introduced the main variable used in the simulation, then the result will be exposed and, finally, the comparison with the commercial plant using similar power block will be shown. The main input data are the DNI, Azimuth angle and zenith angle.

The simulation has a resolution of one-minute but, for a clear explication, the 21st of June will be used as reference day.

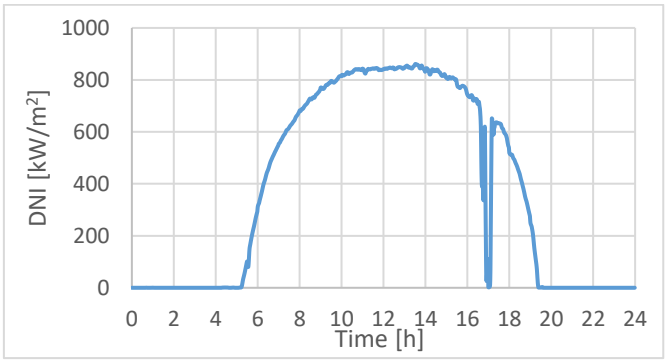

Figure 6.37: DNI trend of the 21st June (GTER Seville)

In figure 6.37, it is possible to observe the DNI of the referred day, used to explain the results.

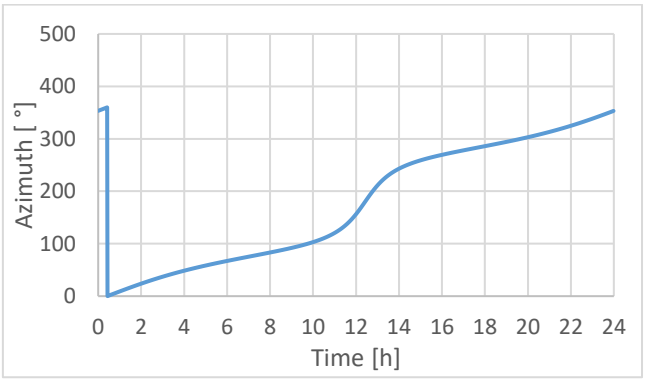

Figure 6.38: Azimuth trend of the 21st June (GTER Seville)

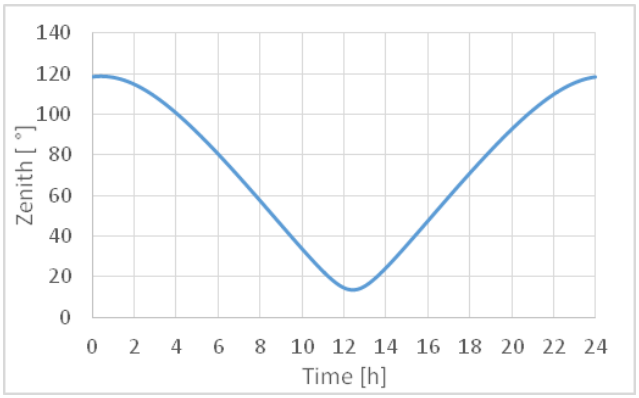

Figure 6.39: Zenith trend of the 21st June (GTER Seville)

The results regarding the main follows parameters:

- Heliostats field efficiency;
- Incident thermal power on the receiver;

- Air mass flow rate;
- Pressure in the receiver;
- Absorbed power from HTF;
- Temperature inlet turbine;
- Thermal receiver losses;
- Receiver flux;
- Heliostat defocused;
- Electrical power production;
- Cycle efficiency.

6.4.1. Heliostats field efficiency

The following figure 6.40 shows the efficiency result for the three heliostats size, for solar multiple equal to 1.

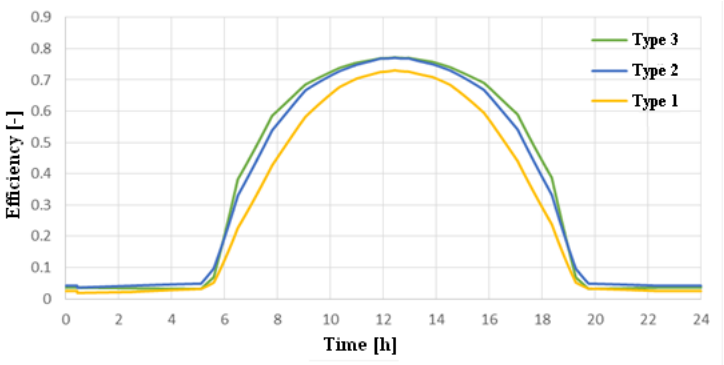

Figure 6.40: Heliostats filed efficiency for three heliostats type and SM 1

The size of the heliostats affects the performance of the field because, increasing the size, the difficulty to obtain the optimal position and focusing of the reflecting surface increases. This effect causes a 2 % of efficiency decrease between the type 3 and type 2 heliostats, while it is relevant in the case of the type 1 heliostats (5%).

The variation of the solar multiple does not affect the field efficiency, as it is possible to observe in figure 6.41 and 6.42, which do not exhibit appreciable differences among the four configurations. There is only a small decrease in efficiency in the central hours because a higher number of heliostats (SM 1.3) cause an increase in spillage losses.

.

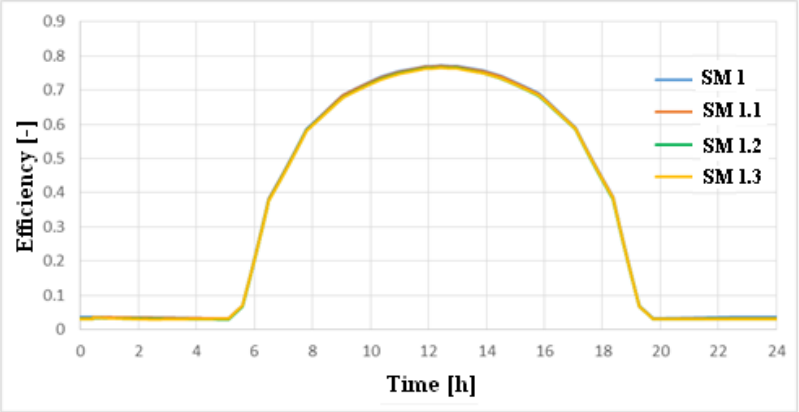

Figure 6.41: Heliostats filed efficiency of heliostats type 3 for the four SM

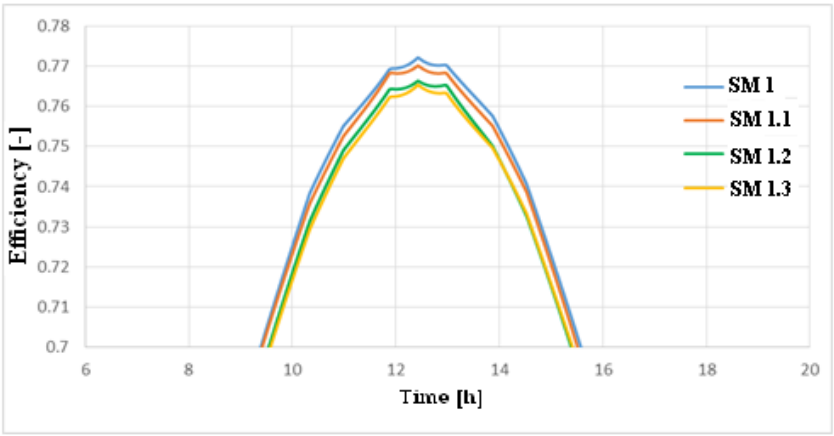

Figure 6.42: Zoom in of fig 6.40 of the hours middle day of the trend efficiency.

6.4.2. Receiver incident power

The incident power on the receiver decreases when the heliostats size increases, due to the lower efficiency of the solar field. In the case of the solar multiple which results in an increase in the incident power when the SM increases.

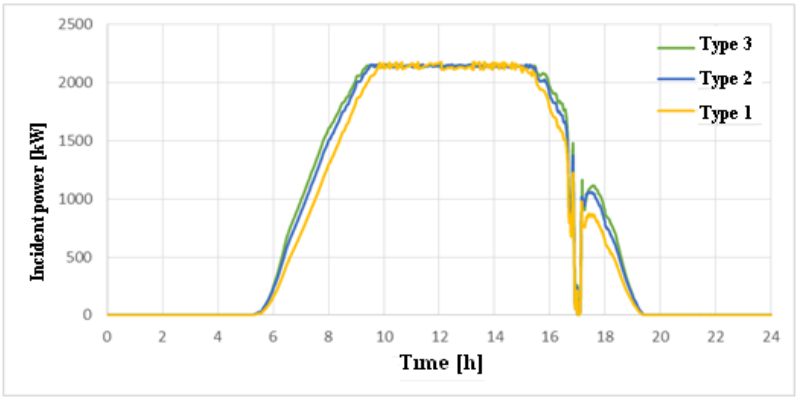

Figure 6.43: Incident power on the receiver for SM 1.3

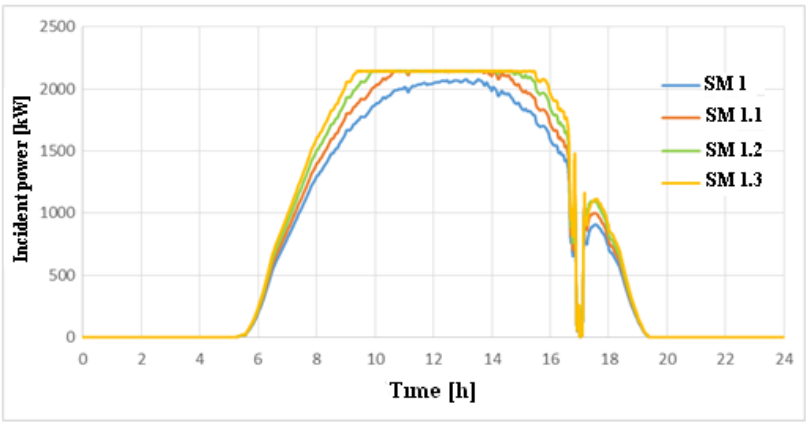

Figure 6.44: Incident power on the receiver of heliostats type 3

6.4.3. Receiver incident flux

The same considerations made for the power incident on the receiver can be made for the flux. It should be notices, however, just as for the solar multiple values greater or equal than 1.1, the defocusing system intervenes. As can be seen from figure 6.45, the system intervenes before for SM 1.3 compared to SM 1.

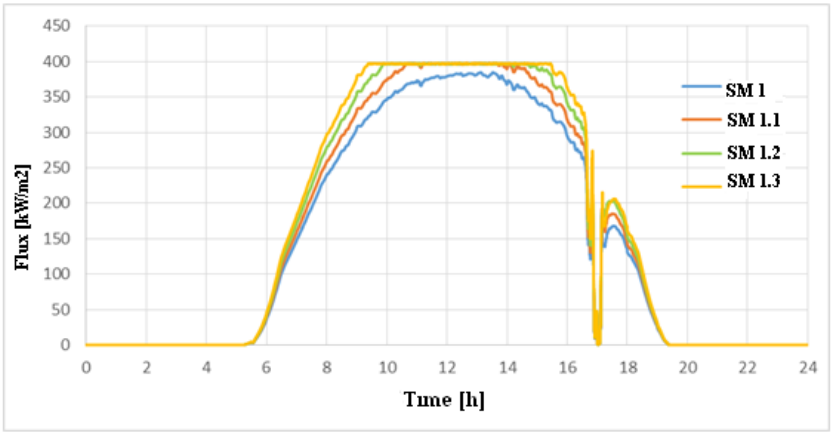

Figure 6.45: Incident flux on the receiver of heliostats type 3

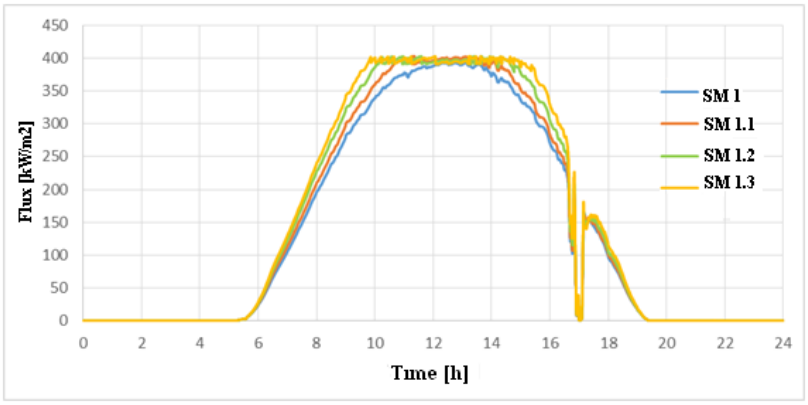

Figure 6.46: Incident flux on the receiver of heliostats type 1

It should be emphasized, observing figures 6.45and 6.46, how the control of the flux is more difficult for the larger heliostats than the smaller ones; this can be seen in particular in Figure 6.46 through fluctuations of the flux trend around the value of 400 kW/m²:in fact, the small heliostats (type 3) allow a more accurate and gradual control.

6.4.4. Mass flow, pressure on the receiver and power to working fluid

The trends of the pressure in the receiver and of the power transferred to the heat transfer fluid, are correlated to the air mass flow rate of the cycle and at the flux.

Higher flow values allow the heating and cooling of the receiver to be anticipated and postponed respectively; the consequence is that the plant

operation time is prolonged. In addition, an increase in the solar multiple, with the same size of the heliostats, or a decrease in the size of the latter, with the same solar multiple, make it possible to obtain a higher flow rate. In this way the maximum mass flow flows for a longer time, increasing the energy production of the plant.

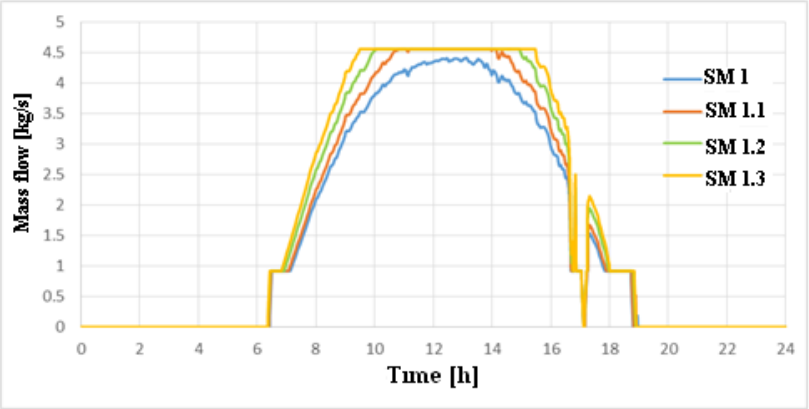

Figure 6.47: Receiver mass flow results of heliostats type 2

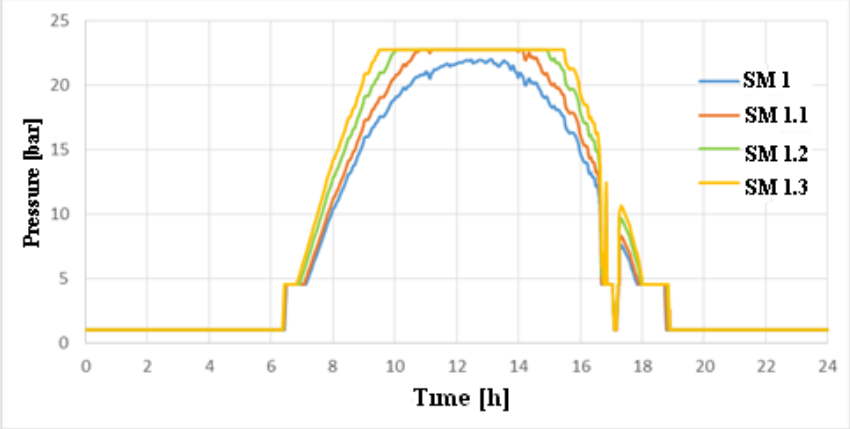

Figure 6.48: Receiver pressure results of heliostats type 2

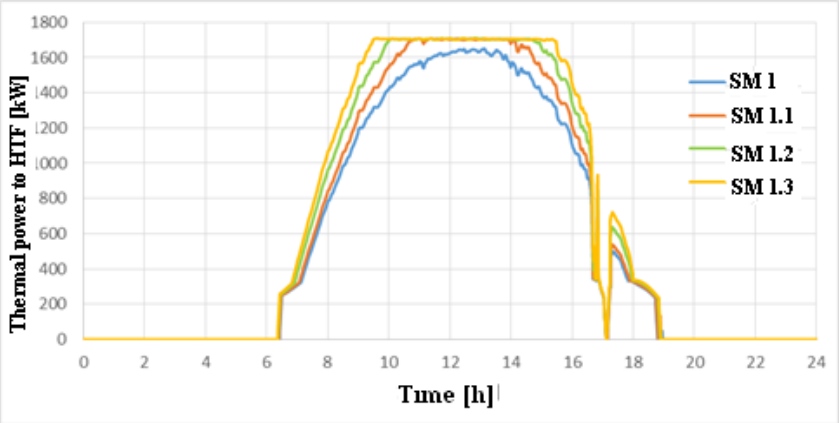

Figure 6.49: Power to HTF results of heliostats type 2

6.4.5. Temperature inlet turbine and thermal losses

As mentioned in the past session, the air exit temperature from the receiver has been supposed equal to the temperature inlet turbine; so no thermal losses have been considered. As it is possible to notice from figure 6.49, smaller heliostats are able to reflect more efficiently the solar radiation; they manage to warm up more quickly of the receiver and loosen the cooling.

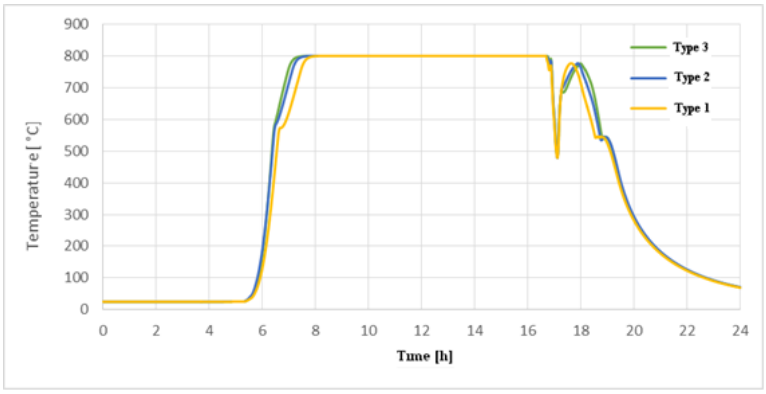

Figure 6.50: Temperature inlet turbine trend SM 1

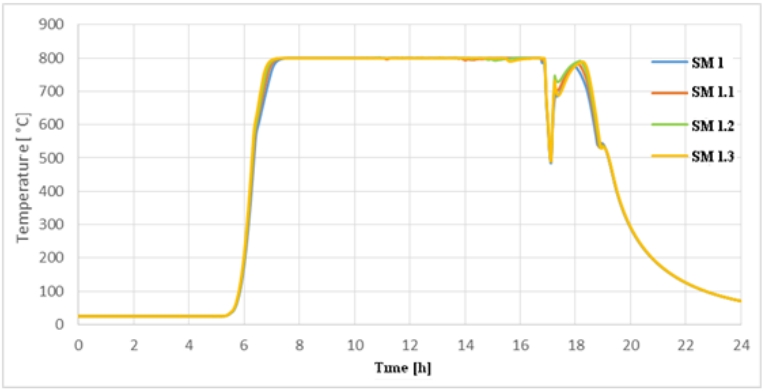

Figure 6.51: Temperature inlet turbine trend heliostats type 3

Thermal losses have the same trend of the temperature inlet turbine, in follow figure 6.52 are reported this trend.

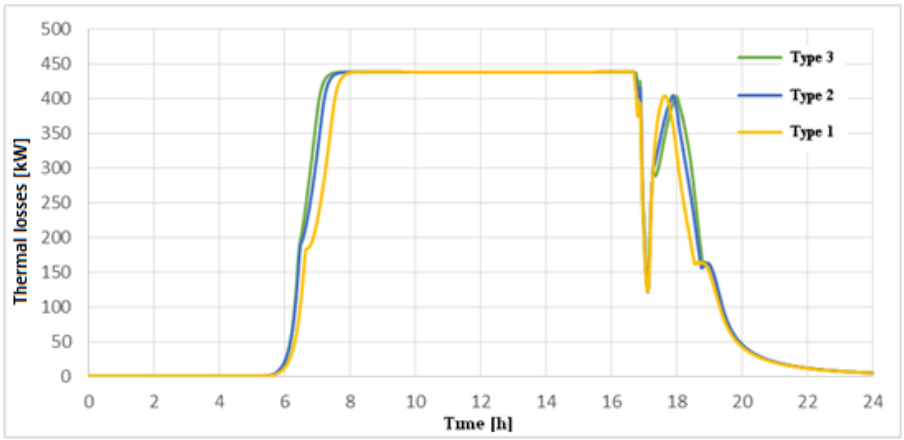

Figure 6.52: Thermal losses trend SM 1

6.4.6. Heliostats defocused

In this session the defocusing adjustments results will be shown. In figure 6.53 it can be seen how, for a unit value of the solar multiple, the only defocusing mechanism is the temperature control.

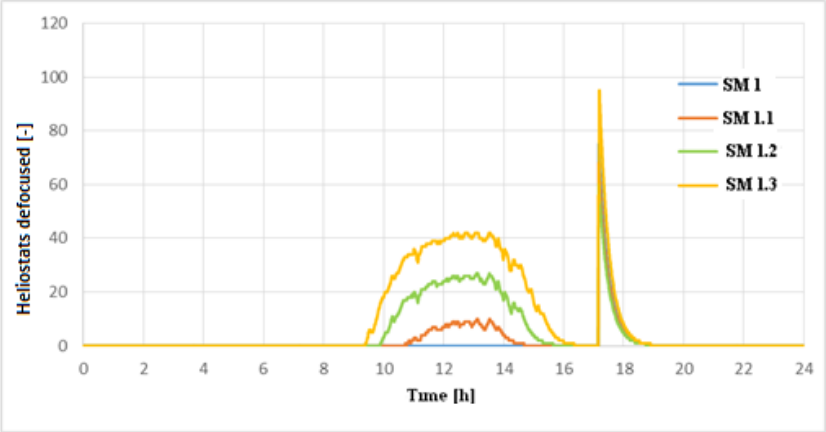

Figure 6.53: Heliostat defocused trend heliostats type 3

For SM values greater than 1 the system that controls the flux also intervenes, defocusing a part of heliostats. The defocusing implemented by the temperature derivative does not have the same adjustment strategy: in fact, it is possible that a higher solar multiple value has lower defocused heliostats respect to a solar field with SM1. The reason for this is because, as mentioned, there is the overshoot of the temperature and of the heliostats size as can be possible to observe from figure 6.54.

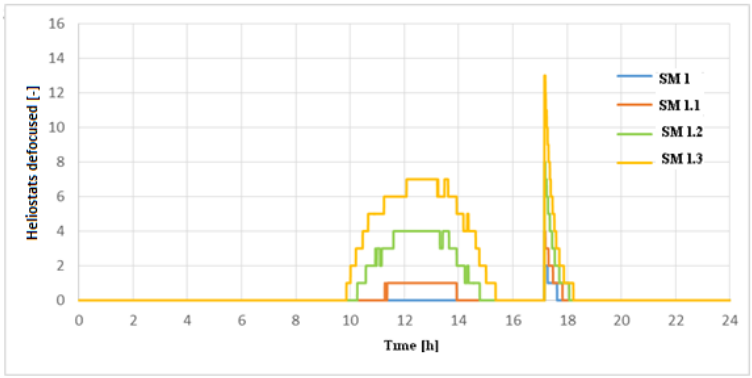

Figure 6.54: Heliostat defocused trend heliostats type 1

6.4.7. Net power and efficiency

As it can be possible to observe in figure 6.55 the best power production has been reached for SM 1.3 configuration employing heliostats type 3 (small). The heliostats type 1, could not control efficiently the incident flux, therefore the power production has a fluctuating trend around 500 kW value.

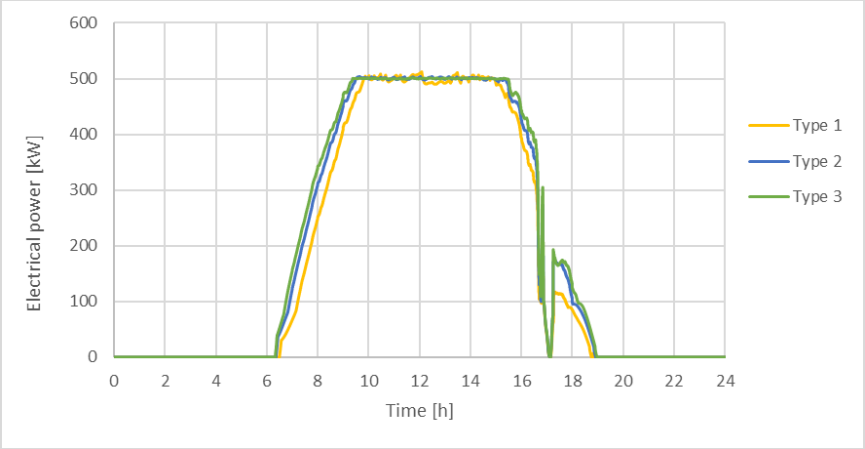

Figure 6.55: Power production heliostats types SM 1.3.

In figure 6.55 could be possible to observe as increasing the solar multiple, at the same time, increases the power production, in particular in this figure it is possible to observe the power production trend, while in figure 6.57 it is shown the efficiency trend for heliostats type 3

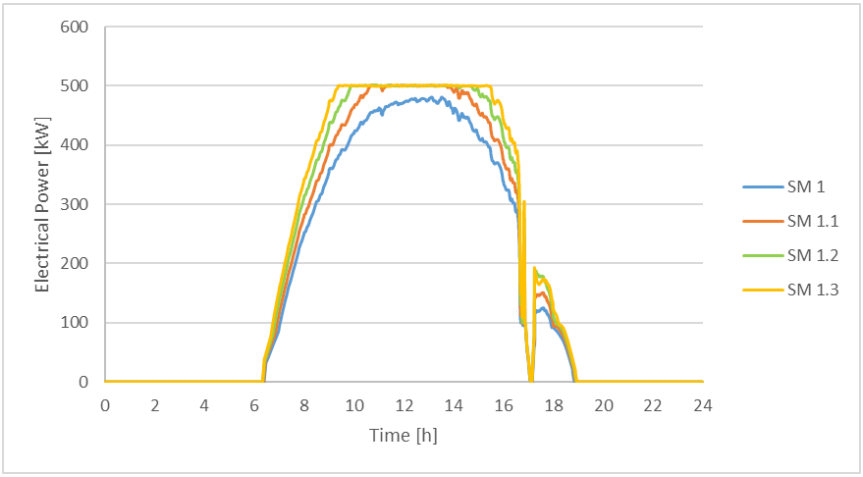

Figure 6.56: Power production heliostats type 3.

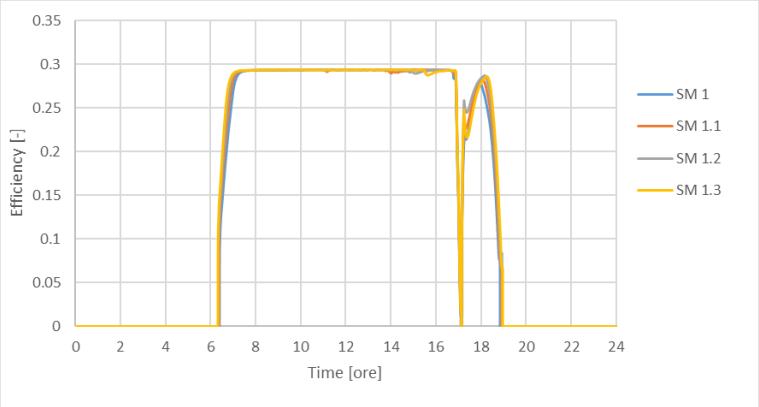

Figure 6.57: Cycle efficiency heliostats type 3.

6.4.8. Energy production and utilization factor

In this part will be illustrated the results of the energy production and the one of the utilization factor (UF). In table 6.7 are resumed the energy production results for the three kinds of heliostats for all solar multiple. As possible to observe increasing the SM increases the energy, but the best energy production is for the heliostats type 3, or rather the smallest kind that allows the production of higher energy amounts.

The heliostats type 3 in heliostats field of SM 1.3 has the heights energy productions.

SM	1	1.1	1.2	1.3
Type 1	0.90	0.94	0.99	1.03
Type 2	0.92	0.97	1.02	1.06
Type 3	0.94	1.00	1.04	1.08

Table 6.10: Annual energy production [MWh]

In the follow table 6.10 are shown the utilization factor results of all the configurations that are around the 10-20 %; as can possible to observe the best configuration is confirmed the SM 1.3 with heliostats type 3.

SM	1	1.1	1.2	1.3
Type 1	0.21	0.22	0.23	0.23
Type 2	0.21	0.22	0.23	0.24
Type 3	0.21	0.23	0.24	0.25

Table 6.11: Utilization factor [MWh]

The energy production results as well as the utilization factors, show that the best configuration is represented by SM 1.3 and the heliostats type 3. This configuration will be used for the comparison with commercial system Aora Tulip [107]

6.4.9. Comparison

As mentioned, in this part the results of the closed cycle, in term of systems dimension and energy production have been compared with Aora Tulip [107] referring the data, to the system installed on the "Plataforma Solar de Almeria".

The configuration with SM 1.3 and heliostats type 3 have been taken into account for the best performance offered, as shown in the past session. No economical data has been used in this comparison.

In table 6.9 are shown the data of both considered system with their main parameters.

	Units	AORA Tulip	Closed loop
Receiver height	m	1	1.8
Receiver width	m	1.1	3
Receiver area	m^2	1.1	5.4
Tower heigth	m	32	57
Mass flow rate	Kg/sec.	0.8	4.5
Outlet receiver temperature	° C	900-1000	800
Heliostat number	-	52	257
Nominal Thermal Power	kW	330	2200
Nominal Pressure	bar	4.5	22.5
Annual energy production	MWh	0.78	1.08

Table 6.12: Comparison of Tulip data with closed loop model results.

Keep in mind that a power plant of a peck power of 500 kW (this is the power of the pressurized cycle) employing only air as HTF with a hybrid solar power plant have been compared. From the comparison it is possible to note that the plant using the mass flow control system produces 35% of more energy respect the hybrid one. In this analysis the same engine micro gas turbine has been considered, while the receiver dimension as well as the heliostat size have been optimized in order to increase the energy production.

6.5.Conclusion

In this chapter a dynamic model of the solar power plant employing the mass flow control system has been analysed. In particular, a numerical model in Matlab/Simulink has been implemented in order to estimate the behaviour of the plant under transient conditions.

First of all, an optimization of the heliostat field has been performed for three different heliostats size and four solar multiples.

The results, obtained employing SolarPilot, in term of optical matrix efficiency and solar field dimension, have been used in the numerical model.

In the model, two different adjustment heliostat logical have been implemented, in order to control the average receiver incident flux and overshoot of TIT, both to the mass flow control system.

The results show as the best configuration has SM 1.3 with small size heliostats; this configuration has been compared with a commercial system.

From the comparison it was possible to observe how the plant with mass flow control system produces, in best configuration, 35% of energy surplus without fuel employing respect the hybrid commercial plant, keeping constant the cycle efficiency under all solar load conditions.

Conclusions and outlook

In this work, it has been conducted the study of an unfired closed Joule-Brayton cycle employing a novel mass flow control system.

This type of adjustment is able to control the turbine inlet temperature (TIT) of the engine gas turbine, when the direct normal irradiance changes.

Because the characteristic temperatures of the cycle does not change as well as the volumetric flow and the speed triangles, the TIT control allows to adjust the electrical power production, without lowering the efficiency.

Based on the state of art regarding the concentrating solar systems, nowadays, no system is developed in such way. Many analyses treat the use of the supercritical carbon dioxide (SCO_2) [42, 74] as HTF for the closed cycle, or others that concern the hybridization, employing fuel [33, 36, 59, 102] in an open cycle.

Several simulations, in this work, were performed employing available software, as Thermoflex for the yearly plants steady state simulation, Matlab/Simulink for the dynamic plants behaviour, Win Delsol and Solar pilot for the solar field (heliostats and receivers) design.

The results, oriented to the observation of the operating temperature and of the overall efficiency, are influenced by the engine main parameters, for example, the polytropic efficiency or the size parameters, as described in chapter 2.

The peak power of the gas turbine engine changes, with the mass flow rate imposed by the control system, depending on pressure ratio and receiver operating pressure.

The simulations performed for different sizes, at MW scale, show that the cycle efficiency is almost constant around 40%, under different load of solar radiation, in all analysed configuration.

The energy production is more consistent of around 9 %, the operational hours increasing up of about 220, and the average yearly efficiency is higher than 15%, for each plant configuration, comparing the closed cycle with the open

one, when the control of TIT is performed by IGV in an open cycle, as shown in chapter 3.

The design of the solar field is also influenced by the mass flow control system, and the results of the parametric analysis on the solar multiple shows that the SM 1.2 represents the optimum value in order to obtain a saving investment costs of 3.57 M$.

A selection on the innovative molten salts shows that Manganese-chloride ($KCl-MgCl_2$) is suitable for this kind of application. The economic analysis, performed by the LCoE method, shows as the best configuration could be SM 2.4 and 7 hours of storage, while the LCoE value could be 22.5 c$/kWh, as described in chapter 5.

An analysis on the dynamic performance of the cycle with mass flow control system in chapter 6 have been performed. A case of study of a micro gas turbine of a peak power of 100 kW has been considered. In particular, a parametric analysis on the heliostats size have been made, in order to select the best type, suitable to increase the efficiency and the energy production of the solar field.

The results show how the mass flow control system, interacts with the heliostats field adjustment, in order to control the flux on the receiver and the turbine inlet temperature. In addition the power of the gas turbine increases, becoming of 500 kW because the mass flow is increased, due to the pressurized cycle.

The results obtained with a commercial system [107] were compared; as expected, the energy production is higher respect to the hybrid plant while the overall efficiency keeps constant under all incident load, at about 30%.

In general, in this work several aspect regarding devices, for example, the engine gas turbine, heliostats field, solar receiver or heat exchanger, as well as financial issues, have been taken into account.

It has been a difficult task to analyse in detail the system, and it has not always been possible, but the goal of this work was to try to demonstrate the feasibility of a closed Brayton cycle, which uses air as a working fluid.

The use of air could be interesting and innovative in CSP systems with gas turbine applications for different reason:

- Closed cycle gas turbine (in CSPs) can achieve higher efficiency than the steam cycle at high temperature;
- The possibility of operating at higher pressure gives compact components and smaller plant footprint. Higher power-to-size ratio and reduced capital cost can then be achieved;
- Finally and not less important, is the concept that air is not flammable, at height pressure, therefore not dangerous, easy to manage respect other fluids (ex SCO_2) and totally free.

In this research it have been analysed a possibility of energy production without use of fuels. The commercialization stage is greatly faraway, and it is extremely important to analyse the technical issue about the engine, the receiver, the heat exchanger and to perform a deeper economic analysis, in order to evaluate a more accurate effective cost of electricity.

The next analysis step will regard the use of this kind of cycle, with new thermal storage system technology, in a smart/micro electric grid, to demonstrate the capability of the plant to follow the load electric demand curve.

In addition the feasibility of a bottom cycle (ex: ORC) or cogeneration system employing, will be analysed in order to increase the overall efficiency, energy production, or satisfy the heat demand curve.

Appendix

Appendix A

Input data set for calculation of the compression ratio

Input data set for calculation

Compressor adiabatic efficiency = 0.88

Expansion adiabatic efficiency = 0.86

$\frac{k-1}{k} = 0.27$ Compression

$\frac{k-1}{k} = 0.265$ Expansion

R = regeneration level

T3 = 800 °C

T1 =35 °C

Appendix B

Optical matrix heliostat type 3 SM 1

	Zenit [°]									
Azimut [°]	-	0.5	7	15	30	45	60	75	85	90
	0	0.733	0.71	0.677	0.608	0.506	0.386	0.282	0.108	0.036
	30	0.734	0.714	0.686	0.618	0.528	0.43	0.304	0.09	0.034
	60	0.735	0.721	0.704	0.656	0.596	0.526	0.361	0.07	0.032
	90	0.735	0.734	0.728	0.71	0.68	0.609	0.418	0.061	0.039
	120	0.736	0.745	0.752	0.758	0.747	0.692	0.455	0.065	0.052
	150	0.736	0.753	0.769	0.789	0.794	0.757	0.494	0.094	0.078
	180	0.737	0.756	0.776	0.801	0.811	0.793	0.508	0.109	0.092
	210	0.737	0.753	0.77	0.79	0.795	0.76	0.496	0.093	0.078
	240	0.736	0.746	0.755	0.76	0.751	0.696	0.459	0.064	0.052
	270	0.736	0.734	0.731	0.713	0.685	0.614	0.422	0.061	0.04
	300	0.735	0.723	0.705	0.659	0.601	0.53	0.367	0.069	0.032
	330	0.734	0.714	0.686	0.62	0.531	0.433	0.309	0.091	0.036

Optical matrix heliostats type 3 SM 1.1

	Zenit [°]									
Azimut [°]	-	0.5	7	15	30	45	60	75	85	90
	0	0.731	0.708	0.676	0.605	0.504	0.384	0.28	0.106	0.036
	30	0.731	0.711	0.684	0.618	0.526	0.427	0.302	0.09	0.034
	60	0.731	0.719	0.701	0.653	0.593	0.522	0.359	0.07	0.032
	90	0.733	0.731	0.726	0.708	0.679	0.607	0.418	0.059	0.037
	120	0.733	0.743	0.75	0.755	0.747	0.689	0.454	0.063	0.051
	150	0.733	0.751	0.768	0.787	0.791	0.755	0.492	0.087	0.074
	180	0.734	0.754	0.774	0.798	0.808	0.79	0.505	0.104	0.089
	210	0.734	0.751	0.768	0.788	0.793	0.758	0.492	0.088	0.073
	240	0.733	0.743	0.752	0.758	0.749	0.695	0.457	0.065	0.051
	270	0.733	0.732	0.727	0.711	0.682	0.613	0.422	0.061	0.04
	300	0.732	0.72	0.703	0.655	0.598	0.527	0.365	0.068	0.031
	330	0.731	0.712	0.683	0.618	0.529	0.431	0.307	0.088	0.032

Optical matrix heliostats type 3 SM 1.2

	Zenit [°]									
Azimut [°]	-	0.5	7	15	30	45	60	75	85	90
	0	0.728	0.706	0.673	0.602	0.495	0.376	0.274	0.1	0.033
	30	0.729	0.708	0.68	0.612	0.518	0.419	0.293	0.084	0.031
	60	0.729	0.717	0.698	0.648	0.585	0.518	0.356	0.068	0.029
	90	0.73	0.729	0.723	0.703	0.673	0.607	0.415	0.058	0.032
	120	0.73	0.74	0.747	0.751	0.743	0.69	0.45	0.065	0.052
	150	0.732	0.748	0.764	0.783	0.788	0.751	0.486	0.081	0.067
	180	0.732	0.751	0.77	0.795	0.804	0.784	0.501	0.097	0.084
	210	0.731	0.749	0.765	0.784	0.789	0.753	0.488	0.083	0.07
	240	0.73	0.741	0.748	0.752	0.746	0.694	0.452	0.064	0.052
	270	0.73	0.729	0.724	0.705	0.677	0.612	0.417	0.058	0.033
	300	0.729	0.718	0.699	0.649	0.59	0.52	0.36	0.068	0.03
	330	0.728	0.709	0.68	0.613	0.52	0.423	0.296	0.083	0.031

Optical matrix heliostats type 3 SM 1.3

	Zenit [°]									
Azimut [°]	-	0.5	7	15	30	45	60	75	85	90
	0	0.727	0.704	0.672	0.601	0.5	0.381	0.278	0.104	0.034
	30	0.727	0.707	0.678	0.614	0.522	0.423	0.296	0.085	0.029
	60	0.727	0.714	0.696	0.648	0.586	0.516	0.355	0.071	0.031
	90	0.728	0.726	0.721	0.701	0.672	0.606	0.414	0.056	0.03
	120	0.729	0.738	0.745	0.749	0.742	0.688	0.452	0.065	0.053
	150	0.729	0.746	0.762	0.782	0.786	0.75	0.487	0.078	0.065
	180	0.73	0.75	0.769	0.794	0.803	0.783	0.501	0.093	0.081
	210	0.73	0.747	0.763	0.784	0.788	0.754	0.489	0.078	0.066
	240	0.729	0.738	0.746	0.753	0.745	0.692	0.455	0.064	0.051
	270	0.728	0.727	0.723	0.705	0.679	0.612	0.419	0.057	0.032
	300	0.727	0.716	0.698	0.652	0.593	0.523	0.363	0.068	0.03
	330	0.726	0.708	0.68	0.614	0.524	0.427	0.3	0.084	0.03

Appendix C

Optical matrix heliostats type 2 SM 1, SM1.1

	Zenit [°]									
Azimut [°]	-	0.5	7	15	30	45	60	75	85	90
	0	0.728	0.7	0.662	0.564	0.442	0.317	0.176	0.076	0.036
	30	0.729	0.703	0.667	0.582	0.477	0.362	0.217	0.086	0.042
	60	0.73	0.713	0.687	0.63	0.556	0.457	0.294	0.094	0.049
	90	0.731	0.728	0.717	0.696	0.66	0.571	0.391	0.119	0.062
	120	0.731	0.738	0.747	0.75	0.745	0.662	0.46	0.136	0.102
	150	0.733	0.751	0.768	0.789	0.795	0.729	0.521	0.197	0.172
	180	0.732	0.753	0.775	0.802	0.812	0.75	0.548	0.196	0.168
	210	0.731	0.749	0.768	0.787	0.794	0.731	0.525	0.199	0.175
	240	0.732	0.74	0.748	0.752	0.745	0.666	0.466	0.14	0.104
	270	0.729	0.727	0.721	0.699	0.661	0.574	0.393	0.119	0.063
	300	0.73	0.714	0.688	0.634	0.562	0.462	0.297	0.093	0.049
	330	0.729	0.703	0.67	0.583	0.479	0.363	0.219	0.087	0.042

	Zenit [°]									
Azimut [°]	-	0.5	7	15	30	45	60	75	85	90
	0	0.726	0.696	0.654	0.551	0.429	0.308	0.177	0.069	0.032
	30	0.726	0.7	0.661	0.57	0.455	0.349	0.212	0.082	0.04
	60	0.727	0.708	0.684	0.619	0.54	0.442	0.28	0.086	0.045
	90	0.728	0.723	0.714	0.687	0.648	0.554	0.378	0.11	0.053
	120	0.729	0.736	0.743	0.747	0.736	0.654	0.449	0.131	0.1
	150	0.731	0.748	0.765	0.786	0.791	0.723	0.515	0.185	0.16
	180	0.728	0.752	0.774	0.8	0.809	0.745	0.531	0.18	0.155
	210	0.73	0.747	0.766	0.788	0.794	0.725	0.515	0.186	0.159
	240	0.729	0.737	0.745	0.751	0.741	0.659	0.452	0.131	0.1
	270	0.727	0.724	0.716	0.693	0.655	0.561	0.379	0.114	0.055
	300	0.726	0.71	0.685	0.625	0.546	0.45	0.287	0.086	0.046
	330	0.725	0.699	0.665	0.571	0.462	0.355	0.217	0.082	0.039

Appendix C

Optical matrix heliostats type 2 SM 1.2, SM 1.3

	Zenit [°]									
Azimut [°]	-	0.5	7	15	30	45	60	75	85	90
	0	0.722	0.695	0.655	0.557	0.436	0.312	0.172	0.069	0.03
	30	0.723	0.697	0.662	0.575	0.466	0.355	0.21	0.08	0.037
	60	0.724	0.706	0.681	0.624	0.551	0.452	0.291	0.083	0.043
	90	0.725	0.721	0.712	0.689	0.652	0.567	0.388	0.103	0.059
	120	0.727	0.734	0.742	0.746	0.736	0.655	0.448	0.118	0.09
	150	0.726	0.744	0.762	0.783	0.789	0.717	0.503	0.175	0.151
	180	0.727	0.748	0.771	0.797	0.807	0.743	0.532	0.169	0.145
	210	0.728	0.744	0.764	0.785	0.787	0.722	0.508	0.18	0.156
	240	0.727	0.735	0.744	0.749	0.742	0.661	0.456	0.126	0.099
	270	0.725	0.721	0.715	0.693	0.658	0.572	0.394	0.111	0.066
	300	0.724	0.708	0.681	0.628	0.557	0.459	0.296	0.081	0.042
	330	0.723	0.698	0.662	0.576	0.47	0.359	0.214	0.078	0.034

	Zenit [°]									
Azimut [°]	-	0.5	7	15	30	45	60	75	85	90
	0	0.722	0.693	0.654	0.56	0.439	0.316	0.174	0.067	0.028
	30	0.723	0.697	0.661	0.575	0.468	0.357	0.212	0.077	0.033
	60	0.724	0.707	0.681	0.625	0.553	0.454	0.292	0.078	0.038
	90	0.724	0.721	0.714	0.689	0.653	0.57	0.387	0.107	0.058
	120	0.725	0.734	0.741	0.748	0.737	0.654	0.448	0.123	0.097
	150	0.726	0.743	0.761	0.782	0.786	0.714	0.496	0.166	0.143
	180	0.727	0.749	0.77	0.795	0.802	0.742	0.524	0.158	0.138
	210	0.725	0.744	0.762	0.782	0.787	0.715	0.498	0.165	0.142
	240	0.725	0.734	0.742	0.745	0.737	0.653	0.445	0.118	0.092
	270	0.724	0.721	0.713	0.691	0.654	0.57	0.389	0.109	0.057
	300	0.723	0.707	0.682	0.627	0.553	0.457	0.294	0.082	0.043
	330	0.723	0.696	0.66	0.573	0.469	0.357	0.212	0.076	0.033

Appendix D

Optical matrix heliostats type 1 SM 1, SM 1.1

	Zenit [°]									
Azimut [°]	-	0.5	7	15	30	45	60	75	85	90
	0	0.669	0.633	0.581	0.45	0.304	0.178	0.097	0.039	0.02
	30	0.671	0.641	0.592	0.475	0.342	0.218	0.116	0.04	0.022
	60	0.67	0.653	0.624	0.546	0.446	0.327	0.188	0.043	0.028
	90	0.672	0.67	0.665	0.634	0.574	0.47	0.305	0.074	0.044
	120	0.673	0.686	0.7	0.702	0.679	0.599	0.407	0.129	0.099
	150	0.674	0.698	0.718	0.739	0.74	0.689	0.484	0.194	0.16
	180	0.674	0.705	0.725	0.755	0.758	0.728	0.531	0.248	0.214
	210	0.673	0.699	0.721	0.741	0.742	0.691	0.483	0.194	0.16
	240	0.673	0.688	0.698	0.701	0.68	0.601	0.406	0.128	0.099
	270	0.672	0.67	0.663	0.636	0.576	0.474	0.308	0.077	0.045
	300	0.671	0.654	0.625	0.547	0.448	0.328	0.189	0.044	0.028
	330	0.671	0.638	0.592	0.476	0.343	0.22	0.116	0.039	0.022

	Zenit [°]									
Azimut [°]	-	0.5	7	15	30	45	60	75	85	90
	0	0.676	0.64	0.588	0.461	0.317	0.187	0.101	0.04	0.019
	30	0.678	0.648	0.599	0.485	0.351	0.224	0.118	0.04	0.022
	60	0.679	0.66	0.63	0.554	0.449	0.324	0.185	0.049	0.032
	90	0.68	0.678	0.669	0.638	0.574	0.467	0.297	0.073	0.041
	120	0.68	0.689	0.705	0.704	0.677	0.6	0.408	0.139	0.106
	150	0.681	0.705	0.725	0.744	0.743	0.694	0.493	0.21	0.172
	180	0.682	0.709	0.736	0.759	0.768	0.737	0.541	0.257	0.217
	210	0.683	0.707	0.726	0.743	0.75	0.698	0.495	0.203	0.169
	240	0.68	0.696	0.707	0.711	0.69	0.609	0.416	0.144	0.115
	270	0.679	0.68	0.675	0.646	0.586	0.483	0.312	0.076	0.045
	300	0.676	0.662	0.634	0.563	0.461	0.336	0.195	0.049	0.033
	330	0.677	0.647	0.6	0.489	0.357	0.229	0.121	0.043	0.025

Appendix D

Optical matrix heliostats type 1 SM 12, SM 1.3

	Zenit [°]									
Azimut [°]	-	0.5	7	15	30	45	60	75	85	90
	0	0.663	0.628	0.575	0.446	0.299	0.176	0.096	0.038	0.019
	30	0.665	0.634	0.585	0.47	0.336	0.216	0.114	0.037	0.02
	60	0.664	0.647	0.614	0.534	0.439	0.323	0.187	0.037	0.023
	90	0.667	0.662	0.654	0.623	0.566	0.469	0.3	0.069	0.038
	120	0.668	0.68	0.691	0.689	0.67	0.593	0.399	0.117	0.088
	150	0.67	0.691	0.714	0.731	0.737	0.683	0.481	0.192	0.16
	180	0.669	0.694	0.721	0.743	0.752	0.721	0.523	0.232	0.196
	210	0.668	0.692	0.713	0.731	0.73	0.68	0.477	0.192	0.16
	240	0.668	0.681	0.691	0.688	0.671	0.596	0.399	0.118	0.089
	270	0.667	0.662	0.655	0.623	0.568	0.469	0.302	0.069	0.038
	300	0.664	0.648	0.615	0.536	0.441	0.323	0.187	0.037	0.023
	330	0.663	0.631	0.584	0.469	0.336	0.216	0.114	0.037	0.02

	Zenit [°]									
Azimut [°]	-	0.5	7	15	30	45	60	75	85	90
	0	0.66	0.621	0.571	0.444	0.303	0.181	0.098	0.037	0.017
	30	0.66	0.629	0.578	0.462	0.335	0.216	0.112	0.034	0.016
	60	0.662	0.639	0.611	0.527	0.43	0.317	0.184	0.039	0.027
	90	0.662	0.657	0.649	0.614	0.554	0.455	0.291	0.062	0.028
	120	0.662	0.672	0.683	0.68	0.655	0.579	0.388	0.126	0.097
	150	0.663	0.685	0.705	0.725	0.723	0.672	0.464	0.171	0.14
	180	0.66	0.69	0.715	0.742	0.746	0.711	0.51	0.205	0.172
	210	0.664	0.688	0.709	0.728	0.727	0.675	0.469	0.179	0.143
	240	0.662	0.674	0.686	0.69	0.667	0.594	0.398	0.128	0.099
	270	0.661	0.659	0.653	0.621	0.565	0.472	0.299	0.063	0.03
	300	0.661	0.641	0.614	0.533	0.441	0.325	0.192	0.039	0.027
	330	0.658	0.629	0.581	0.469	0.342	0.222	0.115	0.034	0.016

Appendix E

Temperature [K]	Pressure [MPa]									
	0.001	0.005	0.01	0.02	0.03	0.04	0.05	0.06	0.07	0.08
150	0.02323	0.11616	0.23239	0.46506	0.69802	0.93127	1.16480	1.39861	1.63272	1.86711
160	0.02177	0.10889	0.21784	0.43590	0.65418	0.87267	1.09139	1.31032	1.52947	1.74884
170	0.02049	0.10248	0.20501	0.41019	0.61553	0.82105	1.02673	1.23259	1.43861	1.64480
180	0.01935	0.09679	0.19361	0.38734	0.58121	0.77522	0.96935	1.16362	1.35801	1.55255
190	0.01834	0.09169	0.18341	0.36692	0.55053	0.73425	0.91807	1.10199	1.28602	1.47016
200	0.01742	0.08710	0.17423	0.34854	0.52293	0.69740	0.87196	1.04660	1.22132	1.39613
250	0.01394	0.06968	0.13936	0.27875	0.41817	0.55761	0.69708	0.83657	0.97609	1.11564
300	0.01161	0.05806	0.11613	0.23226	0.34840	0.46455	0.58071	0.69687	0.81304	0.92922
350	0.00995	0.04977	0.09953	0.19907	0.29860	0.39814	0.49767	0.59721	0.69674	0.79627
400	0.00871	0.04355	0.08709	0.17418	0.26127	0.34835	0.43543	0.52250	0.60957	0.69664
450	0.00774	0.03871	0.07741	0.15482	0.23223	0.30963	0.38703	0.46442	0.54181	0.61919
500	0.00697	0.03484	0.06967	0.13934	0.20900	0.27866	0.34832	0.41797	0.48761	0.55725
550	0.00633	0.03167	0.06334	0.12667	0.19000	0.25333	0.31665	0.37996	0.44327	0.50658
600	0.00581	0.02903	0.05806	0.11612	0.17417	0.23221	0.29026	0.34830	0.40633	0.46436
650	0.00536	0.02680	0.05359	0.10718	0.16077	0.21435	0.26793	0.32150	0.37507	0.42864
700	0.00498	0.02488	0.04977	0.09953	0.14929	0.19904	0.24879	0.29854	0.34828	0.39802
750	0.00464	0.02322	0.04645	0.09289	0.13933	0.18577	0.23221	0.27864	0.32507	0.37149
800	0.00435	0.02177	0.04355	0.08709	0.13063	0.17416	0.21769	0.26122	0.30475	0.34828
850	0.00410	0.02049	0.04098	0.08196	0.12294	0.16392	0.20489	0.24586	0.28683	0.32779
900	0.00387	0.01935	0.03871	0.07741	0.11611	0.15481	0.19351	0.23220	0.27089	0.30958
950	0.00367	0.01834	0.03667	0.07334	0.11000	0.14666	0.18332	0.21998	0.25664	0.29329
1000	0.00348	0.01742	0.03484	0.06967	0.10450	0.13933	0.17416	0.20898	0.24381	0.27863
1500	0.00232	0.01161	0.02322	0.04645	0.06967	0.09289	0.11611	0.13933	0.16255	0.18576
2000	0.00174	0.00871	0.01742	0.03484	0.05225	0.06967	0.08709	0.10450	0.12192	0.13933

Temperature [K]	Pressure [MPa]									
	0.09	0.1	0.12	0.15	0.2	0.5	1	2	5	10
150	2.1018	2.3368	2.8076	3.5160	4.7026	11.9835	24.7879	53.4754	188.2025	488.0887
160	1.9684	2.1883	2.6285	3.2907	4.3987	11.1677	22.9409	48.6188	151.4114	397.0863
170	1.8512	2.0577	2.4713	3.0929	4.1325	10.4621	21.3798	44.7465	130.7883	323.5334
180	1.7472	1.9420	2.3320	2.9180	3.8973	9.8446	20.0373	41.5517	116.7444	273.4041
190	1.6544	1.8387	2.2077	2.7620	3.6879	9.2990	18.8669	38.8510	106.2480	239.0637
200	1.5710	1.7460	2.0962	2.6221	3.5002	8.8128	17.8353	36.5262	97.9572	214.1443
250	1.2552	1.3948	1.6741	2.0932	2.7922	7.0001	14.0636	28.3694	72.4959	148.0612
300	1.0454	1.1616	1.3940	1.7427	2.3239	5.8149	11.6455	23.3452	58.6036	116.9333
350	0.8958	0.9953	1.1944	1.4930	1.9906	4.9762	9.9505	19.8878	49.5223	97.8282
400	0.7837	0.8708	1.0449	1.3060	1.7412	4.3506	8.6923	17.3462	43.0204	84.5863
450	0.6966	0.7739	0.9287	1.1608	1.5475	3.8654	7.7196	15.3924	38.0967	74.7409
500	0.6269	0.6965	0.8358	1.0446	1.3926	3.4780	6.9443	13.8406	34.2212	67.0764
550	0.5699	0.6332	0.7598	0.9496	1.2659	3.1614	6.3115	12.5767	31.0826	60.9114
600	0.5224	0.5804	0.6964	0.8705	1.1604	2.8978	5.7849	11.5266	28.4843	55.8293
650	0.4822	0.5358	0.6429	0.8035	1.0711	2.6749	5.3398	10.6397	26.2952	51.5589
700	0.4478	0.4975	0.5969	0.7461	0.9946	2.4838	4.9586	9.8806	24.4240	47.9146
750	0.4179	0.4643	0.5572	0.6964	0.9283	2.3183	4.6283	9.2232	22.8052	44.7645
800	0.3918	0.4353	0.5223	0.6529	0.8703	2.1735	4.3394	8.6482	21.3902	42.0123
850	0.3688	0.4097	0.4916	0.6145	0.8191	2.0458	4.0845	8.1411	20.1424	39.5856
900	0.3483	0.3870	0.4643	0.5803	0.7736	1.9322	3.8580	7.6904	19.0335	37.4288
950	0.3299	0.3666	0.4399	0.5498	0.7329	1.8306	3.6553	7.2871	18.0414	35.4984
1000	0.3134	0.3483	0.4179	0.5223	0.6963	1.7392	3.4729	6.9242	17.1483	33.7602
1500	0.2090	0.2322	0.2786	0.3483	0.4643	1.1599	2.3172	4.6238	11.4808	22.7013
2000	0.1567	0.1742	0.2090	0.2612	0.3483	0.8702	1.7388	3.4716	8.6335	17.1168

References

[1] A. Rabl, *Comparison of solar concentrators*, Solar Energy, 1976; Volume 88, Issue 2: pag. 93-111.

[2] K. Lovegrove, W.Stein, *Fundamental Principles of Concentrated Solar Power*,Woodhead.

[3] Romero-Alvarez, *Concentrating Solar Thermal Power*, Handbook of Energy Efficiency and Renewable Energy, Plataforma Solar de Almeria, CIEMAT, 2007.

[4] C. E. Kennedy, H. Price, *Progress in Development of High-Temperature Solarselective coating*, International Solar Energy Conference, 2005; pag. 749-755.

[5] R. Pitz-Paal, *High temperature solar concentrators*, Solar Energy Conversion and Photoenergy system – Volume I, 2007.

[6] E. Zarza, *DISS Report Summary*, CORDIS, 2004, http://cordis.europa.eu/result /rcn/33558_en.html).

[7] ENEA Working Group. *Solar thermal energy production: guidelines and future programmes of ENEA*. ENEA Report.

[8] A. Kalogirou, G. Panayiotou, *Evalutation of a parabolic trough collector performance*, Archimedes Solar Energy Laboratory, 2004

[9] D. Mills, *Advances in solar thermal electricity technology*, Solar Energy, 2004;Volume 76, Issues 1-3: pag. 19-31

[10] IRENA, *Renewable Power Generation Costs in 2014*.

[11] E. F. Camacho, M. Berenguel, F. R. Rubio et al., *Control of solar Energy Systems*, Advances in Industrial Control, Springer, 2012.

[12] W. B. Stine, M. Geyer, Power from the Sun,2001,(http://www.powerfromthesun.net).

[13] F. Téllez, M. Burisch, C. Villasante et al., *State of the art in Heliostats and definition of Specifications*, STAGE-STE, 2014.

[14] P. Falcone, *A handbook for solar central receiver design*, SANDIA National Laboratories, 1986.

[15] M. E. Elayeb, R. A. Haman, F. F. Siala et al., *Calculation of the blocking factor in heliostat fields*, Energy Procedia, 2014; Volume 57: pag. 291-300.

[16] J. Ballestrin, A. Marzo, *Solar radiation attenuation in solar tower plants*, Solar Energy, 2012; Volume 86, Issue 1.

[17] L.L. Vant-Hull, *Central tower concentrating solar power (CSP) systems*, Concentrating Solar Power Technology, Woodhead Publishing, 2012; pag. 240-283.

[18] Z. Guan, S. Yu, K. Hooman et al., *Dust characterization for solar collector deposition and cleaning in a concentrating solar power plant*, 2015.

[19] Y. Zhou, Y. Zhau, *Heliostat field layout design for solar tower power plant based on GPU*, 19th IFAC World Congress Proceeedings, 2014.

[20] Battleson, K.W*Solar, Power Tower Design Guide: Solar Thermal Central Receiver Power Systems, A Source of Electricity and/or Process Heat*,Sandia National Labs Report SAND81-8005, April 1981.

[21] Vant-Hull LL. Izygon ME. *Guideline to central receiver system - field optimization*. In: Goswami Y, editor. Advances in Solar Energy 15, American Solar Energy Society, 2003.

[22] J. Jorgenson, P. Denholm, M. Mehos et al., *Estimating the performance and economic value of multiple concentrating solar power technologies in a production cost model*, NREL, 2014.

[23] J. E. Pachecho, H. E. Reilly, G. J. Kolb et al., *Final test and evaluation results from Solar Two project*, SANDIA National Laboratories, 2001.

[24] C. K. Ho, B. D. Iverson, *Review of high temperature central receiver designs for concentrating solar power*, Renewable and Sustainable Energy Reviews, 2014; Volume 29: pag. 835-846.

[25] M. Yang, X. Yang, J. Ding et al., *Heat transfer enhancement and performance of the molten salt receiver of a solar power tower*, Applied Energy, 2010; Volume: 87, Issue 9: pag. 2808-2811.

[26] M. Lubkoll, T. W. Von Backström, D. G. Kröger et al., *Survey on pressurized air receiver development*, STERG, 2012.

[27] G. Lozza, *Turbine a gas e cicli combinati* – III edizione, Progetto Leonardo,2006.

[28] V. Casamassima, G. A. Guagliardi, *Modello matematico di un impianto solare a concentrazione ibrido con turbina a gas e simulazione di transitori normali e di emergenza*, Ricerca sul Sitema Energetico (RSE), 2013.

[29] A. L. Ávila-Marín, *Volumetric receivers in solar thermal power plants with central receiver system technology*, Solar Energy, 2011; Volume 85, Issue 5:pag. 891-910.

[30] V.Siva Reddy, S.C.Kaushik, K.R.Ranjan, S.K.Tyagi. *State-of-the-art of solar thermal power plants—A review.* Renewable and Sustainable Energy Reviews. Volume 27, November 2013, Pages 258-273.

[31] Commonwealth Scientific Industrial Research Organisation Solar Air Turbine Project Final report: project results. Principal Research Scientist , CSIRO Energy Transformed Flagship 29 July 2014.

[32] Steven A. Wright, Ross F. Radel, Milton E. Vernon, Gary E. Rochau, and Paul S. Pickard. *Operation and Analysis of a Supercritical CO_2 Brayton Cycle.* SANDIA REPORT, SAND2010-0171, September 2010.

[33] European Commission. *Solgate: Solar hybrid gas turbine electric power system, Final Publishable Report,* Directorate-General for Research, Brussels. (2005).

[34] P. Požívil, V. Aga, A. Zagorskiy, A. Steinfeld. *A pressurized air receiver for solar- driven gas turbines,* SolarPACES 2013 Volume 49 pag. 498 – 503 Energy Procedia 2014.

[35] Kopilovsky K. *AORA's tulips: solar energy in bloom*. Earth Times 2012; Available from: http://www.earthtimes.org/energy/aora-solar- energy-tulips/1997/[cited 27 June 2013].

[36] M. Quero, R. Korzynietz. M. Ebert, AA. Jiménez, A. del Río, JA. Brioso. Solugas – *Operation experience of the first solar hybrid gas turbine system at MW scale*. SolarPACES 2013 Energy Procedia Volume 49, 2014, Pages 1820-183.

[37] https://www.promes.cnrs.fr/index.php?page=themis

[38] M. M. Rahman, Thamir K. Ibrahim and Ahmed N. Abdalla, *Thermodynamic performance analysis of gas-turbine power-plant.* International Journal of the Physical Sciences Vol. 6(14), pp. 3539-3550, 18 July, 2011, DOI: 10.5897/IJPS11.272 ISSN 1992 – 1950.

[39] Dhyia Aidroos Baharoon, Hasimah Abdul Rahman, Wan Zaidi Wan, Omar Saeed Obaid Fadhl. *Historical development of concentrating solar power technologies to generate clean electricity efficiently – A review* Renewable and Sustainable Energy Reviews Volume 41, January 2015, Pages 996-1027.

[40] K Lovegrove,W Stein, *Concentrating Solar Power Technology: Principles, Developments and Applications,* 19th October 2012.

[41] Moreno T.S., et al. *Solar resource assessment in Seville, Spain, statistical characterisation of solar radiation at different time resolutions*, Solar Energy, Vol. 132, pp. 430-441. (2016)

[42] Ma Z, Turchi C., *Advanced supercritical carbon dioxide power cycle configurations for use in concentrating solar power systems*. 2011, 24-5.

[43] Kistler B.L. *A user's manual for DELSOL3: A computer code for calculating the optical performance and optimal system design for solar thermal central receiver plants,* Sandia Report (1986).

[44] THERMOFLEX *Fully-Flexible Heat Balance Engineering Software*. Thermo flow Inc. 2 Willow Street, Suite 100, Southborough, MA 01745-1020, USA. (2016).

[45] Blanco M.J., Santigosa L.R. (2017). Next generation of liquid metal and other high-performance receiver designs for concentrating solar thermal (CST) central tower systems, *Advanced in Concentrating Solar Thermal Research and Technology,* 1st Edition, Amsterdam, Boston, Heidelberg, London, New York, Oxford, Paris, San Diego, San Francisco, Singapore, Sydney, Tokyo, Elsevier, Vol. 7, pp.132-133.

[46] Heller P., Pfänder M., Denk T., et al. *Test and evaluation of a solar powered gas turbine system*, Solar Energy, Vol. 80, pp. 1225-1230. (2006).

[47] Guo S., Liu D.Y.,Wang F., Zhang Y.M. (2009). Power and energy engineering conference, APPEEC 2009, Asia-Pacific. DOI: 10.1109/APPEEC.2009.4918625

[48] Irena(International Renewable Energy Agency*)-"Summary for policy markers: Renewable power Generation cost"*-Novembre, 2012.

[49] Irena(International Renewable Energy Agency)-"*Renewable energy thechnologies: cost analysis series*¬-Volume 1: Power Sector-Concentrating Solar Power"-June, 2012.

[50] J. Spelling, B. Laumert, T. Fransoon-*Advanced hybrid solar tower combined-cycle power plants*-Energy Procedia, SolarPACES 2013.

[51] Craig S. Turchi, Garivin A. Heath, *Molten salt power tower cost model for the system advisor model (SAM),* NREL (National Renewable Energy Laboraty), February 2013.

[52] Gregory J. Kolb, Clifford K. Ho, Thomas R. Mancini, Jesse A. Gary, *Power tower technology roadmap and cost reduction plan,* Sandia report, Aprile 2011.

[53] Irena (International Renewable Energy Agency), *Renewable power generation cost in 2014*, January 2015.

[54] Robert Pitz-Pall, Jurgen Dersch, Barbara Milow, *European concentrated solar thermal road-mapping,* Report ECOSTAR, 2003.

[55] D.F. Williams. *Assessment of candidate molten salt coolants for the ngnp/nhi heat-transfer loop*. Technical report, Oak Ridge National Laboratory, Tennessee, 2006.

[56] K. Nithyanandam and R. Pitchumani. *Cost and performance analysis of concentrating solar power systems with integrated latent thermal energy storage*. Energy, 64(0):793 – 810, 2014.

[57] R. Williams, D. F., Toth L. M., Clarno K. T.,*Assessment of candidate molten salt coolants for the Advanced High-Temperature Reactor (AHTR),* ORNL/TM-2006/12 (2006).

[58] Harin Ullal and Craig Turchi, NREL, Matthieu Jonemann Halotechnics, Inc. Emeryville, California, *Advanced Thermal Storage System with Novel Molten Salt*. NREL/SR-5200-58595, May 2013.

[59] B. Grangea, C. Daleta, Q. Falcoz, F. Siros, A. Ferrière, *Simulation of a Hybrid Solar Gas-turbine Cycle with Storage Integration*, in SolarPACES 2013 International Conference. (2014).

[60] C. K. Ho, G.J. Kolb, C. Turchi and M. Mehos,"Current and Future Costs for Parabolic Trough and Power Tower Systems in the US Market" (SolarPACES 2010), September 2010.

[61] Craig S. Turchi, Garivin A. Heath, *Molten salt power tower cost model for the system advisor model (SAM)*, NREL (National Renewable Energy Laboratory). February 2013.

[62] P. Schwarzbözl, R.Buck, C.Sugarmen,A Ring, Ma.J. Marcos Crespoc, P.Altweggd and J. Enrilee, *Solar gas turbine systems: Design, cost and perspectives,* Solar Energy Volume 80, Issue 10, October 2006, Pages 1231-1240

[63] International Renewable Energy Agency, *Renewable energy technologies: cost analysis series*, Volume 1: Power Sector Issue 2/5 Concentrating Solar Power.June, 2012.

[64] R. Serrano-Lópeza, J. Fraderaa, S. Cuesta-Lópeza, *Molten salts database for energy applications*, Chemical Engineering & Processing: Process Intensification, pp. 87-102 2013.

[65] C. F. Bonilla, *Comparison of Coolants*, in Nuclear Engineering Handbook, H. Etherington editor, Sect. 9-3, Chap. 6.5, pp. 9–90 (1958).

[66] J. P. Sanders, *A Review of Possible Choices for Secondary Coolants for Molten Salt Reactors*, ORNL CF-71-8-10, Oak Ridge National Laboratory, Oak Ridge, TN 1971.

[67] J. H. DeVan and R. B. Evans III, *Corrosion Behavior of Reactor Materials in Fluoride Salt Mixtures*, ORNL/TM-328, Oak Ridge National Laboratory, Oak Ridge, TN ,1962.

[68] K. Cornwell, *The Thermal Conductivity of Molten Salts*, Journal of Physics D: Applied Physics 4, pp. 441–45 ,1971.

[69] S. Kuravi, J. Trahan, D. Goswami, M. Rahman, and E. Stefanakos, *Thermal energy storage technologies and systems for concentrating solar power plants,* Progress in Energy and Combustion Science, 2013.

[70] M. Dunham and B. Iverson. *High-efficiency thermodynamic power cycles for concentrated solar power systems*. Renewable and Sustainable Energy Reviews, 2014.

[71] United Nations, *World Population Prospects The 2015 Revision: Key Findings And Advanced Tables*, 2015

[72] BP *Statistical Review of World Energy*, 64th edition 2015, bp.com/statisticalreview

[73] United Nations Framework Convention on Climate Change. *The Kyoto protocol mechanisms*. International emissions trading clean development mechanism joint implementation.

[74] Chacartegui R, Muñoz de Escalona JM, Sánchez D, Monje B, Sánchez T Alternative cycles based on carbon dioxide for central receiver solar power plants. Appl Therm Eng 2011;31:872-9.

[75] S. Arezki , M. Boudour. *Solutions to the instability problem of the DC input voltages of neutral point clamping multilevel inverter in photovoltaic chain connected to the network,* 2012 2nd International Symposium On Environment Friendly Energies And Applications , September 2012.

[76] V. Marinelli, M. A. Cucumo, G.Oliveti, *Ingegneria Solare Principi ed applicazioni* ISBN 8837107298 Pitagora editors January 1994.

[77] Solar Millennium, *Solar millennium AG annual Report* 2009/2010.

[78] Stoffel, T. ; Renne, D. ; Myers, D. ; Wilcox, S. ; Sengupta, M. ; George, R. ; Turchi, *C. . Concentrating Solar Power: Best Practices Handbook for the Collection and Use of Solar Resource Data (CSP).* National Renewable Energy Lab. (NREL), Golden, CO (United States) 2010.

[79] U.Desideri,F.Zepparelli,V.Morettini,E.Garroni. *Comparative analysis of concentrating solar power and photovoltaic technologies: Technical and environmental evaluations.* Applied Energy Volume 102, , Pages 765-784 February 2013.

[80] M. Liu, N.H.S. Tay, S. Bell, M. Belusko, R. Jacob, G. Will, W. Saman, F. Bruno, *Review on concentrating solar power plants and new developments in high temperature thermal energy storage technologies*, Renewable and Sustainable Energy Reviews 53, 1411–1432, 2016.

[81] S. Kuravi, J. Trahan, D.Y. Goswami, M.M. Rahman, E.K. Stefanakos, *Thermal energy storage technologies and systems for concentrating solar power plants*, Progress in Energy and Combustion Science 39, 285 – 319, 2013.

[82] IRENA, *Renewable power generation cost in 2014*, 2015.

[83] D.Y. Goswami, F. Kreith, *Energy Efficiency and renewable energy handbook*, Taylor & Francis Group, 2016.

[84] M.J.Santos,R.P.Merchán, A.Medina, A. Calvo Hernández. *Seasonal thermodynamic prediction of the performance of a hybrid solar gas-turbine power plant*. Energy Conversion and Management , Volume 115, Pages 89-1021 May 2016.

[85] R.Korzynietz, J.A.Brioso, .delR ío, M.Quero, M.Gallas, R.Uhlig, M.Ebert, R.Buck, D.Teraji, *Solugas – Comprehensive analysis of the solar hybrid Brayton plant*. Solar Energy Volume 135, Pages 578-589 October 2016.

[86] K. Kitzmiller ,F. Miller, *Effect of Variable Guide Vanes and Natural Gas Hybridization for Accommodating Fluctuations in Solar Input to a Gas Turbine*, ASME 2011 Turbo Expo: Turbine Technical Conference and Exposition, Volume 4, pp. 61-74, June 6–10, 2011.

[87] P.Viebahna, Y. Lechon, F. Triebc, *The potential role of concentrated solar power (CSP) in Africa and Europe—A dynamic assessment of technology development, cost development and life cycle inventories until 2050*. Energy Policy Volume 39, Issue 8, , Pages 4420-4430, August 2011.

[88] C. K. Ho, *Software and Codes for analysis of concentrating solar power technologies*, SANDIA National Laboratories, 2008.

[89] W Wang, L Chen, F Sun, C Wu , *Efficiency optimization of an irreversible closed intercooled regenerated gas-turbine cycle* , Proceedings of the Institution of Mechanical Engineers, Part A: Journal of Power and Energy, Volume: 220 issue: 6, page(s): 551-558 Issue published: January 1, 2006.

[90] J.Coventry, J.Pye, *Heliostat Cost Reduction – Where to Now?* , Energy Procedia Volume 49, Pages 60-70, 2014.

[91] Gregory J. Kolb, Scott A. Jones, Matthew W. Donnelly, David Gorman, Robert Thomas, Roger Davenport, and Ron Lumia. *Heliostat Cost Reduction Study*, SANDIA REPORT SAND2007-3293 June 2007.

[92] Schell S. Design and evaluation of esolar's heliostat fields. Solar Energy;85:614-619, 2011

[93] Abengoa Solar. Annual Report, 2009.

[94] Koretz B. Flexible Assembly Solar Technology. In: *Sunshot CSP Program Review 2013*. Phoenix, Arizona, 2013.

[95] Gould WR. *SolarReserve's 565 MWt molten salt power towers*. In: 17th International SolarPACES Symposium. Granada. 2011

[96] Lata J, Alcalde S, Fernandez D, Lekube X. *First surrounding field of heliostats in the world for commercial solar power plants - Gemasolar*. 16th International SolarPACES Symposium. Perpignan 2010.

[97] Abengoa Solar. *Advanced baseload molten salt tower. In: Sunshot CSP program review*. Phoenix, Arizona. 2013.

[98] Tyner CE. *eSolar's modular, scalable molten salt power tower reference plant design*. 19th annual SolarPACES symposium. Las Vegas 2013

[99] G. Xiao, T. Yang, H. Liu, D. Ni, M.L. Ferrari, M. Li, Z. Luo, K. Cen, M. Ni, *Recuperators for micro gas turbines: A review*, Applied Energy 197, 83–99, 2017.

[100] J. Karni, A. Kribus, P. Doron, R. Rubin, A. Fiterman and D. Sagie, The DIAPR: A High-Pressure, High-Temperature Solar Receiver. Journal of Solar Energy Engineering Volume 119 Issue 1 pp. 74-78 ,Feb 01, 1997.

[101] P.Požívil, V.Agab, A .Zagorskiy, A.Steinfeld, *A Pressurized Air Receiver for Solar-driven Gas Turbines* Energy Procedia Volume 49, Pages 498-503, 2014.

[102] Amsbeck L, Buck R, Heller P, Jedamski J, Uhlig R. *Development of a tube receiver for a solar-hybrid microturbine system*. In: Proceedings of the 14th Biennial CSP SolarPACES Symposium 2008.

[103] A.del Río, R.Korzynietz, J.A.Brioso, M.Gallas, I.Ordóñez, M.QueroaC.Díaz. *Soltrec – Pressurized Volumetric Solar Air Receiver Technology* , Energy Procedia Volume 69, Pages 360-368 ,May 2015.

[104] M.A. Rosa do Nascimento, L. de Oliveira Rodrigues, E. Cruz dos Santos, E.E. Batista Gomes, F. L. Goulart Dias, E. I. Gutiérrez Velásques and R. A. Miranda Carrillo. *Progress in Gas Turbine Performance", Chapter 5- Micro Gas Turbine Engine: A Review*. Book edited by Ernesto Benini, ISBN 978-953-51-1166-5, Published: June 19, 2013.

[105] H. Saito, J. Latcovich, M. Fusselbaugh, M.Dinets, K.Hattori, N. Sakaki. Microgas Turbine, Risks and Markets , IMIA Conference, Stockholm-September 2003.

[106] Technical Description T100 Natural Gas, T100 micro turbine system; D 14127-03 Version 3 09/12/29 .

[107] AORA Tulip, Joining hands through sustainable energy for sustainable livelihoods; *Overview of the Technology Solution*. www.aorasolar.com

[108] https://www.nrel.gov/

[109] SolarPILOT User Guide, 2016.

[110] F. Téllez, M. Burisch, Villasente, M. Sánchez, C. Sansom, P. Kirby, P. Turner, C. Caliot, A. Ferriere, C A. Bonanos, C. Papanicolas, A Montenon, R.Monterreal, J.Fernández, *State of the Art in Heliostats and Definition of Specifications*, STAGE STE Projec, Deliverable 12, 2014.

[111] A.Segal, M.Epstein, *The optics of the solar tower reflector*, Solar Energy, Volume 69, Supplement 6, July, Pages 229-241,December 2001

[112] F. Gomez-Garcia, J.González-Aguilar, G. Olalde, M. Romero, *Thermal and hydrodynamic behavior of ceramic volumetric absorbers for central receiver solar power plants: A review*, 2016.

[113] A. Grobler, P.Gauché, *A Review of Aiming Strategies for Central Receivers*, in Proceedings of the second, Southern African Solar Energy Conference, Port Elizabeth, South Africa, 2014.

[114] Personal information.

[115] L. Amsbeck, R. Buck, P. Heller, J. Jedamski, R. Uhlig, *Development of a tube receiver for a solar-hybrid microturbine system*, 14th Biennial CSP SolarPaces Symposium, 2008.

[116] L. Amsbeck, T. Denk, M. Ebert, C. Gertig, P. Heller, P. Herrmann, J. Jedamski, J. John, R. Pitz-Paal, T. Prosinečki, J. Rehn, W. Reinalter, R. Uhlig, *Test of a solar-hybrid microturbine system and evaluation of storage deployment*, SolarPaces Conference, 2010.

[117] J. Christian, C. Ho. *System design of a 1 MW north-facing, solid particle receiver, International Conference on Concentrating Solar Power and Chemical Energy Systems*, SolarPACES 2014 Energy Procedia 69, pag. 340 – 349. 2015

[118] http://www.247solar.com

[119] R. Pitz-Paal, B. Hoffschmidt, M. Bohmer, M. Becker, *Experimental and numerical evaluation of the performance and flow stability of different types of open volumetric absorbers under non-homogeneous irradiation*, Solar Energy 60, 135-150, 1997.

[120] W.Janke, A. Hapka, *Nonlinear thermal characteristics of silicon carbide devices*, Materials Science and Engineering B 176, pag. 289–292, 2011.

[121] D.Canavarro, J.Chaves , M. Collares-Pereira *Simultaneous Multiple Surface method for Linear Fresnel concentrators with tubular receiver*. Solar Energy. Volume 110, December 2014, Pages 105-116